



VNIVERSITAT
D VALÈNCIA [ò] Facultat de
Física

Departament de Física de la Terra i Termodinàmica

Programa de Doctorado en Teledetección



**OPTICAL PROPERTIES OF CLOUDY ATMOSPHERES
THROUGH RADIATIVE TRANSFER AND REMOTE
SENSING: FROM 1D TO 3D APPROACH**

**DOCTORAL THESIS
Caterina Peris Ferrús**

Directed by:
Dr. José Luis Gómez Amo
Dr. María Pilar Utrillas Esteban
Enero de 2021

VNIVERSITAT (ò) VALÈNCIA (ò) Facultat de Física

Departament de Física de la Terra i Termodinàmica



TESIS DOCTORAL

Doctorado en Teledetección

Optical properties of cloudy atmospheres through
Radiative Transfer and Remote Sensing: From 1D to
3D approach

Work directed by:
Dr. José Luis Gómez Amo
Dr. María Pilar Utrillas Esteban

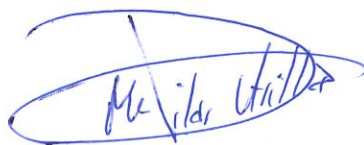
Work presented by:
Caterina Peris Ferrús
Burjassot, enero de 2021

La Dra. María Pilar Utrillas Esteban, catedrática de universidad adscrita al Departament de Física de la Terra i Termodinàmica de la Facultat de Física de la Universitat de València y el Dr. José Luis Gómez Amo, profesor contratado doctor del Departament de Física de la Terra i Termodinàmica e investigador del Grupo de Radiación Solar de la Universitat de València.

CERTIFICAN:

Que la presente memoria titulada: “Optical properties of cloudy atmospheres through Radiative Transfer and Remote Sensing: From 1D to 3D approach”, presentada por Dña. Caterina Peris Ferrús para optar al grado de Doctora por la Universitat de València cursando el Doctorado en Teledetección, ha sido realizada bajo nuestra dirección en el Departament de Física de la Terra i Termodinàmica de la Facultat de Física de la Universitat de València y autorizan su depósito.

Y para que así conste, en cumplimiento de la legislación vigente, firmamos el presente certificado en Burjassot, a 13 de enero de 2021.



Fdo.: María Pilar Utrillas Esteban



Fdo.: José Luis Gómez Amo

A la meua familia

Acknowledgments/Agradecimientos

*With magic, you can turn a frog into a prince.
With science, you can turn a frog into a Ph. D
And you still have the frog you started with.*
(Terry Pratchett)

Parece mentira, pero casi hemos llegado.

Ahora que éste mi doctorado va llegando a su fin, tan largo que cuesta recordar un tiempo anterior a él, toca dar las gracias a todos aquellos que lo han hecho posible, y dedicar un pensamiento a cuantas personas que de una forma o de otra, quedaron tocadas por la onda expansiva de mi tesis doctoral.

En primer lugar, a mis directores, por haber sido un apoyo constante, por vuestra paciencia y guía en este tiempo en el que me he hecho mayor, y por nunca rendiros en la carrera de conseguir financiación. A Pilar, por darme cobijo en este departamento durante tantos años, por tu liderazgo sin parangón del GRSV, tus ideas y tu ejemplo a seguir. Este departamento ha sido mi segunda casa gracias a ti. A José Luis, porque desde aquellas lejanas clases de lidar y desde el trabajo de fin de máster ya decidí que los dolores del doctorado bien podían ser un camino a seguir si era bajo tu auspicio. No tengo palabras para describir todo el agradecimiento acumulado desde que te conozco.

A Josep y Pedro, por sostener sobre vuestros hombros la carga tecnológica del grupo. Esta tesis y muchas más no serían posibles sin vosotros. Josep, gràcies per ser font inagotable de chistes i acudits. Com vaig predir, em trauré abans la tesis que el superior de valencià, però aquells ratets de parlar com alienígenes normativitzats ja són per a mi. Pedro, echaré mucho de menos nuestras conversaciones de arreglar el mundo a martillazos. No sabes cómo me alegro de que siguieses tu carrera ingenieril entre físicos. A Violeta y Francesco, ha sido un honor teneros de compañeros y mucha fuerza para el tiempo que os queda de becarios. Sé que vais a ser grandes investigadores. Y a todos aquellos que formaron y forman parte del grupo, Sara, Carlos, Roberto, David, Anna, María José, Víctor, Fernando, José Antonio... todos dejasteis vuestra impronta en mí y me habéis ayudado de una forma u otra a seguir. I a tu, Lola, et trove a faltar al despatx cada dia.

A Paula i Arantxa, que desde que aterrizamos hace once años en la facultad de física habéis sido soporte, consuelo y confesionario. Sois grandes profesionales, mejores amigas e impagables seres humanos.

Arantxa, desde que te fuiste a Alemania después de haber sido más que compañeras, estudiando codo con codo cada palabra (de tus apuntes, siempre) y cada ecuación del grado y del máster es como si me faltase una mano o una hermana. A Belén, Tatiana, Saray i Virginia, per aguantar cada fosca per culpa de la carrera, màster i tesis. Promet que acabarà tot pronte.

Als meus pares i la meua germana, per haver-me donat sempre el seu suport, afecte i ànims, especialment quan jo mateixa no creia amb mi. Cosa que no faig des-de tercer de primària. Tot el que sóc us ho dec a vosaltres, i a qui dedique aquesta tesi.

Und unendlich danke an Lucas. Das Beste an diesem Doktorat war die Gelegenheit dich kennenzulernen. Jetzt haben wir unser ganzes Leben vor uns.

Este trabajo ha sido posible gracias al apoyo recibido mediante los proyectos CGL2015-64785-R, financiado por el Ministerio de Economía y Competitividad, y el proyecto RTI2018-096548-B-I00, financiado por el Ministerio de Ciencia e Innovación, así como el programa ERASMUS+ en su modalidad de Movilidad de Doctorado y a la colaboración del grupo de Remote Sensing and Radiative Transfer de la Ludwig-Maximilians Universität -LMU liderado por Bernhard Mayer.

List of Acronyms

AERONET	Aerosol Robotic Network
BRDF	Bidirectional reflectance distribution function
CAH	Cloud Average Height
CBH	Cloud Base Height
CC	Cloud Clover
CCN	Cloud Condensation Nuclei
CF	Cloud Field
CMOS	Complementary metal-oxide-semiconductor
COD	Cloud Optical Depth
CTH	Cloud Top Height
DC	Digital Counts
DISORT	Discrete Ordinate Radiative Transfer solver
FOV	Field of View
GCRM	Global Cloud Resolving Model
IPA	Independent Pixel Approximation
iqr	Intequartile Range
ISCCP	International Satellite Cloud Climatology Project
LES	Large Eddy Simulation
libRadtran	Library for radiative transfer
LUT	Lookup Table
LW	Longwave
LWC	Liquid Water Content
LWP	Liquid Water Path
MC	Monte Carlo
MYSTIC	The Monte Carlo Code for the Physically Correct Tracing of Photons in Cloudy Atmospheres
RMSE	Root Mean Square Error
RT	Radiative Transfer
RTE	Radiative Transfer Equation
RTM	Radiative Transfer Model

SAA	Solar Azimuth Angle
SONA	Sistema de Observación de Nubes Automático
SW	Shortwave
SSA	Single Scattering Albedo
TOA	Top of the Atmosphere
VAA	Viewing Azimuth Angle
VZA	Viewing Zenith Angle
WMO	World Meteorological Organization

Content

INTRODUCCIÓN Y RESUMEN	13
1. RADIATIVE TRANSFER THROUGH ATMOSPHERE	25
1.1 ATMOSPHERIC COMPONENTS	25
1.2 RADIATIVE PROCESSES	31
1.3 RADIATIVE TRANSFER MODELS	47
2. PROPERTIES OF CLOUDS, INSTRUMENTATION AND SIMULATIONS.....	63
2.1 CLOUD FORMATION AND CLOUD TYPES.....	63
A. MACROPHYSICAL, MICROPHYSICAL AND RADIATIVE PROPERTIES OF CLOUDS	67
B. CLOUD PROPERTIES RETRIEVALS	72
C. INSTRUMENTATION.....	74
3. METHODOLOGY, DATA AND ANALYSIS	93
3.1. COD ACQUISITION WITH A SKY CAMERA. A 1D APPROACH	93
3.1.1. <i>Sky Camera Characterization and Images pre-treatment.....</i>	<i>94</i>
3.1.2. <i>Cloud Optical Depth Determination</i>	<i>122</i>
3.2. SYNTHETIC STUDY WITH 3D MONTE CARLO	140
4. RESULTS.....	163
4.1. EXPERIMENTAL STUDY. 1D APPROACH FOR SKY CAMERA MEASUREMENTS	163
4.2. SYNTHETIC 3D EVALUATION OF METHODOLOGY AND RESULTS	197
CONCLUSIONS AND FUTURE WORK.....	247
ANNEX.....	255
BIBLIOGRAPHY	261

Introducción y resumen

Las nubes son hidrometeoros en suspensión, que cubren aproximadamente un 70% del planeta y que afectan significativamente el balance radiativo terrestre (Boucher et al., 2013). Dicho impacto depende del rango espectral y los tipos de nubes. Las nubes bajas realzan el albedo planetario, reflejando una gran cantidad de radiación solar, mientras que las nubes altas contribuyen al efecto invernadero, pues reducen la cantidad de radiación térmica que sale al espacio. (Wild et al., 2015). Los cambios en el balance radiativo terrestre afectan a las condiciones térmicas del planeta, así como a la circulación oceánica y el ciclo hidrológico (Lin et al., 2000), entre otros elementos climáticos (Wild et al., 2012).

Con ello, las nubes ejercen un importante efecto radiativo en la superficie terrestre y en la troposfera. El flujo neto de radiación descendente depende de la distribución vertical y horizontal de las nubes, que producen una disminución sustancial de la componente directa, y un incremento de la radiación difusa. Esto por consiguiente conlleva la disminución de la radiación global (Alados-Arboledas et al., 2003; de Miguel et al., 2011).

La influencia de las nubes en la radiación solar tiene asimismo una dependencia espectral significativa, siendo ésta más débil cuanto más corta es la longitud de onda (McBride et al., 2011; Bilbao et al., 2011; de Miguel et al., 2011). Las nubes atenúan parte de la radiación ultravioleta que llega a la superficie (Esteve et al., 2010). Por otro lado, bajo ciertas circunstancias de ángulo cenital solar y cobertura nubosa las nubes pueden producir un aumento de la radiación que llega a la superficie terrestre, en el espectro ultravioleta y también en el espectro visible (Berg et al., 2011; Inman, et al., 2016; Aebi et al., 2017). Este fenómeno se llama realce, y puede alcanzar valores de radiación superiores a los del techo de la atmósfera (Calbó et al., 2005; Núñez et al., 2016).

Las nubes han sido durante décadas objeto de estudio, pero a pesar de todos los esfuerzos e incontables trabajos dedicados a determinar la influencia de las nubes en el clima, este tema sigue representando una incertidumbre importante para los modelos climáticos y las predicciones meteorológicas (Crnivec and Mayer, 2019), así como su rol en el calentamiento o enfriamiento en el sistema climático, que permanece incompleto (Schwartz et al., 2017). Los procesos radiativos en las nubes y los mecanismos de feedback son la fuente dominante de dichas incertidumbres

(IPCC, 2013). Un modelo climático que reduce las nubes de la capa límite en respuesta al calentamiento global tiene una sensibilidad climática dos veces mayor que la de un modelo que no incluye esta retroalimentación (IPCC, 2007; Marshak and Davis, 2005). Asimismo, los diferentes tipos de nubes afectan al clima de forma diferente. Algunos tipos de nubes contribuyen al calentamiento global, mientras que otros causan enfriamiento neto. Estos efectos dependen de la altura a la que se encuentran y de sus espesores ópticos (Whitman, 2011). Se ha visto que el efecto de enfriamiento neto de las nubes no es lo suficientemente grande como para compensar completamente el calentamiento global debido al cambio climático, aunque podrían contribuir en mayor o menor medida al calentamiento global causado por los gases de efecto invernadero.

El IPCC de 2007 (IPCC 2007) informó de que se prevé un incremento en la temperatura media de la Tierra de 1.8° a 4° a finales de siglo con respecto a los valores de 1990, aunque más adelante en el Special Report on Global Warming of 1.5°C (IPCC 2018) indicó que es posible limitar el incremento de temperatura a 1.5°C. Marshak y Davis, (2005) indican que si el calentamiento global causara un aumento del número de tipos de nubes de enfriamiento, el efecto de enfriamiento neto actual de las nubes en el clima de la Tierra probablemente aumentaría, y por lo tanto, moderaría o compensaría el calentamiento global, y la temperatura de la Tierra de fin de siglo podría bajar hacia el extremo inferior del rango (1.5-1.8°-4°) previsto. Sin embargo, el efecto contrario también podría ocurrir. La influencia y los efectos de las nubes jugarán un papel fundamental en el escenario final del calentamiento global, pero éste aún es incierto. Además, el efecto radiativo neto de las nubes podría aumentar o disminuir dependiendo de los efectos del calentamiento global futuro sobre el clima (Whitman, 2011), puesto que el clima en sí influirá directamente sobre la formación y características de la cobertura nubosa.

Como ejemplo, los estratos son nubes bajas que se extienden hasta 2km sobre la superficie terrestre bloquean la radiación directa, por lo que actúan como un parasol que ayuda al enfriamiento terrestre. Por tanto, los estratos tienen un efecto de enfriamiento neto que ayuda a compensar el calentamiento. Sin embargo, los cirros son finos y altos, que pueden posicionarse hasta a 20 km sobre la superficie. Los cirros permiten que la luz solar visible pase casi sin obstáculos mientras que al mismo tiempo atrapan radiación de onda larga que llega de la superficie y que debiera escapar hacia el espacio y la vuelven a irradiar. Con ello, los cirros tienen un efecto de calentamiento neto que ayudan a magnificar el calentamiento global (Lynch, 1996). Finalmente, los cúmulos pueden extenderse verticalmente hasta grandes

alturas, tiene bordes definidos, y pueden formarse solos, en líneas o en grupos. Los cúmulos pueden bloquear la luz del sol, y también pueden atrapar el calor de la Tierra. Su efecto neto sobre el calentamiento depende de la altura a la que se encuentran y de su espesor óptico (Whitman, 2011).

Los efectos radiativos de las nubes están fuertemente sujetos a sus propiedades, como la cobertura nubosa, el espesor óptico, el radio efectivo de las gotas y la fase termodinámica. Otras propiedades microfísicas tales como la distribución de tamaños, la concentración de partículas o el contenido en agua son vitales para la comprensión y obtención de las propiedades radiativas de las nubes. Por tanto, para comprender mejor el rol de las nubes en el clima y en el balance radiativo, la observación y obtención de las propiedades de nubes y aerosoles es crucial. Pero la cantidad de las nubes y sus propiedades, así como las de los aerosoles, son extremadamente variables en el espacio y el tiempo, y por tanto las observaciones continuas, sistemáticas y globales son esenciales para reducir las incertidumbres y las incógnitas en el sistema climático. Por ese motivo y durante décadas se han dedicado grandes esfuerzos se han dedicado durante décadas a obtener parámetros nubosos como el espesor óptico de nubes y el radio efectivo mediante teledetección.

Los satélites han sido desde finales de la década de los setenta un soporte para grandes avances en el estudio de las nubes y de su influencia sobre el clima, dando buenos resultados a escala global. Los generadores de imágenes por satélite son los instrumentos más utilizados para los estudios de las nubes, dado que proveen de cobertura global a largo plazo, a un coste aceptable para el usuario. Los métodos de 'retrieval' de datos desde satélite se focalizan sobre todo en la obtención del espesor óptico, el contenido en agua y/o el radio efectivo, debido a la parametrización existente entre estos parámetros y la independencia de la extinción de la radiación en la distribución de tamaños de las partículas y de la longitud de onda (Kokhanovsky, 2004).

Sin embargo, la observación desde satélite ofrece algunos inconvenientes, como la limitación en la resolución temporal. Por ejemplo, la resolución del Meteosat Segunda Generación (MSG) (Werkmeister et al., 2015) es de 15 minutos, mientras que la del Moderate Resolution Imaging Spectroradiometer (MODIS) (NASA, 2019) es de dos veces al día. Además, se ha comprobado que las propiedades de las nubes obtenidas desde satélite son diferentes a las obtenidas desde suelo (McBride et al., 2011), dado que las medidas desde satélite dependen de la reflectancia de las nubes, mientras que las medidas desde suelo dependen de la transmitancia. Con ello, las

capas superiores de las nubes y sus propiedades son las que más influyen en las medidas de satélite, mientras que a las medidas desde suelo contribuyen todas las capas nubosas más uniformemente (Platnick, 2000).

Una ventaja adicional de la observación desde suelo es que la transmitancia no es tan dependiente del radio efectivo como es la reflectancia (McBride et al., 2011) dado que la radiación transmitida es menos sensible a la distribución de tamaños de las gotas (Rawlins and Foot, 1990). Esto puede dar más margen en la obtención del espesor óptico de las nubes mediante estudios de cierre radiativo, que evalúan las diferencias entre radiancias simuladas y medidas. Los modelos de transferencia radiativa resuelven la ecuación de transferencia radiativa mediante diversas aproximaciones, que suelen estar limitadas por las observaciones disponibles de los flujos radiativos y las propiedades de los componentes atmosféricos, que se establecen como condiciones de contorno para las simulaciones. Los modelos de transferencia radiativa más empleados en los trabajos de la bibliografía son SHDOM (en Mejia et al., 2016), MODTRAN (en Aebi et al., 2017) y libRadtran (en Aebi et al., 2020), entre otros.

En los últimos tiempos se han introducido las cámaras de nubes como instrumentos para la detección y análisis de la cobertura nubosa, dada la necesidad de sistemas de observación terrestres extendidos para los estudios de las nubes. Las cámaras de nubes ofrecen la ventaja de una cobertura total del cielo en alta resolución temporal, así como un coste moderado. Varios trabajos empezaron empleando las cámaras de nubes para determinar la cobertura nubosa, como por ejemplo Long et al., (2006), pero más adelante en trabajos como Wacker et al., (2015) lograron clasificar las nubes detectadas en seis tipos diferentes. Mejia et al., (2016) y Schwartz et al., (2017) por otra parte ya usaron las cámaras de nubes para obtener el espesor óptico de las nubes en estudios de cierre. Ellos se ciñeron al modelo unidimensional de atmósfera plano-paralela mediante la aplicación de la Aproximación de Píxeles Independientes (IPA) (Cahalan et al., 1994), aunque Mejia, et al., (2016) ya se aventuró a extraer algunas diferencias entre el modelo plano-paralelo y nubes más realistas en tres dimensiones.

El modelo unidimensional es el método más sencillo de resolver la Ecuación de Transferencia Radiativa, matemática y computacionalmente. En el modelo unidimensional el esquema de la atmósfera varía sólo en la dirección vertical mientras que se ignoran las variaciones horizontales. Sin embargo, estos supuestos implican varias incertidumbres como, por ejemplo, inhomogeneidades verticales y horizontales y un uso inadecuado de la microfísica de las nubes (Zeng et al., 2012),

lo que conlleva que la comprensión del impacto de las nubes en el clima sea incompleta.

Las nubes realmente están lejos de la naturaleza plano-paralela, principalmente debido a los procesos físicos 3D. El primero, es el denominado “Efecto de heterogeneidad 1D” (Cahalan et al., 1994), mediante el cual el albedo medio de una nube con espesor óptico variable horizontalmente es menor que albedo de una nube uniforme con ese espesor óptico medio. El segundo, el llamado “efecto de transporte horizontal” (Song et al., 2016), hace referencia a la transferencia horizontal de radiación entre píxeles o celdas adyacentes. Los estudios 1D trataron de abordar parcialmente la heterogeneidad de las nubes empleando la Aproximación de Píxeles Independientes (IPA), mediante la cual se realiza la transferencia radiativa separada en cada píxel o columna del dominio. Por tanto, cada píxel es considerado horizontalmente infinito y radiativamente independiente de los demás. Con ello, la IPA aborda la heterogeneidad 1D, pero no tiene en cuenta el efecto del transporte horizontal entre píxeles. Esto conlleva desviaciones en los cálculos de espesores ópticos debido a los mecanismos ignorados. Cuanto mayor es la resolución del modelo y el área de bordes de nubes, más importantes son los efectos 3D. Una tercera fuente de error es que la geometría de la nube puede alterar drásticamente el camino óptico, que cambia dentro de las nubes con el cielo parcialmente cubierto (Mejia et al., 2016).

Los fenómenos 3D están considerados por completo en las simulaciones de transferencia radiativa Monte Carlo en tres dimensiones. El método de Monte Carlo aplicado a la transferencia radiativa consiste en trazar fotones en su paso por la atmósfera desde una fuente, comúnmente el Sol o la superficie terrestre, hasta su final (Mayer, 2009). El fin del trazado de los fotones puede darse por absorción en la superficie de la Tierra, por un agente atmosférico, o desaparecer por el techo de la atmósfera. Una de las fortalezas de la transferencia radiativa Monte Carlo 3D es que es un método que considera todos los procesos atmosféricos y de superficie relevantes en un medio complejo en tres dimensiones sin asumir aproximaciones matemáticas negligentes. Uno de los códigos 3D Monte Carlo más versátiles y conocidos para la transferencia radiativa es MYSTIC, ‘the Monte Carlo Code for the physically correct tracing of photons in cloudy atmospheres’ (Mayer, 2009; Emde et al., 2016).

Sin embargo, la integración del método de transferencia radiativa Monte Carlo en 3D como tal en un estudio de cierre para la obtención de propiedades de los agentes

atmosféricos no es banal, dada la complejidad de una atmósfera real y sus procesos radiativos, la falta de información de entrada al modelo en las tres dimensiones y el coste computacional, entre otras limitaciones. Sin embargo, es interesante aplicar las ventajas que ofrece este nuevo tratamiento de una atmósfera más realista y la transferencia radiativa 3D para mejorar los resultados obtenidos mediante la tradicional aproximación unidimensional plano-paralela, así como testear dichos resultados y parametrizar soluciones en la medida de lo posible.

Con todo ello, los objetivos de este trabajo se dividen en dos grandes bloques. El primero consiste en hacer uso de una cámara de nubes y un mecanismo de cierre para la obtención del espesor óptico de las nubes (COD) en el cielo de Valencia a partir de las cuentas digitales medidas por el instrumento en el canal azul. Esto es posible mediante una previa calibración de la cámara geométrica y radiométrica, aplicando el método descrito en Román et al., (2012) y Román et al., (2017). Con ello, establecemos las coordenadas polares de cada píxel de la cámara, y obtenemos la conversión entre cuentas digitales a radiancias para cada canal del instrumento. En cuanto a la obtención del espesor óptico a partir de las radiancias de la cámara, la metodología seguida es una adaptación de las descritas por Schwartz et al., (2017) y Mejía et al., (2016) mediante la aplicación de la Aproximación de los Píxeles Independientes a las simulaciones de transferencia radiativa de todo el dominio visto por la cámara de nubes.

Debido a esta asunción de atmósfera plano-paralela y unidimensional para cada píxel de la cámara de nubes los resultados que obtenemos se acercan en mayor o menor medida a la realidad, a causa de los efectos radiativos 3D y de las limitaciones de la metodología y del instrumento. Por ello, cada valor de espesor óptico para cada imagen de la cámara analizada viene acompañado de un valor adicional, una bandera o ‘flag’ que indica la fiabilidad del valor de COD. Este producto suplementario de calidad de datos aporta información sobre las circunstancias y problemas en la obtención del espesor óptico mediante la aproximación seguida. Gracias a las banderas podemos analizar los resultados obtenidos, clasificarlos y discernir los fallos y limitaciones de la aproximación unidimensional, para su posterior estudio desde la perspectiva de transferencia radiativa 3D Monte Carlo.

Por tanto, el segundo objetivo de este trabajo es el diseño y ejecución de un estudio sintético para probar la metodología unidimensional de obtención de espesor óptico, y para identificar y parametrizar los posibles efectos 3D en las escenas analizadas y obtenidas. Para ello nos servimos del modelo de transferencia radiativa 3D Monte

Carlo MYSTIC y de un set de campos de nubes (cúmulos y estratocúmulos) en tres dimensiones obtenidos con el software University of California, Los Angeles Large Eddy Simulation model (UCLA-LES), para el experimento Rain in Cumulus over the Ocean (RICO; Rauber et al., 2007). Estos sets de datos fueron cedidos al GRSV para este trabajo por el grupo de investigación Remote Sensing and Radiative Transfer de la Ludwig-Maximilians Universität de Munich liderado por el profesor Bernhard Mayer.

Los campos de nubes poseen una alta resolución nominal de 25m en las tres dimensiones, poseen dimensiones horizontales de $6.4 \times 6.4 \text{ km}^2$ y una extensión vertical de 4km. Mediante el software UCLA-LES se obtuvo en su momento la distribución 3D de contenido en agua (LWC), y el radio efectivo correspondiente se asignó siguiendo la parametrización de Bugliaro et al., (2011). Los campos consisten en dos ejemplos de cúmulos rotos y dos ejemplos de estratocúmulos más uniformes, por lo que la cobertura nubosa aumenta entre ellos, desde aproximadamente 70% a 100%. Estos campos son datos de input de las simulaciones llevadas a cabo con MYSTIC a diferentes ángulos cenitales, para analizar la dependencia de nuestra metodología y nuestros resultados con la cobertura nubosa y con la geometría solar. Los resultados de las simulaciones son matrices de radiancias a partir de las cuales obtenemos los campos de espesor óptico y las matrices de Flags de igual modo que en el primer bloque de esta memoria dedicada a las imágenes de las cámaras de nubes.

Para el análisis, calculamos el espesor óptico de cada uno de los campos LES mediante la integración en cada columna o posición [x,y]. Estas matrices de COD son consideradas la 'verdad' con las que comparar los resultados obtenidos. Mediante esta comparación obtenemos parametrizaciones con las que posiblemente mejorar los resultados obtenidos en imágenes reales de la cámara de nubes, y más información acerca de las mejoras que necesita la metodología seguida.

La presente memoria se divide en cuatro capítulos, además de las conclusiones extraídas de todo el trabajo descrito y la bibliografía. En el primer capítulo describimos la transferencia radiativa en la atmósfera terrestre, exponemos los diferentes componentes atmosféricos y su impacto en las diferentes zonas del espectro electromagnético y en especial en la luz solar. Explicamos el estado del arte acerca del balance radiativo terrestre y el impacto que las nubes y aerosoles tienen en el mismo, a la vez que exponemos la motivación de estudiar las nubes desde suelo con el instrumental empleado.

Más adelante en el mismo capítulo, describimos con detalle los procesos radiativos de dispersión, absorción y extinción de la radiación que tienen lugar en la atmósfera, así como la función de ganancia en una dirección dada. Con ello exponemos la construcción de la Ecuación de Transferencia Radiativa (ETR) a partir de todos los procesos descritos (Lenoble, 1993; Coakley and Yang, 2014). La ETR es una ecuación integrodiferencial que debe resolverse simultáneamente para todas las direcciones. Los modelos de transferencia radiativa (Radiative Transfer Models, RTM) son herramientas de computación que obtienen los flujos radiativos en todas las capas de la atmósfera. Los RTM pueden clasificarse en dos grandes categorías: aquellos que resuelven la ETR mediante aproximaciones matemáticas tales como el método ‘discrete ordinate’ (Chandrasekhar, 1960), y aquellos que emplean la metodología de trazado de fotones, o método Monte Carlo (Eckhardt, 1987). Para finalizar el primer capítulo describimos estos dos mismos métodos que son los aplicados en este trabajo, así como los efectos radiativos 3D y la Aproximación de Píxeles Independientes (IPA).

En el segundo capítulo pasamos a centrarnos exclusivamente en las nubes, el objeto de estudio de este trabajo. En primer lugar, exponemos brevemente los mecanismos de formación, los distintos tipos de nubes, divididas en bajas, medias y altas y sus características. A continuación, explicamos las propiedades microfísicas, microfísicas y radiativas de las nubes y su influencia en las distintas zonas del espectro, donde por consiguiente operan los distintos instrumentos desde satélite, aerotransportados y desde suelo. Terminamos la primera parte de este capítulo haciendo un resumen de las diversas metodologías seguidas en la bibliografía para la obtención de las propiedades de las nubes y del espesor óptico en especial, incidiendo en las metodologías desde suelo y en el uso de las cámaras de nubes. Continuamos el capítulo describiendo la instrumentación empleada en este trabajo, la cámara de nubes SONA201-D y el instrumental auxiliar, a saber, el fotómetro solar CIMEL CE-318 integrado en la red de AERONET y el ceilómetro VL-51 de Vaisala.

En el tercer capítulo describimos la metodología seguida, en primer lugar, para la obtención del espesor óptico y materiales auxiliares a partir de la cámara de nubes y en segundo lugar el estudio sintético. La metodología de la primera parte empieza con el pre procesamiento de las imágenes de la cámara de nubes antes de seguir con la caracterización de la cámara de nubes, mediante la calibración y la obtención de las longitudes de onda efectivas. La calibración consta de dos partes fundamentales: la calibración geométrica y la calibración radiométrica. La primera es un paso básico para la obtención de los mapas de las coordenadas polares, zenith y azimuth (viewing

zenith angle, VZA, viewing azimuth angle, VAA). Por otro lado, la calibración radiométrica es primordial para obtener la conversión entre cuentas digitales y radiancias, para cada canal. En el capítulo introducimos también la validación de la calibración radiométrica mediante los datos de radiancia en almucantar de AERONET.

Una vez caracterizada la cámara, describimos las simulaciones que llevamos a cabo con el modelo de transferencia radiativa libRadtran para componer la Lookup Table con la que convertimos las radiancias a espesor óptico, y los métodos de inversión seguidos para componer la LUT y las matrices auxiliares para calcular las Flags e incertidumbres. A continuación, exponemos el algoritmo para la obtención de las matrices de espesor óptico a partir de la cámara de nubes. Para finalizar la primera parte del capítulo tercero, explicamos cómo tratamos los resultados obtenidos y el análisis al que los sometemos para extraer las conclusiones pertinentes.

El cuarto capítulo de resultados está dividido en dos partes como el capítulo de metodología. Así pues, consta de los resultados del estudio experimental aplicando la aproximación 1D a las medidas de la cámara de nubes, y del estudio sintético 3D para la evaluación de la metodología y los resultados. En el estudio experimental clasificamos los resultados obtenidos con la cámara de nubes en cuatro categorías diferentes de acuerdo a la calidad y la fiabilidad de los resultados, en orden descendente de estas características. Analizamos las imágenes de COD juntamente con las incertidumbres y matrices de Flags y aventuramos las causas de los resultados obtenidos cuando no son satisfactorios, siendo algunas achacables a las limitaciones del método, y otras a los efectos 3D no contemplados en la aproximación unidimensional.

Este análisis nos da pie y motivación para la segunda parte del capítulo, el estudio sintético, en el que llevamos a cabo las simulaciones de radiancias en el suelo con campos de nubes en tres dimensiones de alta resolución con diferente geometría solar. Una vez obtenidas las matrices de COD con la metodología del estudio experimental comparamos los resultados obtenidos con las matrices de espesor óptico 'reales'. En este capítulo también llevamos a cabo una intercomparación entre matrices de resultados para analizar la influencia de la geometría solar en los resultados según la cobertura nubosa, y también para analizar y parametrizar los resultados de acuerdo a los valores de las Flags. Finalizamos el capítulo detallando todas las parametrizaciones obtenidas según las variables analizadas.

Introducción y resumen

En base a los resultados obtenidos y a la bibliografía consultada, concluimos el presente trabajo constatando en primer lugar que la metodología diseñada para la obtención del espesor óptico de nubes mediante la cámara de nubes es útil y adecuada para condiciones de cielo completamente cubierto, con campos nubosos uniformes y espesos como los estratocúmulos. Dichas condiciones se adaptan mejor a las aproximaciones unidimensionales y por tanto no se producen grandes negligencias que repercutan en los resultados.

Sin embargo, la metodología seguida requiere mejoras que atañen a la eliminación de la ambivalencia de espesor óptico para un valor de radiancia monocromática dado, y una vez habiendo resuelto esto, se debería proceder a un estudio más exhaustivo de lo que se ha empezado a vislumbrar en este trabajo acerca de los efectos radiativos 3D en las nubes.

Para un futuro trabajo se propone, además del uso de un instrumento que permita la eliminación de la ambivalencia, el empleo de los avances del Grupo de Radiación Solar de Valencia en materia de obtención de imágenes HDR con la cámara de nubes para aumentar el rango dinámico de las medidas y realizar una mejor calibración del instrumento y sus correspondientes incertidumbres. Por otro lado, para un estudio más profundo de los efectos radiativos 3D que permitan mejorar los resultados de las aproximaciones unidimensionales en los estudios de cierre, se propone expandir el presente estudio sintético al estudio del albedo de los campos nubosos de alta resolución y al estudio del transporte horizontal por capas a diferentes escalas.

Con ello se espera que sea posible mejorar con mucho los resultados en los bordes de las nubes, donde tiene lugar la interacción con los aerosoles.

Chapter 1

Radiative Transfer through Atmosphere

In this chapter we describe the several atmospheric components and their impact in the electromagnetic spectrum, especially on solar radiation. The state of the art about the Earth's radiative budget is explained, as well as the impact of clouds and aerosols on it, introducing the motivation of studying clouds by means of ground-based instruments. Next, we describe the transfer of radiation through the atmosphere, by means of the detailed definition of the radiative processes that compose the Radiative Transfer Equation (RTE). To end the chapter, we introduce the Radiative Transfer Models that either solve the RTE by means of mathematical approximations, or employ the photon tracing methodology, or Monte Carlo Method. The chapter finishes with the Independent Pixel Approximation description as well as the 3D radiative effects that occur by the horizontal transport in atmosphere neglection.

1. Radiative Transfer through atmosphere

1.1 Atmospheric Components

1.1.1. The Electromagnetic Spectrum

The Electromagnetic (EM) Spectrum is the energetic distribution of the electromagnetic radiation, in terms of wavelengths and photon energies. The EM spectrum ranges from radio waves, with frequencies below one Hertz, to Gamma rays, with frequencies above 10^{25} Hertz.

The frequencies ranges are divided by bands, and the electromagnetic waves within each band receive different names, as can be seen in Figure 1.1, from lower frequency to higher frequency: Radio Waves, Microwaves, Infrared, Visible Light, Ultraviolet, X-Rays and Gamma Rays. As seen in Figure 1.1 wavelengths corresponding to the EM bands range from thousands of kilometres to the sizes of subatomic particles.

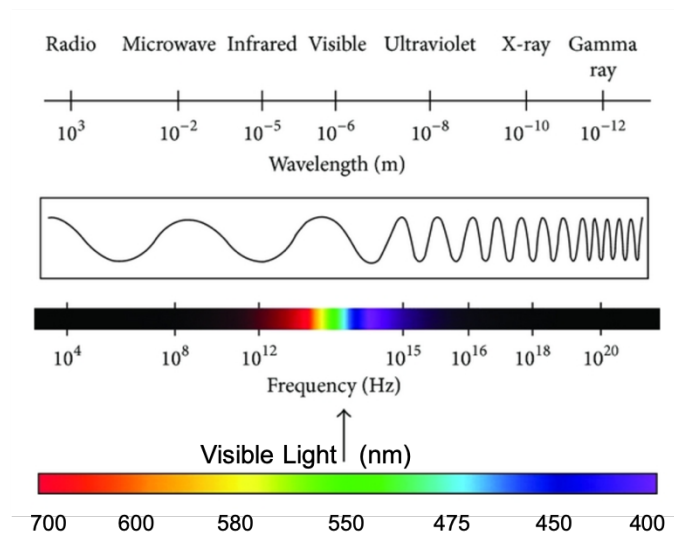


Figure 1.1 : Electromagnetic Spectrum, EM bands in wavelengths and frequencies. Visible Spectrum.

The EM bands are differentiated according to how they are produced and how they interact with the matter. Therefore, the electromagnetic light as it passes through the

1. Radiative Transfer through atmosphere

atmosphere from the Sun gets affected by different atmospheric components in the different band frequencies. Scattering in the atmosphere is a spectrally continuous process, occurring mostly in gases and aerosols, whereas absorption by gases occurs in discrete bands. Atmospheric molecules alter the electromagnetic radiation by absorbing part of its energy at determined wavelengths, corresponding to their rotational, vibrational or electronic transitions. The electromagnetic radiation can also ionize or photo dissociate gas molecules. This means that different gases produce different absorption lines over the solar radiation spectrum.

Figure 1.2 shows the irradiance (yellow) at the Top of the Atmosphere (TOA) coming from the Sun, which approximates a blackbody spectrum at around 6000K (grey line). At the TOA, about 1369W/m^2 of solar radiant energy is incident normally over the atmosphere (Bohren and Clothiaux, 2006) which is distributed from the UV to NIR (280nm - $5\mu\text{m}$). Once the solar irradiance penetrates the atmosphere, gets significantly altered by the atmospheric components. Figure 1.2 shows solar irradiance at the earth's surface for a typical cloudless day, with about 51% of the solar irradiance at Earth's surface lies in the infrared, 42% in the visible, and 7% in the ultraviolet.

The ultraviolet radiation (100nm-400nm) from the Sun gets principally affected by atmospheric gases and the ozone layer in the Mesosphere (Figure 1.2, ultraviolet sector). The higher energy ranges of UV (vacuum UV, UVC) get absorbed by nitrogen and by O_2 in the air (Holton et al., 2003). The ozone layer contributes to extinguish completely the UVC radiation (100nm-280nm) and significantly absorbs the UVB radiation (280nm-315nm) (NASA, 2002). Therefore, in the UVB region, the most important absorbing gases are Ozone and Oxygen, due to their electronic transitions.

The Visible range (400 –750 nm), is characterized the Chappuis Ozone absorption band, which ranges from 440 nm to 650 nm (Shaw, 1979; Brion et al., 1998). The NIR is also influenced by the Oxygen A-Band (~759-771 nm) (Richardson and Stephens, 2018) and narrow water vapor absorption bands, which are also present in the NIR region (wavelengths larger than 750nm), altogether with Ozone and CO_2 bands (Figure 1.2, Near infrared sector).

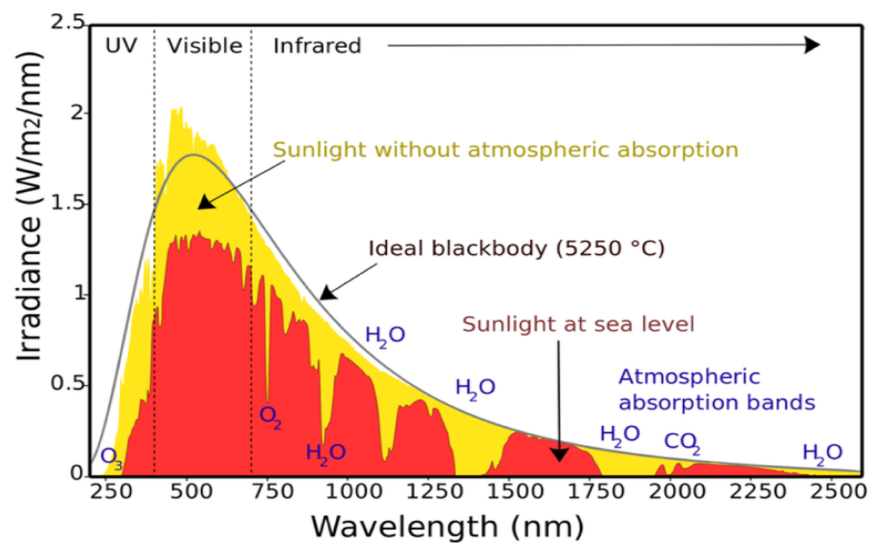


Figure 1.2 : Solar spectrum at TOA, and at Earth's Surface, after the action of the atmospheric absorption bands (Global Warming Art project, Rohde, 2016).

In short, the Earth's Atmosphere modulates the Sun radiation, with each of its components playing a fundamental role in the balance of the Earth-Atmosphere system.

1.1.2. Radiative Budget on Earth

The Earth-Atmosphere system reflects back approximately the 30% of the solar radiation (SW) that reaches the TOA (Graham, 1999), whereas it absorbs the 70% remaining. Approximately, a 70% of the absorption occurs at the Earth surface, mostly over the oceans. The re-emission of the absorbed SW radiation to space is necessary to maintain the equilibrium in the Earth-Atmosphere system. Therefore, the Earth system also emits thermal radiation (LW), which is partly absorbed by the atmospheric gases (National Weather Service, 1999).

Figure 1.3 represents a schematic diagram of the global mean energy balance of the Earth. Most of the components were estimated by Wild et al., 2012 and readapted in Wild et al., (2015), or derived from satellites measurements. The global mean TOA components are 340 Wm^2 and 100 Wm^2 , for the incoming SW irradiance and the

1. Radiative Transfer through atmosphere

reflected SW radiation, respectively. This leaves a net absorbed SW radiation of 240 Wm^2 by the Earth-atmosphere system.

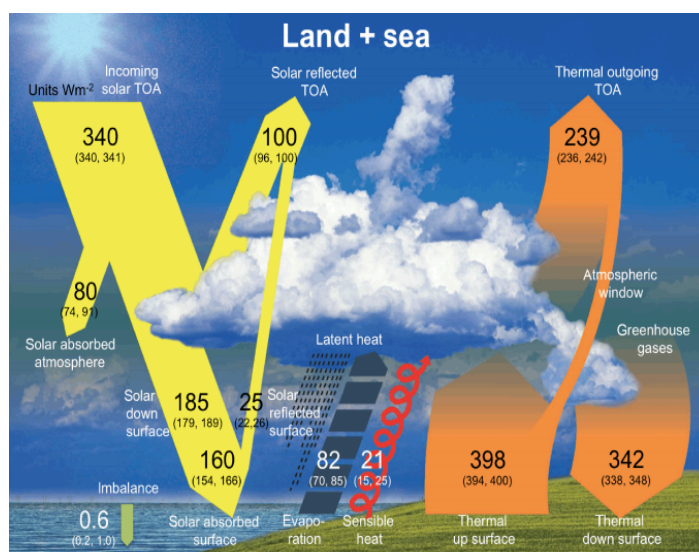


Figure 1.3 : Global mean energy balance components and uncertainties (Wild et al., 2015)

On the other hand, direct surface observations give a better estimate of 185 Wm^2 for the downward SW radiation (Wild et al., 2015). Plus, considering the surface albedo, the reflected SW radiation is obtained as 25 Wm^2 . Therefore, the difference between the downward SW radiation and the reflected SW radiation on surface leaves 160 Wm^2 of solar radiation absorbed at the Earth's surface (see the yellow arrows in Figure 1.3).

With this, given 240 Wm^2 net incoming radiation at TOA (the 340 Wm^2 minus the 100 Wm^2 reflected back to space) and the 160 Wm^2 of SW radiation absorbed at surface, gives an amount of 80 Wm^2 as a residual for the absorption of SW radiation in the atmosphere. This value coincides with the estimation of Kim and Ramanathan, 2008, determined in the Monte Carlo Aerosol-Cloud Radiation (MACR) with global data sets for aerosols, cloud physical properties and radiation fluxes.

On the other hand, the thermal (LW) estimated fluxes at the surface are 342 Wm^2 downward, and 398 Wm^2 upward (see orange arrows in Figure 1.3). The latter was obtained by the surface temperature distribution and the Stefan-Boltzman law. This

leads to a net surface LW cooling of -56 Wm^2 . The LW cooling together with the surface absorbed SW radiation of 160 Wm^2 , gives an excess of radiation on the Earth's surface of 104 Wm^2 , which is divided between the sensible heat flux and the latent heat flux, as 21 Wm^2 and 82 Wm^2 , respectively. A small amount remaining, 0.6 Wm^2 is going to the subsurface, predominantly into the oceans. It is known as the planetary energy imbalance.

Clouds alter the Earth radiative budget by means of absorption and scattering of electromagnetic radiation, although their effects are different according to the spectral range: ultraviolet, visible or infrared, and also according to the cloud type. Low clouds enhance the planetary albedo, reflecting a big amount of SW radiation. This mechanism exerts a global and annual shortwave cooling of approximately -50 Wm^{-2} (IPCC, 2014). On the other hand, high clouds contribute to the greenhouse effect, by means of reducing the quantity of LW radiation escaping to the space. High clouds absorb the thermal radiation from the land surface and re-emit it at a lesser temperature.

Clouds also affect the hydrological cycle and atmospheric dynamics. At regional or local level, vertical and horizontal distribution of clouds affect to the net SW flux of radiation at the surface. Therefore, clouds produce the strongest changes in SW radiation with a substantial decrease of the direct component and an increase of the diffuse radiation, which lead to a decrease in radiation (Alados-Arboledas et al., 2003; de Miguel, et al., 2011). The influence of the cloudiness on SW radiation presents a spectral dependence, being weaker at shorter wavelengths (McBride et al., 2011; Bilbao et al., 2011; de Miguel et al., 2011). On the other hand, clouds can also produce enhancement of SW radiation at surface, reaching levels even higher than its value at the top of the atmosphere (Antón et al., 2011; Núñez et al., 2016).

In the published literature, radiation enhancement is defined as the increase in percentage of the surface irradiance exceeding the clear sky value with the same atmospheric conditions, as sun geometry, gases total columns, aerosols amount, etc (Núñez et al., 2016). This is caused by the presence of clouds in the circumsolar region, which under special circumstances leads to an increasing of the diffuse downwelling SW radiation due to forward scattering from clouds (Inman et al., 2016).

The changes in the SW radiation influences the LW radiation in the radiative budget, as well as atmospheric and oceanic circulation and the hydrological cycle, among other climate elements (Wild et al., 2012). It is difficult to correctly determine these

1. Radiative Transfer through atmosphere

energy exchanges at the Earth's surface on a global level, due to the lack of global coverage of sensors, even though geostationary and polar orbiting satellites fill in some of the gap. For that it is necessary to work with numerical models which calculate the radiative transfer through the atmosphere. Besides, for a comprehensive prediction of changes in cloudiness it is required a global climate model.

Cloud processes have been for decades the dominant source of uncertainty in their representation in climate models and therefore in the understanding of their influence in the climate system (e.g. Randall et al., 2003; Bony et al., 2006). A model that decreases boundary layer clouds in response to global warming has a climate sensitivity twice that of a model that does not include this feedback (Marshak and Davis, 2005). Despite decades of cloud observations, the understanding of their warming or cooling role in the climate system remains incomplete (Schwartz et al., 2017).

In addition, different types of clouds affect the Earth's climate differently. The radiative effects of clouds are strongly subjected to cloud properties such as cloud cover, optical thickness, droplet effective radius and thermodynamic phase. Cloud net cooling effect is not large enough to completely offset the global warming due to climate change, although they might impact the warming effect caused by greenhouse gases. Moreover, cloud net radiative effect could increase or decrease, it depends on the effects of future global warming over climate (Whitman, 2011).

To better understand the role of clouds in climate and the radiative budget of the Earth-atmosphere system, observations of clouds and aerosol optical properties are crucial. Clouds and aerosols amount and properties are extremely variable in space and time. Therefore, continuous and global observations are essential to reduce uncertainties and unknowns in the climate system. The cloud-radiation interactions and the influence exerted by environmental variables are studied using radiative transfer models, which solve the radiative transfer equation through several approaches. Usually, these approaches are constrained by the available observations of radiative fluxes and the properties of the atmospheric components, which are settled as boundary conditions for the simulations.

1.2 Radiative Processes

Electromagnetic radiation is modified by *absorption* and *scattering* in its passage through the atmosphere. These processes are caused by the interaction of the electromagnetic radiation with the atmospheric components: molecules and particles (Lenoble, 1993; Pidwirny, 2006; Chiron de la Casinière and Cachorro Revilla, 2008).

Both processes, absorption and scattering cause a removal of energy from the original incident direction. **Absorption** is the energetic transformation that the electromagnetic radiation suffers, by a net alteration of the energy levels of the molecules and atoms. The electromagnetic wave transfers part or all of its energy to the atom or molecule, exciting it to a higher energy level. Therefore, this process is spectrally discrete and in the framework of quantum physics (Henderson, 1979). There are also spectrally continuous absorption processes that appear in some atmospheric windows, related to the superposition of tails of different absorption lines. On the other hand, **Scattering** determines the change of the incident radiation direction relating to the original direction. This process is spectrally continuous without a net alteration of the energetic levels, and within the framework of classical electromagnetism (Pérez-Juste and Nieto-Faza, 2015). The combined action of absorption and scattering is known as **Extinction** (Lenoble, 1993).

The atmospheric agents also affect radiation by means of scattering, when spatial inhomogeneities in the dielectric constant of the environment are produced, as a consequence of fluctuations in the air density. The size of the particles responsible of scattering ranges from 0.01 μm , corresponding to gas particles, to 1 cm, typical of hail particles (Utrillas, 1995).

The introduction of the Radiative Transfer Equation arises in a natural way when the involved processes are analysed.

i. Scattering processes

Scattering is defined as the deflection process of electromagnetic radiation, which occurs when electromagnetic waves travel from one medium into another with a different refractive index. It can be schematized as in **Figure 1.4**. Radiation strikes the scatterer with the \vec{n}^{inc} incoming direction, and it is deflected in the \vec{n}^{sca} scattered direction. ϕ is the azimuth angle, that defines the direction \vec{n}^{ϕ} and Θ is the scattering

1. Radiative Transfer through atmosphere

angle, and defines the scattering direction, so it is the most important parameter in scattering process. Vectors \vec{u} and \vec{v} lie in the perpendicular plane to the \vec{n}^{inc} .

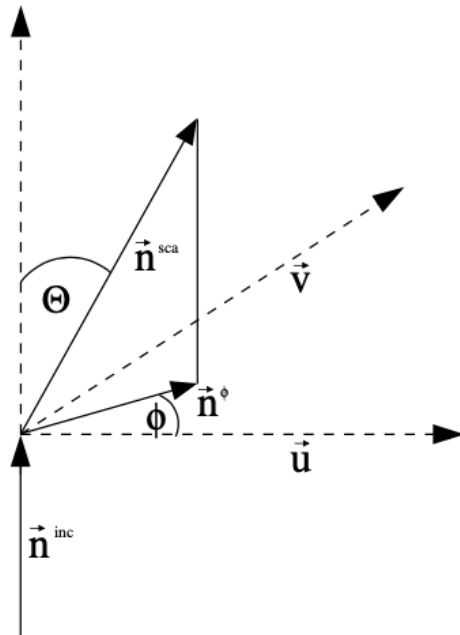


Figure 1.4 : Scheme of the scattering process. The scattering angle

The scattered radiation in the atmosphere can be approached in three different ways: *Rayleigh* or *molecular scattering*, *Mie scattering* and *geometric optics*. The distinction between these three regimes is done by means of the size parameter, $\alpha = \frac{2\pi r}{\lambda}$ (Mie, 1908), which relates the physical size of spherical scatterers by means of the geometric radius, r , and the wavelength of the incident radiation, λ . The size parameter defines the optical properties of particles, as well as the refraction index, m .

Rayleigh scattering is conducted by atmospheric molecules of radius smaller than 0.03λ (Moosmüller and Sorensen, 2018). Such condition does not include atmospheric aerosols in the solar spectrum region. On the other hand, Mie theory is applied when the size parameter ranges from 1 to 100.

For $\alpha \gg 1$, the scattering problem is solved through geometric optics. This is the case of water droplets in many species of clouds.

Rayleigh Scattering

Rayleigh Scattering occurs with the gases in the atmosphere. Their molecules are separated at wider distances than their sizes and their movements are approximately random. This causes that the scattered wave phases by gases are independent of each other, and their intensities can be added. Therefore, this process is treated as ‘independent’ or ‘incoherent scattering’ (Sobrino et al., 2001; Bohren and Clothiaux, 2006).

In Rayleigh theory (Rayleigh, 1899) an incident electric field E induces over the molecule a dipole moment \mathbf{p} that oscillates at the same wavelength frequency. The electric dipole emits radiation and therefore it becomes a source of a secondary electric field E' . The total electric field outside the particle is expressed in equation (1.1).

$$E_T = E + E' \quad (1.1)$$

Being the module of the primary E field, with w the incident frequency, written in eq. (1.2).

$$E = E_0 \sin wt \quad (1.2)$$

On the other hand, the intensity of the secondary field, by means of the module of the Poynting vector, $I = \left(\frac{1}{2}\right) c \epsilon E^2$, takes the shape of eq. (1.3).

$$I' = \frac{\omega^4 p_0^2 \sin^2 \phi}{32\pi^2 \epsilon_0 c^3 R^2} \quad (1.3)$$

Being ϕ the angle between the axis of the dipole and any direction, R any distance in that direction, c the speed of light and ϵ_0 the dielectric constant of the vacuum.

Considering a differential element of volume dV the scattered energy in the direction $\pi - \theta$ with respect to the incident direction, in a solid angle $d\omega$ is given by equation (1.4) (Horvath, 2014).

$$d\Phi_\lambda^2 = \beta_\lambda^2 I_\lambda dV d\omega \quad (1.4)$$

1. Radiative Transfer through atmosphere

Where Φ_λ is the scattered flux, I_λ the density of the incident energy over the Volume element and β_λ the Volume Scattering Coefficient in the θ direction.

The dipole moment can be expressed as a function of the refraction index, m , as in (1.5).

$$\sum p_0^2 = \frac{(m^2 - 1)^2 E_0^2}{16\pi^2 N} \quad (1.5)$$

Where N is the number of the scatters per volume unit.

By means of the calculation of the average value, over a period, of the energy density corresponding to the secondary field (1.6), the volume dispersion coefficient can be written as in equation (1.7).

$$\Phi = \langle I_T' \rangle \cdot R^2 \quad (1.6)$$

$$\beta_\lambda^\theta = \frac{\Phi_\lambda}{I_\lambda} = \frac{(m^2 - 1)^2 (1 + \cos^2 \theta)}{8\epsilon_0^2 N \lambda^4} \quad (1.7)$$

The integration of (1.7) over the solid angle 4π results into the Total Volume (Rayleigh) Scattering Coefficient in eq. (1.8).

$$\beta_{sca.R}^\lambda = \frac{8\pi^3 (m^2 - 1)^2}{3N\lambda^4} \quad (1.8)$$

Mie Scattering

Mie's theory (Mie, 1908) is based on classical electromagnetism equations with boundary conditions at the limit between the particle and its surroundings, as well as ligatures in the infinity. Mie theory defines the *Phase Function* $p(x, m, \theta)$, which describes the angular distribution of the scattered energy by a particle. The phase function can be interpreted as the probability density function for the scattering direction.

Let us consider a plane wave, linearly polarized, with a frequency w , propagating through a spherical, homogeneous particle, with radius r , and refractive index m . The electromagnetic field is partly transmitted into the particle, and partially scattered. As

a result, the field external to the sphere may be described as composed by the incident plane wave plus the scattered wave.

So, it can be proven that the fields outside the sphere, can be written as in equations (1.9) and (1.10). The field components u and v are composed by the incident plane wave plus the scattered wave.

$$u = \exp(iwt) \cos \phi \sum_{n=1}^{\infty} (-a_n)(-i)^n \frac{2n+1}{n(n+1)} P_n^1(\cos \theta) h_n^{(2)}(kr) \quad (1.9)$$

$$v = \exp(iwt) \sin \phi \sum_{n=1}^{\infty} (-b_n)(-i)^n \frac{2n+1}{n(n+1)} P_n^1(\cos \theta) h_n^{(2)}(kr) \quad (1.10)$$

Where $h_n^{(2)}(kr)$ is the Hankel function, which is cancelled at infinity, being r the position vector of the point where we calculate the field, $P_n^1(\cos \theta)$ is a Legendre function, the angles (θ, ϕ) define the propagating plane as Figure 1.4 show, and w is the wave frequency. The coefficients a_n and b_n are determined by the boundary conditions of continuity of the field components on the sphere's surface. They are dependent on the refractive index m , and of the Mie's size parameter, $\alpha = \frac{2\pi r}{\lambda}$.

On the other hand, one of the most employed properties of the scattered wave is the *Intensity*, the energy flux per area unit $\left(\frac{W}{m^2}\right)$. It is also important that the scattered wave anywhere in the distant field ($r \gg \lambda$) has a spherical wave character.

Therefore, the intensity of the scattered wave at a distance r of the particle takes the shape of equation (1.11).

$$I = \frac{I_0 F(\theta, \phi)}{r^2 k^2} \quad (1.11)$$

Being I_0 the intensity of the incident wave, and k the wave number. $F(\theta, \phi)$ is a dimensionless function, or *scattering diagram*, which expresses the angular characteristics of the particle scattering. The relative values of I , or $F(\theta, \phi)$ can be represented in a polar diagram, as a function of θ in a fixed plane defined by ϕ . In Figure 1.5 we can see that aerosols and cloud droplets scatter preferably on the same direction of the incident radiation, a.k.a. forward scattering. Therefore, the distribution pattern of the radiation is highly asymmetric.

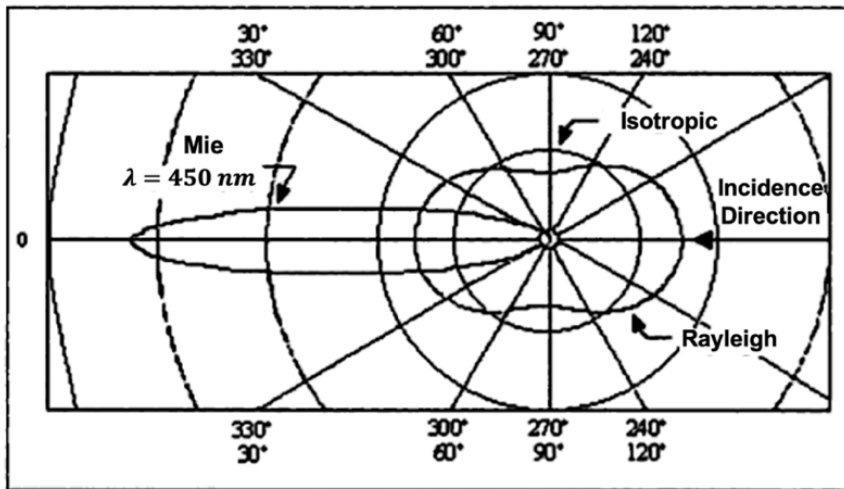


Figure 1.5 : Scattering diagram for a single nucleus, for the particular cases of Isotropic scattering, Rayleigh scattering and Mie scattering (ad. from Sobrino et al., 2001)

Given the characteristics of the scattered wave in a distant field, it can be also written as in eq. (1.12).

$$u = u_0 \cdot S(\theta, \phi) \cdot \frac{\exp(-ikr + ikz)}{ikr} \quad (1.12)$$

Where $S(\theta, \phi)$ is the amplitude function and z refers to the propagation direction in the z axis. When natural light falls on a spherical particle with an intensity I_0 , the scattered light in any direction is partially polarized, and (1.11) can be rewritten as in (1.13).

$$I = \frac{1}{2}(i_1 + i_2) \frac{1}{r^2 k^2} I_0 \quad (1.13)$$

Where the terms i_1 and i_2 refer to the light intensity vibrating in the parallel and perpendicular planes, respectively, to the plane defined by the direction of incidence and dispersion. From (1.12) and the intensity distributions, it can be concluded that i_1 and i_2 take the shape of the functions in equations (1.14) and (1.15).

$$i_1 = |S_1(\theta)|^2 = \left| \sum_{n=1}^{\infty} \frac{2n+1}{n(n+1)} (a_n \pi_n + b_n \tau_n) \right|^2 \quad (1.14)$$

$$i_2 = |S_2(\theta)|^2 = \left| \sum_{n=1}^{\infty} \frac{2n+1}{n(n+1)} (a_n \tau_n + b_n \pi_n) \right|^2 \quad (1.15)$$

Being the terms π_n and τ_n in (1.14) and (1.15), the functions depicted in (1.16) and (1.17).

$$\pi_n = \frac{1}{\sin \theta} P_n^1(\cos \theta) \quad (1.16)$$

$$\tau_n = \frac{d}{d\theta} P_n^1(\cos \theta) \quad (1.17)$$

Since equations (1.14) and (1.15) are functions of the coefficients a_n and b_n , the terms i_1 and i_2 are also dependent of the refractive index, the size parameter and the scattering angle θ .

Equations (1.13) to (1.17) allow characterization of aerosol and cloud droplets radiatively by means of the calculation of scattering cross section and coefficients (Van de Hulst, 1957).

Scattering implies an angular redistribution of the electromagnetic radiation propagating among a non-absorbing environment, with a layer of thickness dx located perpendicular to the propagation direction. Therefore, the radiance disappearing from the original direction of propagation appears again in form of radiance in other directions. The process is schematized in Figure 1.6 where the scattered radiance from the original beam appears as L_s . The fields treated in the previous equations of scattered energy by molecules or particles, are represented in the parameters $L+dL$ and L_s . With it, the *Volume Scattering Coefficient* β_{sca} (Horvath, 2014) can be written in terms of radiance loss as in (1.18). Given the dependencies of the scattered radiation, the Volume Scattering Coefficient is therefore dependent on the Θ scattering angle.

$$dL = -\beta_{sca}(\lambda, x, \Theta) L dx \quad (1.18)$$

1. Radiative Transfer through atmosphere

If we integrate (1.18) for all the atmospheric column, the *Beer Law of Scattering* is obtained, as (1.19) shows.

$$\begin{aligned} L(0) &= L(\infty) \exp\left(-\int_0^{\infty} \beta_{sca}(\lambda, x, \theta) dx\right) \\ &= L(\infty) \exp(-k_{sca}(\lambda, \theta)) \end{aligned} \quad (1.19)$$

Being the term k_{sca} (1.20) the *Scattering Optical Depth*. It is a dimensionless magnitude widely employed in atmospheric physics and in remote sensing. It expresses the opacity of the environment to the signal transmission due solely to the scattering process.

$$k_{sca}(\lambda) = \int_0^{\infty} \beta_{sca}(x, \theta) dx \quad (1.20)$$

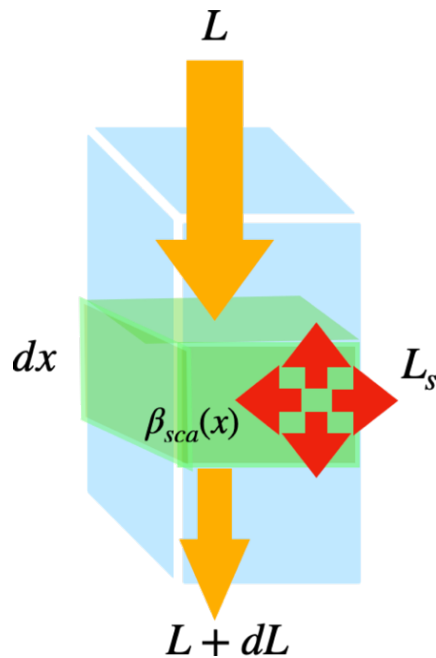


Figure 1.6 : Scattering process in an atmospheric volume element

Finally, a very important magnitude regarding to scattering is the *Single Scattering Albedo* w_0 , which expresses the relative importance of the scattering process as part of the global extinction in the material environment, as in (1.21).

$$w_0 = \frac{\beta_{sca}}{\beta_{ext}} \quad (1.21)$$

ii. Absorption processes

Absorption in the atmosphere is mainly conducted by gases. When an electromagnetic wave with energy E_i interacts with the atom of a gas, it is excited to a higher level of energy, E_f (Elachi and van Zyl, 2006, (1.22)). In this process, some or all of the wave energy is transmitted to the environment.

$$E_f = E_i + h\nu \quad (1.22)$$

The excited atom is not stable and can decay to a lower energy state. In this decay the atom emits part of all the energy in turn as an electromagnetic wave, as (1.23) expresses.

$$E_f - E_i = h\nu \quad (1.23)$$

Therefore, the energetic levels of the atoms are quantized. They cannot absorb any kind of photon with which they interact, but only discrete values, and the absorption and emission patterns are formed by absorption lines and bands.

In the case of the molecules, the total absorbed energy E can be divided in four energy modes (Woodhouse, 2006), as (1.24) shows.

$$E = E_{rot} + E_{vib} + E_{elec} + E_{trans} \quad (1.24)$$

In (1.24) E_{rot} is the rotational energy, E_{vib} is the vibrational energy, E_{elec} is the electric energy and E_{trans} , the translational energy. All the energy forms are quantized and only can take discrete values, except the translational energy, which can take any value.

1. Radiative Transfer through atmosphere

The rotational transitions are the less energetic, and involve the microwaves (Gordy and Cook, 1970). They depend on the shape of the molecules (diatomic, triatomic), related to the moments of inertia in all three axes (Hollas, 2002).

The vibrational transitions occur at higher energies, a.k.a., they absorb photons in the spectrum region with lower λ (Di Lauro, 2013). The H₂O in the IR and the CO₂ at 15 μm produce absorption lines because of vibrational transitions.

By last, electronic transitions are the most energetic ones, and they occur in the VIS and UV regions (Morrill et al., 1981). The Ozone absorption bands, such as the Hartley bands (200 nm – 300 nm), Huggins bands (320 nm – 360 nm) and Chappuis bands (375 – 650 nm) are due to electronic transitions.

Therefore, the different gases produce different absorption lines over the solar radiation and thermal spectrum (Rothman et al., 2013). The absorption is characterized by the *Absorption Coefficient*, $\beta_{abs}(\nu)$, whose units are m^{-1} . The absorption coefficient presents a maximum at a determined frequency, ν_0 , but the coefficient decreases monotonously on both sides of the maximum, tending rapidly to zero, thus forming the absorption lines.

The spectral width of the absorption lines is due to three main contributions: the average life of the excited state or natural width, derived from the uncertainty principle; the gas temperature, which produces Doppler effect by the different relative speeds of the molecules (Siegman, 1986); and the gas pressure, which induces collisions that disturb the excited state (Peach, 1981).

If many absorption lines contribute to the absorption in a $\Delta\nu$, then the sum of all lines N as in (1.25), must be weighted in the interval.

$$\beta_{abs}(\nu) = \sum_{j=1}^N \beta_{abs}^j(\nu) \quad (1.25)$$

When several gases absorb in the same spectral region, the monochromatic transmissivity at one frequency ν , $\bar{\tau}$, is the product of the transmissivities of the individual gases, $\bar{\tau}_i$, as (1.26) shows.

$$\bar{\tau} = \prod_i \bar{\tau}_i \quad (1.26)$$

It must be pointed out that the absorption spectrum could be continuous, due to a non-resonant absorption between the lines, related to the ‘tails’ of the absorption lines, which decay very slowly.

A radiation beam propagating through a non-scattering atmospheric layer of thickness dx , loses energy due to the absorption of the gases that compose it, associated to the wavelength. The process is schematized in Figure 1.7, where the absorbed radiance appears as L_a . With it, the variation of the radiance, due to its conversion to another ways of energy, can be written as in (1.27).

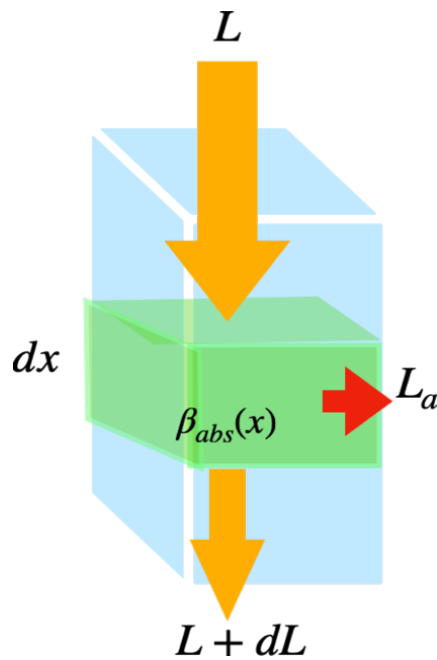


Figure 1.7 : Absorption process in an atmospheric volume element

$$dL = -\beta_{abs}(\lambda, x) L dx \quad (1.27)$$

The term σ_a in (1.27) is the Volume Absorption Coefficient (units of inverse length), which is equivalent to the fraction of the energy absorbed by the dx layer (units of length).

If we integrate (1.27) for all the atmospheric column, the exponential *Beer Law of Absorption* (Bohren and Clothiaux, 2006) is obtained, as in (1.28).

1. Radiative Transfer through atmosphere

$$L(\lambda, 0) = L(\lambda, \infty) \exp\left(-\int_0^{\infty} \beta_{abs}(\lambda, z) dx\right) = L(\lambda, \infty) \exp(-k_{abs}(\lambda)) \quad (1.28)$$

Being the term k_{abs} (1.29) the *Absorption Optical Depth*. It is a dimensionless magnitude defined equivalently to the Scattering Optical Depth. k_{abs} expresses the opacity of the environment to the signal transmission due solely to the absorption process.

$$k_{abs}(\lambda) = \int_0^{\infty} \beta_{abs}(\lambda, x) dx \quad (1.29)$$

(1.28) leads to the definition of the dimensionless magnitude *Transmissivity* (T) (1.30) among the atmospheric layer or column on the propagation direction.

$$T = \frac{L(\lambda, 0)}{L(\lambda, \infty)} = \exp(-k_{abs}(\lambda)) \quad (1.30)$$

And subsequently, the magnitude *Absortivity* (A) is defined as $1 - T$.

iii. Global Extinction

Global extinction is the consequence of the joint action of absorption and scattering (equation (1.31)).

$$\beta_{ext} = \beta_{abs} + \beta_{sca} \quad (1.31)$$

The integration of the *Extinction Coefficient*, β_{ext} from (1.31) leads to the *Optical Depth*, a dimensionless quantity to describe the extinction of radiation passing through the medium (Wallace and Hobbs, 2006).

$$\tau(x, \lambda) = \int_x^{\infty} \beta_{ext}(x', \lambda) dx' = \int_x^{\infty} \sigma_{ext}(x) \rho(x) dx' \quad (1.32)$$

Being σ_{ext} in (1.32), the *Extinction Cross section* in $\text{cm}^2/\text{particle}$, and ρ the number density in $\text{particles}/\text{cm}^3$. The Optical Depth (1.32) describes the extinction of radiation regardless of whether it occurs by dispersion or absorption.

On the other hand, the mass of a unit section column (Figure 1.8), is the section of atmospheric mass (ds) of density ρ that the light passes through propagating with a

certain direction of incidence with respect to the vertical. Since the atmosphere is refractive, the ds integral is monochromatic.

Therefore, this mass is defined as *Absolute Optical Mass* (Bohren and Clothiaux, 2006) and is calculated as in (1.33).

$$m_{abs} = \int_0^{\infty} \rho \cdot ds \quad (1.33)$$

Plus, the *Relative Optical Mass* can be obtained as in (1.34), by means of dividing the Absolute Optical Mass by the column mass integrated over the vertical direction z .

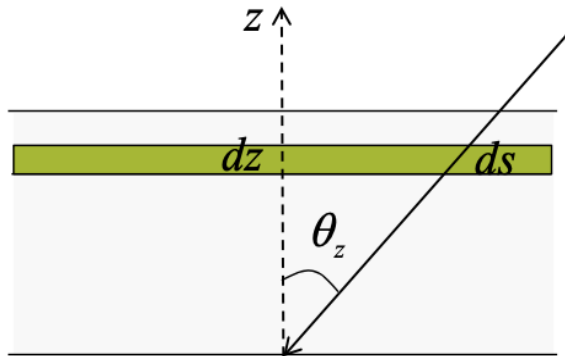


Figure 1.8 : Optical Mass in the atmosphere

$$m = \frac{\int_0^{\infty} \rho \cdot ds}{\int_0^{\infty} \rho \cdot dz} \quad (1.34)$$

If the atmosphere is considered non-refractive, homogeneous and plane-parallel, then, the Optical Mass in (1.35) is interpreted geometrically as the number of atmospheres that the light beam passes through.

$$m = \frac{\int_0^{\infty} \rho \cdot ds}{\int_0^{\infty} \rho \cdot dz} = \frac{\int_0^{\infty} \rho \cdot ds}{\cos \theta_z \cdot \int_0^{\infty} \rho \cdot ds} = \frac{1}{\cos \theta_z} \quad (1.35)$$

The optical mass quantities in (1.33) to (1.35) must be obtained separately for each atmospheric attenuator.

1. Radiative Transfer through atmosphere

We usually work with the Optical Depth on vertical incidence. Therefore, (1.32) can be expressed as in (1.36), by means of (1.35), and regarding to the coordinates system in Figure 1.8.

$$\tau(\lambda, z, \theta_z) = \frac{\tau'(\lambda, z, 0)}{\cos \theta_z} = m \cdot \tau'(\lambda, z, 0) \quad (1.36)$$

Finally, the Beer Law of Scattering in (1.19) and Absorption in (1.28) has the equivalent for extinction, as in (1.37) (Wallace and Hobbs, 2006).

$$L(0) = L(\infty) \exp\left(-\int_0^\infty \tau(\lambda, z) dz\right) = L(\infty) \exp(-\tau) \quad (1.37)$$

The Extinction Coefficient and the attenuator concentration can be expressed with different units, as shows Table 1.1.

Table 1.1 : Radiation Attenuators Magnitudes

Quantity of attenuating matter		Extinction Coefficient	
Name	Units	Name	Units
Path (z) (P,T)	cm	Volume Extinction	cm ⁻¹
Mass per unit section $\frac{m}{s} = \rho \frac{vol}{s} = \rho z$	g · cm ⁻²	Mass Extinction $\sigma_e^m = \frac{\sigma_e}{\rho}$	g ⁻¹ cm ²
Number of molecules per unit section $\frac{N}{s} = \frac{N vol}{s vol} = \frac{N vol}{vol s} = nz$	cm ⁻² ($\frac{molecules}{cm^2}$)	Molecular Cross Section $\sigma_e^{mol} = \frac{\sigma_e}{n}$	cm ² ($\frac{cm^2}{molecules}$)
Reduced Path (P _s = 1atm; T _s = 273.16K) $u = z \left(\frac{P}{T}\right) \left(\frac{T_s}{P_s}\right)$	cm – atm	Reduced Volume Extinction $\sigma_e^u = \sigma \left(\frac{P_s}{P}\right) \left(\frac{T}{T_s}\right)$	(cm – atm) ⁻¹

iv. Source function of Scattering

Besides the energy losses because of the extinction processes, in the material environment there are two processes that imply gain of radiant flux: *scattering in other directions*, that is, radiation scattered into the considered direction, and *thermal emission* of the volume itself (Buglia, 1986; Lenoble, 1985): $J_\lambda^{sca}(x, s)$ and $J_\lambda^{em}(x, s)$ respectively, where x denotes the position of the considered volume and s the direction of the incident energy propagation.

Now, in the case of solar fluxes, which are those of our interest in this work, the atmosphere is considered as a semi-transparent medium in which only short wavelengths propagate. This implies that we do not consider emission sources, necessarily infrared (Chiron de la Casinière, 2003; Chiron de la Casinière and Cachorro Revilla, 2008).

Thus, we consider only the contribution of scattering in other directions as the radiant flux gain process ($J_\lambda(x, s)$, (1.38)), in the atmospheric volume x and in the s direction of the incident energy propagation.

$$J_\lambda(x, s) = J_\lambda^{sca}(x, s) \quad (1.38)$$

If we integrate expression (1.4) of scattered energy in the direction $\pi - \theta$ with respect to the incident direction, integrating over all directions, we obtain (1.39), for the *Source Function of Scattering*.

$$J_\lambda^{sca}(x, s) = \frac{w_0}{4\pi} \int \int_{space} p_\lambda(s, s') L_\lambda(x, s') d\omega' \quad (1.39)$$

Being w_0 the single scattering albedo, $p_\lambda(s, s')$ the scattering phase function, and $L_\lambda(x, s')$ the radiance in the integration direction, and $d\omega'$ the solid angle differential. The scattering phase function $p_\lambda(s, s')$ (1.40) is a normalized magnitude that expresses the angular distribution of the scattered radiation and which, depending on the scattering particle characteristics it is not function of the concentration.

$$p(\theta) = \frac{4\pi}{\beta_{sca}^\theta} \beta_{sca}^\theta \quad (1.40)$$

1. Radiative Transfer through atmosphere

Where $\beta_{sca}^\theta (m^{-1}sr^{-1})$ is the *Scattering Function* or *Volume Scattering Function according to direction θ* , and β_{sca} is again the *Volume Scattering Coefficient*, which can be obtained also as the integral of β_{sca}^θ over the solid angle in all directions.

v. The Radiative Transfer Equation

Once all the physical processes involved in the radiation propagation through the atmosphere have been analysed, the **Radiative Transfer Equation** (RTE) for solar fluxes is introduced (Lenoble, 1993; Coakley & Yang, 2014). (1.41) describes the solar radiation energy transport in the atmosphere. Its formulation is based on the energy conservation and it establishes the radiative balance in a differential volume.

$$\mu \frac{dL_\lambda(z, \mu, \phi)}{dz} = -\beta_{ext}^\lambda(z) \cdot L_\lambda(z, \mu, \phi) \quad (1.41)$$

Being $\mu = \cos \theta$. Analytically, the full RTE has no solution. (1.41) is a simplified version that depends only on the vertical variable z . A more generic equation is shown in (1.42).

$$\frac{dL}{k_{ext} \cdot ds} = -L + \frac{w_0}{4\pi} \int_{4\pi} p(\Omega', \Omega) L(\Omega') d\Omega' \quad (1.42)$$

Being ds a general direction of propagation in the $[x, y, z]$ plane. The scattering phase function, $p(\Omega', \Omega)$ quantifies the probability that radiation from $\Omega' = (\theta', \phi')$ is scattered to direction $\Omega = (\theta, \phi)$. The phase function meets the normalisation condition in (1.43) (Ryder, 2011).

$$\int p(\cos \Theta) \frac{d\omega'}{4\pi} = 1 \quad (1.43)$$

Being $d\omega'$ the solid angle and Θ the scattering angle, as $\cos \Theta = \cos \theta' \cos \theta + \sin \theta' \sin \theta \cos(\phi - \phi')$. θ and ϕ represent the zenith and azimuth angles, respectively. (1.42) is an integrodifferential equation which must be solved simultaneously for all directions. This is so troublesome that even there is not an analytical solution for the simplest scattering problem: a homogeneous conservative medium.

1.3 Radiative Transfer Models

The Radiative Transfer Models (RTM) are computer tools to obtain the radiant fluxes in the atmosphere, in its different layers. These calculation codes can be classified into two big categories: those that solve the RTE, by means of mathematical approximations such as discrete ordinate method (Chandrasekhar, 1960); and those that employ a photon tracing methodology, or Monte Carlo method (Eckhardt, 1987). As regards the use of Radiative Transfer Models in this work, we use a code from each category, each one with its approximations and particularities. Namely, we use the discrete ordinate method on its most widespread form, that is, the code DISORT. The discrete ordinate method relies on the 1D plane-parallel model. Nevertheless, such assumption in some scenarios like cloudy atmospheres has its own limitations, so the 3D radiative effects arise as a result of the approximations and omissions taken in the one-dimensional approach, as the Independent Pixel Approximation. Finally, the codes based in photon tracing as Monte Carlo method contemplate all the possible atmospheric processes in the three dimensions, but are usually computer intensive and difficult to apply for inversion procedures. Below we explain with detail all the applications and approximations followed in this work for obtaining radiant fluxes by means of the Radiative Transfer Models.

1.3.1 One-dimensional, Plane Parallel Model

The 1D plane-parallel assumption in (1.41) is the most common simplification. Given that the horizontal variation of atmospheric variables is much less than the vertical variation, in the plane-parallel assumption the optical properties such as the volume extinction coefficient, the single scattering albedo and the phase function vary only with height, and not also in the horizontal x , y , directions (Coakley and Yang, 2014), as schematized in Figure 1.9.

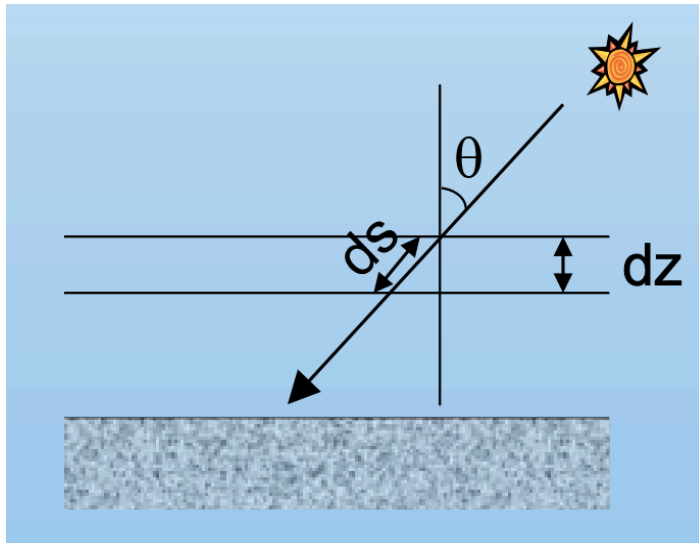


Figure 1.9 : Scheme of Plane Parallel atmosphere

There are several approximations and assumptions to solve the RTE. One of the most employed techniques is the so-called “discrete ordinate technique” (Chandrasekhar, 1960), in which the phase function is expanded in a series of $2N$ Legendre Polynomials as in (1.44) and (1.45).

$$P(\cos \theta) = \sum_{n=0}^{2N} \omega_n P_n(\cos \theta) \quad (1.44)$$

$P_n(\cos \theta)$ in (1.44) is the n -th Legendre Polynomial and is expanded in (1.45).

$$P(\cos \theta) = \omega_0 + \omega_1 P_1(\cos \theta) + \omega_2 P_2(\cos \theta) + \dots \quad (1.45)$$

Where ω_n are the expansion coefficients, which are expressed as (1.46) because of the orthogonality of the Legendre polynomials.

$$\omega_n = \frac{(2n + 1)}{2} \int_{-1}^1 P(\cos \theta) P_n(\cos \theta) d(\cos \theta) \quad (1.46)$$

Being the terms 0 and 1 expressed in (1.47) and (1.48).

$$\omega_0 = \frac{1}{2} \int_{-1}^1 P(\cos \theta) P_0(\cos \theta) d(\cos \theta) = \frac{1}{2} \int_{-1}^1 P(\cos \theta) \cdot 1 \cdot d(\cos \theta) = 1 \quad (1.47)$$

$$\begin{aligned} \omega_1 &= \frac{3}{2} \int_{-1}^1 P(\cos \theta) P_1(\cos \theta) d(\cos \theta) = \frac{3}{2} \int_{-1}^1 P(\cos \theta) \cdot \cos \theta \cdot d(\cos \theta) \\ &= 3g \end{aligned} \quad (1.48)$$

Where g is the *asymmetry factor*, which takes values from 0.7 to 0.9 for aerosols and clouds in the solar spectrum.

On the other hand, the radiation intensity is expanded in a Fourier cosine series in the azimuth direction (ϕ), as in (1.49).

$$L(\tau, \mu, \phi) = \sum_{m=0}^{2N-1} L^m(\tau, \mu) \cos m(\phi_0 - \phi) \quad (1.49)$$

Where ϕ_0 defines together with μ_0 the incidence angle and boundary conditions of radiation at TOA.

With (1.44), (1.45) and (1.49), the radiative transfer equation leads to $2N$ independent equations for L^m . Employing the gaussian integration, the integral is approximated to a sum over discrete angles, as in (1.50).

$$\int_{-1}^1 f(\mu) d\mu = \sum_{j=1}^{2N} a_j f(\mu_j) \quad (1.50)$$

Where the μ_j are the gaussian quadrature angles (streams). μ is the cosine of the θ angle defined with respect to the vertical, positively upwards, as shows Figure 1.10. Plus, the a_j terms are the corresponding weights to the streams.

Therefore, the radiation field is divided in $2N$ discrete directions, N streams upwards, N streams downwards, and the gaussian formula is applied separately to the two half ranges $-1 < \mu < 0$ and $0 < \mu < 1$.

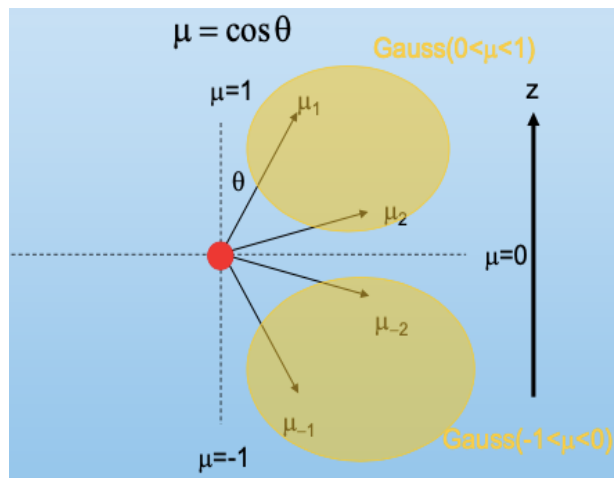


Figure 1.10 : Four streams radiation field system (N=2)

So, it is necessary to solve a system of $2N$ linear differential equations for each μ_j . That makes $(2N)^2$ linear equations, for a homogeneous atmosphere. Being the atmosphere inhomogeneous in z direction, it is divided into M adjacent homogeneous layers in which the atmospheric parameters, the single scattering albedo and the phase function (p) are constant.

Finally, to solve the $M \times (2N)^2$ coupled linear equations it is necessary to provide to the discrete ordinate method solver in the Radiative Transfer Model the following information:

- 1) Number of streams: the discretisation parameter. More streams mean more Legendre polynomials to describe the phase function and therefore higher precision and increased computing time.
- 2) Incoming radiation (L^{INC})
- 3) Lower boundary condition (surface albedo)
- 4) For each layer:
 - Optical depth, τ
 - Single scattering albedo, w_0
 - Phase function, p_i , expressed as a Legendre expansion

Stamnes et al., 1988 adapted the Discrete Ordinate Method to the widely used DISORT (Discrete Ordinate Radiative Transfer solver) code.

Plane parallel approximation in the discrete-ordinate method give reasonably accurate results within a small computational time. Nevertheless, the assumption of horizontal homogeneity is more realistic in stratiform atmospheres, such as clear skies or at most with aerosol loadings, and always in conditions of zenith angles below 70° . The justifications for assuming horizontal homogeneity in the past were more technical than scientific: the computation needs and the lack of 3D input data. These assumptions, however, involve several uncertainties such as vertical and horizontal inhomogeneities in the presence of clouds, to which the net downward flux of radiation at the surface is sensitive (Stocker et al., 2013), as well as and inappropriate use of cloud microphysics (Schwartz et al., 2017). This contributes to the aforementioned uncertainties on the impact of clouds in the climate system.

1.3.2 Independent Pixel Approximation and 3D Radiative Effects

Clouds are far from plane-parallel nature, and this materializes mainly in two physical processes (Benner and Evans, 2001): The first is the so-called “plane-parallel albedo bias” (Cahalan et al., 1994), also called “1D heterogeneity effect”, by which the mean albedo of a cloud with horizontal varying optical depth is less than the albedo of a uniform cloud with the mean optical depth. Numerous studies have found the plane-parallel albedo bias to be significant for a range of cloud types (Cahalan et al., 1994; Zuidema and Evans, 1998; Barker, et al., 1996). The second process, named “horizontal transport effect”, regards to the horizontal transfer of radiation between adjacent grid cells or pixels.

1D studies try to partly address heterogeneity of clouds employing the Independent Pixel Approximation (IPA), or Independent Column Approximation (ICA) (Cahalan et al., 1994). It consists in a simple approach, by which a cloud is subdivided in columns, which are assumed to be radiatively independent. Then, the plane-parallel radiative transfer is applied at each column (Wapler and Mayer, 2008) and the general radiative effect is the sum of the contributions of the individual columns.

Passive imagery from satellite usually relied in the Independent Pixel Approximation. The energy conservation in IPA medium is expressed as in (1.51).

$$R + T = 1 - A \quad (1.51)$$

1. Radiative Transfer through atmosphere

Being R the reflectance, T the transmittance and A the absorptance in a specific pixel.

Nevertheless, (1.51) is incomplete, since it does not account to the lateral net radiative flux from pixel to pixel, a.k.a, the net horizontal photon transport, H . If all radiative mechanisms in a 3D atmosphere are addressed, (1.51) gets modified as in (1.52) (Marshak and Davis, 2005; Song et al., 2016).

$$R + T = 1 - (A + H) \quad (1.52)$$

Thus, the IPA approximation accounts to the 1-D heterogeneity, but not to the horizontal transport effect. Nevertheless, studies have generally found the IPA to be more accurate for domain average fluxes. Cahalan et al., 1994 and Zuidema and Evans, 1998 found the IPA to be highly accurate in stratocumulus. This happens because these clouds have high cloud fraction and are thick enough. The IPA albedo estimate for this kind of clouds has proven to be close to the albedo derived by Monte Carlo and Landsat-derived models (Zuidema and Evans, 1998). Barker et al., (1996) found the IPA albedo to be accurate in stratocumulus for overhead Sun but too low for low Sun. On the other hand, in cumulus clouds, Barker et al., (1996) found IPA albedo to be too high for overhead Sun and too low for low Sun. Chambers, et al., (1997) found generally small optical depth retrieval errors with the IPA, although the uncertainties become larger for broken clouds and overhead Sun. The IPA might be expected to have larger errors in cumuliiform clouds, owing to their greater opportunity for side leakage, side illumination and other 3-D effects.

Anyhow, the limitations of IPA are due to the neglected processes and ignored mechanisms associated with horizontal radiative transfer and cloud side illumination. This entails bias in the conducted retrievals and produce demonstrable errors for solar radiation, instantaneous radiances and irradiances (Ham et al., 2014; Song et al., 2016). The error sources in the shortwave region of the spectrum, the so-called ‘3D effects’, are summarized as follow:

1. **The effective cloud fraction** (Minnis, 1989): Especially relevant for fields of cumulus clouds. The effective cloud fraction seen by the incoming solar radiation or a remote sensor changes with the Sun position. For high solar zenith angles, there is a larger effective cloud area due to cloud side illumination, until the clouds begin to shadow one to another. This results in higher albedo of the medium. This effect is illustrated in Figure 1.11 a).

2. **Side leakage and side illumination** (Benner and Evans, 2001): Relevant for fields of cumulus clouds. For low solar zenith angles photons strike the tops of clouds and leak from their sides, while for high solar zenith angles photons strike the sides and exit the tops. This results in a too high IPA albedo for low solar zenith angles, and too low for large solar zenith angles. This effect is illustrated in Figure 1.11b).
3. **Radiative smoothing** (Marshak et al., 1995): In real cloud fields, photons are allowed to diffuse from optically thick regions to optically thin regions. This results in a smoothing of the radiation field at scales less than about five times the cloud optical depth, since horizontal transport is a geometric effect. This happens to be opposed to the 1D heterogeneity effect, which, as it depends only on the distribution of optical depth, it is especially important for larger scales which have a greater degree of variability.
4. **Geometry of the cloud** (Mejia et al., 2016): It can drastically affect to the optical path, which changes through the cloud for partial cloud cover.

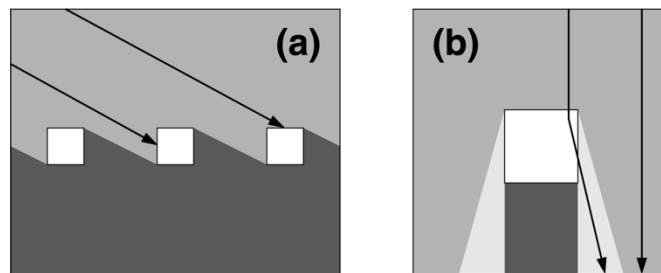


Figure 1.11 : Scheme of some 3D radiative effects in SW. The lighter (darker) colors outside clouds indicate more intense (less intense) radiation. (a) Side illumination, (b) Side escape (adapted from Hogan & Shonk, 2013)

All these uncertainties, common in radiative transfer studies, and problems in the current spatial resolution of remote sensing instruments and cloud-resolving models (Large-Eddy Simulations (LES) and Global Cloud Resolving Models (GCRM)), demand a more realistic treatment of cloud-radiation interaction, as in the 3D Radiative Transfer Models.

1.3.3 Monte-Carlo, 3D Radiative Transfer technique

The 3D phenomena are fully considered in 3D Monte Carlo (MC) simulations. It is a method which considers all relevant atmospheric and surface processes in a complex 3D media without negligent assumptions.

One of the most versatile and known 3D MC codes for radiative transfer is MYSTIC., the Monte Carlo Code for the physically correct tracing of photons in cloudy atmospheres (Mayer, 2009). Roughly, it works as in the following description:

Monte-Carlo radiative transfer use the photon path tracing through the atmosphere, from their origin source until their end. In the Earth's atmosphere, the source is the Sun for the shortwave spectral range. The end of the photon can be either absorption by the surface, by an atmospheric agent, or disappear throughout the TOA.

In a homogeneously illuminated domain, each photon has an initial random position in the x-y plane at TOA, as well as an initial direction determined by the solar zenith and azimuth angles. Afterwards, a step width for the photon is defined, calculated with the probability of survival and the Lambert-Beer's Law, equation 2.48.

$$p_{sur}(\tau) = \exp(-\tau) \quad (1.53)$$

The optical depth τ is the volume extinction coefficient integrated along the photon path in the [x,y,z] plane, as expressed in (1.54).

$$\tau = \int_0^s k_{ext}(s') ds' \quad (1.54)$$

The probability of the photon survival to the optical thickness τ is equivalent to the density of probability that the photon becomes extinct between τ and $d\tau$. The optical depth is a continuous random variable that can be written as a function of cumulative probability density, P_{ext} as in (1.55). Besides, with the cumulative probability density is that it is equally probable that τ falls for example into the interval $P(\tau) \in [0,0.1]$ or $P(\tau) \in [0.3,0.4]$, that is 10%. The respective τ intervals can be calculated inverting P_{ext} as in (1.55).

$$\tau(P_{ext}) = P_{ext}^{-1}(P) = -\ln(1 - P) \quad (1.55)$$

The cumulative probability density can be divided in ten intervals like [0,0.1], or infinite intervals of infinitesimal range. Thus, P in equation (1.55) can be represented

by continuous random numbers ρ between 0 and 1. In that way (1.55) is re-written as in (1.56).

$$\tau = P_{ext}^{-1}(\rho) = -\ln(1 - \rho) \quad (1.56)$$

With it, the pathlength of the photon before it becomes extinct in a random optical thickness is calculated as in (1.57).

$$x = P^{-1}(\rho) \quad (1.57)$$

On the other hand, with (1.57) the actual location of the photon in the physical space is determined. It is done with the 3D distribution of the extinction coefficient k_{ext} , established by the type and number of molecules, aerosol particles and ice and water droplets. For Monte Carlo Radiative Transfer a cubic grid with constant properties is assumed. To determine the location, the extinction coefficient is integrated along the photon path until the optical depth obtained at (1.58).

$$\tau = \sum l_i \cdot k_{ext,i} \quad (1.58)$$

Where l_i is the pathlength which the photon travels in cell i before it becomes extinct, in a location $[x,y,z]$ of the 3D domain.

Then there are two ways of a photon to become extinct within a cell of the domain: scattering and absorption. Which of both happens is determined by the extinction within a cell and its characteristic single scattering albedo. The photon is scattered with a probability of $w_0 = k_{sca}/k_{ext}$, and absorbed with a probability of $1 - w_0 = k_{abs}/k_{ext}$.

A random number ρ between 0 and 1 determines which of the two processes takes place, with $\rho \leq w_0$ for scattering and $\rho > w_0$ for absorption.

Absorption itself is the simpler process, as an absorbed photon disappears from the domain and is not needed to trace it anymore. However, if the photon is scattered the new direction has to be determined. This is done with the scattering phase function.

1. Radiative Transfer through atmosphere

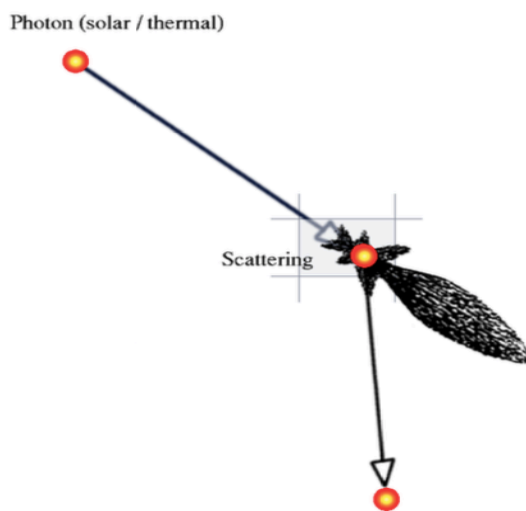


Figure 1.12 : Photon scattering determined by the cell phase function (adapted from Mayer 2009)

It is needed to determine which atmospheric agent is the scattering element. With a probability of $k_{sca,mol}/k_{sca}$ it will be molecular, $k_{sca,aer}/k_{sca}$ for aerosols, $k_{sca,wc}/k_{sca}$ for water clouds, and $k_{sca,ic}/k_{sca}$ for ice clouds. There are different phase functions stored in the model, Rayleigh phase function ($p_{Rayleigh}(\theta)$) for molecules, and Henyey-Greenstein function ($p_{HG}(\theta)$) for aerosols and clouds. Figure 1.12 shows the scattering process suffered by an incident photon over a Mie scattering particle, as well as the angular distribution of the phase function. It shows that the most likely new direction is the forward direction due to the strong forward peak. The phase function determines the scattering angle $\theta_{Rayleigh}$ or θ_{HG} , which is again function of a random number ρ between 0 and 1. The new direction is then defined by θ and a random azimuth angle. In the example in Figure 1.12, the new direction turned out to be the lesser likely sideward step.

The whole process of photon tracing is repeated until 1) the photon is absorbed, 2) the photon leaves the domain by TOA or 3) the photon reaches the ground.

Apart from these steps, a common methodology in Monte-Carlo RT is the so-called ‘photon weighting’, inside the previous procedure. This implies that the photon not only survives or becomes extinct, but alternatively the photon weight among the

previous processes is modified. The photon weight is the probability that the photon survives, and at the beginning of the tracing it is 1. This is specially employed for the surface interaction. If for example, the surface albedo is 0.2, the photon is considered to be reflected and the photon weight multiplied by 0.2. It supposes a great advantage for a definition of BRDF's (bidirectional reflectance distribution function) or complex topography.

In fact, the photon weighting allows a new treatment of absorption in the atmosphere, since it can be handled by reducing the photon weight instead of killing the photon. In MYSTIC scattering is the only process affecting the photon path and absorption is taken in handled by the photon weight. Therefore, the photon weight among two scatterings is reduced according to Lambert-Beer's law, (1.59).

$$\exp(-\tau_{abs}) = \exp\left(-\sum_{cells} l_i \cdot k_{abs,i}\right) \quad (1.59)$$

Being the absorption optical thickness τ_{abs} obtained from the absorption coefficient k_{abs} in a similar way to (1.58).

On the other hand, the reason of tracing photons is to calculate radiation quantities at one or more locations in the domain. Therefore, all that must be done is to trace many photons and count the photon when it reaches the desired location. So, in order to calculate irradiance at the surface the model code counts the photon weights w_i of all the photons reaching the surface following equations (1.60) and (1.61).

$$E = E_0 \cdot \cos \theta_0 \cdot \frac{1}{N} \cdot \sum_{i=1}^{N_s} w_i \quad (1.60)$$

Being N and N_s in (1.60), the total number of photons traced and hitting the surface, respectively. E_0 corresponds to the incoming irradiance at the TOA, and the cosine of the solar zenith angle θ_0 corrects the oblique incidence of the sun rays. The counting is done each time a photon hits the desired location, and the irradiance can be calculated at each model height level. This is a technique in which each photon is recycled and contributes to several irradiance values at different locations.

Also, the irradiance calculation in a horizontal grid with user-defined spacing is obtained by counting the photons falling into each grid box (k, l) , as in (1.61).

1. Radiative Transfer through atmosphere

$$E = E_0 \cdot \cos \theta_0 \cdot \frac{1}{N} \cdot \frac{A}{A_{kl}} \cdot \sum_{i=1}^{N_{s,kl}} w_i \quad (1.61)$$

Where A and A_{kl} are the area of the model and of the grid box (k, l) , respectively. The ratio $\frac{A}{A_{kl}}$ works as the area normalization factor and implies that a fraction $\frac{A_{kl}}{A}$ of photons entering the domain hit the box (k, l) .

The calculation of radiances is done in a similar way. Photons that hit the desired location but also from a specific direction are counted for the calculation.

Trying to sample photons that statistically can barely fall within the sampling cone is computationally inefficient. Therefore, MYSTIC has additional simulations that are better suited for radiance calculations.

One of these modes is the so-called Backward Monte-Carlo (MC). It is based on the reciprocity principle by Hermann Von Helmholtz, by which the path of light from A to B is reversible. That means that, unlike the previous forward Monte-Carlo, Backward MC tracks the photon from the target to the source. In this way all photons can contribute to the result, if they hit the source, that is, the sun. To calculate radiance the photons are started from the target into the desired radiance direction. To improve the efficiency the so-called local estimate technique is employed. It consists in calculating at each scattering point the probability that the photon is scattered towards the direction of the source. This probability is again given by the phase function, and the extinction between the scattering and the target is taken in account. With this, at each scattering point the radiance is weighted by w_v (1.62).

$$w_v = w_0 \cdot p(\Theta_p) \cdot \frac{\exp(-\tau_{ext})}{\cos \Theta_d} \quad (1.62)$$

Where w_0 is the photon weight, and Θ_p is the scattering angle. Therefore, the phase function $p(\Theta_p)$ gives the probability that the photon is actually scattered towards the sun. It can be expressed as a virtual photon generated at the scattering point that suffers the extinction according to the term $\exp(-\tau_{ext})$, where τ_{ext} is the extinction over all cells on the way to the target. Finally, Θ_d is the angle between the virtual photon and the sun direction, to take in account the slant area in the definition of radiance. With the local-directional technique the model samples the radiance at each point in the domain where the photon would potentially change its direction into the

sun direction, and multiply the photon weight by the probability that this actually happens.

MYSTIC possesses many simulation tricks and techniques, apart from those aforementioned. One of them is the so-called variance-reduction method. This is applied to diminish the noise derived from the photon weighting methodology. The expression (1.56) causes values of weight much larger than 1, but they happen in rare occasions. This implies that when they occur appears a spike because of the lack of smooth convergence of the result. A common solution is to simplify the phase function and removing the strong forward peak (Figure 1.12) and establishing that the removed fraction does not get scattered. Unfortunately, this introduces biases in the solution. However, the “variance-reduction” techniques may improve convergence but without introducing biases. The main idea of this technique is to manipulate the contributions of photons to prevent the appearance of isolated spikes, but also to balance the weights accordingly (Buras and Mayer, 2011).

Chapter 2

Properties of Clouds, Instrumentation and Simulations

This chapter has two different parts. On a one hand we focus exclusively on clouds, the main object of this work. We expose the types of clouds and their characteristics, as well as their macrophysical, microphysical and radiative properties, related to their influence in the electromagnetic spectrum. Such influence is used by remote sensing instrumentation to retrieve the physicochemical characteristics, with satellite, airborne or ground-based devices. We summarize the several methodologies followed in the bibliography to obtain the properties of clouds and the optical thickness in particular, focusing on methodologies from the ground and the use of sky cameras. We finish this chapter describing the instrumentation employed in this work, namely the sky camera SONA201-D, the sun photometer CIMEL CE-318 integrated in the AERONET network and the ceilometer VL-51 from Vaisala.

2. Properties of Clouds, Instrumentation and Simulations

2.1 Cloud Formation and Cloud Types

The rising air expands and cools, or moistens until it is supersaturated enough to activate some of the available condensation or freezing nuclei, turning aerosols into water droplets, which allows the cloud formation in the air. The nucleated cloud particles are initially very small, but grow by vapor deposition. Other microphysical mechanisms, such as coagulation and coalescence, can produce a broader spectrum of particle sizes and shapes.

The balance between a number of radiative, dynamical and microphysical processes govern the cloud evolution. Dynamical processes produce variations in cloud properties on scales from kilometres to less than a centimetre. For example, atmospheric convection organizes and gathers clouds into coherent systems having scales from tens to thousands of kilometres. On one hand, the rising air of convective origin is localized in cells surrounded at least partially by sinking air. On the other hand, stratiform uplift tends to be more uniform and horizontally widespread. This process is also slow, allowing for cloud-top surface erosion by longwave cooling, in the so-called upside-down convection (Marshak and Davis, 2005).

The combination of these processes causes a wide range of clouds shapes. At one extreme, there are heterogeneous clouds composed by small elements localized and surrounded by clear air, as happens with the fair-weather cumulus. At the other extreme, there are the continuously overcast stratiform clouds with irregular cloud-top structure. In between of the two extremes there are numerous heterogeneous examples, sometimes showing certain degrees of self-organization in quasi-periodic horizontal variability. Clouds usually present horizontal gradients in their water concentration, and thus they are not homogeneous horizontally. This heterogeneity makes the one-dimensional plane-parallel paradigm not suitable for most of cases.

Eventually cloud particles are sized enough to form precipitation, which is a very complex and important variable that depends on the extent and moisture of the cloud, and also aerosol particles (Stocker et al., 2013).

2. Properties of Clouds, Instrumentation and Simulations

Clouds are hydrometeors in suspension. They are classified in the International Atlas of the Clouds in genres or types (WMO, 2017), according to its base height, depicted in Table 2.1.

Table 2.1 : Clouds types and their heights by regions

REGIONS	CLOUDS HEIGHT (km)		
	High Clouds	Medium Clouds	Low Clouds
Tropical	6-18	2-12	0-2
Mid-latitude	5-13	2-7	0-2
Polar	3-8	2-5	0-2

HIGH CLOUDS

Due to the cold tropospheric temperatures at heights of 5km and above, the temperature of the high clouds is below zero and are primarily composed by ice crystals. They are often thin, white and in the shape of stripes (Figure 2.1). The three main types of high clouds are **cirrus**, **cirrocumulus** and **cirrostratus**.

- Cirrus (Ci): White clouds with fibrous appearance, distributed in thin layers or in the form of filaments.
- Cirrocumulus (Cc): Thin cloud layer composed of small elements in the shape of waves or grains. These elements can be together or separated and distributed in a regular way. They don't produce shadows.
- Cirrostratus (Cs): White or transparent clouds. They have the shape of a thin veil and fibrous or straight appearance. They cover all or part of the sky and can produce halos.

MEDIUM CLOUDS

The medium clouds are composed by liquid water droplets, ice crystals, or a combination of the two, depending on the time of year, the altitude and the vertical temperature structure of the troposphere. The three main types of medium clouds are **altocumulus**, **altostratus** and **nimbostratus**. Altostratus and altocumulus do not produce significant precipitation, whereas nimbostratus bring rain or snow.

2. Properties of Clouds, Instrumentation and Simulations

- **Altostratus (As):** Layer of greyish or bluish clouds of fibrous appearance or uniform. They cover all or part of the sky, although they allow to glimpse the Sun. They do not produce halos.
- **Nimbostratus (Ns):** Layer of grey clouds, usually dark, with diffuse appearance due to the rain or snow that they produce. They have the thickness enough to hide the Sun. Under these layers there are often found other irregular clouds with which they can merge.

LOW CLOUDS

Low clouds normally consist of liquid water droplets. The two main types are the **stratus** kind of clouds, that develop horizontally, and the **cumulus** kind, that develop vertically (see Figure 2.1). Cumulus and cumulonimbus cover most of the troposphere (Lenoble, Atmospheric Radiative Transfer 1993).

- **Stratocumulus (Sc):** Layer of grey or whitish clouds, with more dark areas, composed by rounded masses that form a pattern and can be merged. They are not fibrous, except when they produce precipitation that does not reach the surface.
- **Stratus (St):** Grey cloud layer with uniform base that can produce drizzle or snow. Sometimes they are formed by irregular elements. When the Sun is visible it is possible to distinguish the cloud contour, and can produce halos at low temperatures.
- **Cumulus (Cu):** Dense clouds with well-defined edges. They develop vertically in the form of mounds or domes. The parts of these clouds illuminated by the Sun are bright and white, while its base is darker and has a flat shape.
- **Cumulonimbus (Cb):** Dense and robust cloud with considerable vertical development. A part of its upper region is usually flat and smooth or fibrous, and it can extend in the shape of an anvil. Its base is very dark and with frequent lower and irregular clouds below it. Sometimes they produce precipitation.

2. Properties of Clouds, Instrumentation and Simulations

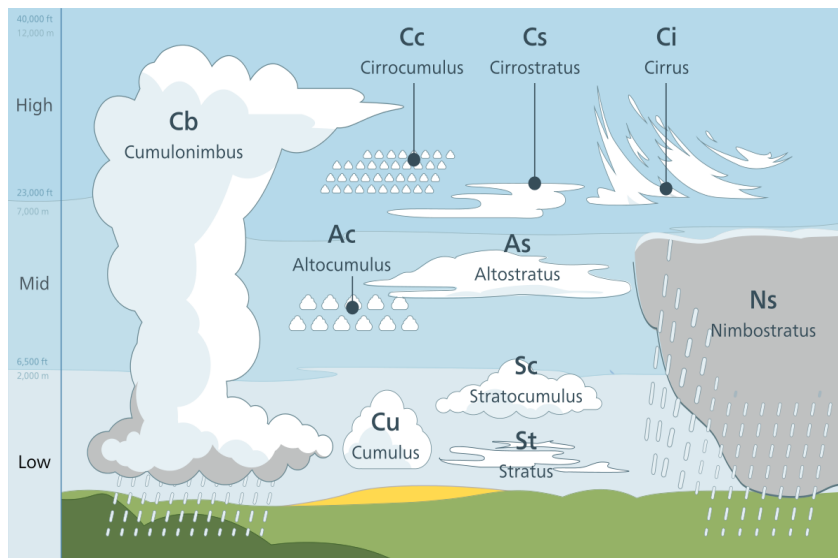


Figure 2.1 : Distribution of cloud types by height (de Bruyn 2014).

A second classification is available based on cloud top pressure and Cloud Optical Depth from the International Satellite Cloud Climatology Project (ISCCP, 2014). This classification is done to determine the influence of the cloud types on climate (Table 2.2), and it's a guide of typical values of COD for each cloud type in Figure 2.1.

Table 2.2 : ISCCP cloud classification, Cloud top pressure and COD

Optical Depth			Pressure (hPa)
0 - 3.6	3.6 - 23	23 - 379	
CIRRUS	CIRROSTRATUS	CUMULONIMBUS	50 - 440 HIGH
ALTOCUMULUS	ALTOSTRATUS	NIMBOSTRATUS	440 - 680 MIDDLE
CUMULUS	STRATOCUMULUS	STRATUS	680 - 1000 LOW

a. **Macrophysical, Microphysical and Radiative Properties of Clouds**

The effects of the clouds on climate and radiative budget depend on cloud properties. Hereunder we describe the properties used to characterize clouds. They are distinguished between macrophysical and microphysical properties.

The macrophysical properties describe the shape and thermodynamic state of the clouds as a whole. These include cloud cover, height, geometrical thickness, pressure and temperature, in addition to the optical thickness.

The cloud cover indicates the proportion of sky that is covered by clouds. Generally, cloud cover is expressed as a percentage or fractions of 1, when it is obtained automatically, or with the help of instruments and semi-automatic procedures. On the other hand, when a human observer determines cloud cover, or less accurate estimate of cloud cover is obtained, it is expressed in oktas. This unit is defined as the number of eights occupied by clouds in the sky (see Figure 2.12). This unit ranges from 0 to 8, being these two extreme values reserved only for situations of complete clear or complete covered sky (WMO, 2008; Aelsnet, 2013).

Microphysical properties are related to the liquid or solid particles that form the clouds: its shape, concentration and form. As it will be shown in further chapters we focus exclusively on water clouds, whose interaction with radiation is different to ice clouds, due to the nonsphericity of the particles. Cloud microphysics is described by the Liquid Water Content (LWC), the Cloud Droplet Effective Radius (r_{ef}), the Cloud Optical Depth (COD), the thermodynamic phase, the Cloud Droplet Number Concentration (N), and the Cloud Droplet size distribution ($f(r)$).

In the case of liquid water particles, the average radius of droplets in non-raining water clouds is usually around 10 μm and its shape is considered spherical. Nevertheless, natural clouds are not composed of uniform size droplets due to the variability in the physical properties of the surrounding air in both space and time (Twomey, 1977).

The scattering of radiation by liquid water particles is highly dependent on the particles size. **The size distribution $f(r)$** indicates how particles distribute in a range of possible sizes. The distribution function is normalized as in (2.1).

2. Properties of Clouds, Instrumentation and Simulations

$$\int_0^{\infty} f(r) dr = 1 \quad (2.1)$$

Also, the integral in (2.2) gives the fraction of particles with radius between a_1 and a_2 in a unit volume of a cloud.

$$F(r) = \int_{a_1}^{a_2} f(r) dr \quad (2.2)$$

It is usual to employ an analytical form of the function $f(r)$, since it is a very good representation of real situations occurring in natural clouds. However, most of the optical characteristics of a cloud as a whole do not depend on the structures of particle size distributions, in a similar fashion to the refractive index, extinction coefficient and liquid water content.

By contrast, Hansen and Travis, (1974) found that the **effective radius** r_{ef} is one of the most important parameters of any particle-size distribution. It is proportional to the average volume/surface ratio of droplets and can be written as in (2.3).

$$r_{ef} = \frac{\langle r^3 \rangle}{\langle r^2 \rangle} = \frac{\int r \pi r^2 f(r) dr}{\int \pi r^2 f(r) dr} \quad (2.3)$$

Being $f(r)$ the size distribution function and r the radius, in (2.1) and (2.2). Light extinction in clouds is governed mostly by values of r_{ef} and liquid water content, which is independent on the particle size distribution (Kokhanovsky, 2001).

On the other hand, the **Liquid Water Path (LWP)**, w , is defined in (2.4).

The limits Z_{cbh} and Z_{cth} correspond to the **Cloud Base Height (CBH)** and the **Cloud Top Height (CTH)**, respectively. The CBH is the lowest height of the cloud, and the CTH is defined as the maximal height of a visible cloud part. From these two terms, the **Cloud Geometrical Thickness (CGT, Z_{cgt})** can be defined as the maximum visible vertical extension (2.5) (Höppler et al., 2020).

$$LWP = w = \int_{Z_{cbh}}^{Z_{cth}} C_w(z) dz \quad (2.4)$$

The parameter $C_w = \rho C_v$, (being $\rho = 1 \text{ g/cm}^3$ the density of water), is the **Liquid Water Content (LWC)**. It is the product of the liquid water density (ρ) and the volumetric concentration of droplets (C_v). This in turn is the product of the **number concentration of particles, N** , and the average volume of particles ($C_v = N\langle V \rangle$) (Kokhanovsky, 2004).

$$Z_{cgt} = Z_{cth} - Z_{cbh} \quad (2.5)$$

One of the most employed parameterizations of The Liquid Water Content can be related to the extinction coefficient and the effective radius as in (2.6) (Liou, 1992; Kokhanovsky, 2004). But there are other different parameterizations depending on the presence of aerosols (Reid et al., 1999) or the change of r_{ef} with altitude (Wood and Hartmann, 2006).

$$\sigma_{ext} = \frac{3 C_w}{2 \rho r_{ef}} \quad (2.6)$$

On the other hand, the **extinction coefficient** is the main parameter in the local optical characteristics of water clouds. As seen in Chapter 1, it defines the attenuation of a direct light beam within the cloudy media, as expresses (2.7).

$$I = I_0 \exp(-\tau / \cos \theta_0) \quad (2.7)$$

Where I_0 is the direct incident light beam, I is the intensity of the transmitted direct light, and θ_0 is the solar zenith angle.

The term τ in (2.7) is the **Cloud Optical Depth**, the integration of the extinction coefficient over the projection on the vertical (H) in the cloud, as shows (2.8).

$$\tau = \int_0^H \sigma_{ext}(z) dz \quad (2.8)$$

Thus, combining equations (2.4), (2.6) and (2.8), the Cloud Optical Depth is also expressed as in (2.9).

$$\tau = \frac{3 LWP}{2 \rho r_{ef}} \quad (2.9)$$

In (2.9) we can see that the extinction from clouds is independent of wavelength (λ). Extinction depends only on the ratio of liquid water path to the effective radius r_{ef} .

2. Properties of Clouds, Instrumentation and Simulations

Therefore, clouds do not change the spectral composition of a direct light beam in visible. That is the reason why particulate media microstructure cannot be obtained by means of spectral transmittance methods (Shifrin and Tonna, 1993).

From equations (2.6) and (2.9) we can also deduce that the extinction is independent of the particle-size distribution (2.1). Thus, satellite methods for cloud microphysics acquisition are focused mainly with the retrievals of r_{ef} and LWC.

Nowadays the globally and continuous observation of clouds has derived in some values employed as typical for effective radius and cloud optical depth. The effective radius for water clouds range from 5 μm to 15 μm (Han et al., 1994). Water clouds with effective radius higher than 15 μm are rare, and in any case are often raining (Masunaga et al., 2002; Pinsky and Khain, 2002). The effective radius of ice clouds are 5 to 10 times higher in comparison to water droplets.

Regarding to typical values of Cloud Optical Depth, they are as variable as clouds themselves. Anyhow, the values range from 0 to 4 for ice clouds, and from 0 to 400 for water clouds (Table 2.2), and are a good indication in average or a rough parameterization.

Thus, according to (2.9) and the aforementioned numbers, the typical values for LWC range from 0.01 to 1 g/m^3 (Kokhanovsky, 2004).

To end, clouds both scatter and absorb incident radiation. The probability of photon absorption, β , is defined in (2.10).

$$\beta = \frac{\sigma_{abs}}{\sigma_{ext}} \quad (2.10)$$

Where σ_{abs} is the absorption coefficient and σ_{ext} is the extinction coefficient. The absorption coefficient in turn is defined as in (2.11).

$$\sigma_{abs} = N \int_0^{\infty} C_{abs} f(r) dr \quad (2.11)$$

Where N is the number concentration of particles and C_{abs} is the absorption cross section (Shifrin, 1951).

The absorption cross section can be calculated from Mie theory for spherical particles, and is proportional to the size parameter α (see Section 1.2 of Chapter 1)

and to the Liquid Water Content C_w . The spectral dependences of σ_{abs} make that the value of β is close to zero in the visible and near infrared.

Clouds can also scatter the incident light in all directions. Usually, the probability of photon scattering by a cloud droplet depends on the size of the droplet and the wavelength of the incident photon. The probability dP that radiation from $\Omega' = (\theta', \phi')$ is scattered to direction $\Omega = (\theta, \phi)$ inside the solid angle $d\omega'$ can be expressed as in (2.12).

$$dP = x(\Omega', \Omega) \frac{d\omega'}{4\pi} \quad (2.12)$$

Where the coefficient of proportionality, $x(\Omega', \Omega)$ in (2.12), is called the scattering indicatrix (Van de Hulst, 1980).

When (2.12) is integrated over a sphere, as in (2.13), P represents the probability of photon survival in the scattering process.

$$\int_{4\pi} x(\Omega', \Omega) \frac{d\omega'}{4\pi} = P \quad (2.13)$$

Therefore, P is equivalent to the single scattering albedo (Chapter 1, (1.21)).

In the visible, since the probability of photon absorption, or β ((2.10)) is a small parameter for water clouds, then $P = w_0 = \frac{\sigma_{sca}}{\sigma_{ext}} = 1 - \beta \approx 1$.

The term $p(\cos \Theta) = x(\Omega', \Omega) / P$ is known as **the phase function**, as a function of the cosine of the scattering angle Θ , being $\cos \Theta = \cos \theta' \cos \theta + \sin \theta' \sin \theta \cos(\phi - \phi')$. θ and ϕ represent the zenith and azimuth angles, respectively. As it is stated in Chapter 1 the phase function can be calculated by Mie theory. It depends on the refractive index of the particles and their size. The main features of phase functions of water clouds include sharp forward-backward asymmetry and a strong forward peak.

On the other hand, light scattering by water droplets is azimuthally symmetric due to their spherical shape. Therefore, the phase function meets the condition in (2.14).

$$\frac{1}{2} \int_0^\pi p(\phi) \sin \phi d\phi = 1 \quad (2.14)$$

2. Properties of Clouds, Instrumentation and Simulations

Several authors have proposed approximate equations for the phase function over decades (e.g. Van de Hulst, 1957; Kokhanovsky and Zege, 1997; Grandy, 2000; Kokhanovsky, 2004). Henyey and Greenstein, (1941) introduced the function (2.15) which varies smoothly from isotropic ($g=0$) to a narrow forward peak ($g=1$), or to a narrow backward peak ($g=-1$) (Van de Hulst, 1980).

$$P(\theta) = \frac{1}{4\pi} \frac{1 - g^2}{(1 + g^2 - 2g \cdot \cos\theta)^{\frac{3}{2}}} \quad (2.15)$$

Being g the **asymmetry factor** and varies from 0.7 to 0.9 for clouds in shortwave (Section 1.3). As is also stated in Chapter 1, g is derived from the expansion coefficients of the Legendre polynomials of $P(\theta)$ and takes the shape of (2.16).

$$g = \frac{1}{2} \int_0^\pi p(\theta) \sin\theta \cos\theta d\theta \quad (2.16)$$

The asymmetry factor gives the average cosine of the photon scattering angle.

Most of Radiative Transfer Models use the Henyey-Greenstein function as one of the input options to define the phase function for aerosols and clouds.

b. Cloud properties retrievals

Great efforts have been made for decades to obtain parameters such as Cloud Optical Depth and effective radius, by means of remote sensing. The methodologies rely on satellites-based measurements (e.g., Wielicki and Parker, 1992; Ohring et al., 2005; Platnick et al., 2017), air-borne measurements (e.g., Zuidema and Evans, 1998; Finger et al., 2016; Höppler, et al., 2020), and ground-based measurements (e.g. Chiu et al., 2010; Chiu et al., 2012; Serrano et al., 2014).

In addition, the remote sensing techniques to obtain the cloud parameters can be classified as active, such as lidars and radars (Winker et al., 2009; Fielding et al., 2015; Gouveia et al., 2017), and passive (e.g., Niple et al., 2016; Mejia et al., 2016; Schwartz et al., 2017). Satellite measurements using passive imagery offer the advantage of global coverage, and lidar-based remote sensing such as the Cloud-Aerosol Lidar with Orthogonal Polarization (CALIOP) are characterized by a high vertical resolution. Unfortunately, the temporal resolution of satellite products is

2. Properties of Clouds, Instrumentation and Simulations

limited, namely 15 min for Meteosat Second Generation (MSG) (Werkmeister et al., 2015) or twice per day for MODIS (EarthData MODIS Overview). On the other hand, the acquisition of cloud properties by means of aircrafts offer detailed, accurate and three-dimensional perspectives of clouds. However, the campaigns are cost-intensive and this translates to low temporal and spatial resolution.

Ground-based observing systems with high temporal and spatial resolution are needed. Besides, the cloud characteristics obtained from the ground are different that those obtained from above (McBride et al., 2011). Satellite-based retrievals rely on cloud reflectance, whereas ground-based retrievals depend on transmittance. While in the reflectance of clouds the upper layers offer the most influence, in the transmittance all the layers contribute more evenly (Platnick, 2000). In addition, transmittance is not as dependent on effective radius as reflectance (McBride et al., 2011), since transmitted radiation is less sensitive to cloud-droplet size distributions (Rawlins and Foot, 1990).

For transmittance, a large number of studies have retrieved Cloud Optical Depth using passive ground-based instruments, such as broadband pyranometers (e.g., Leontyeva and Stamnes, 1994; Aebi et al., 2017; Aebi et al., 2020), sunphotometers (Chiu et al., 2010), UV radiometers (Serrano et al., 2014) and microwave instruments by means of LWP acquisition (Dupont et al., 2018). Irradiance measurements offer the advantage of a one-to-one relationship with Cloud Optical Depth, over radiance measurements (Marshak et al., 2004; McBride et al., 2011). However, the undeniable advantage of radiance measurements over irradiance measurements is the directionality and the reduced field of view, which is of vital importance when evaluating the 3D effects of clouds (See Chapter 1).

In order to avoid the ambivalence of Cloud Optical Depth for a given measured radiance, many works rely on the so-called bi-spectral method or dual-wavelength technique, that explores the different interaction of clouds with light frequency, in order to develop an index that does present a one-to-one relationship with COD. For instance, Marshak et al., (2004) retrieved COD from transmitted radiance at 673nm and 870nm, whereas Chiu et al., 2010 implemented the Cloud Mode in AERONET Network for COD retrieval by means the sunphotometer measurements at 440nm and at 870nm. Mejia et al., 2016 evaluated his Radiance Red-Blue Ratio (RRBR) Algorithm, applied to the COD retrieval with a sky camera, altogether with the other common indices involving blue and red channels, the Red-Blue Ratio (RBR) and the Red-Blue difference (RBD).

2. Properties of Clouds, Instrumentation and Simulations

Many of the existing studies consist on radiative closure studies, that assess the differences between modelled and measured radiances. The radiative transfer models employed for the radiative closure studies are SHDOM (Mejia et al., 2016), MODTRAN (Aebi et al., 2017) or libRadtran (Aebi et al., 2020).

On the other hand, the use of sky cameras has become quite widespread lately, given the need of an extended ground-based observing systems for cloud studies. Sky cameras offer the advantage of full sky coverage in high temporal resolution, as well as a moderate cost. Several studies employed sky cameras worldwide to determine the cloud coverage like Long et al., (2006) or Alonso et al., (2014). Later, Román et al., (2012) and Román et al., (2017) used the technique to retrieve aerosols properties. In addition, works like Wacker et al., (2015) developed an algorithm to classify the detected clouds in six types, algorithm later adapted in Aebi et al., (2017) and Aebi et al., (2020). Mejia et al., (2016) and Schwartz et al., (2017) employed sky cameras to obtain Cloud Optical Depth from the instrument measurements in closure studies. They followed the atmospheric one-dimensional, or plane-parallel model to perform their simulations, by means of the Independent Pixel Approximation (Schwartz et al., 2017), although Mejia et al., (2016) already ventured to extract some differences between the plane-parallel model and more realistic 3D clouds.

Mejia et al., (2016) and Schwartz et al., (2017) are those studies that motivated the present one to obtain the Cloud Optical Depth by means of a sky camera and a radiative transfer model.

c. Instrumentation

The measurements used along this work are taken from the instrumentation deployed in the Burjassot atmospheric station. It is located in the Faculty of Physics in the Universitat de València Science Campus. Specifically, in a latitude and longitude of 39.51°N and 0.42°W, respectively, and at 59m over sea level. The city of Burjassot is located northwest of the city of Valencia, within its metropolitan area and at 8.5 km away from the Mediterranean Sea.

The station is maintained and operated by the Solar Radiation Group (GRSV) of the Earth Physics and Thermodynamics Department. The measurements are devoted to study and monitor radiation, aerosols, clouds and some atmospheric components (e.g. water vapour, ozone) from remote sensing and in situ instrumentation (Estellés et al., 2007; Esteve et al., 2014; Segura et al., 2016; Gómez-Amo et al., 2017). In particular,

only measurements of the all-sky camera, ceilometer and sun-photometer have been used in this work. Next, these instruments and their measurements will be described in more detail.

On the other hand, Radiative Transfer Models can be used to simulate irradiances and radiances under several clear-sky and cloudy atmospheric conditions. It is useful for instruments calibrations and characterizations, as well as for cloud properties retrievals and algorithm testing (Chapter 3). To do that, we use the libRadtran software package in the 2.0.2 version of the free model (Mayer and Kylling, 2005; Emde et al., 2016), and the 2.0 of the one including the MYSTIC extension (September 2018-January 2020). The utilities and the simulations performed with the model are further described in this chapter and the next one.

i. Sky Camera

The employed Sky Camera is a model SONA (*Sistema de Observación de Nubes Automático*) from SIELTEC Canarias S.L. The current configuration consists in a model SONA 201-D settled inside a case of 202-O, after some rain water filtered inside the former case and damaged it. The new system was installed and began to take measurements on May 2018.

2. Properties of Clouds, Instrumentation and Simulations



Figure 2.2 : Sky Camera SONA 201-D / 202-O

The instrument consists in a digital color CMOS (complementary metal-oxide-semiconductor) camera with a fisheye lens encapsulated in an environmental housing that is temperature regulated with a Peltier cell. The camera is composed of:

- Aluminium housing: it contains the image capture element and the control electronics and protects the instrument in extreme environments.
- Acrylic dome: it protects the system from the weather conditions like rain or snow.
- Image sensor element: it is a CMOS sensor with three channels: red, green and blue, with vision in the near infrared.
- Standard infrared filter: blocks the vision in the NIR and modulates the three channels in the visible.

2. Properties of Clouds, Instrumentation and Simulations

- Fisheye Lens: from Fujinon. The field of view guarantees 180° projected into the CMOS.
- Control electronics: it is the hardware that controls the system operation.
- Electrical protection system: it prevents the system from signal peaks, discharges and other interferences.
- Temperature control system: it adjusts the instrument temperature to maintain it within the operation range.

The CMOS sensor is the model e2v EV76C570 CMOS 1/1.8'' with a nominal resolution of 1600 (H) x 1200 (V) pixels, and a pixel size of $4.5 \times 4.5 \mu m^2$. Its nominal digital resolution is 10 bits. The spectral response in percentage, or quantum efficiency of the sensor for the three channels (RGB, in red, green and blue respectively), provided by the manufacturer, as well as the monochrome response, are depicted in Figure 2.3.

Inside the camera, the sensor works altogether with a filter that blocks the wavelengths in the infrared region. The spectral responses of the camera channels convolved with the IR filter have a slightly different shape for blue and green, which are centered around 470 nm and 530 nm. The red channel, however, gets a drastically different shape under the filter, and gets centered around 610 nm (Figure 2.4).

2. Properties of Clouds, Instrumentation and Simulations

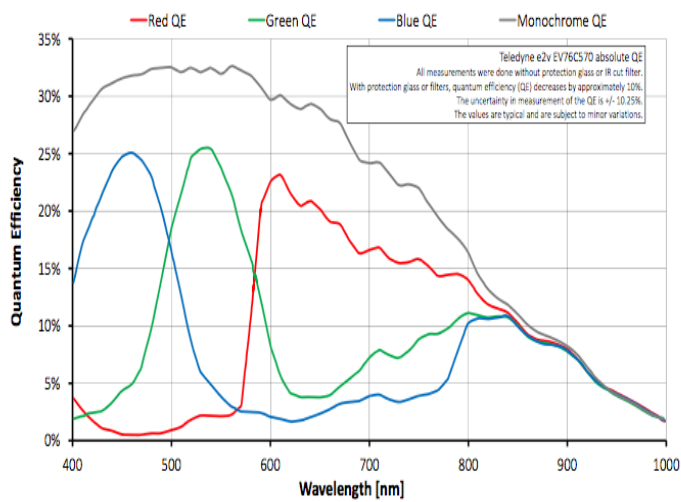


Figure 2.3 : CMOS Sensor Spectral Response (RGB) and monochrome response (grey)

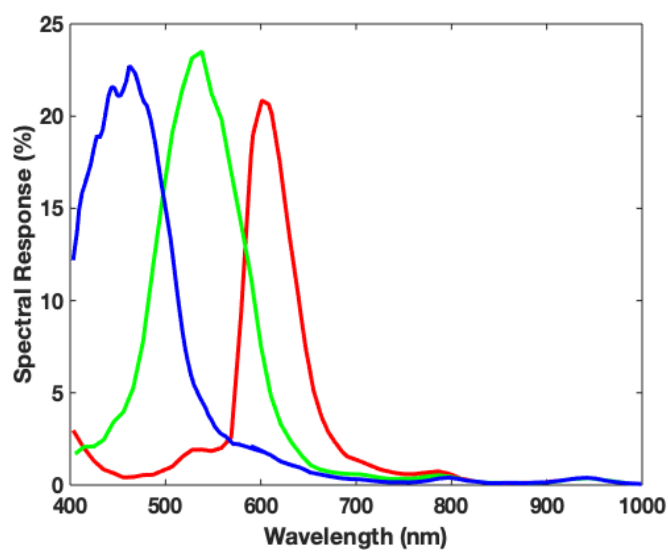


Figure 2.4 : CMOS Sensor Spectral Response convolved by the IR filter

On the other hand, a schematic of the sensor operation is depicted on Figure 2.5.

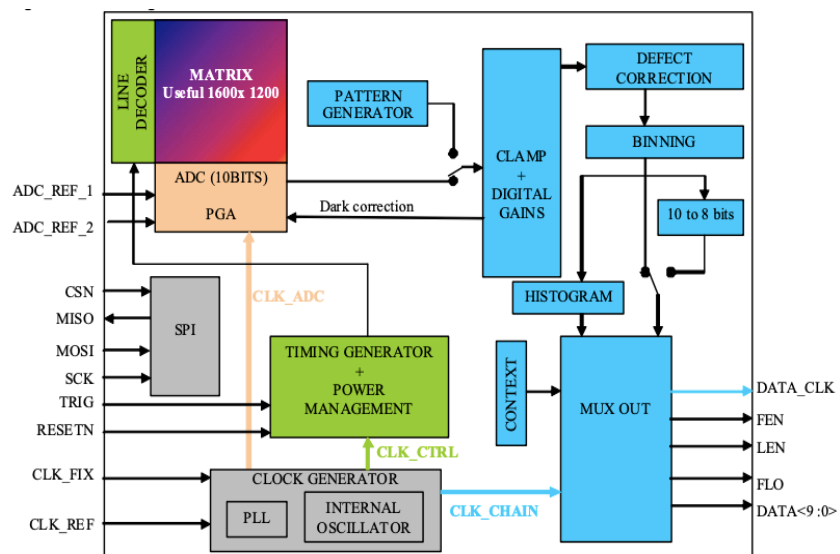


Figure 2.5 : CMOS sensor operation overview

The most important components are the following:

- Analog-to-Digital Converter (ADC): Electronic device capable of converting an analog signal (either voltage or current) into a digital signal by means of a quantizer. In many cases it is encoded in a particular binary code. This one is quantized to 10 bits.
- Synchronous communication bus (SPI): Digital system that transfers data between the components of a computer. The clock signal (SCK) governs all the activities of the bus, which take place in an integer number of clock cycles. The input and output signals are MOSI (*Master Output Slave Input*) and MISO (*Master Input Slave Output*), respectively. The CSN (*Chip Select N*) input corresponds to the chip selection.
- Focal-plane array (FPA): Image sensing device consisting in a typically rectangular array of light-sensing pixels at the focal plane of a lens, of 0.0014 m. FPAs detect photons at particular wavelengths and then generate an electrical charge, voltage or resistance according to the number of

2. Properties of Clouds, Instrumentation and Simulations

photons detected at each pixel. This signal is then measured, digitized (ADC) and used to construct an image of the scene that emitted the photons.

- Timing Generator + Power Management: Generates the clock signals to the FPA and the ADC.
- Clamp + Digital Gains: Signal amplifier. Introduces gain to the signal coming from the ADC. It also blocks the dark current.
- Pattern Generator: generates a signal in the shape of a pattern for the Clamp module with which to identify the dark current.
- Mux Out: Data output module.

The sensor (Figure 2.5) is governed by the PLL (*Phase-Locked Loop*), an internal oscillator that synchronizes the clock signals. The receiver is the FPA, composed by 1600x1200 useful pixels, whose analog signal is digitized at 10 bits by the ADC. From here, the signal goes to the Clamp module, which amplifies the signal by introducing gain. This module also receives patterns from the Pattern Generator, which identifies the dark current and blocks it. The digitized, amplified and corrected signal then goes to the Defect Correction module, where the faulty pixels are treated.

Next, the signal goes to the Binning module, where all the pixels are added to generate histograms. The Binning output is selected with the SPI, and can be the histogram itself, the raw signal, or the 10-bit to 8-bit transformed signal, by the least significant 2 bits elimination. The latter is the selected configuration for the Sky Camera.

Finally, the Mux Out has the function of dumping the data (DATA_C) that has been selected in the SPI to display.

The exposure time for the image capture is 0.2 seconds. Although the dark current is identified and eliminated by the sensor, there is still a signal offset composed by the white noise or the cosmic microwave background, and a remaining dark current. This noise is further treated in the Methodology Section (Chapter 3).

The camera products are RGB images of 1158 x 1172 pixels (Figure 2.6) with 8 bits digitalization per channel. The instrument is set to provide images of the full sky every minute, 24 hours per day, in JPG and in PNG format.

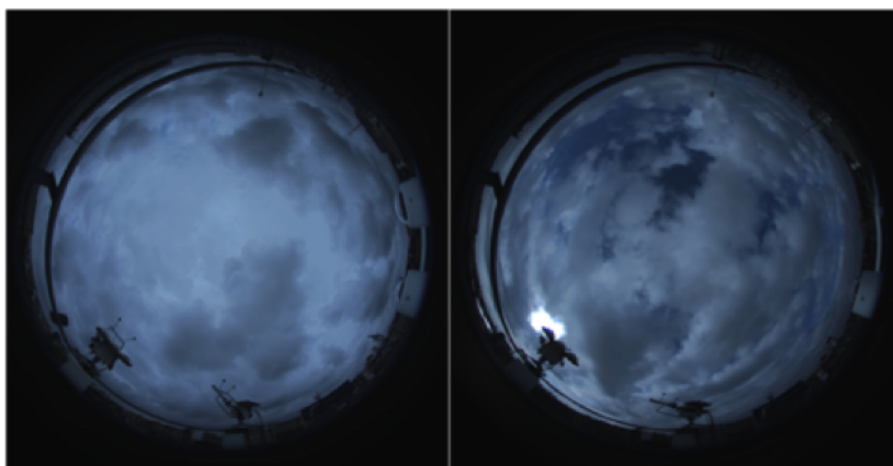


Figure 2.6 : Camera images from the 2nd June 2018 (left) and 13th October 2018 (right)

ii. Sun Photometer CIMEL CE-318 and AERONET Network

The CE-318 (Figure 4.6) is an automatic sun tracking photometer designed by Cimel Electronics. It has all the qualities of a field instrument: portable, motorized, autonomous (powered by solar energy) and automatic. It is composed of an optical head, an electronic box and a robot. The optical head has two channel systems: the sun collimator without lenses, and the sky collimator, with lenses. The sun-tracking system is equipped with a 4-quadrant detector.

2. Properties of Clouds, Instrumentation and Simulations



Figure 2.7 : Sun Photometer CE 318 from CIMEL Electronique

The electronic box contains two microprocessors for data acquisition and motion control in real time operation. On the other hand, the computation of sun equations as air mass is performed by two CPU cards. The robot moves in zenith and azimuth planes by step-by-step motors.

The data from the memory of the CE-318 is transferred once per day, in night time to the AERONET Network. The instrument was acquired by the GRSV and set in December 2001 for the study of the atmospheric aerosols, and participated in field campaigns and calibration campaigns, such as VELETA 2002 as a federated instrument from the AERONET network (Estellés et al. 2004a and 2004b). In Table 2.3 are depicted more instrumental details from the device in the Burjassot atmospheric station on its current configuration (Gómez-Amo et al., 2017).

On the other hand, AERONET (AErosol RObotic NETwork, <https://aeronet.gsfc.nasa.gov>) is a federated network of ground-based remote sensing of aerosols and clouds, established in 1993 by NASA and PHOTONS (PHOtométrie pour le Traitement Opérationnell de Normalisation Satellitaire, Univ. de Lille, CNES, CNRS-INSU).

2. Properties of Clouds, Instrumentation and Simulations

AERONET is greatly expanded and supported by universities, observatories and research institutes of all types worldwide. Figure 2.8a depicts the full network, and in Figure 2.8b the stations in the Iberian Peninsula, south of France and north of Africa are shown.

The AERONET Network employs measurements from the CIMEL CE-318 automatic sun-photometers to derive aerosols properties (Holben et al., 1998) and cloud properties (Chiu et al., 2010; Chiu et al., 2012). The CIMEL CE-318 in the Burjassot station performs direct-sun measurements with a 1.2° of field of view every 15 min at all the nominal wavelengths specified in Table 2.3, except the 1640nm. These spectral measurements are used to obtain the spectral Aerosol Optical Depth (AOD) and Angström Exponent (AE), except the 940 nm, which is employed to retrieve the total column water vapor.

In addition, the angular distribution of sky radiance is measured at 440, 675, 870, 1020 and 1640 nm. The measurements are taken with the Sky Collimator and high gain and at different angles in the almucantar and in the principal plane directions. These measurements are employed to retrieve aerosol optical and microphysical properties like columnar aerosol size distribution, complex refractive index, particle fraction and single scattering albedo at different wavelengths, following the AERONET procedures (Holben et al., 1998; Dubovik and King, 2000).

Table 2.3 : Specifications of CIMEL CE-318 Sun-photometer

SPECIFICATIONS	CE-318
FOV Solar Collimator	1.2°
FOV Sky Collimator	1.2°
Nominal Wavelengths	340, 380, 440, 675, 870, 940, 1020, 1640 nm
Bandwidth	2nm (UV); 10 nm at FWHM (VIS, NIR)
Operating Temperature	-30°C to 60°C
Sun tracking accuracy	<0.1°

2. Properties of Clouds, Instrumentation and Simulations

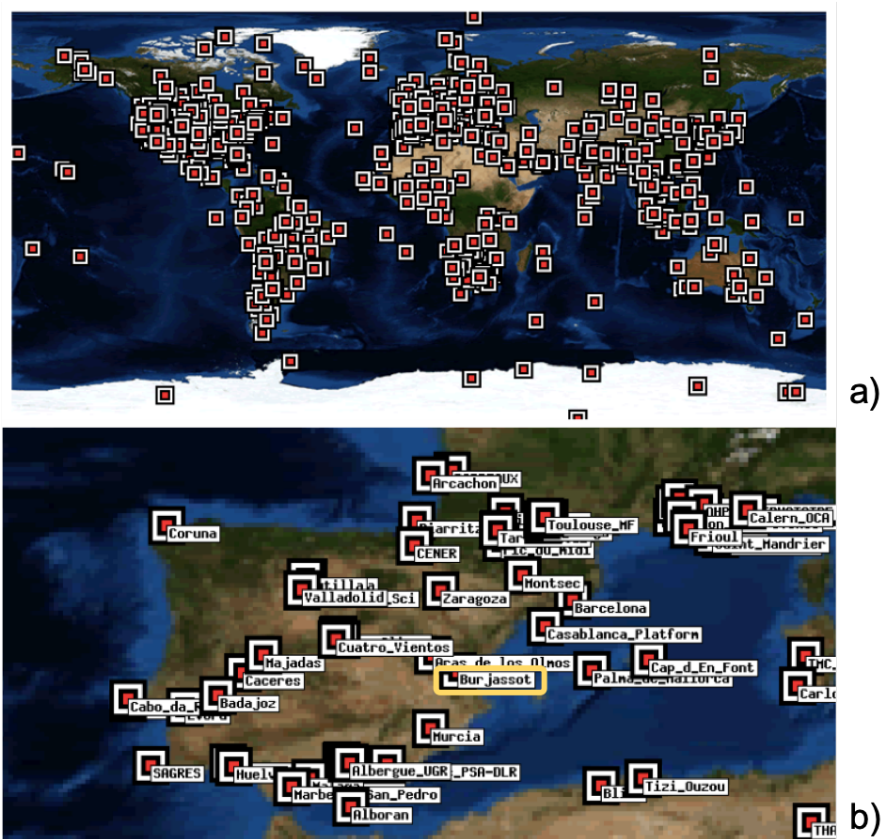


Figure 2.8 :a) AERONET network (2020); b) AERONET sites in Western Mediterranean. Burjassot station

Figure 2.9 schematizes the sun-photometer operation in Almucantar configuration. There are two sides considered respect to the Sun, counting positive angles in the right side and negative angles in the left side. As the sequence shows, the CE-318 makes the measurements at the right side, then returns to the Sun position, afterwards makes the measurements at the left side and returns to the Sun position. Then, the filter is changed and the measurement sequence begins again.

2. Properties of Clouds, Instrumentation and Simulations

Also, radiance is measured with different gains depending on the measurement angle. Sky gain is employed in the angles range between 6 to 180° (from the Sun), and from -6 to -180°, with steps of 1°, 2°, 5°, 10° and 20°. Aureole gain is employed at the angles 2° to 6° and -2° to -6°, with measurement steps of 0.5° and 1°. Finally, the Sun gain is employed at the Sun position (angle 0°) to measure the Direct Radiance. The Radiance data is provided in $\frac{\mu m}{cm^2 sr}$.

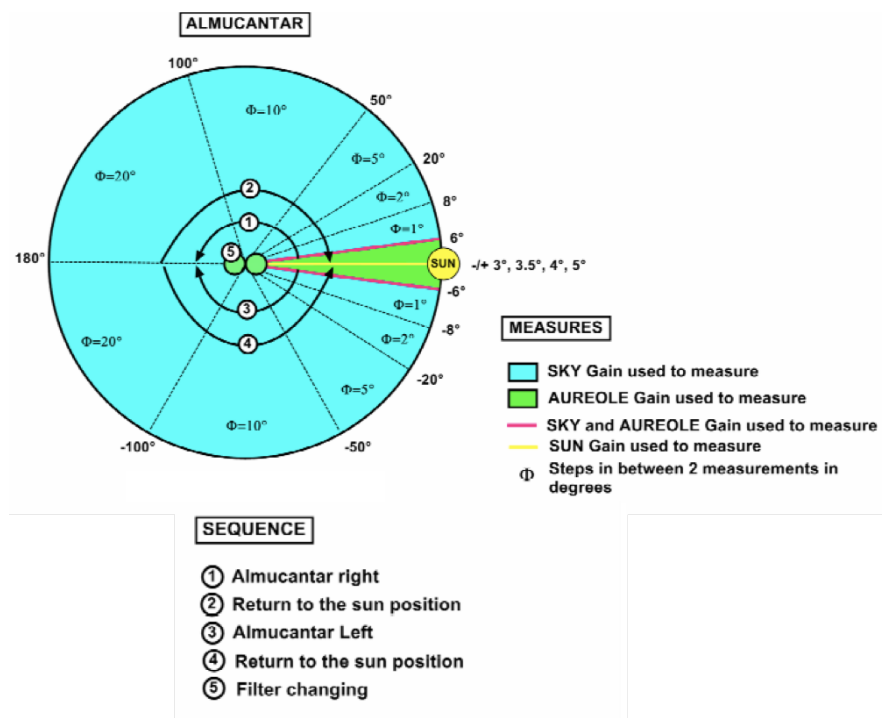


Figure 2.9 : Almucantar sun-photometer measurements of Sky Radiance for AERONET (adapted from the CIMEL CE-318 User's manual)

The AERONET products are divided according to the Direct Sun measurements and the Sky Radiance measurements. The former is composed of aerosol's AOD, AE, and precipitable water vapor, at data quality levels 1.0 (unscreened), 1.5 (cloud-screened and quality controlled) and 2.0 (quality assured). The latter is composed by Radiance data, taken in the Almucantar and Principal Plane configurations, and a Hybrid product as well, at levels 1.5 and 2.0 in the Burjassot measurement station. It

2. Properties of Clouds, Instrumentation and Simulations

also includes the Inversion products, as single scattering albedo, asymmetry factor and phase function.

However, when clouds completely block the Sun, direct Sun and sky radiance are not appropriate for retrieving aerosol optical properties. In these situations, the radiometer is placed into the so-called ‘cloud-mode’. Then the radiometer points directly up (i.e. zenith) and performs 10 zenith radiance measurements at intervals of 9 seconds for each wavelength.

The Cloud Mode Retrieval Method (Chiu et al., 2010) for each measurement period, provides instantaneous retrieval of COD, and COD retrieved from averaged radiances at 1.5 minutes interval. The averaging technique includes an exclusion method of the measurements below and above the 25th and 50th percentile, respectively. This is done to avoid clear-sky contamination which would bias the retrieval toward larger values of Cloud Optical depth (COD). The choice of the numbers 25 and 50 were chosen empirically, according to the authors.

The COD product is derived following a closure methodology combining radiance measurements and radiative transfer-simulations at 440 nm and 870nm. This is done in order to circumvent the ambivalence of Cloud Optical Depth for a given radiance value. The method followed by Chiu et al., 2010 is based on the ‘RED vs NIR plane’ methodology from Marshak et al., 2004, which exploits the spectral contrast in the reflectance on vegetated surfaces to retrieve cloud properties. The plane method has the advantage over the spectral indices-based methodologies such as NDCI (Marshak, et al. 2000) of two spectral values instead of one number obtained by algebraic transformation (Marshak et al., 2004). Each pair of spectral values can be depicted as a point in the plane of two coordinates, subtraction and addition of spectral normalized radiance at 440nm and 870nm and with it the retrieval of cloud parameters such as cloud cover and COD is univocal.

The comparison depicted in Chiu et al., 2010 with the results provided by the Oklahoma Atmospheric Radiation Program, that uses the MFRSR (MultiFilter Rotating Shadowband Radiometer), derived an average uncertainty for the AERONET retrieval around 20% and a correlation coefficient of 0.86 for the instantaneous retrievals. The uncertainty diminishes to 15% with a correlation coefficient of 0.92, in case of the average retrievals (Chiu et al., 2010).

The Cloud Mode is not present in all sites of the AERONET network. Figure 2.10a shows the stations operating also in Cloud Mode in the year 2020, and Figure 2.10b

the Cloud Mode sites in detail in the Iberian Peninsula and Western Mediterranean, with the Burjassot measurement station among them.

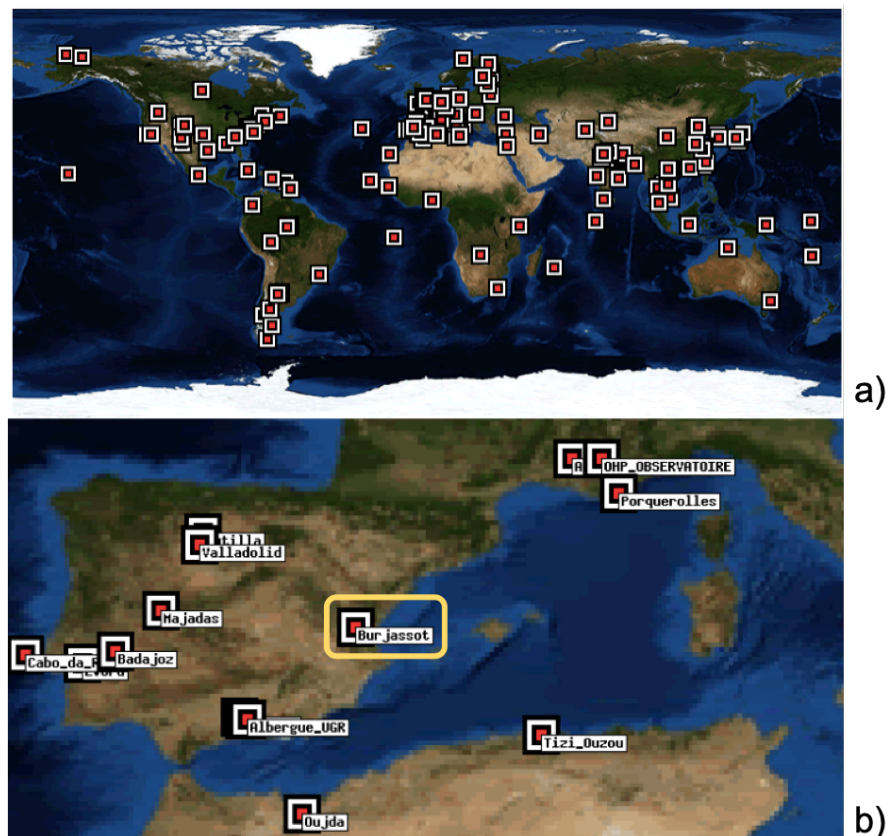


Figure 2.10 : AERONET sites operating in Cloud Mode (2020) a) worldwide and b) Western Mediterranean. Burjassot station

iii. Vaisala CL-51 Ceilometer

The Ceilometer CL-51 from Vaisala (Figure 2.11) operating in the Burjassot measurement station is mainly used to determine the height of the clouds base, as well as vertical visibility and height dependent cloud cover. The instrument uses a

2. Properties of Clouds, Instrumentation and Simulations

laser diode working at 910 nm operating as a low power LIDAR (Light Detection and Ranging) system. The ceilometer emits pulses to the atmosphere of 110 ns width at a repetition rate of 6.5 kHz. The back-scattered light is detected with a vertical resolution of 10 m. The system is tilted 12° towards North to decrease the background Sun radiation and to eliminate the condensation and rain drops.

The ceilometer measures the atmospheric back-scattered profile, from which the height of clouds is obtained (Vaisala, 2010b). It can detect until three different layers simultaneously. The employed algorithm is known as Sky Condition Algorithm (Vaisala, 2010a). It retrieves the cloud cover employing the previous 30 minutes of measurements, although with more weight over the last 10 minutes.



Figure 2.11 : Ceilometer CL-51 (Vaisala)

2. Properties of Clouds, Instrumentation and Simulations

Cloud height and time are used to determine cloud cover. To determine the cloud cover (CN_{CL}) in a height interval between h_0 and h_f , the clouds are assumed to be uniformly distributed in the horizontal plane, and a methodology schematized in (2.17) (Marcos 2017) is applied.

$$CN_{CL} = 1 - \prod_{h_0}^{h_f} (1 - CN_{CLh}) \quad (2.17)$$

First, the cloud cover of the closest layer to the ground is obtained, in oktas. This unit is defined as the number of eights of the sky occupied by clouds (Figure 2.12). For the next layer, the ceilometer measures the cloud cover of the remaining piece of sky, and it is added to the first value. The coverage of the next layer is obtained in the same way for the remaining clear sky, and so on.

CN_{CL} in (2.17) represents the total cloud cover provided by the instrument, and CN_{CLh} is the cloud cover at a height h . The cloud cover (CC) raw data is provided in oktas, for both full and layered cloud coverage. Afterwards the CC is converted to percentage, which is the way we use the data in the present work. The results obtained with the algorithm from Vaisala coincide with observations in the 90% of the cases (Vaisala, 2010b).

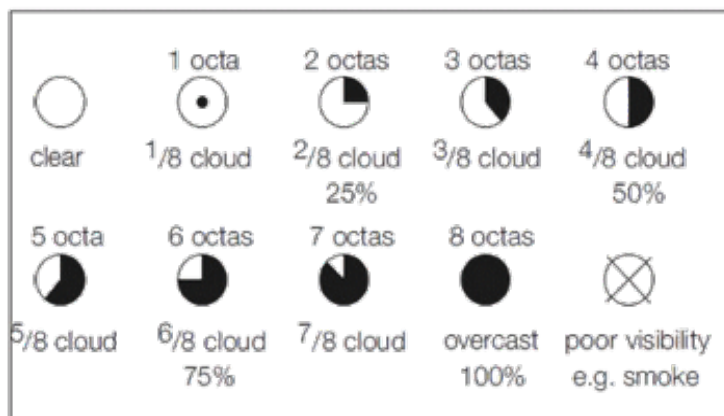


Figure 2.12 :Correspondence between oktas and the proportion of sky covered by clouds (Aelsnet, 2013).

2. Properties of Clouds, Instrumentation and Simulations

In The CL-51 was set in Burjassot in July 2013 and since then it has continuously been working, providing measurements with 1-minute temporal resolution.

Table 2.4 are included some more specifications of the instrument. With the ceilometer it is also possible to determine aerosols amounts, water vapor and atmospheric pollutants (Vaisala, 2010b; Marcos et al., 2018). The CL-51 was set in Burjassot in July 2013 and since then it has continuously been working, providing measurements with 1-minute temporal resolution.

Table 2.4 :Technical specifications of the Vaisala CL-51 ceilometer

SPECIFICATIONS	CL-51
Cloudiness range	0-13 km
Backscatter profile range	0-15 km
Resolution	10 m
Laser	InGaAs Diode
Temperature range	-55° to +60°C
Relative Humidity	0 – 100%
Wind	Until 55 m/s

Chapter 3

Methodology

The third chapter is devoted to the full methodology followed in this work, first to obtain the cloud optical depth and ancillary information from the sky camera, and second the synthetic study by means of the 3D Monte Carlo Radiative Transfer. The methodology for the first part consists in the camera's images pre-processing before the instrument calibration and the acquisition of the effective wavelengths. The calibration in turn consists in the geometric calibration and the radiometric calibration. In this chapter the validation of the radiometric calibration with AERONET is also included. Next, we describe the simulations performed with the radiative transfer model in order to compose the Lookup Table (LUT) for the COD acquisition, the LUT construction and the Retrieval Algorithm as well. The chapter ends with a discussion of the analysis and results obtained.

3. Methodology, Data and Analysis

3.1. COD acquisition with a Sky Camera. A 1D approach

The main objective of this Section is to obtain the Cloud Optical Depth from the images provided by the SONA 201-D Sky Camera. To do so, we follow a series of steps that culminate in this purpose. These steps are schematized in Figure 3.1 with a flow diagram.

On the one hand, we need to characterize the sky camera that provides the images of the whole sky over the Burjassot atmospheric station, as well as its measurements. The steps and procedures that compose the camera characterization are marked in blue in Figure 3.1. This characterization, consists into two main tasks: The Sky Camera Calibration and the determination of the effective wavelengths of the three channels. Later the concept of effective wavelengths and the procedure to calculate them are detailed.

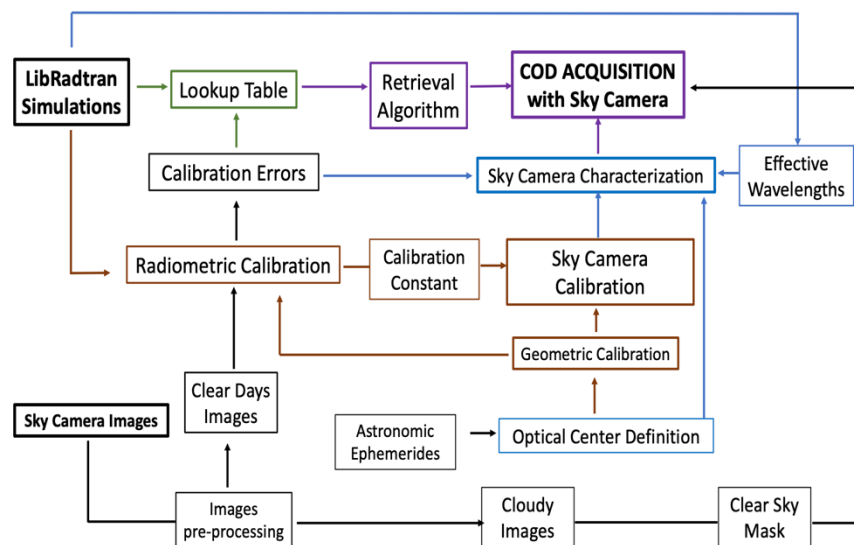


Figure 3.1 : Flux Diagram of the Methodology for COD acquisition with the Sky Camera

3. Methodology, Data and Analysis

The Sky Camera Calibration in turn, (marked in brown in Figure 3.1) is composed of two fundamental parts: *Geometric Calibration* and *Radiometric Calibration*. The former is a basic step to obtain the maps of viewing coordinates of the camera associated with each pixel, the Zenith map and the Azimuth Map. On the other hand, the radiometric calibration is needed to obtain the radiometric constant that converts the digital counts of each pixel of the camera to radiance. In the forecoming Section 3.1.1, the two calibrations are explained in detail.

With the Sky Camera characterization, the COD acquisition can be achieved, using a Retrieval Algorithm based on the methodology proposed by Mejia et al., (2016) and Schwartz et al., (2017). Its construction and operation are explained in the forecoming Section 3.1.2. The core of the Retrieval Algorithm is a *Lookup Table of COD* (Figure 3.1) that is built from Radiance simulations of libRadtran. The calculations with libRadtran, both of radiance and irradiance on the ground, support several important parts of the methodology, as Figure 3.1 illustrates.

To end the present Section 3.1, we explain the data management and treatment applied over the algorithm outcomes. With it we perform the analysis and discussion over the results, in Section 3.1.3.

3.1.1. Sky Camera Characterization and Images pre-treatment

The Sky Camera Characterization consists in obtaining the effective wavelengths and the Camera Calibration. The images pre-treatment is the processing to which we submit all the camera images that we employ in this work, before using them in the rest of the methodology (Figure 3.1, lower branch).

As Figure 3.2 shows in the upper left panel named ‘Raw Image’, the Sky Camera images provide a whole-sky sight that reaches the horizon and the surrounding objects to the device. In turn, the sight of the camera appears delimited by a black frame, which is an image of the inside of the device. The objects appearing in the edges of the whole-sky sight include the city of Burjassot, lamp posts, radiometers and sun trackers, as well as the security railing in the rooftop of the Faculty of Physics. The appearance of such objects can be inconvenient and misleading, and requires manipulation and removal.

Therefore, every Sky Camera image to be employed in this work, previously separated into the three channels (RED, GREEN and BLUE), is cut to erase the black frame as much as possible. The cutout in the left area of the image reaches the security

railing, since the remaining pixels between it and the horizon are not enough to be profitable. With this cutout the original dimension of the Sky Camera product (1158x1172) is reduced to a square matrix of 966x966. This procedure is illustrated in Figure 3.2, over an image taken at 12h on the 6th June of 2018, in the step from raw image to cut image in the top left and center figures.

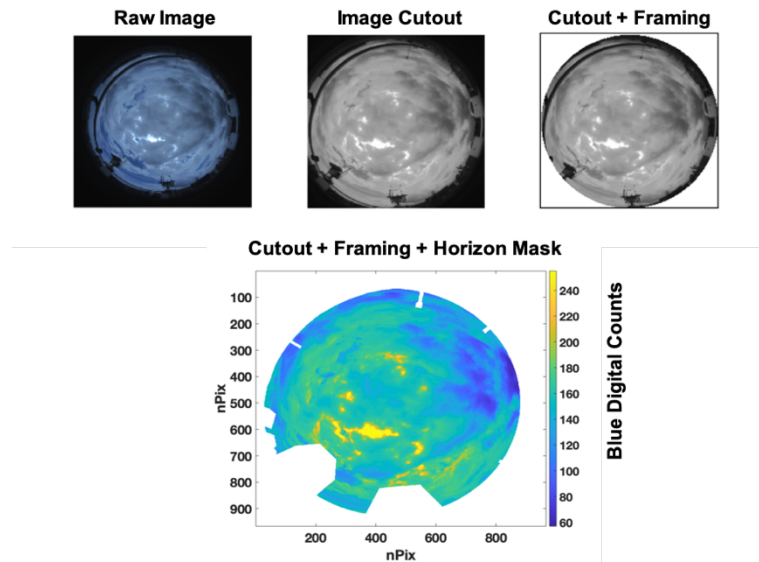


Figure 3.2 : Steps of Sky Camera images pre-treatment: Cutout, framing and Horizon Mask

It is also easier to define a perfectly circular edge for the sky image with a square matrix. So, the digital counts of every pixel located at a distance to the center of the matrix ($i=483, j=483$) greater than a radius of 483 are no longer considered. In that way we ensure that we avoid internal reflections in the camera, an important process for objects located on the horizon. Figure 3.2 top right shows the result of this step, where the whole-sky sight appears delimited by a perfectly circular frame. The pixels of the corners of the square figure are subsequently painted in white.

Nevertheless, after the cutout and framing of the sky image there are still objects on the horizon visible, such as part of the security railing, radiometers, sun trackers and the weather station of the Faculty of Physics. In the final step of image pre-processing, we superimpose a mask over these horizon objects. The mask covers the

3. Methodology, Data and Analysis

undesirable artifacts and also covers the pixels located on a viewing zenith angle higher than 80° . Therefore, this mask is completed once the forthcoming geometric calibration is done, when all camera pixels have their coordinates assigned. Figure 3.2 bottom shows the final appearance of the Blue channel matrix after pre-treatment, depicted on its scale of digital counts, from 0 to 255.

Clear Sky Mask

The last processing of the images from the Sky Camera before passing them to the algorithm for the COD acquisition is the calculation and application of the *clear sky (CS) mask*, as Figure 3.1 shows. With the CS masking the clear sky pixels are eliminated from the calculations which estimate COD. This step is important because with it we calculate the cloud coverage of the image, by means of separating cloudy pixels from clear sky pixels. Apart from that, elimination of clear sky pixels from the calculations removes systematic errors due to the limitations of the present approach as will be explained in detail later in this Section 3.1.

The clear sky mask is obtained with the ratio between the blue and red digital counts (B/R), as a function of the solar zenith angle. The blue-red ratio (B/R) or its inverse, red-blue ratio has been used for decades as the default method to separate clear sky pixels from cloudy pixels (e.g. Koehler et al., 1991; Chow et al., 2011; Ghonima et al., 2012). That is because it takes advantage of Rayleigh scattering being greater in the blue wavelengths than the red wavelengths. For a given view angle and solar zenith angle, the quotient is higher for clear skies rather than for cloudy skies, when Mie scattering dominates (Mejia et al., 2016).

Table 3.1 : B/R quotient thresholds for CS mask, as a function of SZA

Angles ranges	Q
$SZA < 25^\circ$	2.4
$25^\circ < SZA < 35^\circ$	2.3
$35^\circ < SZA < 55^\circ$	2.2
$SZA > 55^\circ$	2.1

In Table 3.1 we summarize the thresholds (Q) employed as a function of SZA, obtained through empirical work, as well as the dependency with the solar zenith angle. We consider that a pixel is cloudy if the B/R ratio is less than the corresponding Q threshold, depending on the SZA. Otherwise, the pixel is labeled as clear sky.

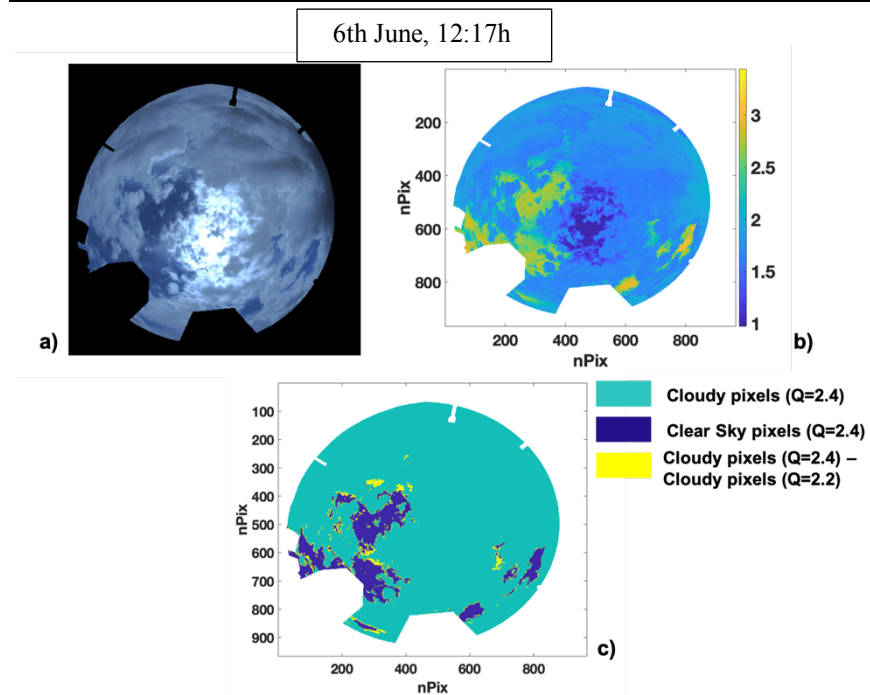


Figure 3.3 : a) Sky Camera image at $SZA = 17^\circ$; b) corresponding B/R quotient; c) changes in CS Mask with the threshold.

In Figure 3.3 and Figure 3.4 corresponding to cases from June and December respectively, can be seen the dependency of the B/R quotient with SZA . In Figure 3.3 the solar zenith angle is 17.2° , and the B/R ratio for clear skies (Figure 3.3b) is higher than in Figure 3.4b, whose solar zenith angle is 62.7° . The maximum value of the B/R quotient in Figure 3.3b is 3.44, while in Figure 3.4b is 2.88, a 16% lower. That's why the threshold for the case in Figure 3.3 is 2.4, and the one for Figure 3.4 is 2.1. The variation among the thresholds is one tenth between them, but this tenth is more significant the less cloud cover there is. The thresholds of course affect to the edges of clouds and very thin clouds. Figure 3.3c and Figure 3.4c show the pixels involved when a different threshold from the assigned in Table 3.1 is taken. In such depictions the cloudy pixels are shown in green and the clear sky pixels in dark blue, for the corresponding threshold depending on the SZA .

3. Methodology, Data and Analysis

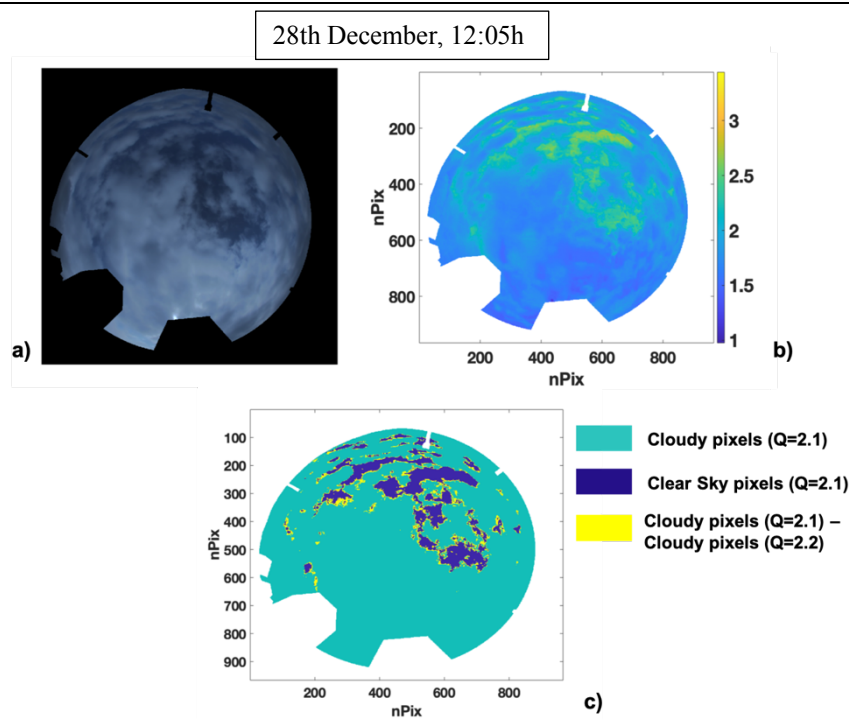


Figure 3.4 : a) Sky Camera image at $SZA = 63^\circ$; b) corresponding B/R quotient; c) changes in CS Mask with the threshold.

The yellow pixels are those in which the cloud cover changes if a threshold of 2.2 is taken, 2 tenths and 1 tenth respectively in absolute value from the one in Table 3.1. Those pixels represent a 3% and 5% of the cloudy domain, but also a 22% and 31% of clear sky pixels, respectively. These percentages increase the further we move away from the thresholds indicated in Table 3.1. With these figures we see that setting a single threshold can eliminate a significant number of cloud edges pixels and thin clouds entirely from the further COD retrieval.

Geometric Calibration

Geometric calibration consists of assigning to each camera pixel the corresponding celestial observation coordinates, in units of degrees of zenith (θ) and azimuth (ϕ). Therefore, the outcome of the geometric calibration are two matrices, the Viewing Zenith Angle matrix (VZA, Θ) and the Viewing Azimuth Angle matrix (VAA, Φ). These matrices are essential for a number of applications, such as the forthcoming radiometric calibration, the accurate remote sensing of clouds, the construction of the algorithms of cloud properties retrieval, the conversions of coordinates system, the positioning and determining of the dimensions of a cloud, among others.

Geometric calibrations of sky cameras are usually carried out by the use of a chessboard (e.g. Software Ocamlib for Matlab/Python, Scaramuzza, Crispel and Roberts, 2018). Nevertheless, there are other methods that relate the pixel positions with astronomic Ephemerides. This can be done because the camera position is fixed, and every pixel always measures the same area of the celestial vault. The method goes by locating celestial bodies of known position, in zenith and azimuth coordinates, and relating them to the position in the camera. We opted for this method to obtain the coordinates maps, following the procedure described in Roman et al., (2017). Therefore, we employ night images since stars and planets occupy regions of 2x2 pixels at most. The position of the body is uniquely related to the Ephemerides, that have been obtained from the software Stellarium (www.stellarium.org).

The employed images are from March 2019, with measurement hours ranging from 20h (after sunset) to 5:25h (before sunrise). We track in them some celestial bodies which cover a wide range of zenith viewing angles (20°-70°). For example, we have used the trajectories of Arcturus, Regulus, Procyon, Capella, Sirius, Betelgeuse, Vega, Jupiter, Altair, Spica, Antares and Saturn. Besides, in order to cover all the range of zenith values and reach those closer to 0, we also employ images from July 2018 in which Vega was very visible and in transit through the zenith of the camera from 23h to 1 a.m. We also track Jupiter's transit in that period of time to cover the most extreme angles (70° -90°). We elaborate a database of stars positions in Zenith and Azimuth and their position in rows (pos_y) and columns (pos_x) in the camera's images.

Next, we relate the sky positions of the celestial bodies with the corresponding calculated zenith and azimuth angles θ and ϕ . We do this to obtain two respective fit lines, to apply over the pixels' positions and calculate the matrices Θ and Φ . To obtain

3. Methodology, Data and Analysis

θ , we relate the Star Zenith Angles to the radial distance of the pixels (d_{rad} , (3.3)) to the optical center, $C = [C_x, C_y]$. To obtain Φ , we relate the Stars Azimuth Angles with the calculated camera azimuth angles (ϕ , (3.4)). The parameters d_{rad} , ϕ , and zenith angles θ are obtained from the pos_y and pos_x and the optical center, C as shown in equations (3.1) to (3.4). The optical center is obtained through iteration by varying C_x and C_y , subject to two conditions: the optical center must maximize the correlation coefficient between the Star Zenith Angles and d_{rad} , as well as minimize the standard deviation between the Stars Azimuth Angles and ϕ .

$$\sin \theta = C_x - pos_x \quad (3.1)$$

$$\cos \theta = C_y - pos_y \quad (3.2)$$

$$d_{rad} = \sqrt{\sin^2 \theta + \cos^2 \theta} \quad (3.3)$$

$$\phi = \text{atan}\left(\frac{\sin \theta}{\cos \theta}\right) \quad (3.4)$$

We establish these two conditions for the optical center calculation, because displaced centers close to the correct optical center have also a very high correlation coefficient. The wrong center can be easily identified in such cases since it causes a stars' zenith values vs. d_{rad} scatter plot with two distinct branches. Figure 3.5 left shows the scatter with the wrong center and its correlation coefficient, as opposed to Figure 3.5 right, obtained with the correct center, $C = [pos_x, pos_y] = [450, 497]$. With the center C the correlation coefficient of the zenith scatter is 0.99998 as Figure 3.5 right, Figure 3.6 and (3.5) show, and the standard deviation between Stars Azimuth Angles and ϕ values is 0.11.

Once C is identified, we calculate the correct d_{rad} values and the θ and ϕ coordinates in the camera's images of the celestial bodies. The fit line of Star Zenith Angles vs d_{rad} in Figure 3.6 is further applied to the matrix of radial distances to the center (D_{rad}) of all the 966x966 pixels to obtain the Θ matrix, as (3.5).

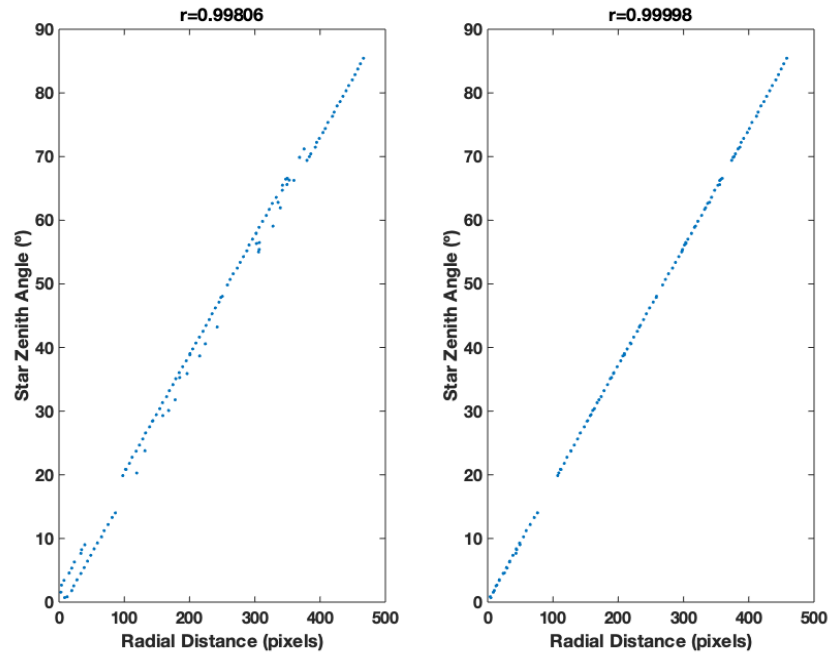


Figure 3.5 : Stars Zenith Angles vs d_{rad} with a wrong optical center (left) and the correct center (right)

$$\Theta = 0.1857(\pm 0.0002) \cdot D_{rad} + 0.05(\pm 0.05); r^2 = 0.99996 \quad (3.5)$$

The matrix Θ is depicted in Figure 3.7. The minimum value of Θ is 0.1182° and is located in the optical center. The maximum values of Θ are up to 133° . However, as it has been previously stated, for the applications of this work we limit the domain to 80° , to be sure that we remove any disturbance from the horizon.

The offset of the VAA is obtained from a second fit depicted in Figure 3.8 top, of Stars Azimuth Angles (AZ) vs calculated Azimuth Angles ϕ . The corresponding fit line and r^2 are depicted in (3.6).

$$AZ = \phi \cdot 1(\pm 0) + 4.40 (\pm 0.02); r^2=1 \quad (3.6)$$

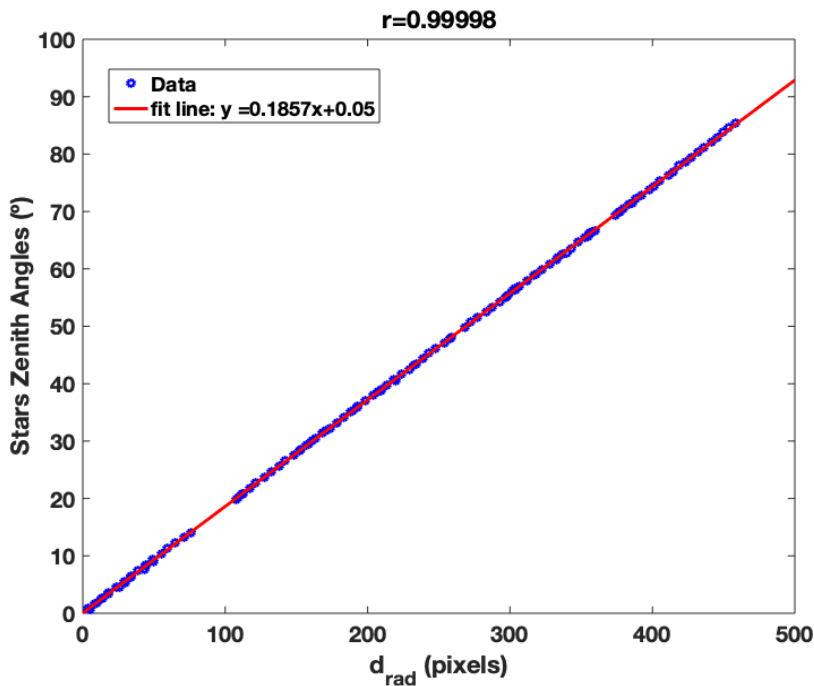


Figure 3.6: Fit line of Stars Zenith Angles vs d_{rad} and correlation coefficient (r)
 $r^2=0.99996$

In Figure 3.8 down are also plotted the differences between ϕ and AZ . From this plot and (3.6) we deduce that the camera is shifted $+4.4^\circ$ in the North direction.

The Φ matrix is calculated from the arctangent values between the X, Y vectors of each pixel to the center, rescaling with $+90^\circ$ for negative X and with $+270^\circ$ for positive X. This is done to follow the criteria of N = 0° , E = 90° , S = 180° and W = 270° . To these values, we also subtract the 4.4° offset. The result is a matrix of azimuth angles between 0° and 360° (Figure 3.9).

From Θ and Φ matrices we obtain the field of view (FOV) of each pixel as the solid angle (ω) calculated from the zenith (θ) and azimuth (ϕ) values, following (3.7) and (3.8).

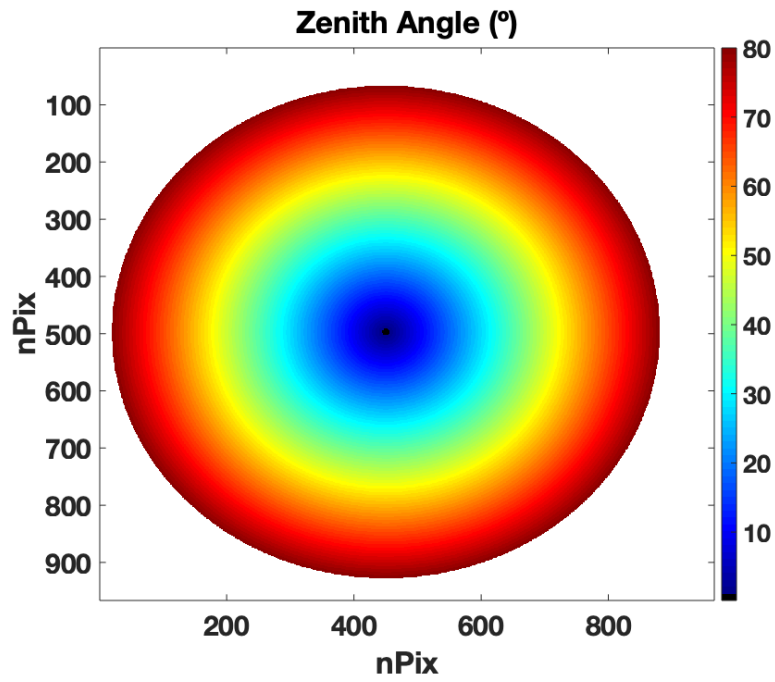


Figure 3.7 : Viewing Zenith Angle matrix, Θ in degrees

$$d\omega = \sin\theta d\theta d\phi \quad (3.7)$$

Expression (3.7) in cartesian coordinates takes the shape of (3.8).

$$d\omega = - \sin\left(\sqrt{x^2 + y^2}\right) \frac{dxdy}{\sqrt{x^2 + y^2}} \quad (3.8)$$

The FOV of each pixel $P_{i,j}$ of the image is obtained integrating the eq. 3.8. We obtain the cartesian coordinates $x_{i,j}$, $y_{i,j}$ of each $P_{i,j}$ by the expressions depicted in (3.9).

$$x_{i,j} = \Theta_{i,j} \cdot \cos \Phi_{i,j} ; y_{i,j} = \Theta_{i,j} \cdot \sin \Phi_{i,j} \quad (3.9)$$

Being $\Theta_{i,j}$ and $\Phi_{i,j}$ each element of the matrices Θ and Φ .

3. Methodology, Data and Analysis

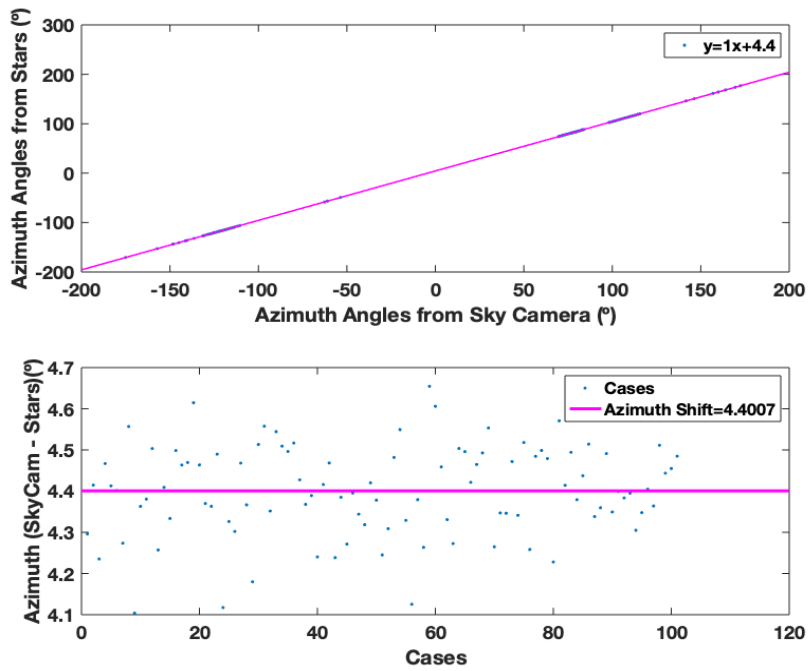


Figure 3.8 : Camera's Azimuth fit and shift to Stars Azimuth Values

The integration limits for x and y coordinates of each pixel in (3.8) are expressed in (3.10).

$$\begin{aligned}
 x_1 &= \frac{x - side1}{2}; x_2 = \frac{x + side1}{2}; \\
 y_1 &= \frac{y - side2}{2}; y_2 = \frac{y + side2}{2}
 \end{aligned}
 \tag{3.10}$$

Being, $side1 = abs(X2 - X1)/2$; $side2 = abs(Y2 - Y1)/2$.

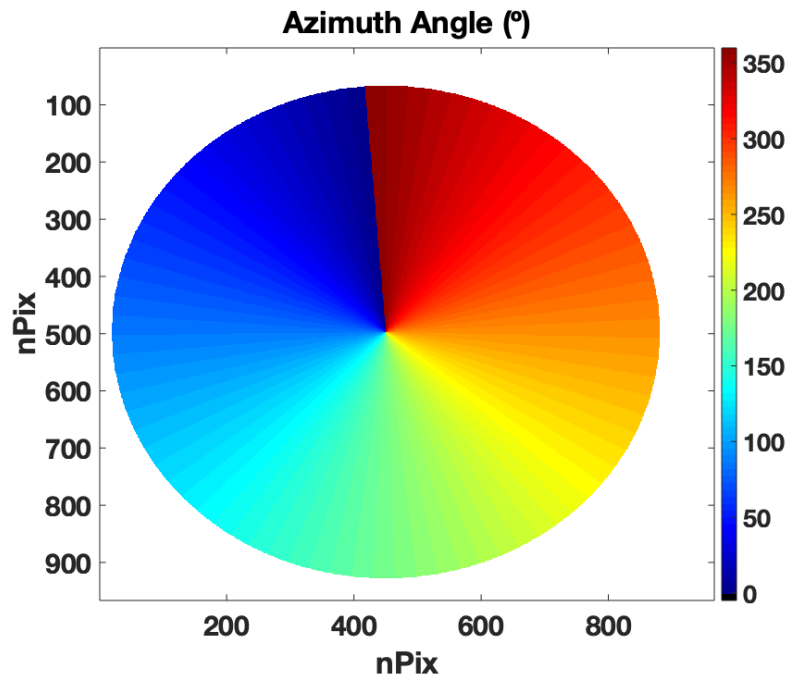


Figure 3.9 : Viewing Azimuth Angle matrix, Φ in degrees

Terms X1, X2, Y1 and Y2 are fully developed in (3.11).

$$\begin{aligned} X1 &= ZEN_{i+1,j} \cdot \cos AZ_{i+1,j}; X2 = ZEN_{i-1,j} \cdot \cos AZ_{i-1,j}; \\ Y1 &= ZEN_{i,j+1} \cdot \sin AZ_{i,j+1}; Y2 = ZEN_{i,j-1} \cdot \sin AZ_{i,j-1} \end{aligned} \quad (3.11)$$

X1 and X2 are the x positions of the pixel $P_{i+1,j}$ and the pixel $P_{i-1,j}$, respectively, so $side1$ is the distance between both of them. Same occurs for Y1, Y2 and $side2$, concerning the pixels $P_{i,j+1}$ and $P_{i,j-1}$. Therefore $side1$ and $side2$ divided by two are the x and y sizes of the pixel $P_{i,j}$.

The result of the integrations in the whole domain is the Field of View matrix (Ω), depicted in Figure 3.10, as the FOV of every pixel of the camera's image. The FOV values decrease as the Zenith values increase, and vary smoothly, from a maximum value of $1.64 \cdot 10^{-5}$ sr in the central pixel to $\sim 6.65 \cdot 10^{-6}$ sr at the horizon.

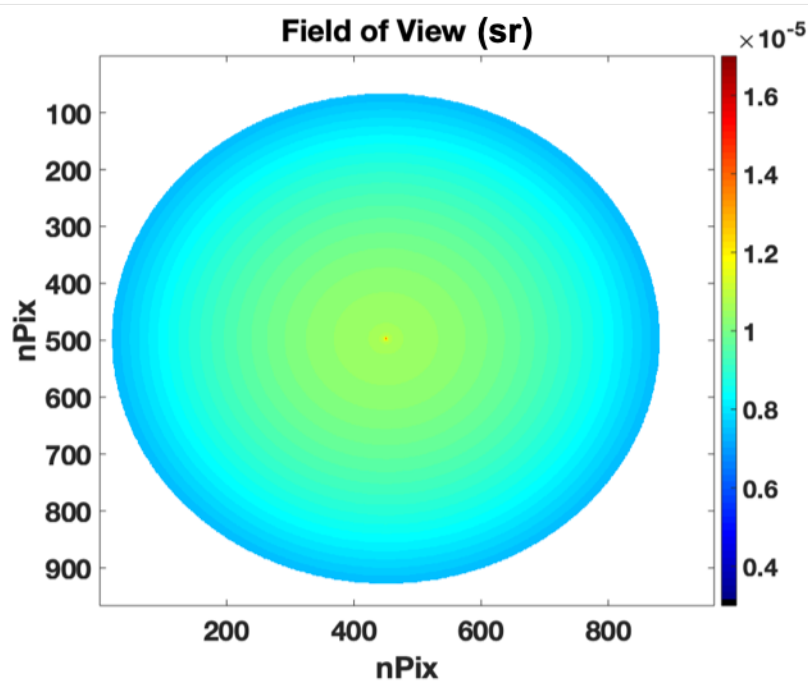


Figure 3.10 : Field of View matrix, Ω in steradians

Effective Wavelengths

One important step of the Sky Camera Characterization is the Effective Wavelengths acquisition. The importance of these wavelengths relies in the radiative simulations that are conducted in all this work. One way to determine the radiance in the visible band reaching every single pixel of the Sky Camera, is to simulate spectral radiances between 400 and 700 nm and weight them with the spectral response of the CMOS (convolved by the IR filter, see Chapter 2), depicted in Figure 2.4.

Nevertheless, there is another method: the concept of effective wavelength from Kholopov, (1975) and applied in Román et al., (2012) and Román et al., (2017):

The quotient of two broadband measurements, taken with the same instrument with its self-spectral response, under different conditions, equals to the ratio of the same measurements but measured with an instrument that is only sensitive at the effective wavelength λ_{ef} .

Thus, the monochromatic simulation of the radiometric magnitudes with each effective wavelength is equivalent to the broadband simulation, convolution and integration (Román et al., 2012).

In order to calculate the effective wavelengths, we follow (3.12).

$$\lambda_{ef} = \frac{\int_{\lambda} \lambda I(\lambda) S(\lambda) d\lambda}{\int_{\lambda} I(\lambda) S(\lambda) d\lambda} \quad (3.12)$$

Where λ is the wavelength, I is the irradiance reaching the instrument, and S is the spectral response of the channel.

To calculate the effective wavelengths for each color, a set of different irradiances of clear sky reaching the device are simulated with libRadtran. These irradiances correspond to the $I(\lambda)$ in (3.12): a total of 200 simulations changing the variables Solar Zenith Angle (SZA) and Angström α and β parameters, as in Table 3.2, following the same procedure as Roman et al., (2012). The reason for simulation clear sky irradiances is that the next radiometric calibration is done with clear-sky examples. On the other hand, varying the illumination and aerosols background is done to take in account the spectral variability of irradiance reaching the sky camera in clear sky conditions.

Table 3.2 : Variables employed in the simulations to obtain the λ_{ef} (R, G, B)

Variable	Range	Step
SZA	10° - 80°	10°
Angström α	0.2 - 1.8	0.4
Angström β	0.01 - 0.21	0.05

Besides, some parameters in the simulations remain constant for the 200 simulations. For instance, the aerosols phase function employed in the simulations is the Henyey-Greenstein function (Henyey and Greenstein, 1941), and the values of the asymmetry parameter and single scattering albedo (SSA) are 0.7 and 0.9 respectively, as well as a fixed value of Ozone column concentration of 300DU, for all wavelengths. These values are employed in Román et al., (2012) as reference values in mid-latitudes summer atmospheres.

3. Methodology, Data and Analysis

The broadband irradiances for each color are simulated from 400nm to 998nm, well past the limit of visible radiation, to include all the wavelength range of the spectral response of the CMOS (see Figure 2.4 in Chapter 2). Before calculating the effective wavelengths, the spectral response is convolved by the Infrared spectrum of the filter that is included in the camera, to obtain the $S(\lambda)$ used in (3.12). This reduces the spectral response to the minimum at around 800 nm and beyond, (Figure 2.4). After convolution, the spectral responses of blue and green are quite wide compared to that of red, with the FWHM being 105 nm, 103nm and 60 nm, for blue, green and red, respectively. However, the blue and green responses remain in a relatively gaussian shape, with only one maximum, while the red response exhibits a pair of relative maxima in both green and blue region. This is of significant influence to the value of the effective lambda in the red channel.

Finally, we substitute the broadband irradiances and convolved spectral responses into (3.12) and obtain 200 λ_{ef} values for each color, that is, 600 values in total. The average λ_{ef} and its standard deviation (std.) for each channel are shown in Table 3.3 and are those employed in the subsequent simulations in libRadtran.

Table 3.3 : Effective Wavelengths of the Sky Camera

Channel	$\lambda_{ef} \pm \text{std.}(\text{nm})$
Blue	472 ± 8
Green	534 ± 4
Red	592 ± 9

As can be seen in Table 3.3, the value of the effective wavelength in red is not within the spectrum of red itself, due to the relative maxima in the response spectrum of the sensor in this channel (Figure 2.4). In addition, convolving clear sky irradiance in equation (3.12) will shift the effective wavelengths towards the blue.

In order to decide which method to apply in this study, we carried out a small comparison between the two methods, namely, the channel radiance represented by the corresponding effective wavelength, and the spectral radiances convolved by the channel response of the CMOS sensor. Therefore, we analyze the relative difference between the spectral radiance obtained by means of broadband simulation and spectral response convolution, and the radiance obtained with the effective wavelengths. In blue channel and red channel, the differences reach as much 5% and

10%, respectively. The biggest differences are found in the green channel, that reach 15%. On the other hand, the monochromatic simulation with the effective wavelengths it's instantaneous, while the broadband simulation takes about 15 minute each.

Therefore, and for the sake of saving computation time in the forecoming calculations, we choose to make all the libRadtran simulations of the Sky Camera measurements with the effective wavelengths in Table 3.3.

Radiometric Calibration

The objective of the radiometric calibration is to calculate the radiometric constant for each color or channel (K_R , K_G , K_B) of the Sky Camera. They are obtained as the slope of the regression line that relate Irradiance ($\text{mW}\cdot\text{m}^{-2}$) values with the corresponding digital counts in the camera's images, according to (3.13), where the independent variable is the Digital Counts and the dependent variable is the Irradiance values.

$$K_{R,G,B} = \frac{R_{R,G,B}[i,j] \Omega_{i,j}}{P_{R,G,B}[i,j]} \rightarrow P_{R,G,B}[i,j] \cdot K_{R,G,B} = R_{R,G,B}[i,j] \Omega_{i,j} \quad (3.13)$$

The $K_{R,G,B}$ factors of (3.13) are the calibration constants for the Red, Green and Blue (R, G, B) channels, and the elements ($[i, j]$) of the matrices Ω of FOV (sr), Radiance ($R_{R,G,B}$, $\text{mW}\cdot\text{m}^{-2}\cdot\text{sr}^{-1}$) and Digital Counts ($P_{R,G,B}$) in the three channels. The radiometric calibration, as has been previously stated, is conducted under clear-sky conditions, as Radiance in clear-sky is widely known and unequivocally simulated by the Radiative Transfer model.

We have used a set of 525 Sky Camera images in the year 2018 for the calibration. Figure 3.11 shows a pair of them. These images must fulfill two requirements: cloudless conditions for 24 hours and the solar zenith angle must be under 70° .

The images cover different times (morning, midday and afternoon) and three seasons (summer, autumn and winter). With it we intend to cover a wide variety of situations, in order to guarantee an unbiased calibration.

3. Methodology, Data and Analysis

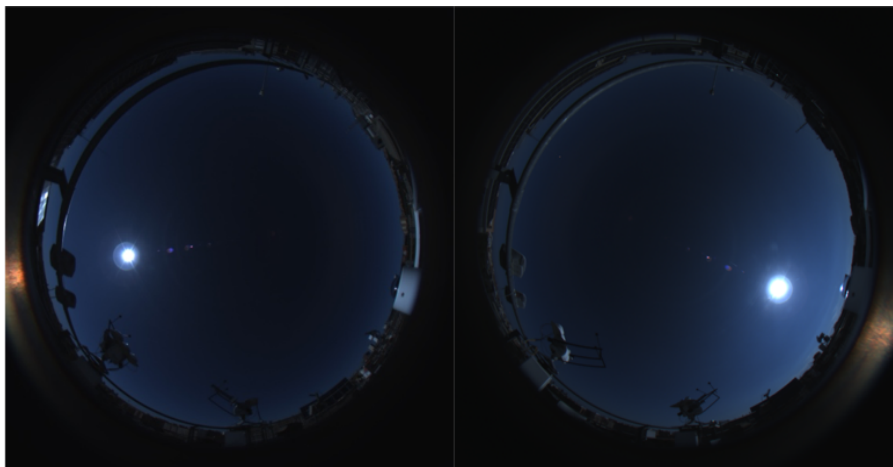


Figure 3.11 : Sky Camera images from the 5th June 2018, 8:25h (left) and 11th September 2018, 15:00h (right)

The spectral radiances corresponding to the camera's images are simulated at the three effective wavelengths with libRadtran. The simulations are performed with the parameters specified in Table 3.4. Namely, a standard atmosphere of mid-latitudes, Ozone column concentration, water vapor concentration, aerosol parameters, and a fixed surface albedo of 0.08 for blue channel, 0.15 for green channel and 0.30 for red channel. The surface albedo is obtained from AERONET database, and it is calculated as the average of the data employed in the measurement station from 2015 to the present.

Table 3.4: Input parameters at simulations for calibration

Parameters	Values (and origin)
wavelengths	472 nm, 534 nm, 592 nm (calculated)
Atmosphere	Midlatitude Summer (libRadtran)
Surface Albedo	0.08(B),0.15(G),0.30(R) (AERONET)
Ozone Column	287-359 DU(AERONET)
H ₂ O Column	6- 38 mm (AERONET)
Single Scattering Albedo	0.78 -1(B, G, R) (AERONET)
Asymmetry Parameter	0.60-0.79(B),0.59-0.78(G),0.57-0.77(R)(AERONET)
AOD	0.03-0.41(B),0.02-0.34(G),0.02-0.28(R)(AERONET)

Values of aerosol ssa, asymmetry factor (gg) and Aerosols Optical Depth are obtained from AERONET and interpolated to obtain the values at the effective wavelengths. Table 3.4 shows the maximum and the minimum values of the spectral variables for the three channels and the gases' column concentration. The aerosols' phase function is also from the AERONET database, and converted to 200 Legendre moments with the *pmom* tool in the libRadtran package.

Simulations are run at the Latitude, Longitude and altitude of the Burjassot measurement station, with the solar geometry corresponding to the selected images.

The radiance values are obtained for a range of 0° - 90° of viewing zenith angle (θ) and 0° - 360° of viewing azimuth angle (ϕ), with a step of 0.5° in zenith and azimuth. The *uvspec* outputs for each simulation are Radiances in $\frac{mW}{m^2nm \cdot sr}$, each 0.5° in θ and ϕ . The simulations' results of radiance are interpolated to the $\Theta_{i,j}$, $\Phi_{i,j}$ coordinates, to construct the matrices $R_{R,G,B}_{i,j}$ in (3.13).

Once the Radiances are calculated, the camera's images are separated in red, green and blue matrices of digital counts ($P_{R,G,B}_{[i,j]}$) and pre-processed with the cutout and masking of obstacles and pixels of $\theta > 80^\circ$. Next, the product of $IRR_{i,j} = R_{i,j} \cdot \Omega_{i,j}$ is obtained for each channel, and the datasets $[DC_i, IRR_i]_{[R,G,B]}$ are defined.

Also, we suppress the dark current and the background radiation, which remain as digital counts even when the irradiance is zero. To identify it, a linear regression of digital counts vs irradiance is performed for the three channels. In that way, the vertical intercept of the fit lines is the offset in Digital Counts, and we subtract it (less than 1 DC) at the three channels to the $DC_{i_{R,G,B}}$ vectors. Subsequently, we obtain the datasets $[x_i, y_i]_{[R,G,B]}$ for the calibration.

Figure 3.12, Figure 3.13 and Figure 3.14 show the scatter plots of the datasets for Blue, Green and Red channels, respectively. Likewise, and given the spread of points, we perform a weighted fit according to the number of points, and the fit lines and parameters of the scatter plots are depicted in Figure 3.12 to Figure 3.14 as well.

3. Methodology, Data and Analysis

In order to analyze the spread of values, we process the data set. First of all, we notice the straight lines at low irradiances in Figure 3.12 to Figure 3.14. These are points of a wide range of digital counts, and correspond to reflections of the sun inside the camera dome (example in Figure 3.15). These reflections occur always in clear-sky days, and appear as random spots located in the Principal Plane (PP). Therefore, in the position around the Principal Plane where the reflections appear (see Figure 3.15) the simulated Radiance is much less than the one that appears.

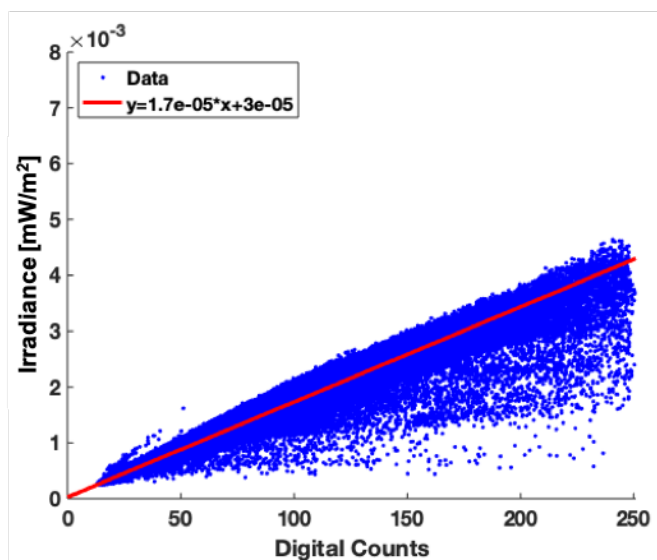


Figure 3.12 : Irradiance vs Digital Counts for Blue channel radiometric calibration; $r^2 = 0.9685$

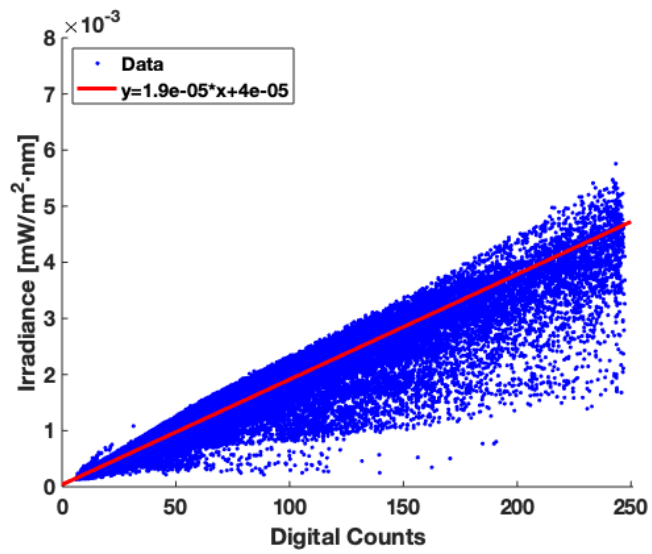


Figure 3.13 : Irradiance vs Digital Counts for Green channel radiometric calibration, $r^2 = 0.9622$

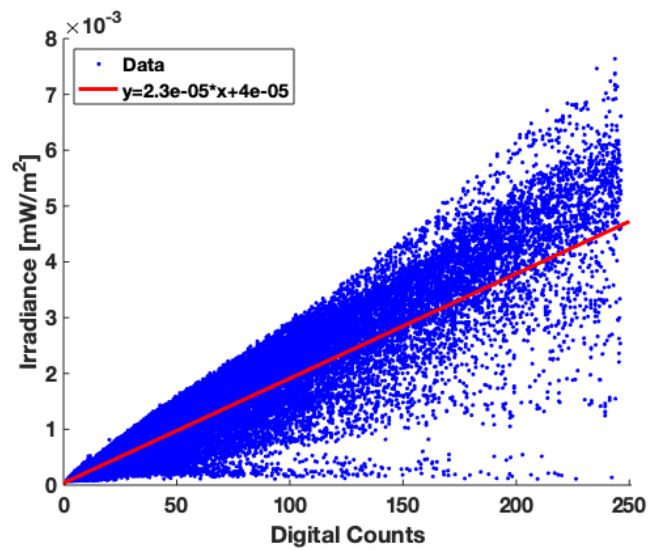


Figure 3.14 : Irradiance vs Digital Counts for Red channel radiometric calibration, $r^2 = 0.9417$

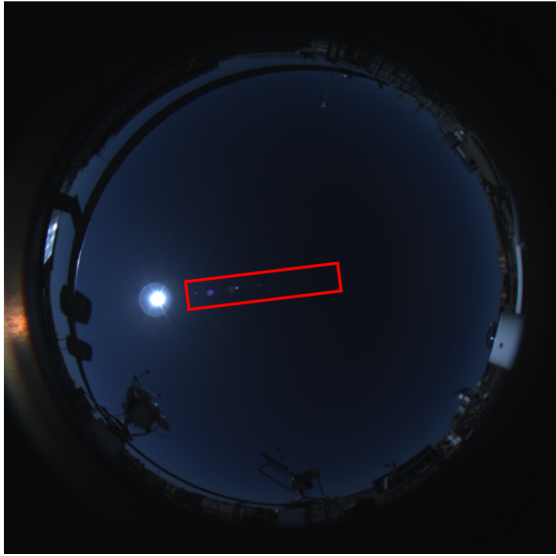


Figure 3.15 : Reflexes in the camera's dome (red square)

On the other hand, a further analysis carried away by the GRSV has determined that the variability of points that occur at higher digital counts belong to the circumsolar area, and it is related to the Aerosol Optical Depth. Such points, even if they occupy a big part of the graph actually represent only 5% of the entire dataset.

With it, we rely on statistics to process the datasets $[x_i, y_i]_{[R,G,B]}$ and suppress variability from it, to obtain the correct fit lines and ultimately the calibration constants for the three channels of the sky camera.

First, from the set of points that appear in Figure 3.12, Figure 3.13 and Figure 3.14 we calculate a vector (δ) of bias or residuals (res_i), that is, the difference between the Irradiance values and the fit lines, for each channel, as in (3.14). Next, we calculate the average ($\bar{\delta}$) and the standard deviation (σ) of δ . For the data correction, we consider outliers those points whose irradiance bias with the corresponding fit line is greater(lesser) than the sum (subtraction) of $\bar{\delta}$ plus (less) three times the standard deviation of the bias vector. Contrary, the new set of points $[x'_i, y'_i]_{[R,G,B]}$ are those whose bias is inside the interval of 3σ above and below $\bar{\delta}$, as (3.15) expresses.

$$\delta_{[R,G,B]} = \{res_i = f(x_i) - y_i\}_{[R,G,B]} \quad (3.14)$$

$$[x'_i, y'_i]_{[R,G,B]} = \{res_i < \bar{\delta} \pm 3\sigma\}_{[R,G,B]} \quad (3.15)$$

After applying (3.15) the new dataset for the three channels $[x'_i, y'_i]_{[R,G,B]}$ are depicted in Figure 3.16, Figure 3.17 and Figure 3.18. They suppose a 98% of the $[x_i, y_i]_{[R,G,B]}$ dataset.

With Figure 3.16, Figure 3.17 and Figure 3.18, we obtain the fit lines for the radiometric calibration for the whole domain, taking the assumption that all pixels are equal and have the same $K_{R,G,B}$. The fit lines for the blue, green and red channels are displayed in (3.16), (3.17) and (3.18) respectively. The terms between parenthesis in (3.16), (3.17) and (3.18) are the errors of the slope and vertical intercept. We obtain then from the Confidence Intervals of 95% of the fits.

From (3.16), (3.17) and (3.18) we extract that $K_B = 1.795(\pm 0.001) \cdot 10^{-5} \frac{mW}{m^2}$; $K_G = 2.051(\pm 0.003) \cdot 10^{-5} \frac{mW}{m^2}$ and $K_R = 2.52(\pm 0.01) \cdot 10^{-5} \frac{mW}{m^2}$.

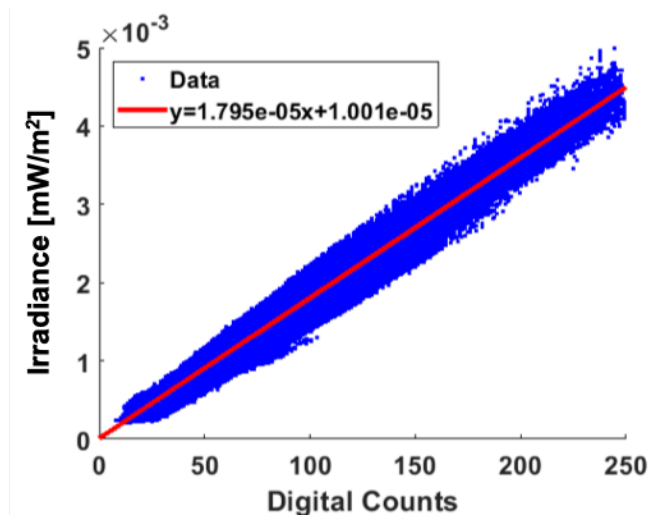


Figure 3.16 : Radiometric Calibration for Blue Channel; $r^2 = 0.9864$

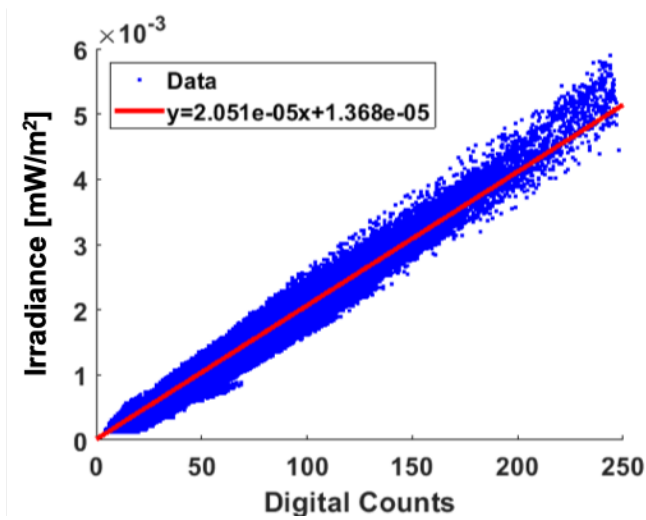


Figure 3.17 : Radiometric Calibration for Green Channel; $r^2 = 0.9864$

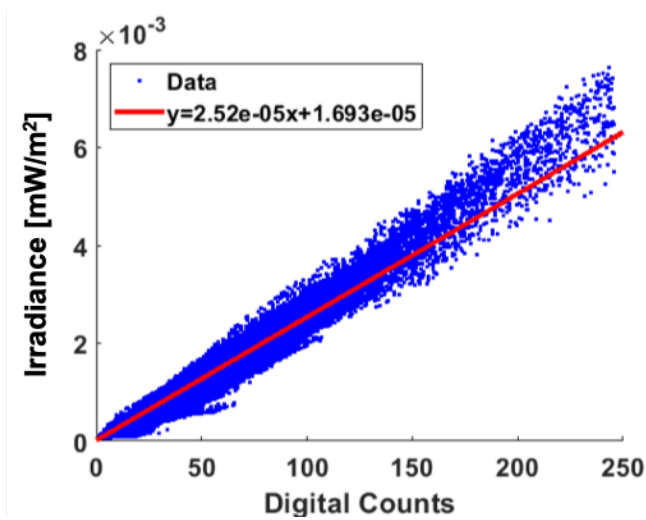


Figure 3.18 : Radiometric Calibration for Red Channel; $r^2 = 0.9779$

$$\begin{aligned}
 IRR &= 1.795(\pm 0.001) \cdot 10^{-5} * DC + 1.001(\pm 0.004) \cdot 10^{-5} \\
 r^2 &= 0.9864
 \end{aligned}
 \tag{3.16}$$

$$\begin{aligned}
 IRR &= 2.051(\pm 0.001) \cdot 10^{-5} * DC + 1.368(\pm 0.004) \cdot 10^{-5} \\
 r^2 &= 0.9864
 \end{aligned}
 \tag{3.17}$$

$$\begin{aligned}
 IRR &= 2.52(\pm 0.01) \cdot 10^{-5} * DC + 1.693(\pm 0.004) \cdot 10^{-5} \\
 r^2 &= 0.9779
 \end{aligned}
 \tag{3.18}$$

In addition to the radiometric constant we obtain the uncertainties for the calibration for a range of Digital Counts and a range of Viewing Zenith Angle. To do that we use the complete datasets (Figure 3.12, Figure 3.13 and Figure 3.14) without the reflections. The uncertainties are obtained as a function of the Viewing Zenith Angle and a range of Digital Counts. To obtain the calibration uncertainties we employ the RMSE equations from the fit residuals (res_i , (3.14) and (3.19)) of each point i , as equations (3.19), (3.20) and (3.21) show.

$$res_i = f(x_i) - y_i \tag{3.19}$$

$$RMSE = \sqrt{\left(\frac{\sum_{i=1}^{i=N} (res_i)^2}{N - 1}\right)} \tag{3.20}$$

$$RMSE_r = \left(\frac{RMSE}{\left(\frac{\sum_{i=1}^{i=N} f(x_i)}{N}\right)}\right) \cdot 100 \tag{3.21}$$

Being y_i each irradiance value in the scatter in Figure 3.16, Figure 3.17 and Figure 3.18, and $f(x_i)$, the fit equations (3.16), (3.17) and (3.18) evaluated at each Digital Count value, x_i . From the residuals, the RMSE is calculated as in (3.20). The absolute error has Irradiance units, and to obtain it in percentage we calculate also the relative error $RMSE_r$, dividing the RMSE by the mean value of the fit line in that sector of values.

3. Methodology, Data and Analysis

Table 3.5 : Uncertainties in the calibration for blue channel as a function of VZA and DC ranges

VZA	DC range				
	<50	50-100	100-150	150-200	>200
<40°	20.1%	7.2%	9.9%	12.4%	22.4%
40°-60°	16.4%	6.3%	8.5%	10.6%	34.5%
60°-80°	10.4%	4.4%	7.2%	8.7%	34.7%

Table 3.6 : Uncertainties in the calibration for green channel as a function of VZA and DC ranges

VZA	DC range				
	<50	50-100	100-150	150-200	>200
<40°	18.1%	9.9%	10.4%	16.8%	20.0%
40°-60°	22.6%	8.2%	16.2%	20.6%	24.8%
60°-80°	7.3%	7.7%	18.7%	16.4%	19.4%

Table 3.7 : Uncertainties in the calibration for red channel as a function of VZA and DC ranges

VZA	DC range				
	<50	50-100	100-150	150-200	>200
<40°	22.4%	16.4%	20.3%	25.6%	26.5%
40°-60°	9.0%	15.4%	23.8%	30.2%	35.0%
60°-80°	4.9%	10.9%	17.3%	28.8%	34.9%

As can be figured out from Table 3.5 - Table 3.7 and Figure 3.16 - Figure 3.18, the uncertainty in the calibration increases with Viewing Zenith Angle and with Digital Counts for the three channels. The maximum uncertainty is ~35% for brighter pixels in the blue and red channels, and ~25% in the green channel.

Validation with AERONET Radiance

We validate our results of radiometric calibration by means of radiance comparison. To do that we use the AERONET Sky Radiance values in Almucentar configuration for the same cases employed for the calibration. We employ the Almucentar measurements to avoid the lens reflection spikes that occur in the Principal Plane (Figure 3.15).

First of all, we convert the Digital Counts of the Sky Camera images to Radiances rearranging (3.13), and using the FOV matrix ($\Omega_{i,j}$) and the $K_{R,G,B}$.

For the comparison with AERONET we extract from the sky camera's radiance image the same sky sectors that the CE-318 measured. Following the scheme in Figure 2.9 of Chapter 2, we find the scattering angles positions (ϕ_{sc}) employing the Θ and Φ matrices. As the sun photometer measurement has a field of view of 1.2° , we extract around each ϕ_{sc} a sector with the same FOV employing the Ω matrix and obtain the average value.

However, the AERONET measurement wavelengths are different from the effective wavelengths of the Sky Camera. The closest sun photometer wavelengths are 440, 500 and 675 nm. In order to be able to compare both radiances, we must convert one set of data to the other's wavelengths, by means of a conversion factor, that works as $\Gamma = \frac{IRR_{SKYCAM}}{IRR_{AERONET}}$. Such factors are obtained by means of the Irradiance spectra simulated to obtain the effective wavelengths. We calculate the ratios between the Irradiances at 592nm and 675nm (red channel), 534nm and 500 (green channel) and 472 nm and 400nm (blue channel). As we had 200 spectra from different atmospheric conditions, we obtain 200 conversion factors for each channel. The average value of them are $\Gamma_R = 1.1708$, $\Gamma_G = 0.9449$ and $\Gamma_B = 1.1107$ for red, green and blue channel, respectively.

Therefore, AERONET Sky Radiance values are converted to our wavelengths by multiplying them by $\Gamma_{R,G,B}$, and our measurements can be converted to AERONET wavelengths by multiplying by $\frac{1}{\Gamma_{R,G,B}}$.

3. Methodology, Data and Analysis

The validation is shown in Figure 3.19. We represent AERONET radiances ($RAD_{AER,[R,G,B]}$) vs Sky Cam Radiances ($RAD_{SKYCAM,[R,G,B]}$), for blue, green and red in the Sky Camera effective wavelengths: 472.43nm, 533.88nm and 592.07nm, respectively. The fit lines for the three channels are shown in equations 5.13 and in Figure 3.19 as well, with correlation coefficients of 0.9884, 0.9831 and 0.9883, respectively.

$$\begin{aligned} RAD_{AER,B} &= 0.91(\pm 0.03) \cdot RAD_{SKYCAM,B} - 1(\pm 2) \\ r^2 &= 0.9770 \end{aligned} \quad (3.22)$$

$$\begin{aligned} RAD_{AER,G} &= 1.15(\pm 0.04) \cdot RAD_{SKYCAM,G} - 9(\pm 2) \\ r^2 &= 0.9666 \end{aligned} \quad (3.23)$$

$$\begin{aligned} RAD_{AER,R} &= 1.196(\pm 0.034) \cdot RAD_{SKYCAM,R} - 12(\pm 1) \\ r^2 &= 0.9767 \end{aligned} \quad (3.24)$$

From (3.22), (3.23) and (3.24), we observe that whereas the green and red channels underestimate the radiance with respect to AERONET in a 15% and 20%, respectively, with the blue channel the radiance gets overestimated in a 9%. The vertical intercept values -9 and -12 in green and red channels respectively also show worse calibration in comparison to the blue channel.

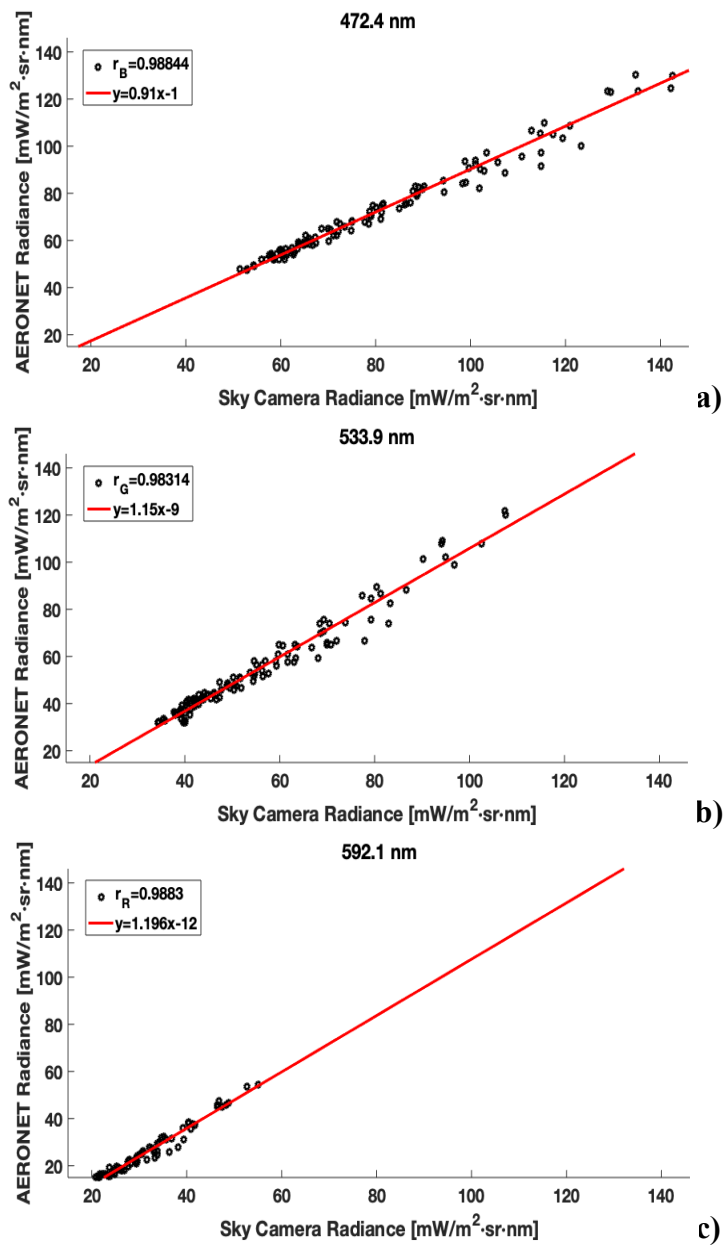


Figure 3.19 : Sky Camera Radiance validation through AERONET data

3.1.2. Cloud Optical Depth Determination

As we indicated at the beginning of this chapter, the objective of this work is to obtain the COD from the Sky Camera. In this work the COD acquisition is done through the so-called ‘Retrieval Algorithm’ (Figure 3.1). The core of the Retrieval Algorithm is an inversion method based on a Lookup Table for converting Radiances to optical cloud thicknesses. The methodology is based in the principle followed in works such as Schwartz et al., (2017), whereby, the dependence of the Radiance with the COD can be inverted at a solar geometry to obtain COD from Radiance measurements. In this work the inversion method is defined straight from Radiances in the blue channel, unlike other works as Chiu et al., 2010, 2012 and Mejia et al., 2016 that use ratios or indices of two channels. Our reason is fundamentally the effective wavelengths of the Sky Camera, that are not far enough away. With it, it has not been possible to define a ratio between channels as a function of COD better than the simple monochromatic Radiance itself.

Therefore, and given the results of the radiometric calibration validation ((3.22), (3.23), (3.24) and Figure 3.19a), we employ the blue channel to obtain the cloud properties.

LibRadtran Simulations

LibRadtran is a radiative transfer code designed for computing radiances, irradiance and actinic fluxes in Earth’s atmosphere. Its main tool is the *uvspec* program. The *uvspec* software as a core of the radiative transfer model calculates the radiation field for a variety of atmospheric and spectral conditions. The libRadtran code is developed under Linux environment but the package runs under Unix, Macintosh OS X and several Microsoft Windows platforms. The input files are a free format ASCII files which contain options and parameters defined by the user, as solar and viewing geometry, surface integrated or spectral albedo, aerosols profile, aerosols parameters, total trace gases columns, BRDFs, etc. The user can also include some cloud parameters as the cloud profile, cloud cover and parameterization.

The model outputs are ASCII files as well, consisting in the standard output of *uvspec* (*stdout*), plus additional files to provide the radiances, fluxes and other products when specific commands are settled.

LibRadtran possesses a wide variety of solvers of the radiative transfer equation. Among them we can find DISORT (Chandrasekhar, 1960; Stamnes et al., 1988), see

Chapter 1) and its variations, which is possibly the most employed 1D radiative transfer solver. DISORT solves the radiative transfer equation in one dimensional, plane-parallel, and pseudo-spherical geometry with accurate calculations of the radiometric parameters.

We employ libRadtran to simulate the ground Radiances that are used to build the Lookup Table for the inversion method in the Retrieval Algorithm. The model runs with the parameters summarized in Table 3.8.

The simulations are carried out at 440nm, the measurement wavelength of AERONET for blue channel. This is done first of all because we will validate our results with AERONET, but also in anticipation of future work in which we could change the Sky Camera or alter the response function of the device and thereby the effective wavelengths. Therefore, we consider that is better to calculate the LUT at wavelengths of recognized efficiency such as those of AERONET, and next convert the results of Radiance to the values of the device employed at that time.

The steps (between brackets in Table 3.8) define the vectors' intervals of the Lookup Table construction. The values of Total Ozone Column and Total Water Vapor Column are obtained from AERONET and are calculated as the average values of the year 2018.

On the other hand, the Solar Zenith Angle range (Table 3.8) cover all possible values from dawn to dusk among the year in Valencia, in steps of 5°. Nevertheless, we are only interested in examining episodes with angles under 70°, due to the change in exposition time of the sky camera at night time (Chapter 2). The simulations cover a wider enough range to avoid extrapolation in all cases. Same for the Solar Azimuth Angle (SAA) range, which for the Sky Camera geometry (Figure 3.9) takes extreme values of ~80° (East, left side of the camera) and ~300° (West, left side of the camera) in the measurement location.

The grid of Viewing Zenith Angle, Viewing Azimuth Angle employed to perform the simulations, cover the whole matrix coordinates. The Zenith final value of 80° coincides with the horizon mask applied to the images.

3. Methodology, Data and Analysis

Table 3.8 : Input parameters for libRadtran simulations

Parameter	Values (and Steps)
wavelength	440 nm
solver	disort
Streams number	18
Latitude/Longitude	39.5°N / 0.42°W
Albedo	0.08(B),0.15(G),0.30(R)
Ozone Column	320 DU
H ₂ O Column	20 mm
aerosols	Default
Clouds LWC	0.1 g/m ³
Clouds r_{eff}	10 μm
Clouds base and top	1-2km
Solar Zenith Angle	16° - 86° (5°)
Solar Azimuth Angle	80° - 300° (50°)
Viewing Zenith Angle	0° - 80° (20°)
Viewing Azimuth Angle	0° - 360° (30°)
Cloud Optical Depth	0 - 150 (5,20,30)

We define the cloud base at 1km altitude, which is the most frequent low-cloud basis height on average throughout the year 2018. This information has been obtained analyzing the ceilometer data from June 2018, when the sky camera began to measure, to March 2019. On the other hand, the LWC and r_{eff} employed in the cloud file definition are typical values for low water clouds (Kniffka et al., 2014; Kokhanovsky, 2004). The τ product out of LWC and r_{eff} remains therefore constant, but the model rescales it to each of the desired values in Table 3.8.

We carry out a brief study of the sensitivity of the model to the variation of these three cloud parameters: LWC, effective radius and the cloud location. For a fixed COD ($\tau = 5, 20$), we vary one of the parameters from the reference value in the LUT, to each one of the values specified in Table 3.9. With the new atmosphere configuration, we obtain the corresponding Radiance matrix (Rad'). The matrix σ of relative differences, between Rad' and the reference Radiance matrix (Rad) is calculated as in (3.25). In Table 3.10 we show the mean value of the σ matrices for each varied value of each parameter, and the total average value.

$$\sigma = \left(\frac{Rad' - Rad}{Rad} \right) \cdot 100 \quad (3.25)$$

When the total Cloud Optical Depth is set, we can see in Table 3.10 that the influence of r_{eff} value is small, being maximum when $\tau = 20$ and $r_{eff} = 5\mu\text{m}$. That is because transmitted radiance is more sensitive to COD than to r_{eff} in the blue region of the spectrum, where the water vapor is non-absorbing (McBride et al., 2011).

On the other hand, the influence of LWC is completely null for fixed r_{eff} and τ , and the cloud location has also proven to be of little influence for the 1D approach, as they saw in their sensitivity study for shortwave irradiance (Wapler and Mayer, 2008).

Table 3.9 : Cloud parameters and variation of values

Parameter	LUT Values	Variation values
Clouds LWC	0.1 g/m ³	0.05 g/m ³ -- 1 g/m ³
Clouds r_{eff}	10 μm	5 μm – 15 μm
Cloud base	1 km	0km – 2km

Table 3.10 : Sensibility to cloud parameters at fixed values of $\tau = 5, 20$

τ	LWC	Reff			Cloud base		
		5 μm	15 μm	Average	0km	2km	Average
5	0.0%	3%	1%	2%	0.7%	0.6%	0.6%
20	0.0%	5%	2%	4%	0.1%	0.2%	0.1%

With all that, the main variable on the libRadtran simulations is the Cloud Optical Depth, which takes values from 0 to 150 in steps of 5 (until $\tau=60$), 20 (until $\tau=120$) and 30 for the last step. This is because lower values of τ are more likely for low clouds, except for the stratus clouds and cumulonimbus (Ch. 2, Table 2.2).

All the simulations are run with a cloud cover of 1, since we are applying the Independent Pixel Approximation, defined in Chapter 2, and therefore each pixel is considered cloudy and independent from all the other pixels, in a similar way to Schwartz et al., (2017).

3. Methodology, Data and Analysis

The default aerosols properties correspond to the model of Shettle (1989). They consist in a rural type in the boundary layer, as well as background aerosols above 2km, spring-summer conditions and a visibility of 50 km.

Lookup Table

The Lookup Table is constructed in order to obtain the COD at each desired value of Θ , Φ , SZA, SAA and Radiance. It consists in values of COD as a function of the five variables in **Table 3.8** plus Radiance, as (3.26) shows.

$$T_{i,j,k,l,m} = f(VZA, SZA, SAA, VAA, Radiance) \quad (3.26)$$

Therefore, $T_{i,j,k,l,m}$ is calculated and constructed depending on the other five variables.

As indicated previously, the vectors of the COD Lookup Table construction are defined by the same simulations of the model, and are specified in Table 3.11.

Table 3.11 : Variables of the COD LUT

vector	Variable	Range
x ₁	VZA (θ)	0° - 80°
x ₂	SZA ($s\theta$)	16° - 86°
x ₃	SAA ($s\phi$)	80° - 300°
x ₄	VAA (ϕ)	0° - 360°
x ₅	Radiance (<i>Rad</i>)	0.7-1000.7 $\frac{\text{mW}}{\text{m}^2 \cdot \text{sr}}$

To obtain each value of $T_{i,j,k,l,m}$ we must perform an inversion procedure, since simulations of the model provide Radiance as a function of τ , and we need just the opposite. As we don't know the exact function of $Radiance = f(\theta, \phi, s\theta, s\phi, \tau)$, each $T_{i,j,k,l,m}$ is obtained from the relationship of each *Rad* value in x₅ (plus the uncertainties induced by the calibration error ($\epsilon_R(cal)$)). with the function $\mathbf{R} = \mathbf{f}(\boldsymbol{\tau})$. In the function $\mathbf{R} = \mathbf{f}(\boldsymbol{\tau})$ (Figure 3.20) the *R* corresponds to the simulated values of surface incoming Radiance by libRadtran, for each set of sun and viewing geometry conditions ($geo. = \{\theta, s\theta, s\phi, \phi\}$).

Figure 3.20 to Figure 3.28 show some examples of the variations of Radiance with τ for different solar and observation geometries. Figure 3.20 illustrates the fact of ambivalence of τ for a given value of radiance in monochromatic inversion procedures. Depending on the value of x_5 with respect to functions such as Figure 3.20, obtaining the τ value for the $T_{i,j,k,l,m}$ is more or less feasible, and such τ value is more or less reliable. We can distinguish up to five different situations or cases depending on the nature of the τ acquisition. They are all summarized in Table 3.12 and explained in detail below.

Table 3.12 : Different cases of the $T_{i,j,k,l,m}$ construction

N°	Case
1	Ordinary
2	Neutral
3	Ambivalence
4	Out of Range
5	Mixed Cases

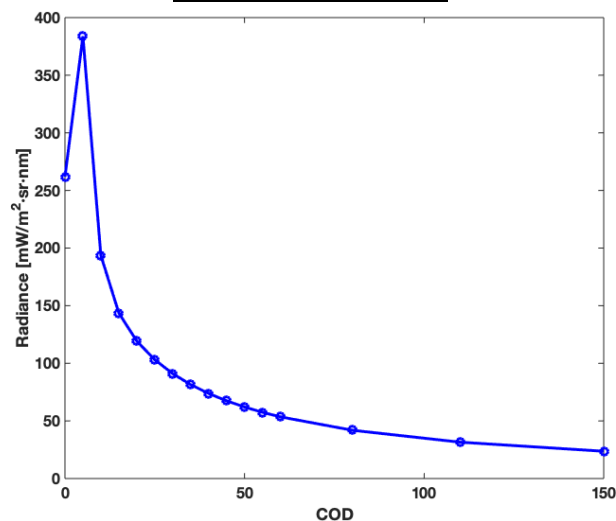


Figure 3.20 : Example of $R = f(\tau)$ function, maximum of Radiance located at $\tau = 5$

3. Methodology, Data and Analysis

Besides the $T_{i,j,k,l,m}$ matrix we build two more matrices with the same dimensions as T .

First, a matrix of data quality Flags, $FL_{i,j,k,l,m}$, to point out which one of the cases in Table 3.12 are we dealing with, and therefore the reliability of the τ values in the $T_{i,j,k,l,m}$ and ultimately the COD ones. The values assigned to the $FL_{i,j,k,l,m}$ descend with the quality of the results, so the more reliable COD values have the higher, positive flags, and the less reliable values, the lower, even negative flags.

Also, we obtain a third matrix of Radiance uncertainties $ERR_{i,j,k,l,m}$, on which each value depends on the case (Table 3.12) to which it belongs, and is constructed to give an overall value of the retrieval errors. We explain the cases in Table 3.12 and illustrate them with the help of Figure 3.21 to Figure 3.28.

First of all, the ordinary cases are those whose Radiance value from x_s plus uncertainties, or $Rad(LUT) \pm \epsilon_R(cal)$, fall within the determined range of Radiance by the $\mathbf{R} = \mathbf{f}(\boldsymbol{\tau})$ function, at a given $geo. = \{\theta, s\theta, s\phi, \phi\}$. Such range is defined by the maximum and minimum value of Radiance in the $\mathbf{R} = \mathbf{f}(\boldsymbol{\tau})$ function, that is, Rad_{MAX} and Rad_{MIN} in Figure 3.21, respectively. These limits are usually established by the absence of ambivalence. Therefore, in Figure 3.21 we can see that the Radiance at Clear Sky (Rad_{CS} , or Radiance when $\tau = 0$) coincides with Rad_{MAX} which is typical of ordinary cases. When all these conditions are met, the $T_{i,j,k,l,m}$ is obtained through a Cubic Hermite interpolation (Kreyszig, 2005) of Rad (LUT) with the $\mathbf{R} = \mathbf{f}(\boldsymbol{\tau})$ function, and a Flag of 16 is given, that is, $FL_{i,j,k,l,m} = 16$ (Figure 3.21).

Ordinary cases are the ideal ones, and all the others will carry flags of lesser value. The error assigned to the $ERR_{i,j,k,l,m}$ in all ‘within range’ cases (WR), Ordinary Case and those that come next, is the corresponding calibration uncertainty (Table 3.5) or $\epsilon_R(cal)$.

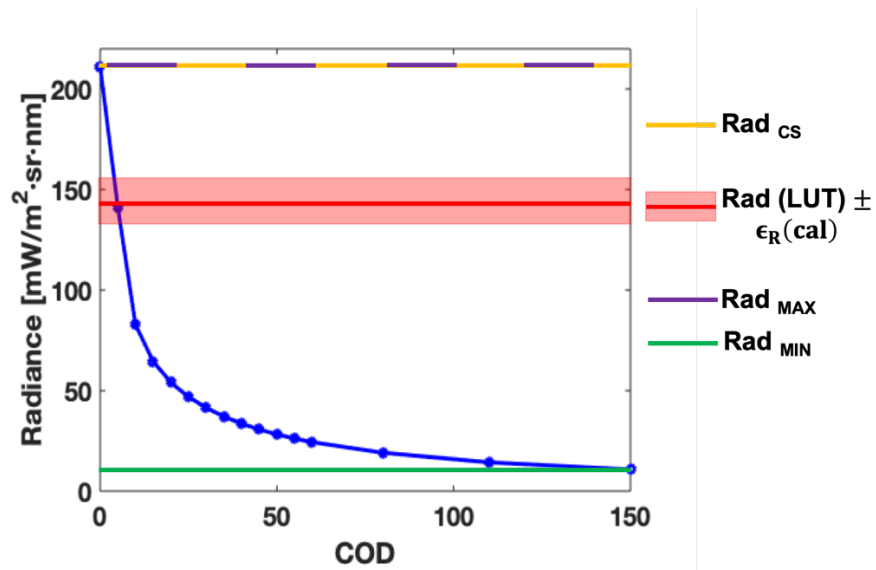


Figure 3.21 : WR, Ordinary Case - $FL_{i,j,k,l,m} = 16$

Unfortunately, in the construction of the LUT we find very often ambivalence in the $\mathbf{R} = \mathbf{f}(\boldsymbol{\tau})$ functions for small cloud optical depths. As it is pointed out in Section 3.1.5. of Atmospheric Agents simulations, transmitted radiance (as opposed to reflected radiance) does not present a one-to-one relationship with τ . Increasing optical depths for thin clouds lead to an increasing the number of scattering particles, which causes an increase in the diffuse radiation scattered downwards, towards the field of aperture of the sensors (McBride et al., 2011), and therefore increasing the radiance. Once a sufficient high optical thickness is reached ($\tau = 5$ to 10) the attenuation of radiation dominates and the transmitted signal to the ground decreases with increasing COD (e.g. Figure 3.20) This effect depends on the directions of observation and solar geometry ($geo. = \{\theta, s\theta, s\phi, \phi\}$), and hence the form and Radiance range of the $\mathbf{R} = \mathbf{f}(\boldsymbol{\tau})$ changes for each set of geometric angles.

Figure 3.22 to Figure 3.24 show the three possible situations found when $Rad(LUT) \pm \epsilon_R(cal)$ is within the range of Radiance and there is ambivalence. To distinguish them, we look at the value of Rad_{CS} and its position relative to $Rad(LUT) \pm \epsilon_R(cal)$. Figure 3.22 illustrates the case named ‘Neutral’, in which $Rad(LUT) \pm \epsilon_R(cal)$ is below Rad_{CS} . In this case, although there is ambivalence, it does not affect to the obtention of $T_{i,j,k,l,m}$ by interpolation, in a similar way to the

3. Methodology, Data and Analysis

ordinary cases. Neutral cases get assigned in $FL_{i,j,k,l,m}$ a Flag of 12, and the corresponding error is also $ERR_{i,j,k,l,m} = \epsilon_R(cal)$.

The most problematic cases are those whose value of $Rad(LUT) \pm \epsilon_R(cal)$ is within range and above Rad_{CS} in the presence of ambivalence. In this case unfortunately, it is out of the scope of this approximation to unequivocally obtain the optical thickness of the clouds. However, we venture to give values to the LUT in the three matrices, T , FL and ERR mainly for three reasons:

- 1) the operation of the subsequent Retrieval Algorithm: for matrix $T_{i,j,k,l,m}$ to work in the acquisition of COD must be complete, so insert NaNs in $T_{i,j,k,l,m}$ is not an option.
- 2) The shape of the $\mathbf{R} = \mathbf{f}(\boldsymbol{\tau})$ functions: after considerable analysis and review of the diverse functions we observe that, for the wavelength considered (440 nm), there is a high incidence of graphs like the one in Figure 3.20, that is, Rad_{CS} located between Rad_{MAX} and $R = f(\tau = 10, 15)$. This process causes the COD retrieval error to be not extremely big in a significant number of $\{i,j,k,l,m\}$ cases.
- 3) The possibility of later finding a parameterization that corrects the errors committed by ambivalence, as far as possible: Entering a value even if it is wrong in the $T_{i,j,k,l,m}$ and marking it with its specific flag will help us later to identify the problem in the future and to try to find a way to approximate the value to the correct one.

With that, in the case of finding the situations illustrated in Figure 3.23 and Figure 3.24, the τ for the $T_{i,j,k,l,m}$ is obtained by means of a Cubic Hermite interpolation of $Rad(LUT)$ with the $\mathbf{R} = \mathbf{f}(\boldsymbol{\tau})$ function, but only with the right branch, that is, the part of the function from Rad_{MAX} to Rad_{MIN} , that decreases monotonically with the increasing COD. A certain arbitrariness results here, we could have chosen the left branch, or settle a fixed value as $\tau = 0$ or 5. The reason of choosing the right branch is the largest amount of information (or points) than in the left branch. In this way we will obtain a greater range of values to work with, compared to the left branch (with two or three points) or if we limited ourselves to insert an absolute value. According to this, we signal these cases with the corresponding flags, in order to later take in account that these results need further processing and are not as reliable as they should be.

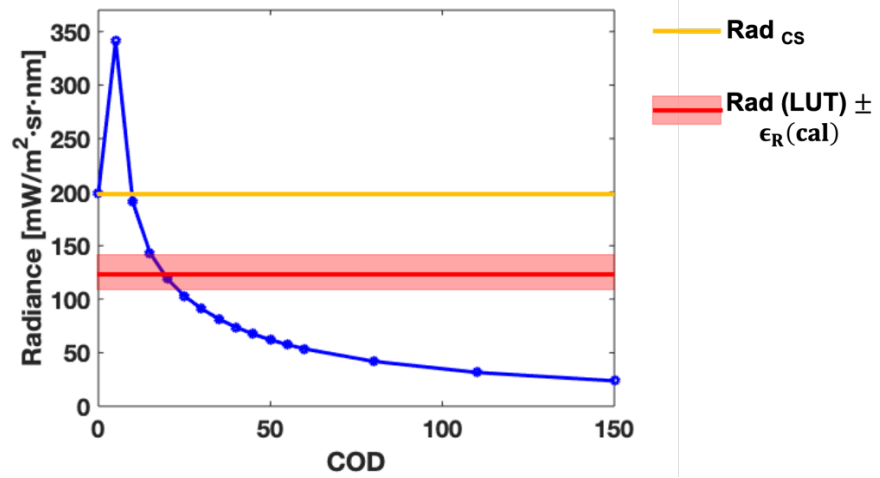


Figure 3.22 : WR, Neutral Case - $FL_{i,j,k,l,m} = 12$

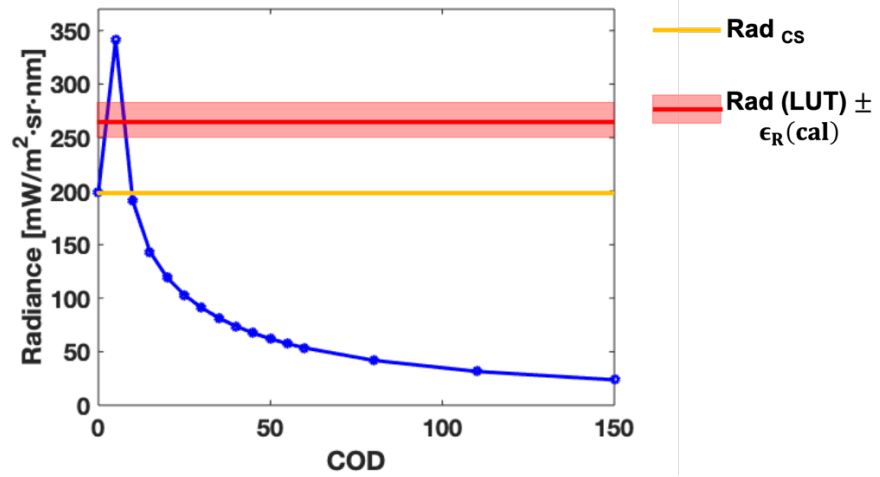


Figure 3.23 : WR, Ambivalence Case - $FL_{i,j,k,l,m} = 6$

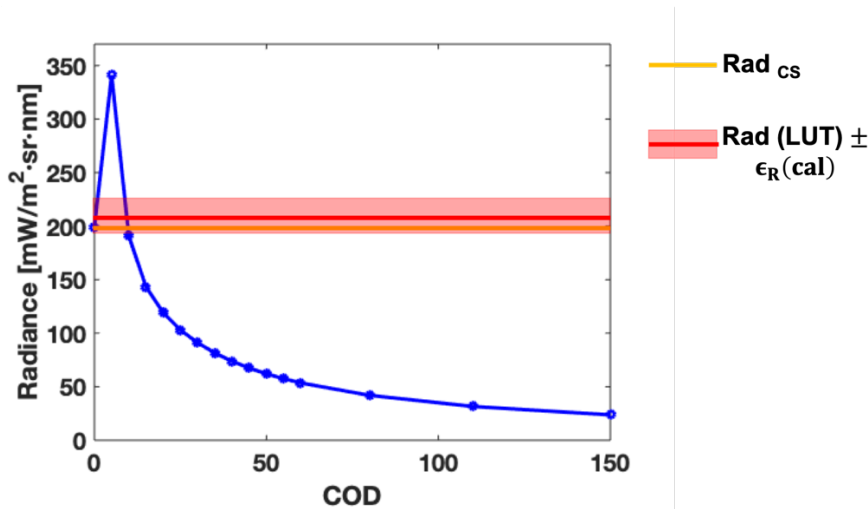


Figure 3.24 : WR, Ambivalence / Neutral Case - $FL_{i,j,k,l,m} = 9$

The assigned flag of Ambivalence cases (Figure 3.23 and Figure 3.24) depends on whether the relative difference between $Rad(LUT)$ and Rad_{CS} is contained within $\epsilon_R(cal)$. If it is not contained as in Figure 3.23, the flag inserted in $FL_{i,j,k,l,m}$ is 6. If, on the contrary, the situation on the Figure 3.24 occurs, then it could be that the calibration error tips the balance toward ambivalence case, rather than toward ‘Neutral’ case. Therefore, in situations like Figure 3.24, the flag assigned is 9, halfway between Ambivalence (flag=6) and Neutral case (flag=12).

On the other hand, the out of range cases (ORC) occur when the Radiance is too high for the given solar and view geometries, with regard to the 1D simulations. Therefore, in the 1D approach there is no COD value responsible for such out of range Radiance (e.g. Figure 3.25). In that case, depending on how much higher is the Radiance of the maximum value in the function (Rad_{MAX}), the methodology proceeds differently. The flags assigned to the $FL_{i,j,k,l,m}$ follow the principle of decreasing values as the case $\{i,j,k,l,m\}$ is further from the ideal.

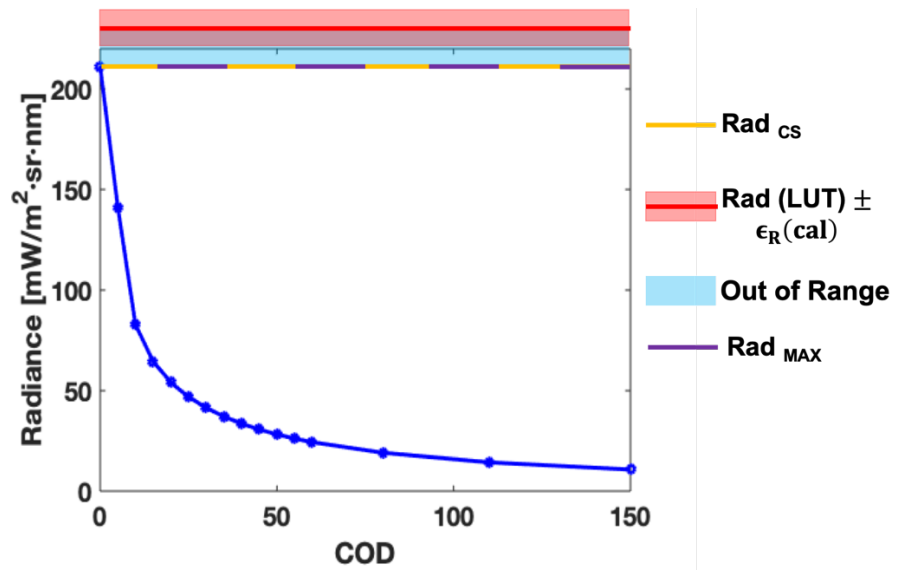


Figure 3.25 : Out of Range Case without Ambivalence - $FL_{i,j,k,l,m} = -5$

Also, the out of range cases can occur with or without ambivalence (Figure 3.25 and Figure 3.28, respectively). In the event that the LUT Radiance (from x_s) and Rad_{MAX} present a relative difference smaller than $\epsilon_R(cal)$ (Figure 3.26), then the interpolation is done with the left branch of the function (lower values of τ). This is done because the aforementioned quality of thin clouds, to cause the brightest sky due to their strong forward scattering. An Out of Range Radiance can be produced by either the thinnest clouds, or by non-considered 3D effects. In cases such Figure 3.26 the assigned flag is 1 ($FL_{i,j,k,l,m} = 1$), halfway between Ambivalence (flag=6) and pure Out of Range (flag=-5).

We can also have events like in Figure 3.27, in which there is no ambivalence and the relative difference between the ORC Radiance and the Rad_{MAX} is less than the calibration error. If this event is given, the τ value assigned to the $T_{i,j,k,l,m}$ is 0. We do that because without ambivalence a Radiance higher than Rad_{CS} can only be due to a COD = 0, or non-considered 3D effects. Therefore, we set the $T_{i,j,k,l,m}$ to 0 and signal it with one of the lowest flags, $FL_{i,j,k,l,m} = -3$.

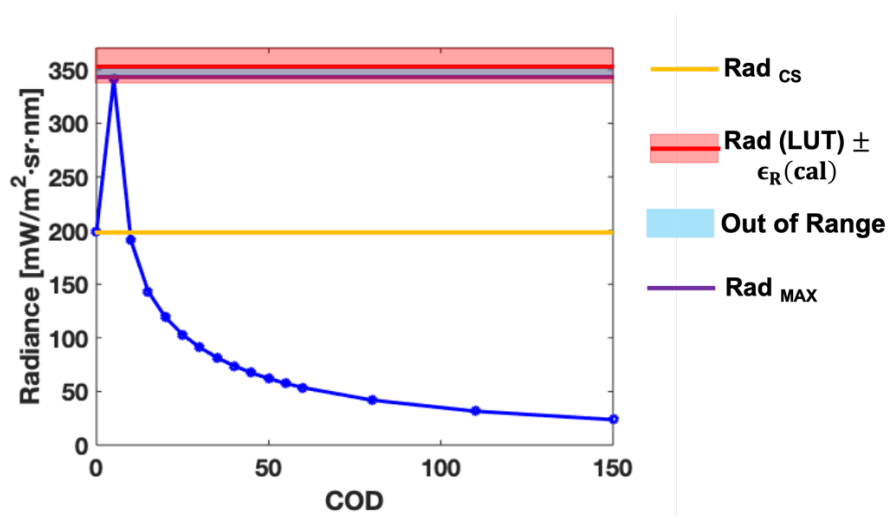


Figure 3.26 : Radiance's ORC less than calibration error and Ambivalence,
 $FL_{i,j,k,l,m} = 1$

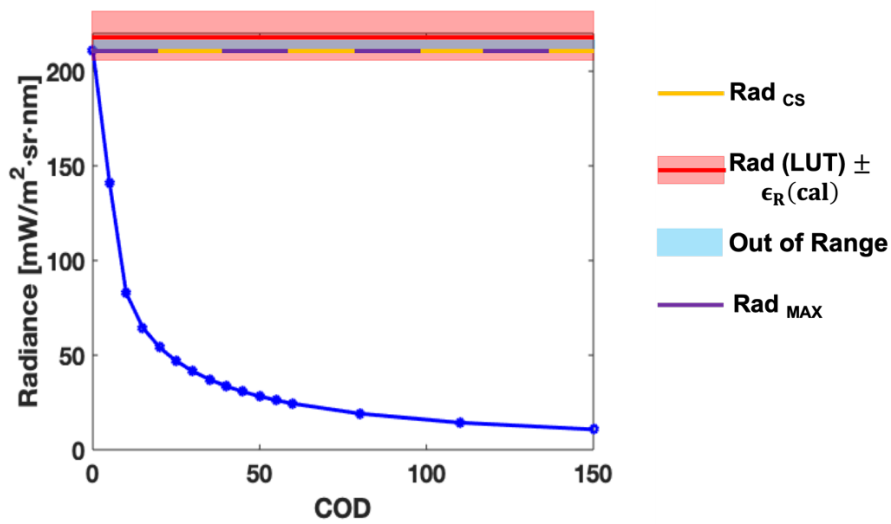


Figure 3.27 : Radiance's ORC less than calibration error without ambivalence.
 $FL_{i,j,k,l,m} = -3$

The lower flag, $FL_{i,j,k,l,m} = -5$ corresponds to the last possible case in which the difference between the Rad (LUT) and Rad_{MAX} is greater than the calibration error, with or without ambivalence. Here the τ value assigned to the LUT is also 0, as in Figure 3.25 and Figure 3.28. In all out of range cases, the calibration error is assigned to the $ERR_{i,j,k,l,m}$, except in the cases with $FL_{i,j,k,l,m} = -5$, whose error is the relative difference between the Radiance LUT and the Rad_{max} .

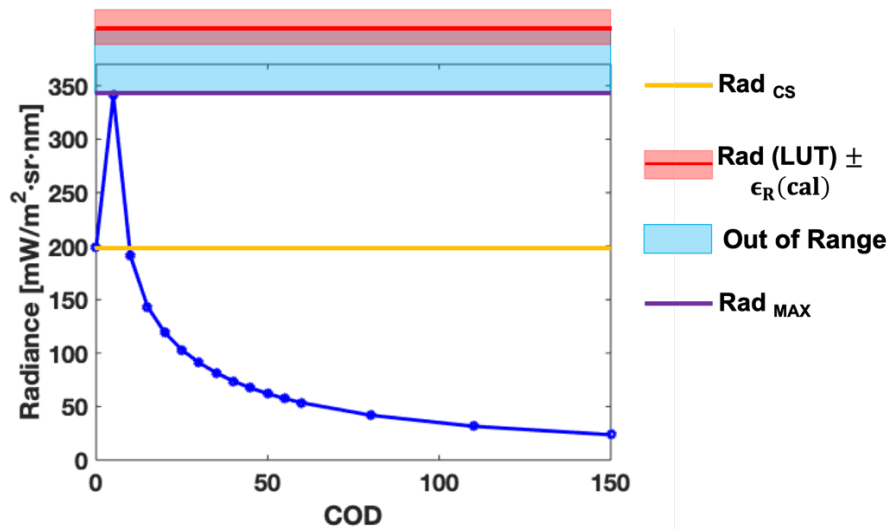


Figure 3.28 : Out of Range Case with Ambivalence - $FL_{i,j,k,l,m} = -5$

To end, it must be pointed out that another type of out of range radiance values can be found, when the radiance is lower than the simulated radiances for the given variables. Nevertheless, that is something that could be fixed with a higher COD than the range considered for the LUT. Therefore, we do not treat it the same way as the Out of Range by excessive radiance (ORC) and label this case, ORCI, as ordinary, with flag=16. However, the assigned uncertainty to the $ERR_{i,j,k,l,m}$ matrix is the difference between the lowest radiance possible, Rad_{min} , and the Radiance LUT.

To sum up, we summarize in Table 3.13 all the cases considered and the flags assigned, within range (WR) and out of range (ORC, ORCI) in descending value.

3. Methodology, Data and Analysis

Table 3.13: All the Cases found in the $T_{i,j,k,l,m}$ construction and flags assignment

Case	FLAG
Ordinary (WR,ORCI)	16
Neutral, WR	12
Ambivalence and Neutral, WR	9
Ambivalence, WR	6
ORC within the calibration error and ambivalence	1
ORC within the calibration error, no Ambivalence	-3
Pure ORC, with or without Ambivalence	-5

Retrieval Algorithm

The Retrieval Algorithm consists of a series of mathematical calculations to obtain the optical thickness of clouds from the blue channel from the Sky Camera images. The Retrieval has as a core the COD Lookup Table, and as inputs, the pre-processed and masked blue channel matrices. Another ancillary input file is a summary of the day, hour and minute of measurement, for each Sky Camera image. The Retrieval carries included a routine to obtain the sun position from the day and time data, as well as the latitude, longitude and altitude of the measurement site.

Next, for each image analyzed the Digital Counts are converted to Radiances employing (3.22). These Radiances are calculated at the effective wavelength of the camera for the blue channel, 472nm. Given that the LUT is calculated at 440nm we convert the Radiance matrices to 440nm by multiplying them by $\frac{1}{\Gamma_B}$, as it was previously stated in Section 3.1.1. With this step, the Radiance matrices are ready as input files for the Retrieval.

Therefore, the Retrieval obtains from each Sky Camera image a Cloud Optical Depth image ($COD_{i,j}$), a Data Quality image ($FLAG_{i,j}$) and Uncertainties image for Radiance ($E_{i,j}$) in the Sky Camera resolution of 966x966 pixels, by means of $T_{i,j,k,l,m}$, $FL_{i,j,k,l,m}$ and the $ERR_{i,j,k,l,m}$ respectively, and the $\Theta_{i,j}$ and $\Phi_{i,j}$ matrices.

On the other hand, the Uncertainties for the COD matrices are also obtained. To do so, we observe the dependencies in (3.26). First of all, we evaluate the dependencies of the Radiance calculations and simulations, as well as the uncertainties associated with such dependencies.

$$Radiance = f(VZA, SZA, SAA, VAA, COD, calibration) \quad (3.27)$$

As (3.27) shows, the Radiance as it is considered in this work depends on the geometry and solar angles, as well as the Cloud Optical Depth. This makes that the simulated Radiance is dependent on the sensitivity of the model to the variables and also to the sun position calculations. Nevertheless, the errors induced by both the sensitivity and the sun position calculations are much less than the uncertainties associated with the instrument characterization. As we discussed earlier in this chapter, the calibration consists of a geometric and a radiometric part. We observe, in the parameters obtained from fits in (3.5) and (3.6), that the geometric calibration error is composed mostly by the uncertainty associated to the slope in (3.5) and the vertical intercept in (3.6), consisting in 0.1% and 0.5%, respectively. A combined error derived from both is obtained by error propagation and results in 0.5%.

On the other hand, Radiance is obtained from the Digital counts in the blue channel by means of (3.16). We can see that the uncertainties associated to the fit parameters are much less than the radiometric calibration uncertainties (Table 3.5).

From all this we deduce that the greatest and most important uncertainty associated to the radiance calculation is given by the radiometric calibration, and the uncertainties range from 4% to 35%.

Regarding to the inversion for the calculation of the Cloud Optical Depth, the dependencies with the geometric and solar angles are the same as for Radiance, negligible in comparison with the uncertainties associated to the Radiance itself. Therefore, we deduce that the error of COD ($\epsilon(COD)$) must be proportional to the Radiance errors (ϵ_R), as expresses (3.28).

$$\epsilon^2(COD) \propto \epsilon_R^2(cal, flags) \quad (3.28)$$

Besides, given that the calibration errors obtained from the fit residuals are the most significative ones, the COD error is therefore dependent of them. With it, the equation for COD error is transformed from (3.28) to (3.29).

Nevertheless, we know that the uncertainties of Radiance are not always the calibration one, due to the incidences of out-of-range values (see Figure 3.28). The Lookup Table section explains that the $ERR_{i,j,k,l,m}$ includes the calibration errors in the Within Range cases, but for the Out of Range cases the value is the relative distance in percentage between the out-of-range radiance and the Rad_{MAX} in the

$\mathbf{R} = \mathbf{f}(\boldsymbol{\tau})$ function (light blue area in Figure 3.28). So, the uncertainty of each element $COD_{i,j}$, known as $ECOD_{i,j}$, is calculated as the product of the COD value and the error in percentage of the radiance matrix, $E_{i,j}$, as expressed in (3.30).

$$\epsilon(COD) = \tau \cdot \epsilon_R(cal, flags) \quad (3.29)$$

$$ECOD_{i,j} = COD_{i,j} * E_{i,j} \quad (3.30)$$

On the other hand, it must be mentioned that the $FL_{i,j,k,l,m}$ for the retrieval has absolute values according to the previous explanations, that is, $FL_{i,j,k,l,m} = \{-5, -3, 1, 6, 9, 12, 16\}$. However, the retrieval algorithm involves also interpolation for all given values in the Radiance matrices and to their corresponding geometric locations (Viewing Zenith, Θ and Azimuth, Φ , Matrices, Figure 3.7 and Figure 3.9).

This results in intermediate values in the $FLAG_{i,j}$ products between the absolute ones given in the LUT grid ($L_{i,j,k,l,m} = \{-5, -3, 1, 6, 9, 12, 16\}$). These intermediate values also give information about the circumstances surrounding each τ calculation. Nevertheless, to make the foregoing analysis more understandable we define 4 categories of resulting Flags, flag1 to flag4, according ranges of values, which are:

- FLAG1: Ranges from $FLAG_{i,j} = -5$ to $FLAG_{i,j} = 0$. Includes the pure Out of Range cases ($FL_{i,j,k,l,m} = -5$, Figure 3.28 and $FL_{i,j,k,l,m} = -3$, Figure 3.27) with $T_{i,j,k,l,m} = 0$, and the following negative flags. This includes interpolating cases of ORC and Ambivalence ($FL_{i,j,k,l,m} = -5, -3$ and $FL_{i,j,k,l,m} = 6$, Figure 3.23). The resulting interpolated flag value in $FLAG_{i,j}$ has predominant influence of the ORC until values of around -2, and with more balance weight as $FLAG_{i,j}$ approaches to 0.
- FLAG2: Ranges from 0 to 6. Includes positive resulting flags until pure ambivalence cases ($FL_{i,j,k,l,m} = 6$). This involve interpolating events of mixed cases and ambivalence cases, that is, $FL_{i,j,k,l,m} = 1$ (Figure 3.26), balanced with ORC until resulting flags values of 3. $FL_{i,j,k,l,m} = 12$ (Figure 3.22) cases are also involved with a minor occurrence.
- FLAG3: Ranges from 6 to 10. Includes only ambivalence cases, close to the Rad_{MAX} ($FL_{i,j,k,l,m} = 6$) and away from it, that is, $FL_{i,j,k,l,m} = 9$ (Figure 3.24) and $FL_{i,j,k,l,m} = 12$. At $FLAG_{i,j} \sim 10$, Ambivalence, Neutral and mixed ($FL_{i,j,k,l,m} = 9$) have similar weight.

- FLAG4: Ranges from $FLAG_{i,j}=10$ to $FLAG_{i,j}=16$. Includes cases with Ambivalence and ideal cases ($FL_{i,j,k,l,m} = 16$). At $FLAG_{i,j} \geq 10$, there is predominance of the $FL_{i,j,k,l,m} = 12$ events as well as some isolated $FL_{i,j,k,l,m} = 6$ events.

Validation of COD calculations

For a validation of the COD acquisition we employ images from the Sky Camera taken simultaneously to the AERONET Cloud Mode measurements. The validation is done for Sky Camera observations in zenithal direction. To do so, the central part of the image is used. The value of COD is averaged within the FOV of the Cimel CE-318 (1.2°) and compared with the COD provided by AERONET Network in Cloud Mode (zenith) measurements. The validation is conducted in Figure 3.29 and the fit line is expressed in (3.31), as well as the r^2 factor.

$$COD_{AER} = 0.996(\pm 0.045) \cdot COD_{SKYCAM} + 1.3(\pm 1.5) \quad (3.31)$$

$$r^2 = 0.9226$$

(3.31) shows a little overestimation of the COD with respect to AERONET values, and some spread in the scatter points which generally fit the line. An RMSE between the two data sets of 5.1 (COD units) has been found.

To end the calculations of this Section, we perform a statistical analysis using the results obtained from all the considered Sky Camera images, that is, over the COD_sX and F_sX matrices (see Annex to the Results chapter). We obtain the frequency of each interval of Flags occurrence (flag1, flag2, flag3 and flag4), and the corresponding conditions of cloudiness and solar geometry. With this, we intend to identify the conditions that must be studied under the perspective of 3D Radiative Transfer, since the out of range cases cannot get satisfactory values of COD in the 1D Approximation.

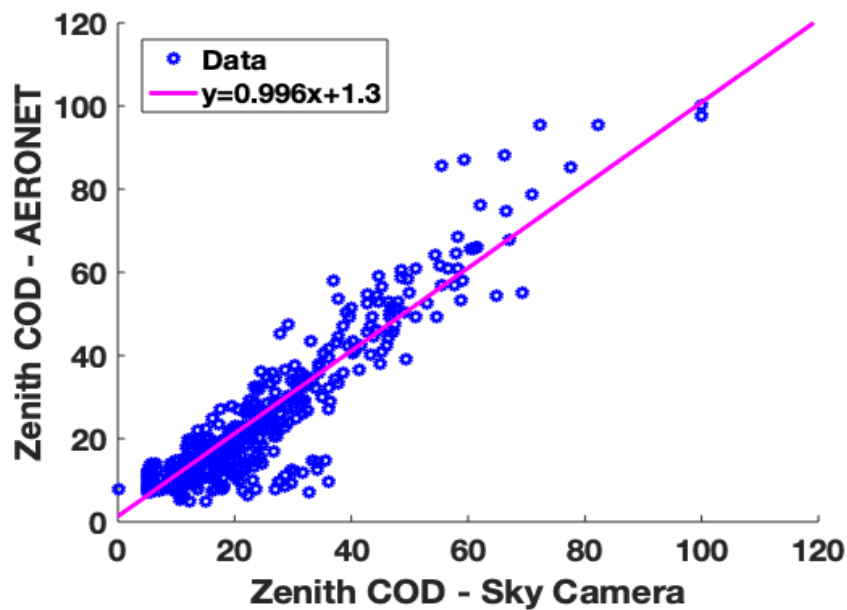


Figure 3.29 : Sky Camera COD validation through AERONET data; $r^2 = 0.9226$

3.2.Synthetic Study with 3D Monte Carlo

In the last part of this work we perform a synthetic study to test the previous 1D methodology for COD retrieval, and to identify and parameterize the possible 3D effects in the scenes. Such effects, which make the traditional plane-parallel scheme incomplete or inappropriate in certain situations, are due to the vertical and horizontal inhomogeneities in the atmosphere, the cloud field resolution, the cloud cover and the cloud structure itself, as well as the sun position among other causes.

The 1D-approach, partially addresses the heterogeneity of clouds employing the Independent Pixel Approximation (IPA, Cahalan et al., 1994). Each pixel is considered horizontally infinite and radiatively independent of the others. Nevertheless, this approach completely neglects the horizontal transport (radiative transfer among pixels), which induces systematic errors in the inversion procedure, such as out of range cases that cannot be properly solved in this atmospheric scheme.

The 3D phenomena are fully considered in 3D Monte Carlo (MC) simulations. Nevertheless, MC is computationally too expensive for many applications. Thus, in

the present work we use the strengths of the 3D Radiative Transfer model MYSTIC, which is part of the libRadtran software package (www.libradtran.org ; Mayer and Kylling, 2005; Emde et al., 2016) to address the 3D cloud effects.

MYSTIC provides radiation products (radiance, irradiance and actinic flux) and can be employed for remote sensing and climate applications. MYSTIC allows the definition of complex 3D cloud scenes, inhomogeneous surface albedo as well as topography. The MYSTIC outputs include the *stdout* (the standard output of *ivspec* in libRadtran) with the horizontally averaged irradiance and actinic flux, and several additional output files. In these files two types of results are distinguished, monochromatic and spectral. The monochromatic ones do not consider the extraterrestrial irradiance in the calculations, neither the distance Sun-Earth correction, making the spectral ones the most suitable for real-world applications. These outputs files include spectral radiance, spectral actinic flux and irradiance at different atmospheric levels.

3.2.1. 3D Cloud Fields

The microphysical properties of the cloud fields used as input are converted to optical properties by means of pre-calculated Mie tables, interpolated to the desired wavelength.

The input microphysical properties belong to a set of shallow cumulus clouds evolving in time from one scene to another. The cloud fields are courteously released by the research group of Remote Sensing and Radiative Transfer from the Ludwig-Maximilians Universität in Munich and appear in recent works such as Crnivec and Mayer (2019).

The cloud fields were simulated with the University of California, Los Angeles Large Eddy Simulation model (UCLA-LES), regarding to the Rain in Cumulus over the Ocean (RICO; Rauber et al., 2007) experiment. Therefore, they are Highly Resolved Large Eddy Simulations (LES) cloud fields, with a horizontal domain size of 6.4x6.4 km², a vertical extent of 4km with a 25m resolution in the three (*x, y, z*) directions. From the UCLA-LES simulations the 3D distribution of LWC is obtained, and the corresponding effective radius is assigned to each LWC value following the parameterization in (3.32) by Bugliaro et al., (2011).

3. Methodology, Data and Analysis

$$r_{eff} = \left(0.75 \left(\frac{LWC}{\pi \cdot k \cdot N \cdot \rho} \right) \right)^{\frac{1}{3}} \times 10^{-6} \quad (3.32)$$

Where N is the water droplet density $N= 150.0 \text{ e}^6 \text{ 1/m}^3$, and k describes the ratio between the volumetric radius of droplets, i.e the mean volume radius, r_v and the effective radius (r_{eff}), which are expressed in (3.33) and (3.34).

$$k = \frac{r_v^3}{r_{eff}^3} \quad (3.33)$$

$$r_v = \left(\frac{\int n(r) r^3 dr}{\int n(r) dr} \right)^{\frac{1}{3}} = \left(\frac{\int n(r) r^3 dr}{N} \right)^{\frac{1}{3}} \quad (3.34)$$

Figure 3.30 to Figure 3.33 show the 3D cloud fields (CFN, $N=\{7,8,9,10\}$) used in this work. They are part of a larger set among which the total cloud cover and the vertically integrated optical thickness increase. This particular subset that we employ consists in two examples of broken cumulus (CF7 and CF8) and two examples of more uniform stratocumulus clouds (CF9 and CF10). We chose them because they have enough amount of cloudiness to test our retrieval, which in turn is applied in overcast conditions in most cases, but also in broken clouds conditions.

These cloud scenes have highly variable optical thickness, with maximum COD of $\sim 109, 115, 171, \text{ and } 230$. Both LWC and R_{eff} profiles grow with height as is the typical trend in cumulus clouds (e.g. Brenguier et al., 2000). Table 3.14 summarizes the characteristics of cloud cover, base height, top height and average COD in each of the domains with its standard deviation in parenthesis.

Table 3.14 : 3D Cloud Fields characteristics

Cloud Field	Cloud types	Cloud Cover	Base Height	Top Height	$\bar{\tau}$ (σ)
CF7	Shcu.	69.5%	1.1 – 1.5km	1.75km	16 (17)
CF8	Shcu.	82.4%	1.2 – 1.6km	1.9km	16 (18)
CF9	Sc.	90.6%	1.2 – 1.7km	2.1km	24 (26)
CF10	Sc.	99%	>1.4 – 2.2km	2.8km	42 (33)

CF7 and CF8 (Figure 3.30 and Figure 3.31) consist in a cluster of shallow cumulus clouds (Shcu.) that evolves from CF7 to CF8 growing thicker and higher. They both have an important clear sky gap in the central area of the domain. The average cloud-base height in CF7 and CF8 scenes are 1.56 km and 1.69km, respectively.

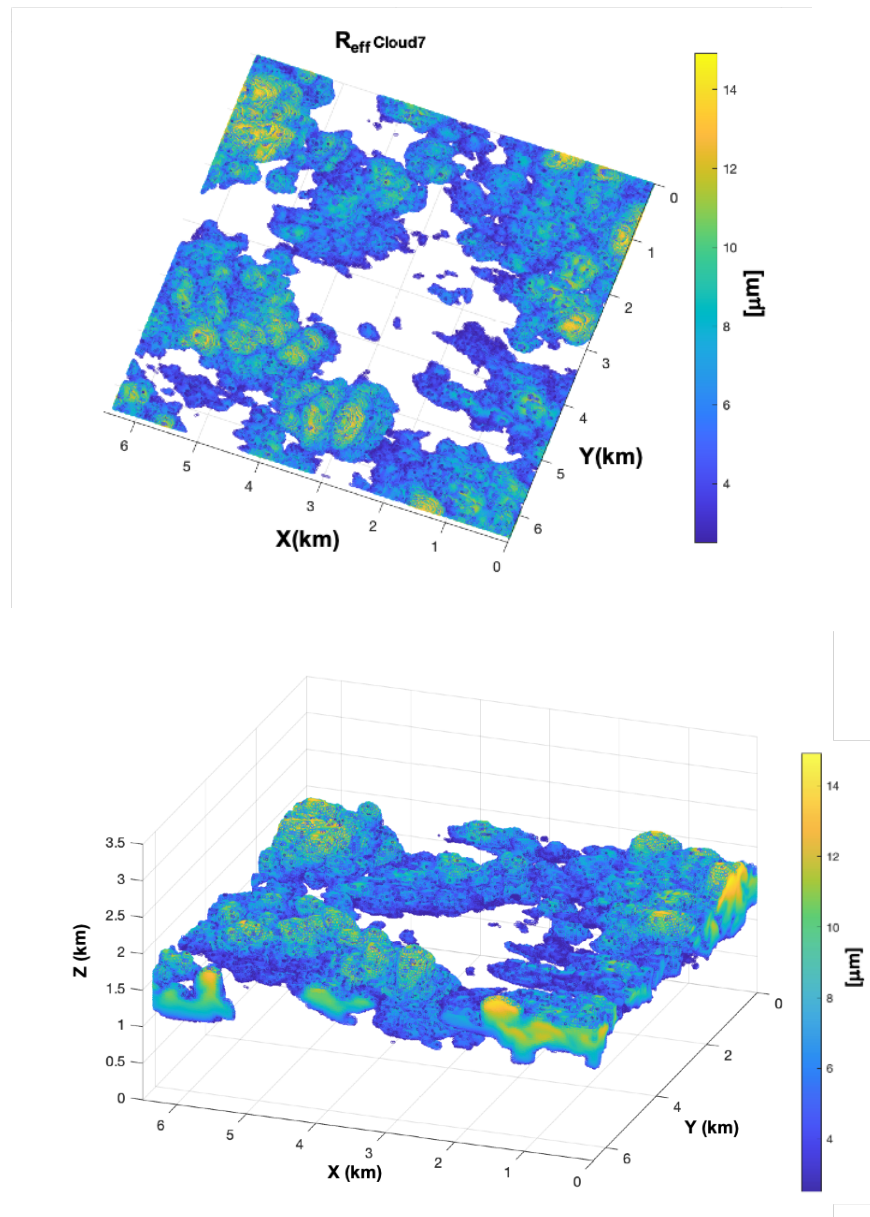


Figure 3.30 : R_{EFF} (μm) of the CF7, nadir view (top) and lateral view (bottom)

3. Methodology, Data and Analysis

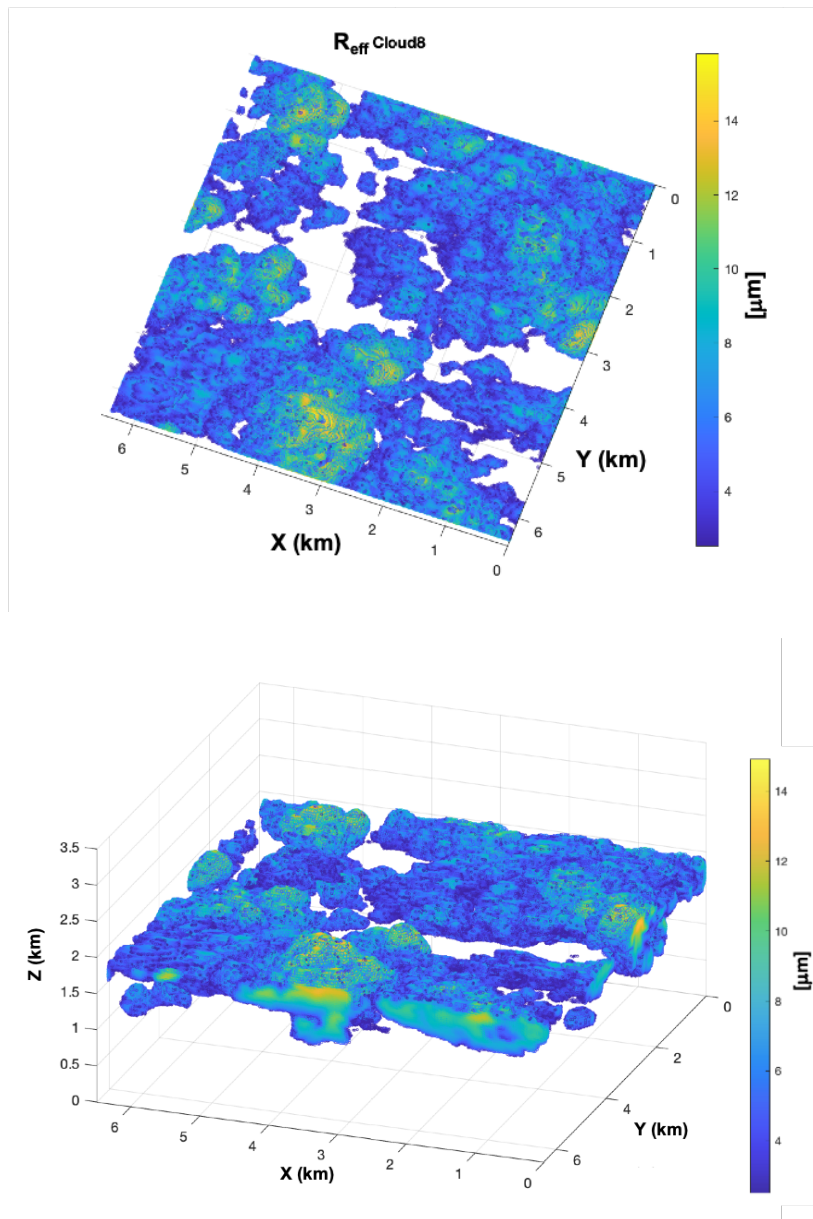


Figure 3.31 : R_{EFF} (μm) of the CF8, nadir view (top) and lateral view (bottom)

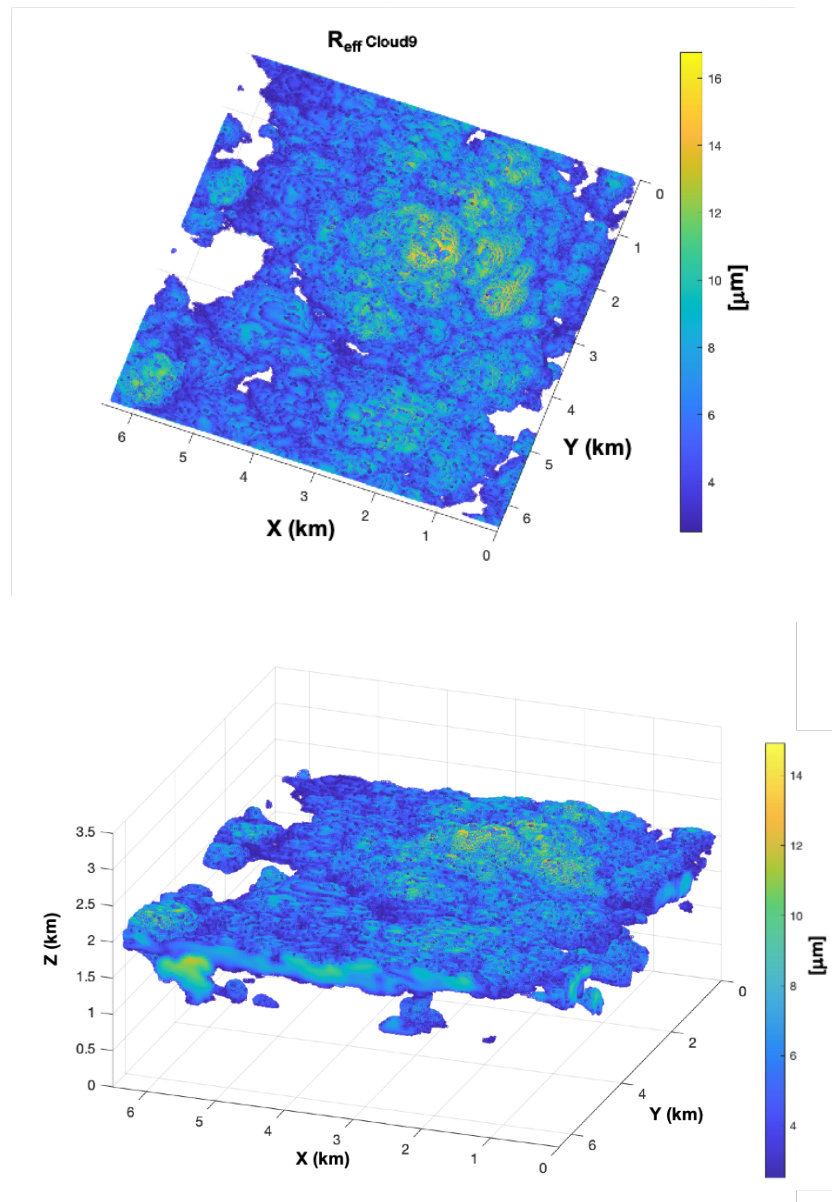


Figure 3.32 : R_{EFF} (μm) of the CF9, nadir view (top) and lateral view (bottom)

3. Methodology, Data and Analysis

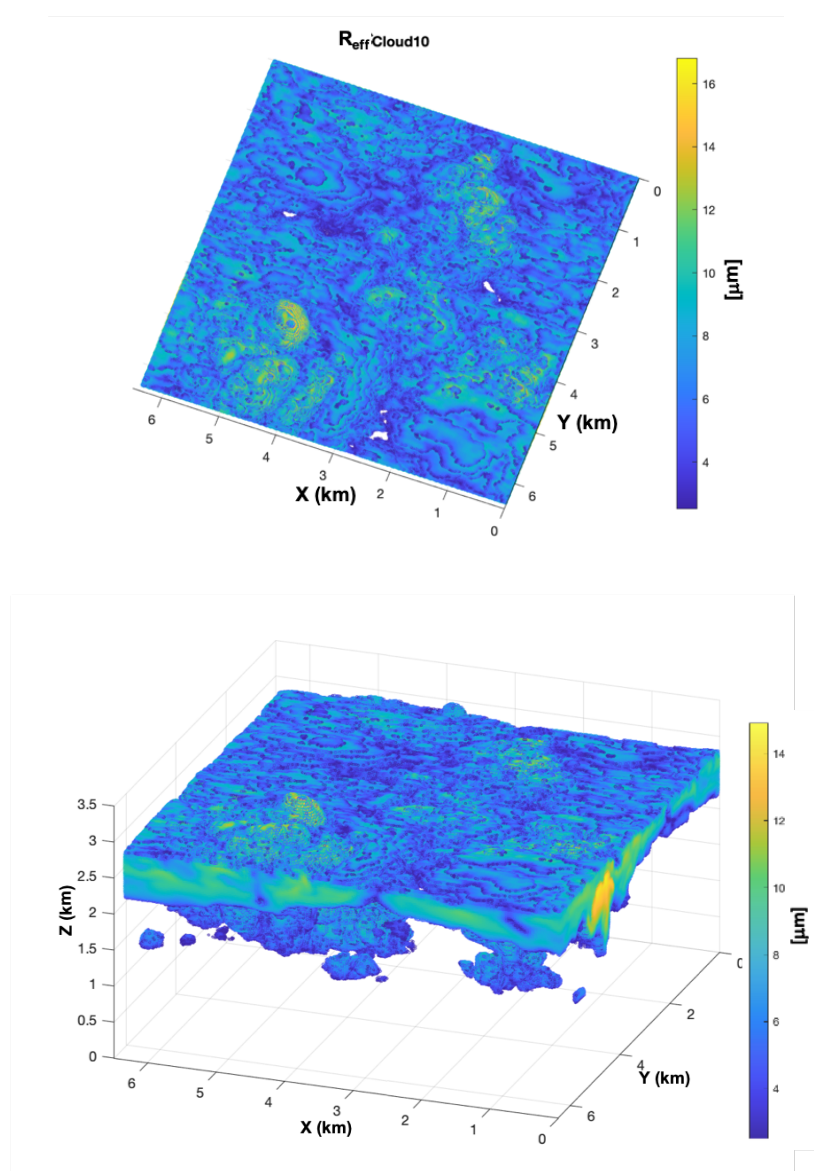


Figure 3.33 : R_{EFF} (μm) of the CF10, nadir view (top) and lateral view (bottom)

On the other hand, CF9 and CF10 are overcast stratocumulus clouds (Sc. Figure 3.32 and Figure 3.33). The central gap of the previous cloud fields has disappeared, with some clear spaces in the CF9 right edge. They show the final evolution of the CF7, CF8 cumulus clouds, in a more uniform, thicker cloud form. The average height also increases from 1.9 km for CF9 to 2.43 km for the CF10.

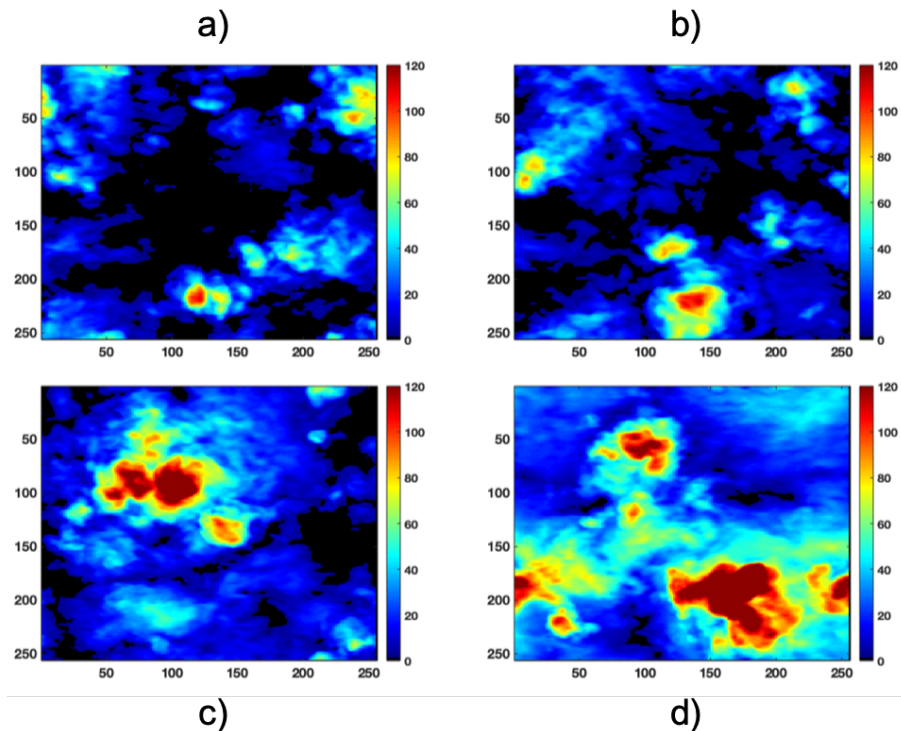


Figure 3.34 : COD from LES fields CF7 (a), CF8 (b), CF9 (c) and CF10 (d)

We calculate the Cloud Optical Depth of each LES field by means of column integration for each $[x,y]$ position. These COD matrices, depicted in Figure 3.34 are considered the ‘truth’ to which compare the retrieved COD_sX matrices. We can see that as the Cloud Cover and Cloud Thickness shown in Figure 3.30 to Figure 3.33 and Table 3.14, the τ values in COD matrices increase from CF7 to CF10, as well as the average COD ($\bar{\tau}$). In general, the pixels with higher τ values (COD \sim 109, 115, 171, and 230, Figure 3.34) are associated with a greater cloud geometrical thickness.

3.2.2. 3D Monte Carlo Simulations

We perform full 3D RT simulations over several Highly Resolved Large Eddy Simulations (LES) cloud scenes under diverse illumination conditions. In that way we can study the influence of the sun position as well the cloud structures and properties in the retrieval.

The output radiance of the simulations is then treated with the inversion procedure described in Section 3.1., to obtain the Cloud Optical Depth in the 1D approach. The differences between the retrieved COD field for the diverse illumination conditions, and the ‘truth’ COD (provided by column integration of the LES fields), altogether with the Data quality Flags product (described in Section 3.1.2) are employed to parameterize the deviations due to the neglect of horizontal photon transport and geometry issues in 1D approaches. We also use them to determine and quantify additional errors inherent to monochromatic radiance inversion procedures, that must be solved with a refinement of the algorithm in the critical situations.

As we indicate and explain in detail in Section 1.3.3 from Chapter 1, MYSTIC possesses several simulation modes, each of them suitable for different purposes and applications. Specifically, and since one of the objectives of this section is to test the retrieval with the sky camera, we perform the simulations at 440nm in the ‘panorama view’ mode. It works only with backward Monte-Carlo and with a defined sensor position, which we settle at the center of the domain. The panorama view, as the name suggests, simulates a panorama, and therefore it is the way to simulate what a camera pointing to the sky sees. The area covered by the sensor is also indicated in the command lines, which in our case range from 0° to 90° in zenith and from 0° to 360° in azimuth. Other specified commands needed for this application are the sample grid and the area of it to be calculated, which for this work is the whole domain. The latter is settled inside the specific commands of the Monte-Carlo backward. The input conditions are summarized in the Table 3.15.

Table 3.15 : Input commands for the 3D Radiative Transfer simulations

libRadtran commands	characteristics
Monte Carlo Mode	Backward
Projection	Panorama View
Wavelength	440 nm
Background Atmosphere	Midlatitude Summer
Aerosol Properties	Default
Water Cloud Properties	Mie interpolated
libRadtran Solver	mystic
Number of photons	10000 (per pixel)
Variance Reduction Method	Activated
Sensor Position	Center of the domain
Simulation area	Azimuth: 0° - 360° / Zenith: 0° - 90°

On the other hand, Monte Carlo is a method where a number of photons is randomly traced through the atmosphere. Therefore, the result is inherently noisy. The calculation of any radiation quantity can be seen as a sequence of yes/no experiments regarding to whether the photon makes it into the result with a probability ‘p’, or not with a probability (1-p). This results in a binomial distribution with the average calculated as $\mu = N \cdot p$ and the standard deviation as $\sigma = \sqrt{p \cdot N \cdot (1 - p)}$, where N is the number of tries. Taking the approximation of the number of photons sampled into the result is $N_s \approx p \cdot N$, and substituting the unknown probability ‘p’ = $\frac{N_s}{N}$, we obtain the ratio σ/μ expressed as in (3.35).

$$\frac{\sigma}{\mu} \approx \sqrt{\frac{N - N_s}{N N_s}} \quad (3.35)$$

The approximation in (3.35) is better as higher is N. Otherwise if $p \ll 1$, (3.35) turns into the Poisson distribution, as shows (3.36).

$$\frac{\sigma}{\mu} \approx \frac{1}{\sqrt{N_s}} \quad \text{if } N_s \ll N \quad (3.36)$$

3. Methodology, Data and Analysis

Therefore with (3.36) it is possible to calculate the required number of photons for a desired accuracy. Equation (3.36) also shows that the noise of the model decreases with the number of photons.

Apart from that, in Monte Carlo simulations the computational cost must be taken in account. For applications in which calculations are done in multiple directions a compromise between accuracy and computational cost must be reached. In clouds studies the computational cost for a single direction is much higher, as well as when horizontal distributions are calculated. That is because in cloud studies the number of cells in the domain in which the photons interact is much higher than in clear skies domains. In our simulations of cloudy domains, we choose to track 10000 photons per pixel. This number of photons keeps the noise of the model at 1%, according to equation (3.36). With it, a simulation with a cloud cover of 82% with the dispositive employed (a PC with a 1,8 GHz Intel Core i5 dual core), takes around 32 h, tracing 1398 photons per second. The computational time increases with the cloud cover and with the solar height.

Also, the variance reduction method is also applied (VROOM, Buras and Mayer, 2011; see Section 1.3 of Chapter 1) because of the strong forward peak in the clouds phase function. The application of this technique does not affect the result but the noise is significantly reduced.

Additionally, the background atmosphere is also defined, specifically with the same Midlatitude Summer atmosphere from the AFGL (Air Force Geophysics Laboratory, 1986) that is also employed in Section 3.1, as well as the aerosols background. The total column content of atmospheric gases (H_2O , O_3) are also modified in the same way as in the Lookup Table calculations (see Section 3.1.2), with annual average values of 2018.

In order to test the COD retrieval and study the 3D effects we perform the simulations varying the solar zenith angle in the radiative transfer model, the LES cloud field and the previously defined atmosphere. In that way, we address the influence of the sun position on the COD retrieval, in different observation geometries.

On the other hand, it must be pointed out that MYSTIC and the Sky Camera have different coordinate systems, and that to perform the simulations first of all we must convert the system of MYSTIC to the one in the Sky Camera by rearranging the fields.

Therefore, we perform MYSTIC simulations keeping the SAA to values close to 180°, and varying the solar zenith angle. For the SZA, we use values of 17°, 30°, 42°, 53° and 57° (Table 3.16) which cover the minimum values obtained in Valencia at midday during the whole year. The SAA values in Table 3.16 are the corresponding values found in Valencia at noon along the year.

Table 3.16 : Solar geometry in the Radiance simulations

Solar Geometry	Rad_s17	Rad_s30	Rad_s42	Rad_s53	Rad_s57
Zenith Angle	17°	30°	42°	53°	57°
Azimuth Angle	182°	180°	187°	185°	185°

Henceforth we name Rad_sX to the model output Radiance matrices at each solar ‘s’ zenith angle X, as in Table 3.16.

After we pass the Rad_sX matrices to the retrieval algorithm explained in Section 3.1, and we obtain a series of results, analogously to the first part of the work (see Section 4.1). These results include the COD matrices and the FLAGS matrices, named COD_sX and F_sX, respectively. In the forecoming analysis we will be referring both to specific values of the COD_sX matrices, and to average values of the whole image.

On the other hand, in the analysis we convert the COD_sX matrices in spherical coordinates (ρ, θ, ϕ) to cartesian coordinates (x, y, z) , employing (3.37), (3.38) and (3.39).

$$x = \rho \cdot \sin(\theta) \cdot \cos(\phi) = \frac{CAH}{\cos(\theta)} \cdot \sin(\theta) \cdot \cos(\phi) \quad (3.37)$$

$$y = \rho \cdot \sin(\theta) \cdot \sin(\phi) = \frac{CAH}{\cos(\theta)} \cdot \sin(\theta) \cdot \sin(\phi) \quad (3.38)$$

$$z = \rho \cos \theta = CAH \quad (3.39)$$

Being CAH in (3.37), (3.38) and (3.39) the Cloud Average Height, and the z coordinate, that we extract from the LES fields. The value employed in these equations is obtained from the LES fields average height (the average between the base heights and the top heights in Table 3.14). It is needed to calculate the coordinate

3. Methodology, Data and Analysis

ρ , the radius from the center of the domain to the pixel in (θ, ϕ) , as (3.37), (3.38) and (3.39) show.

We do this conversion for the future comparison with the LES Cloud Fields, which is expressed in cartesian coordinates with a 25 m spatial resolution. A second reason is that MYSTIC replicates the cloud field in order to keep the same cloud properties in the whole domain. Therefore, the cloud fields fit in a smaller sector of the Viewing Zenith Angle matrix, given the cloud base height of the cloud fields (Figure 3.35, inside the red circle). The pixels from the field limits until the horizon, are affected by the same replicated cloud properties (Figure 3.35, outside the red circle).

Therefore, with the coordinates conversion, the Zenith Viewing Angle sector of 0° to 60° comprises practically in its entirety the equivalent to the LES field, and the coordinates conversion is useful to suppress the replicated part of the domain (see Figure 3.36).

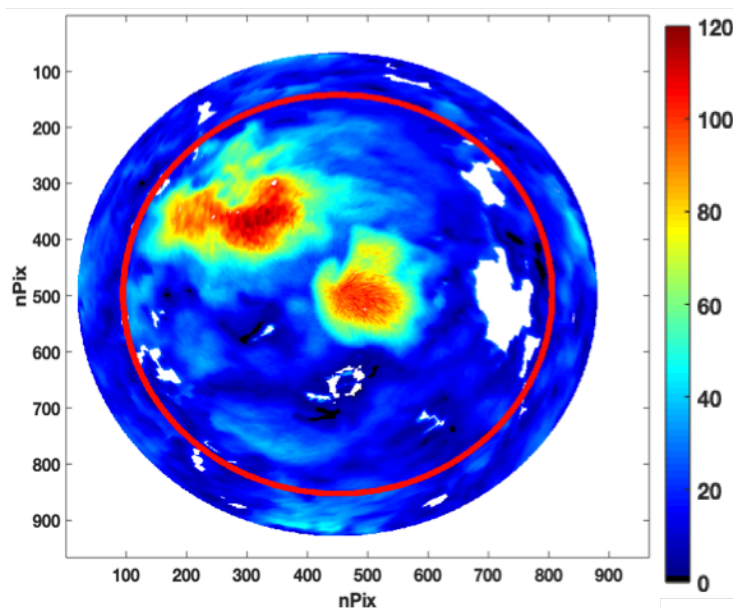


Figure 3.35 : Retrieved COD in polar coordinates. Replicated cloud field outside the red circle. CS mask in white.

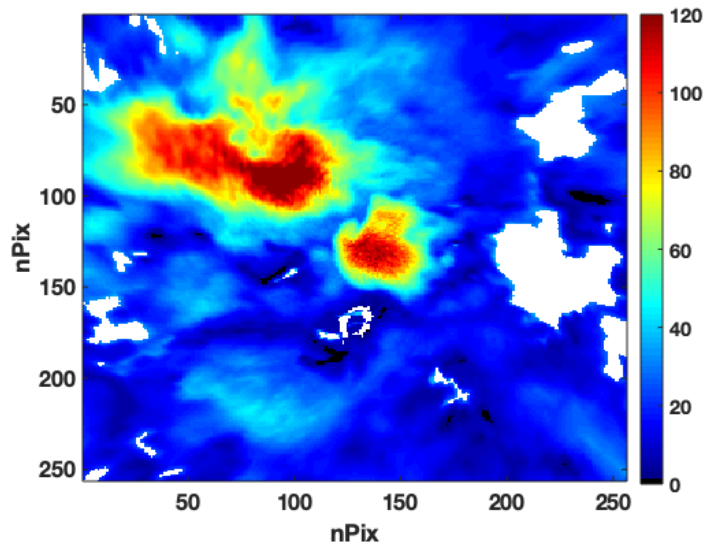


Figure 3.36 : Retrieved COD in cartesian coordinates. CS mask in white.

3.2.3. Analysis I: Comparison with LES fields

The objective of this Synthetic study is to validate the COD retrieval, employing the Radiance images and the inversion methodology defined for the 1D approach. To do this, the COD results of the retrieval are compared with the COD obtained by column integration from the original LES fields.

Ideally this comparison should be done via the scatter plot of the retrieval COD matrices (COD_sX) versus the LES COD matrices. However, we choose not to do it this way, due to the fact that the conversion of the COD_sX matrices from spherical to cartesian coordinates ((3.37), (3.38) and (3.39)) is not perfect and we have observed discrepancies in the cartesian position of the elements of the cloud fields.

Therefore, we rely on an ancillary parameter, the ‘distance to clear sky’ (DCS), or distance of each pixel to the edge of clouds. The DCS ($\Delta_{i,j}$) for each pixel (i, j) is the distance in km of that pixel to the nearest clear sky pixel in the matrix, a pixel from the clear-cloud boundaries ($P_{m,n}$). The DCS helps us to determine which pixels of the COD_sX image and the CFN image correspond to the same spatial position in the

3. Methodology, Data and Analysis

sky, even if they are in different positions of the image (given the deformation that occurs in the change of coordinates).

The cloud edges pixels ($P_{m,n}$) are defined as those pixels from the clear-sky mask in which any of the surrounding pixels ($P_{m-1,n}, P_{m+1,n}, P_{m,n-1}, P_{m,n+1}$) have a value other than zero optical thickness. As an example, in Figure 3.37 the clear-cloudy boundaries, $P_{m,n}$ for CF8 are depicted. In the case of CF10 the clear-sky mask does not exist and we replace it by a mask of pixels of $\tau \leq 2$. This is a value that falls between steps $\tau = 0$ and $\tau = 5$ of the LUT composition, close enough to $\tau = 0$ not to remove a significant number of pixels from the analysis, but also far enough from it so that the CF10 ‘clear sky’ mask has delimited zones, with defined boundaries. As an example, in Figure 3.37 the clear-cloudy boundaries, $P_{m,n}$ for CF8 and CF10 are depicted.

Next, we calculate the distance of each pixel in the COD_sX matrix, whose τ value is non-zero, to each of the edge pixels $P_{m,n}$ at positions m for rows and n for columns. We assign the minimum value of all the calculations as the distance to clear sky, as (3.40) shows. The distance in (3.40) is calculated in pixels units, and can be converted to km by multiplying by 0.025km, the resolution of the cloud fields in Cartesians.

$$\Delta_{i,j} = \min \left\{ \text{sqrt} \left(\left(i - \bigcup_{c=1}^N m \right)^2 + \left(j - \bigcup_{c=1}^N n \right)^2 \right) \right\} \quad (3.40)$$

Being N in (3.40) the total number of edge pixels at the matrix.

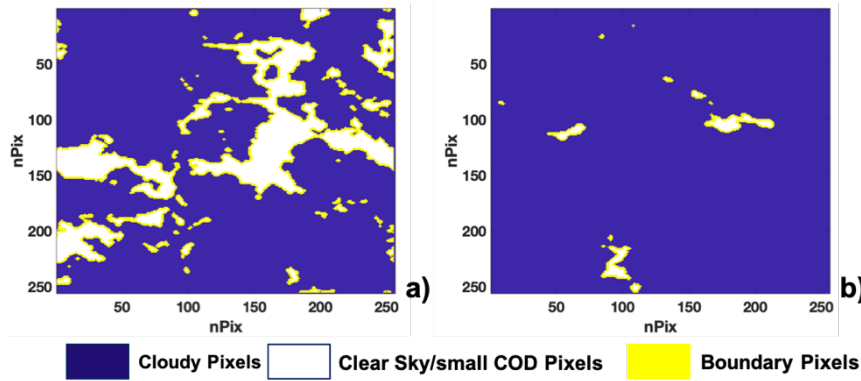


Figure 3.37 : Cloud field edges from CF8 (a) and from CF10 (b)

With this we configure the distance to clear sky (Δ) matrix, whose values range from 0 to 3.55 km in the case of the cloud field with the maximum cloud coverage, CF10. The Δ matrices for the CFN and for the COD_sX are depicted in Figure 3.38 and Figure 3.39, respectively. They are quite similar among them, but there are some differences in the maximum values of DCS derived from the clear sky mask determination, which are more important in the CF8 and CF9.

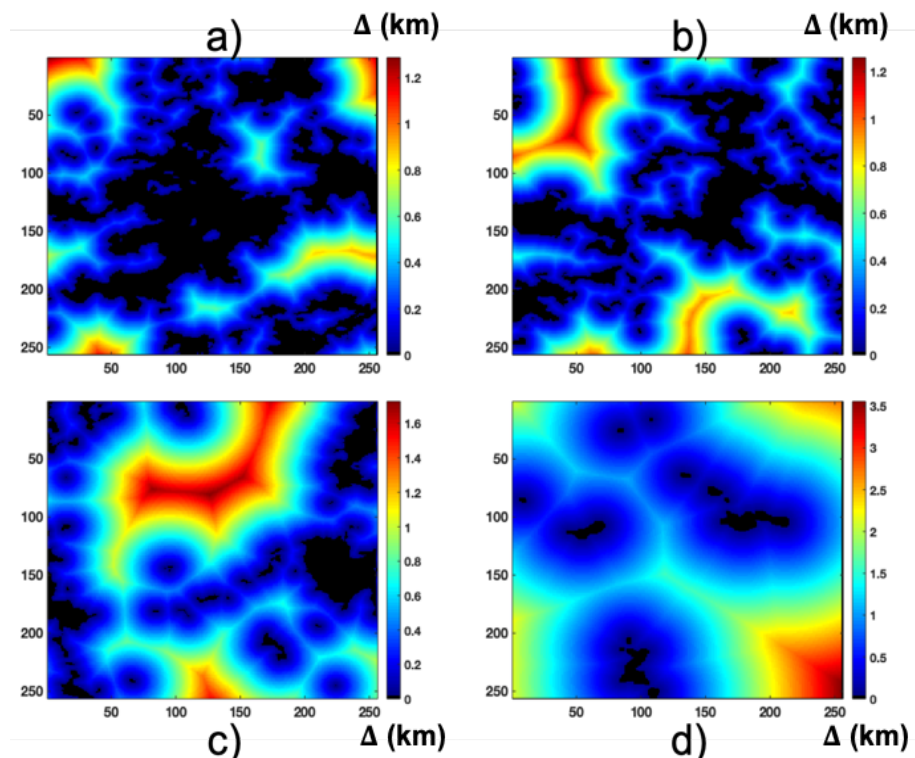


Figure 3.38 : DCS (km) in LES field CF7 (a), CF8 (b), CF9 (c) and CF10 (d)

Next, we define the DCS values in which to evaluate the COD_sX matrices and CFN matrices. The values range from 0 to the maximum possible at each case study, with an interval of one pixel. For each of these DCS values, we get all the pixels located at that distance, and calculate the mean and standard deviation, for both, the COD_sX and CFN fields. Figure 3.40 illustrates the pixels at distance 250m from the clear sky in the COD_s42 matrix derived from CF8.

3. Methodology, Data and Analysis

Then we can use scatterplots to compare the COD obtained from COD_sX and CFN images for a fixed distance. This comparison is conducted with representing the COD values of CFN versus our results (COD_sX). On the other hand, we represent on the same graph the COD values from all the COD_sX and CFN, against DCS. We do this to see the differences between the results from the retrieval, and the differences between each of COD_sX matrices and the CFN. We do these comparisons for all the case studies (CF7 to CF10) and all the analyzed solar zenith angles (17°,30°,42°,53°,57°).

The main objectives of the COD intercomparison is the evaluation of the COD retrieval procedure, and a parameterization of the differences between calculations and ‘the truth’. To obtain the fit line we establish the condition that the number of points evaluated at each distance must be similar between the results and the LES field, so we only employ coincidences of numbers of pixels higher than 70%.

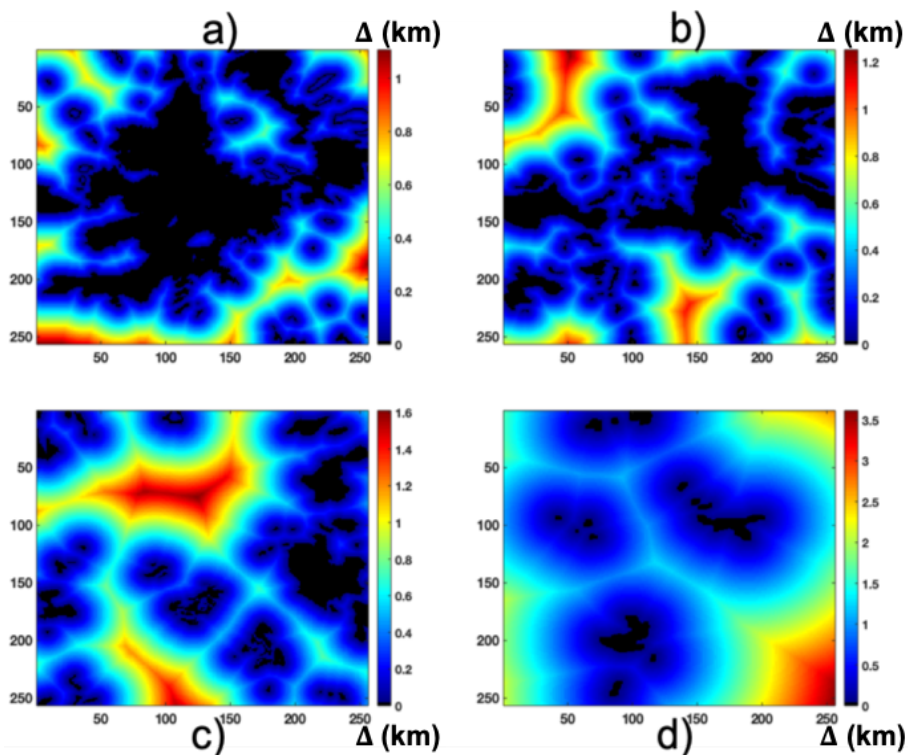


Figure 3.39 : DCS (km) in COD retrieval results derived from CF7 (a), CF8 (b), CF9 (c) and CF10 (d)

The fit functions are obtained through a weighted fit that gives less weight to outliers in the calculations. Likewise, we obtain the RMSE of the intercomparisons applying the formerly employed (3.19), (3.20) and (3.21) (see Section 3.1), as well as the average, minimum and maximum deviation of each case study results from the equivalents in the LES fields.

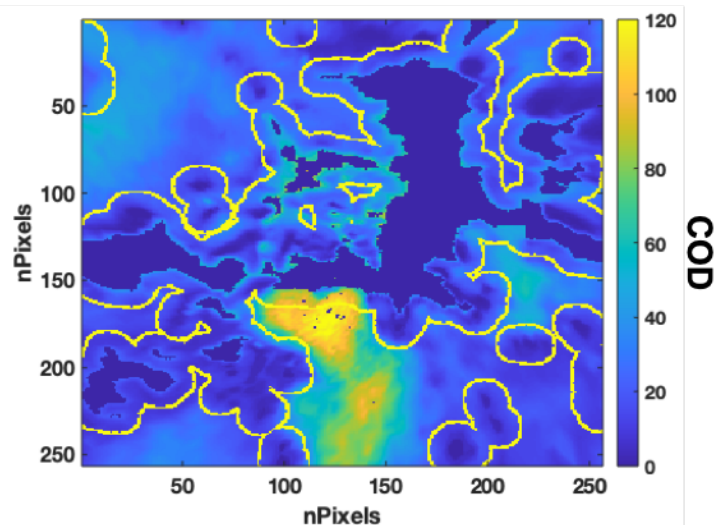


Figure 3.40 : COD_s42 obtained from CF8. Pixels at a distance to clear sky of 250 m in yellow

3.2.4. Analysis II: Results intercomparison

For the last part of the analysis we perform an intercomparison between the COD_sX matrices for a fixed CFN. Here we intend to look for the differences among the results obtained varying the solar zenith angle, and the influence of the flags associated to such differences.

Therefore, we define a methodology of intercomparison so, in combination with the results of Section 3.2.3 we can:

3. Methodology, Data and Analysis

- Quantify the uncertainty of measuring and working under certain solar position angles.
- Quantify the reliability of the COD products, for each range of τ values.
- Find the differences between the COD_sX matrices under the influence of the corresponding flags in the F_sX.
- Quantify and parameterize the effect of the flags associated with 3D effects or limitations of the followed 1D approach.

So, in order to settle which COD_sX is closest to the truth, and which overestimate or underestimate the mean COD, first of all we obtain the average COD and standard deviation of each COD_sX, as well as of the corresponding LES CF. These values have been obtained from the whole images. On the other hand, and since the accuracy of the results might be related to the flags influence, we obtain the percentages of flag1, flag2 and flag3 areas at each COD_sX. With it we determine the influence of each flag associated to the sun position. With the Flags percentages and the results obtained from Section 3.2.3, we settle which, among the COD_sX matrices, is the best to perform as a reference in comparison with the other resultant matrices.

In that way, we represent in scatter plots the COD_sX intercomparison, as well as the fit lines of the distribution. The fit lines parameters are obtained with their 95% confidence bounds from the degrees of freedom for error and from the root mean squared error. From the confidence bounds we obtain the confidence interval for the slope and the vertical intercept of each fit line. From the parameters of the fit lines, we obtain different kind of information for the analysis. With the slope we can see the underestimation or overestimation of the COD field with respect to the reference, and the vertical intercept is related to the ambivalence of τ for a given Radiance value, which increases the uncertainty of the retrieval at small COD.

On the other hand, as we intend to parameterize the influence of the flags, we mark in the scatters the pixels affected by flag1, flag2 and flag3, to see if these sub-scatters follow any distribution different from the whole scatter plot fit line. If that is the case, we obtain for each sub-scatter the fit line parameters and their confidence intervals. Also, we obtain the uncertainty associated to the flags at each sub-scatter following (3.19), (3.20) and (3.21). For each range, the fit residuals are calculated being x_i and y_i each pair of τ values in the scatter.

To end, if the scatter plot shows a large spread of points or trends different to the general fit, we analyze to which part of the COD_sX it belongs, trying to determine the causes of these deviations. Outliers are characterized as such if the y_i values are more than 2σ away from the fit line. σ is calculated as the standard deviation of the y_i values corresponding to the $f(x)$ value in the scatter.

Chapter 4

Results

In this chapter we describe all the results obtained in this work. It is divided in two parts as the methodology chapter. The first one consists in the experimental study carried out with the sky camera measurements, radiative transfer and the 1D Independent Pixel Approximation. In this section the results are classified in four categories according to their quality and reliability. The images of COD obtained from the sky camera are analyzed altogether with the ancillary materials of uncertainties and flags, and we venture some explanations to the unsatisfactory results. Some of the reasons are attributed to the limitations of the methodology, but others to the 3D radiative effects non-contemplated in the 1D approach.

Such conclusions give us motivation for the second part of the chapter, that consists in the synthetic study with the 3D RT for the evaluation of the methodology in the first part and the results. We carry it out by means of 3D RT simulations with a Monte-Carlo based RTE solver over highly resolved cloud fields in the three dimensions with different characteristics of COD and cloud coverage. The simulations are done under different solar geometry, in a simulation mode that mimics the observation of a sky camera. The outputs of the model are ground radiance matrices that are in turn inputs to the Retrieval Algorithm of the first part of this work, to obtain the COD of the original 3D fields. The differences with the real COD and their reasons and relationship with the solar geometry are carried out in two different methodologies. We finish the chapter venturing some parameterizations to solve some of the 1D approach limitations as a function of the analyzed variables.

4. Results

4.1. Experimental study. 1D approach for Sky Camera measurements

The products obtained from the sky camera images are: the radiance of the whole sky and its matrix of uncertainties, the COD retrieved and its matrix of uncertainties, plus the Data Quality Flags matrix. The Flags matrix and the uncertainties matrices indicate the reliability of the results. Within the large database of sky camera images analyzed by the algorithm, we select several representative cases for analysis and discussion, and classify them in four different categories: Category 1 to Category 4, in descending order of quality and reliability of results. The Categories are summarized in Table 4.1 with the characteristics that define each of them. Namely, the presence and percentage of the different types of flags, the comparison with AERONET's zenith COD and the solar zenith angles of the cases classified in them.

Table 4.1 : Categories of results and respective characteristics

Category Number	Characteristics
1	<ul style="list-style-type: none"> • Null presence of flag1 • best coincidence with AERONET <ul style="list-style-type: none"> • all SZA present
2	<ul style="list-style-type: none"> • Presence of all Flags types • good coincidence with AERONET <ul style="list-style-type: none"> • medium to high SZA
3	<ul style="list-style-type: none"> • Presence of all Flags types • Overestimation of AERONET's zenith COD <ul style="list-style-type: none"> • AERONET's zenith less than 20 <ul style="list-style-type: none"> • all SZA present
4	<ul style="list-style-type: none"> • Presence of flag1 over 50% • Underestimation of AERONET's zenith COD <ul style="list-style-type: none"> • only high SZA

4. Results

As Table 4.1 summarizes, within Category 1 we find the best possible results within the capabilities of the methodology followed. The results show high Flags in the whole sky (that is, flag3 and flag4), with a negligible percentage of Flags type 1 or flag1 ($F(z, a) < 0$, see Section 3.1.2.). Also, in this Category we find cases corresponding to the whole period of study (June-December 2018) and range of solar zenith angles (17° - 70°). On the other hand, Category 2 also shows a high coincidence with AERONET's zenith COD, but differs from Category 1 in that the results show greater percentages of flag1 and flag2 despite the estimated satisfactory retrieval of COD. Besides, the case studies in the Category 2 occur at medium to high solar zenith angles, with a range of 50.6° to $\sim 70^\circ$, also belonging to the whole period of study.

Regarding to the two remaining Categories, in Category 3 and Category 4 we find the less satisfactory results, due to errors mainly associated to the limitations of the followed methodology, but also to the 3D effects that the 1D approach does not consider and therefore cannot overcome. In the Category 3 the results show errors due to COD overestimations and in Category 4 the errors are due to COD underestimations. In the Category 3 cases, the solar zenith angle ranges from 17° to 62° , whereas the underestimations on Category 4 cases occur always at the highest solar zenith angles (65° to 69°). In these categories we haven't found any seasonal dependence.

Following the classification, we make a first guess of the causes of miscalculations of τ , with the characteristics in common to that Category. The causes might be either by the 3D effects not contemplated in the plane-parallel model, either by the algorithm limitations. With that knowledge, we identify the possible factors to improve with the help of 3D Radiative Transfer.

We proceed now to describe some selected examples of each Category. Figure 4.1b to Figure 4.9 belong to Category 1, whereas Figure 4.10 to Figure 4.14 are representative of Category 2. On the other hand, Figure 4.15 to Figure 4.21 are from Category 3 and Figure 4.22 to Figure 4.28 from Category 4. Figure 4.1b to Figure 4.28 are labeled from C1 to C4 to indicate their category, and are all composed in the same way. They are formed by the input and output matrices to the Retrieval (Ret.) algorithm. From top/down and left/right there is the original sky camera image, the equivalent blue radiance in $\frac{\text{mW}}{\text{m}^2 \cdot \text{sr}}$ and radiance uncertainties in percentage (see e.g. Figure 4.1b). In the bottom part appear the retrieved COD matrix, the flags matrix (ranging from -10 to 16) and the COD uncertainties in COD units. All the matrices have in the horizontal and vertical axis of pixel number (966x966). The color bars

depict each magnitude represented. Nevertheless, given the big differences among figures, the limits of the color bars are different for each Figure, except for the flags' matrices, that do have a fixed axis from -10 to 15. The comparison with AERONET's Cloud Mode product is done by averaging the central part of the retrieved COD matrix at the camera's zenith angle 0° and surroundings within the 1.4° FOV of AERONET. The area is marked in white in Figure 4.1a to illustrate the extension and position of the samples. The AERONET error is obtained by the uncertainties in percentage provided by Chiu et al., (2010).

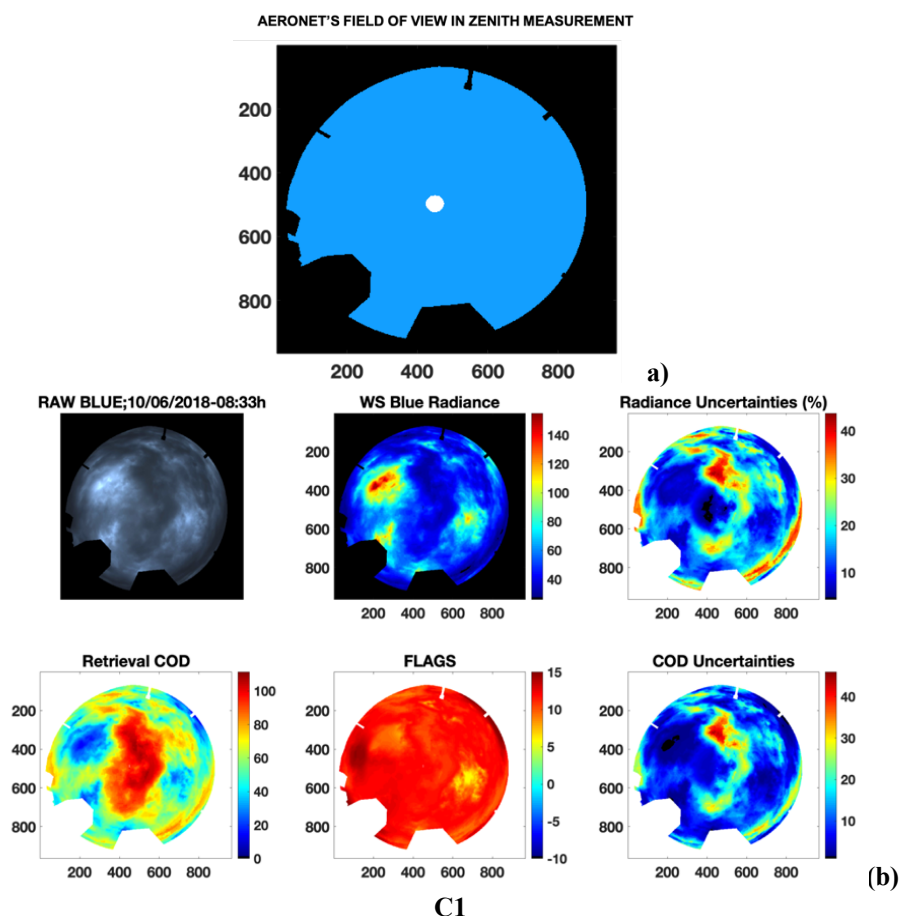
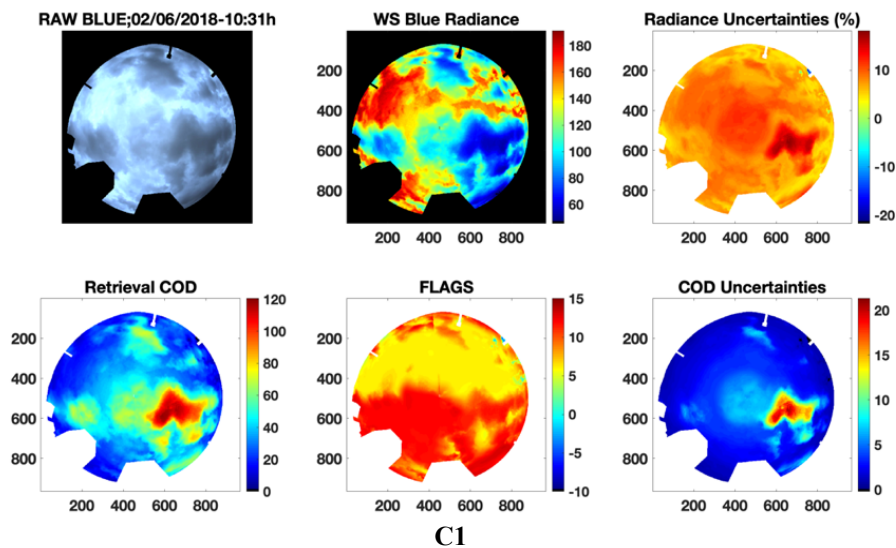


Figure 4.1 : (a) AERONET's FOV in Zenith view over the camera domain. (b)Ret. Results ($sza = 46.7^\circ$). Zenith COD: 93 ± 6 ; AERONET COD: 100 ± 17

4. Results

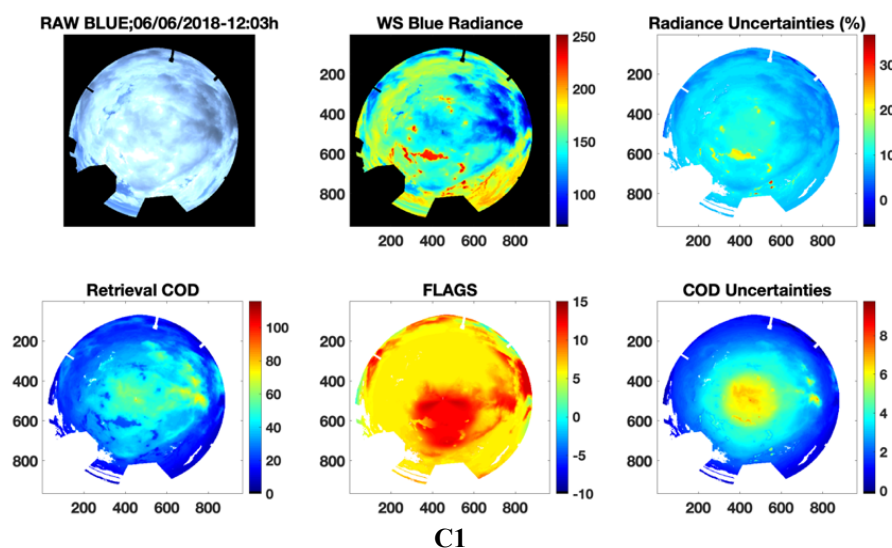
Figure 4.1b is taken on the 10th June at 10:30h. It is an example of a completely covered sky, appearing only three areas of greater clarity in an otherwise very dark domain. This translates into maximum radiance values in these light areas of ~ 145 $\text{mW}/\text{m}^2\text{sr}$, while in the darker areas like in the center of the domain the radiance is $20\text{-}30$ $\text{mW}/\text{m}^2\text{sr}$. The sector of highest COD of above 90 is easily identifiable in the original camera image. The averaged value of COD over the zenith area in Figure 4.1a is 93 ± 6 and is within the range defined by the AERONET value of 100 ± 17 . The error is obtained also from the same averaged area over the COD Uncertainties matrix. The flags of Figure 4.1b are mostly over 12 (at 90% of the pixels), except in two of the lighter areas of the original image, with a presence of 10% of the domain with flag3 (yellow and orange pixels). The uncertainties in the Radiance matrix are all positive and that denotes that all radiance values were within range for the solar geometry and viewing geometry.



**Figure 4.2 : Retrieval Results ($sza=25.4^\circ$). Zenith COD: 59 ± 6 ;
AERONET COD: 54 ± 10**

Figure 4.2, from the 2nd June at 10:31h is also a covered sky example, with three distinguishable areas of darker clouds. In these darker pixels, radiance is around 70 $\text{mW}/\text{m}^2\text{sr}$, and in the lighter areas' radiance can reach 185 $\text{mW}/\text{m}^2\text{sr}$. The highest COD value is 100 to 120 in the western part of the image. The averaged zenith value of COD is 59 ± 6 , very similar to the value provided by AERONET of 54 ± 10 . In the flags' matrix of Figure 4.2, there are two differentiated parts. 41% of the pixels have

flag4, and are located mostly in the southern half, and 48% have flag3, being distributed in the northern half. There is a minimum presence of negative uncertainties of radiance, in the very few pixels in the northern west part with flag1 pixels. As Section 3.1.2 indicated, the $ERR_{i,j,k,l,m}$ matrix is constructed with the sky camera calibration uncertainties (Chapter 3, Table 3.5), plus the radiance enhancement with respect to the 1D corresponding maximum, for the i, j, k, l, m conditions. Therefore, negative uncertainties denote how out of range is the radiance for the given geometry. In the case of Figure 4.2 that effect is negligible (0.07%).



C1

**Figure 4.3 : Retrieval Results ($sza=16.8^\circ$). Zenith COD: 55 ± 6 ;
AERONET COD: 57 ± 10**

The camera image of Figure 4.3 was taken on the 6th June at 12:03h. It is a practically overcast situation with very few patches of clear sky in the south east, as show the CS mask in white. The clouds have some openings where the sun is located, which generates very bright areas of over $220 \text{ mW/m}^2\text{sr}$ of radiance. In any case, all the radiance values in this Figure 4.3 are within range, as indicated in the radiance positive uncertainties matrix. The darkest area of the camera image is retrieved as around 60 of COD. It is in the few dark areas in the center of the image that the comparison with AERONET is carried out, with very similar values (55 ± 6 and 57 ± 10). The patches of openings have the smallest values, of around 10 of COD. In the flags' matrix of Figure 4.3 pixels with flag2 and flag3 are majority, with

4. Results

percentages of 24% and 59% respectively, forming the yellow area in Figure 4.3, leaving a 17% to flag4. The presence of flag1 pixels is also close to 0 in this figure.

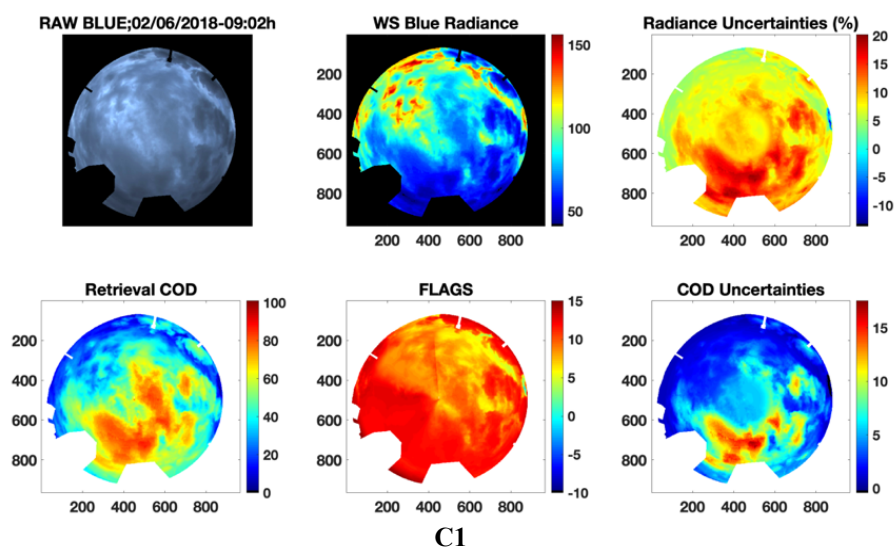


**Figure 4.4 : Retrieval Results (sza:41.3°). Zenith COD: 60 ± 5 ;
AERONET COD: 58 ± 10**

Figure 4.4 (2nd June, 9:02h) is also a full coverage situation, with no openings near the sun. However, there are areas somewhat lighter than the rest of the domain, which are equivalent to radiance values of 130-150 mW/m²sr. Very dark areas predominate in the image, with radiance values of ~40 mW/m²sr. In these dark areas, the retrieval obtains optical thickness values of up to 90-100. The values in zenith are not that high, according to the retrieval (60 ± 5) and the AERONET counterpart (58 ± 10). In this figure flag1 is typically less than 0.1% of the image, being these few pixels (0.02%) the responsible for the negative uncertainties of around -13% in the north west. All other radiance values are within range, with maximum values of uncertainty in radiance of 20% due to the calibration of the instrument. The flag4 type is the most abundant with a 57% of the pixels. Flag3 on the other hand affect to the lighter areas, involving a 40% of the domain. Pixels with flag2 are located close to the pixels of flag1 and are less than 3%.

Regarding to Figure 4.5, of the 19th November at 9:45h it is one of the examples of with highest coverage and cloud optical depth. The image is dark enough, also due to the high solar zenith angle (65°), keeping the radiance values under 60 mW/m²sr,

despite the fact that both the retrieval and AERONET indicate that this episode is not the one with the highest COD (60 ± 5 vs 58 ± 10). The structure of COD is easily recognizable in the original image. Such uniform coverage does not have sky patches and therefore all radiance values are within range, with maximum radiance uncertainties of 50% in the thickest areas. This also translates in pixels with flag4 being majority, of 59%. In the central area of the image there are pixels with flag3, up to 33%, and a minimum presence of flag2 of 8%. Given that all the radiance values are within the range, in this central zone we find the values of the radiance uncertainties (and therefore the COD uncertainties) among the lowest in the domain, from 10% to 30%, and due to only the instrument calibration.

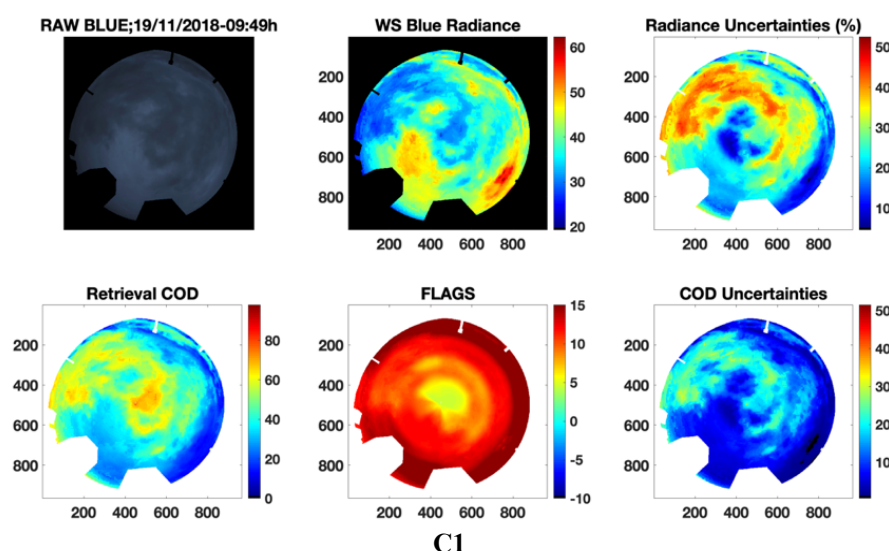


**Figure 4.5 : Retrieval Results ($sza=65^\circ$). Zenith COD: 67 ± 19 ;
AERONET COD: 61 ± 11**

Figure 4.6 on the other hand corresponds to an image that is even more covered than that of Figure 4.5, with lower radiance values (from 15 to 55 mW/m^2sr). The retrieved COD in much part of the image is over 40, reaching values of 100. The area of less optical thickness includes the central area where the AERONET measurement takes place. In this Figure 4.6 again both COD Zenith values, the one measured with the camera and the one measured with AERONET are very similar, differing by 10% and 4 units of COD. The flags percentages and positions are very similar in the figure to Figure 4.5, with values of 61%, 36% and <3% respectively for flag4, flag3 and

4. Results

flag2. There are no pixels with flag1 in this case. Also, Figure 4.7 is another example from December, the 13th with full, uniform coverage. Most of the domain has the same COD of around 40, including the zenith measurements, as we can see in the COD matrix and in the comparison with AERONET (38 ± 2 and 42 ± 7). In Figure 4.7 the smallest radiance uncertainties are also found in the central part of the image, in a more defined way than in Figure 4.6. This translates in the error of COD of a $\sim 5\%$ in the zenith measurement. In Figure 4.7 flag4 reach the highest percentage in Category 1, of 81%. The yellow pixels in the FLAGS matrix correspond mostly to flag3, with a value of 17%. There are no flag1 pixels neither.

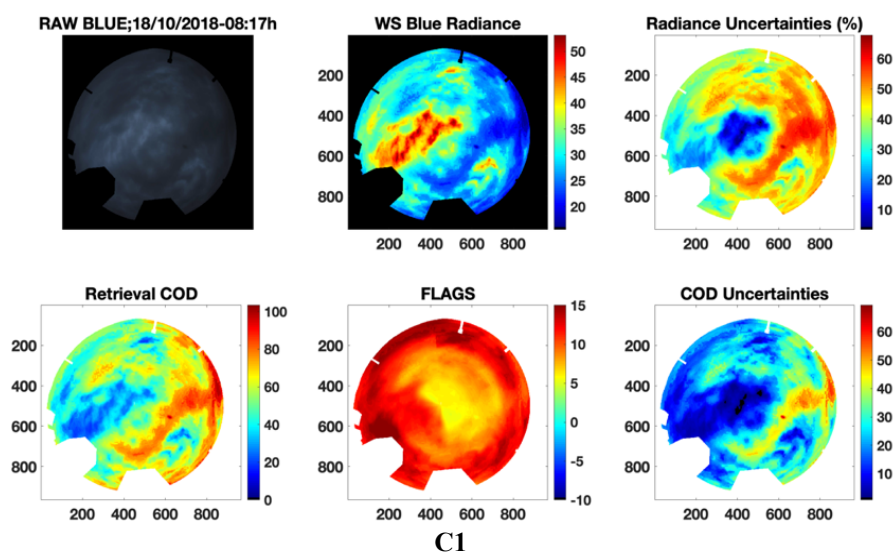


**Figure 4.6 : Retrieval Results ($sza=69^\circ$). Zenith COD: 39 ± 7 ;
AERONET COD: 35 ± 6**

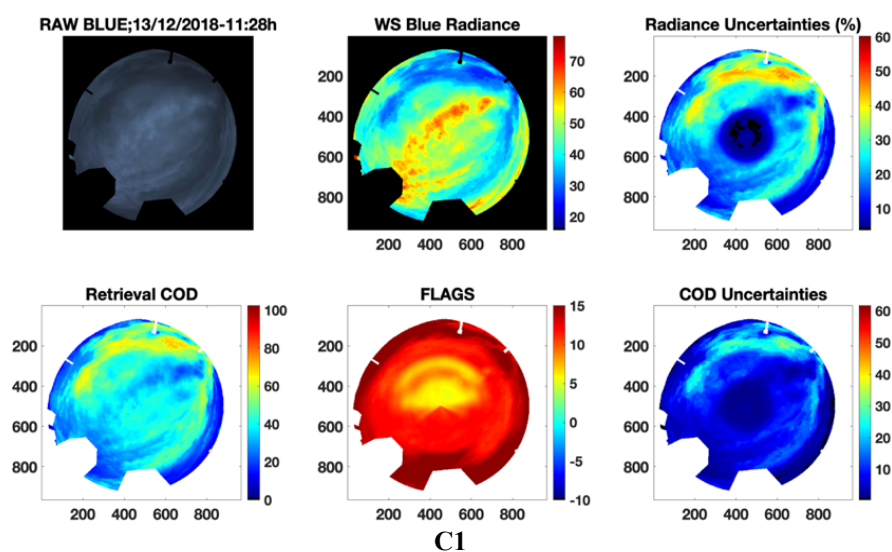
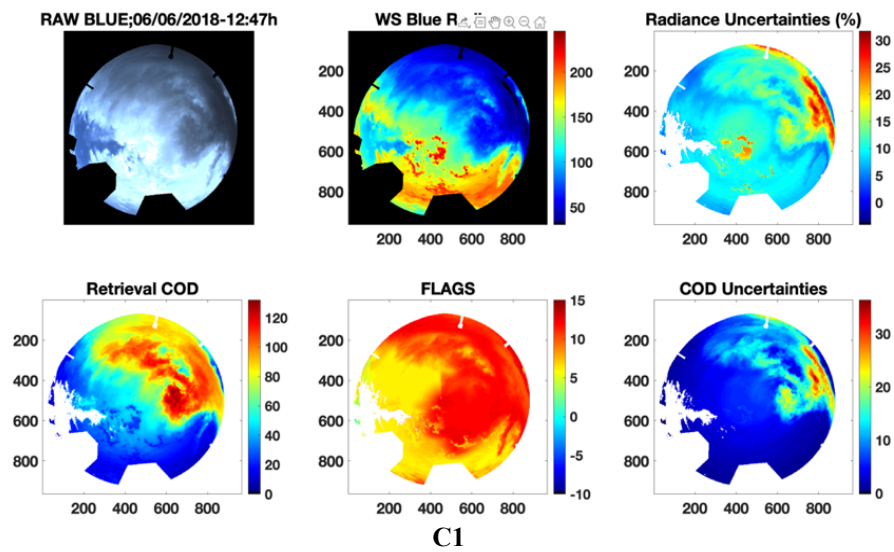


**Figure 4.7 : Retrieval Results ($sza=63^\circ$). Zenith COD: 38 ± 2 ;
AERONET COD: 42 ± 7**

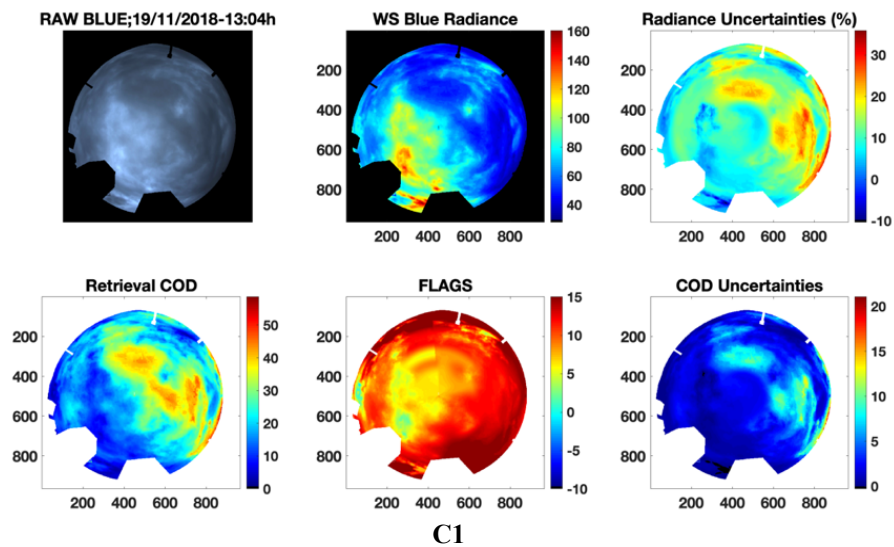
To end the Category 1, we introduce Figure 4.8 and Figure 4.9. These are examples from the 6th June (12:47h) and from the 19th November (13:04h), respectively. They are quite different examples from each other, but the comparison of both with AERONET are the best ones found in this work.

Figure 4.8 corresponds to a partial coverage image, in which all kind of pixels can be found: clear sky, thin clouds and thick clouds. Therefore, the retrieved COD ranges from close to 0 to over 120. The comparison with AERONET only differs in one unit, that is, 2% in this particular case (54 ± 6 and 53 ± 9). Regarding to flags, can be seen in the FLAGS matrix that the percentages of flag3 and flag4 are very similar (46% and 49%, respectively), while flag2 pixels have a minimum percentage of 5%. Flag1 pixels have the usual 0.02% in Category 1 but they are the very few pixels with negative radiance uncertainty. The highest, positive uncertainties are found in the darkest areas of the image (less radiance) and in the openings of clouds close to the center of the image (radiance over $200 \text{ mW/m}^2\text{sr}$). Regarding to COD uncertainties, all the area of thin clouds have the lowest values, under 8, whereas the thickest clouds have uncertainties of around 15 and until values over 30.

4. Results



*Figure 4.8 : Retrieval Results ($sza=19.6^\circ$). Zenith COD: 54 ± 6 ;
AERONET COD: 53 ± 9*



*Figure 4.9 : Retrieval Results ($sza=61.3^\circ$). Zenith COD: 24 ± 2 ;
AERONET COD: 24 ± 4*

Finally, Figure 4.9 is an example of full coverage, similar to Figure 4.6 whose zenith COD coincides with AERONET's zenith COD (24 ± 2 and 24 ± 4). The COD in the whole domain is under 55, with the structure of the cloud field well identifiable between the retrieval and the original image. The light areas have optical thicknesses of 10 to 20, whereas the darkest areas have COD between 30 and 50. The flag2 pixels are more visible in the FLAGS matrix in this particular case, and they suppose an 8% of the domain. Some pixels of flag2 in the southernmost part are those of radiance uncertainties of ~ -10 .

As Section 3.1.2. indicates, we can also find radiances that are too low with respect to the simulated ones, even with the maximum considered optical thickness ($\tau = 150$). With it, the $ERR_{i,j,k,l,m}$ matrix includes the radiance diminution with respect to the 1D corresponding minimum. It should be noted that the highest values of positive radiance uncertainties range from 18% to 68% in Category 1, being this last value (Figure 4.6) due to too small radiances for the simulations performed and the maximum Cloud Optical Depth considered to conduct them. In general the highest radiance uncertainties are found in Figure 4.5, Figure 4.6 and Figure 4.7 whose solar zenith angles are 63° - 69° .

On the other hand, the negative values of radiance uncertainty, found in figures like Figure 4.2, Figure 4.4 or Figure 4.9 belong to radiance enhancement, or radiance too high for the 1D simulation under the corresponding conditions. As it was previously stated, the negative values correspond to pixels with flag1 or flag2, (ranging from -2% to -14%) and therefore have a negligible presence in Category 1.

With it, the average radiance uncertainties range from 8% to 40%. Given this percentages, the uncertainties associated to the Cloud Optical Depth retrieval range from 3 to 24, as average values of the matrices of COD errors. On the other hand, the highest negative values of COD uncertainties range from -0.4 to -0.1. The negative sign indicates that these uncertainties correspond to low flags, that is, out of range pixels, where the Cloud Optical Depth is systematically low and therefore the associated uncertainties.

As we have seen in Category 1, the retrieved COD values in the zenith area range from 24.4 (Figure 4.9) to 93.1 (Figure 4.1) in Zenith. The values of COD range from 0 to more than 120. In this group of case studies, we have found only one case with partial coverage, the one shown in Figure 4.8. From this fact, and because the 3D effects in conditions of total cloud coverage are not so important, we deduce that the

4. Results

best results are obtained in thick cloud fields with full or practically full coverage, as expected according to bibliography (Zuidema and Evans, 1998). In such conditions the solar zenith angle does not influence the results significantly.

Regarding to Category 2, Figure 4.10 is the first example belonging to this Category. First, we see that it is very different from the figures in Category 1. It belongs to a broken cloud field, with a meaningful clear sky mask. The image was taken on the 28th December at 12:05h, and the clouds cover 85% of the domain.

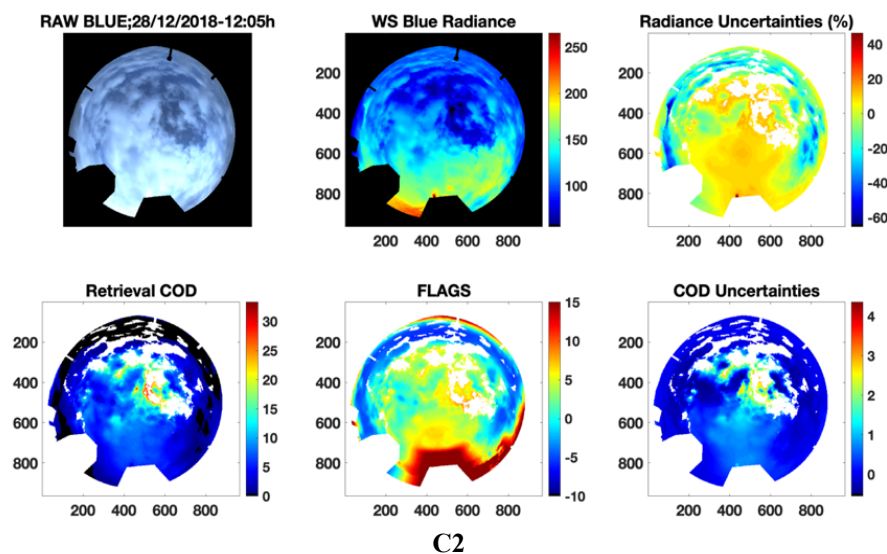
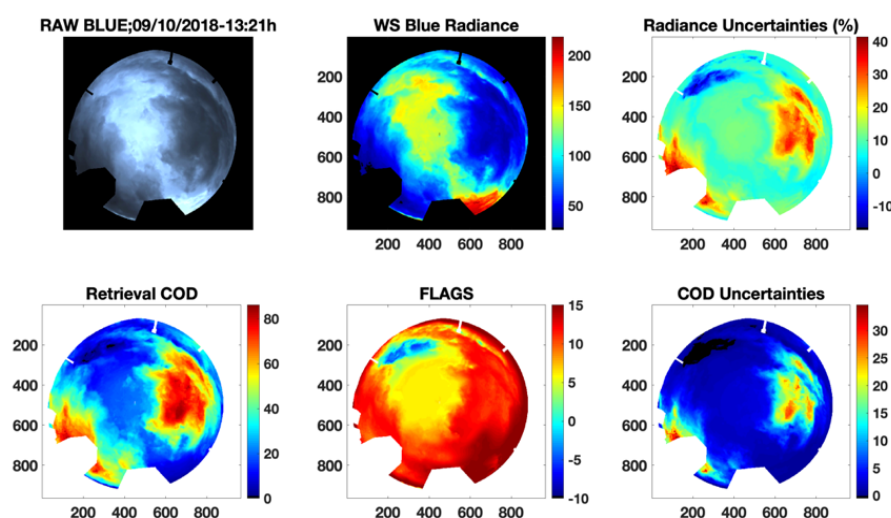


**Figure 4.10 : Retrieval COD ($sza=62.6^\circ$). Zenith COD: 11 ± 1 ;
AERONET COD: 10.3 ± 1.8**

Regarding FLAGS matrix, we see flags occurrences of the four types. In Figure 4.10 lower flags (flag1 and flag2) are majority, with a percentage of 30% and 47% respectively, whereas flag3 and flag4 present a 11% and a 12%. We can see in the FLAGS matrix that the flag1 pixels are all located close to the horizon, in the largest possible scattering angle, whereas flag2 and flag3 pixels are distributed in the cloud borders around the clear sky mask. We can easily determine that the thickest clouds are the closer ones to the sun, and therefore they compose the brightest part of the image, with radiance values between 150 and 200 mW/m^2sr . The highest values of radiance uncertainties in absolute value are, on the one hand, the negative uncertainties, with values ranging from -20% to -60% and located where the flag1 pixels are, and on the other hand, the maximum of positive radiance value in a cloud

opening in the south close to the sun position. Most of the image is affected by positive, moderate uncertainties of around 10%, including the zenith sector where the AERONET measurement takes place. Despite the partial cloud cover and the significant number of lower flags, the comparison with AERONET in the center of the image is satisfactory enough (11 ± 1 and 10.3 ± 1.8). Nevertheless, the retrieval has provided abnormally high COD in some pixels of the cloud sides. That is a flaw in the retrieval that is further analyzed and discussed.



C2

**Figure 4.11 : Retrieval Results ($sza=50.6^\circ$). Zenith COD: 22 ± 3 ;
AERONET COD: 16 ± 3**

On the other hand, Figure 4.11 is another full coverage example, from the 9th October at 13:21h. The cloud field consists of thin clouds and thicker clouds, being that the lighter clouds are distributed all along the solar azimuth. Such thinner clouds have COD values of 10 to 20, including the zenith sample, with a value of 22 which compares with an AERONET value of 16. Both values are in agreement as they are within the error bars of their respective uncertainties. The flags in Figure 4.11 are similar to those found in Category 1, except for the presence of 3% of flag1, located in the opposite position of the sun. Flag3 pixels occupy 30% of the domain and are distinguished from the flag1 pixels and correspond to the thin clouds, unlike flag4 (~58%), that correspond to the thicker clouds, with COD up to 80. Uncertainties for

4. Results

radiance in this case are all positive except the pixels of flag1, that reach values of ~-13%.

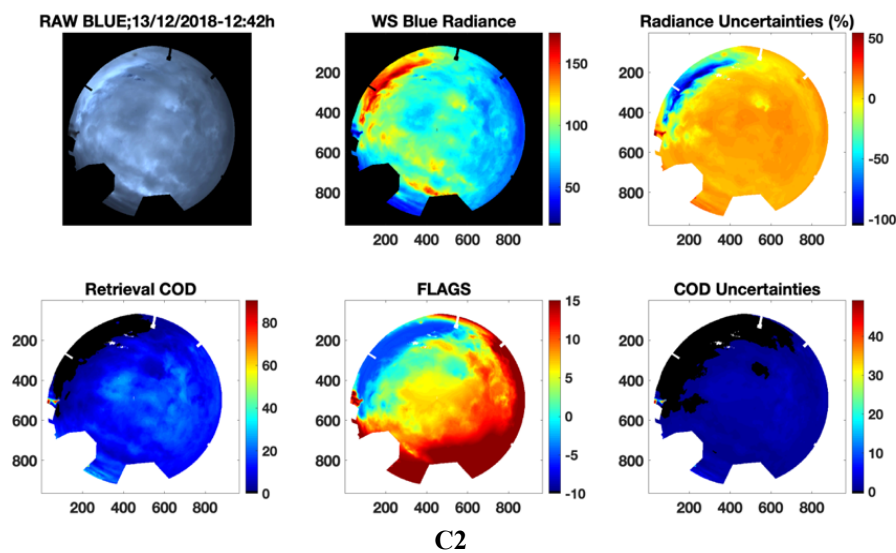
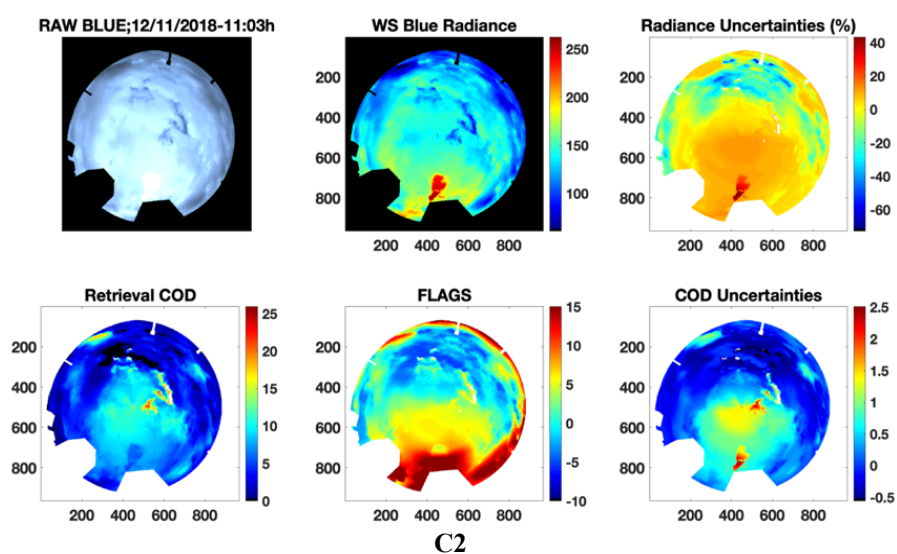


Figure 4.12 : Retrieval Results ($sza=63.6^\circ$). Zenith COD: 18 ± 2 ; AERONET COD: 23 ± 4

To follow, Figure 4.12 is another full coverage example, taken on the 13th December at 12:42h. It is a cloud field more uniform than the one from Figure 4.11, but with some openings close to the south and in the north east. This opening has a significant percentage of flag1 pixels, consisting of 15% of the domain. The radiance uncertainties associated reach values of -100% and more. That means a high radiance out of range for the given solar and viewing geometry. The cause might be cloud enhancement by multiple reflections in the cloud sides in that position. Nearby flag2 pixels are distributed, occupying a 26% of the domain. Flag3 pixels are distributed below, and affect the central part of the image, where the COD of the sky camera differs from the AERONET value in 5 units, but is included inside the error bars. A COD of around 15 to 20 is uniformly distributed all over the domain, except the underestimation related to the flag1 and flag2 pixels, with values assigned by the retrieval of around 0.



**Figure 4.13 : Retrieval Results ($sza=58.1^\circ$): Zenith COD: 11 ± 1 ;
AERONET COD: 8.8 ± 1.5**

Figure 4.13 belongs to an image taken on the 12th November at 11:03h. It consists of thin clouds, as denoted by the brightness of the cloud field due to the radiation enhancement above the clear sky radiance. We can identify easily in the radiance matrix, along with the original image, the cloudy pixels, whose radiance values range from 130 to 260 $\text{mW}/\text{m}^2\text{sr}$ in the brighter pixels, with the highest value found in the vicinity of the Sun. Values of radiance around and below 100 $\text{mW}/\text{m}^2\text{sr}$ are found both in the darker clouds close to the horizon and in the small gap of clear sky, that the CS mask configuration did not identify completely. This is a visual example of the ambivalence of COD for a given value of radiance (in this case, $\sim 100 \text{ mW}/\text{m}^2\text{sr}$). Therefore, the retrieval has overestimated the COD of the pixels in the clear sky gap (15 to 25 of COD, while it should be 0), when they are not labeled as clear by the CS mask. These pixels are labeled with flag2 and flag3, given that their retrieval is directly affected by ambivalence. Most of pixels are marked with flag2 (40%) throughout the upper area, together with the pixels of flag1 which represent 33% of the domain. Flag3 and flag4 affect to the central and southern part of the domain, as a 12% and a 15%, respectively. The optical thickness in the center of the cloud field ranges from 8 to 11, as the comparison with AERONET indicates (11 ± 1 and 8.8 ± 1.5). The COD close to the horizon is acquired from above 0 to 10, and the pixels labeled with flag1 get the assigned value of 0. Such pixels reach a -60% of radiance

4. Results

uncertainty, that is, the radiance measured by the camera is a 60% higher than the simulated radiance for the given solar and viewing geometry. At the other end, the highest positive radiance uncertainty is reached in the vicinity of the sun, where the maximum of digital counts is measured.

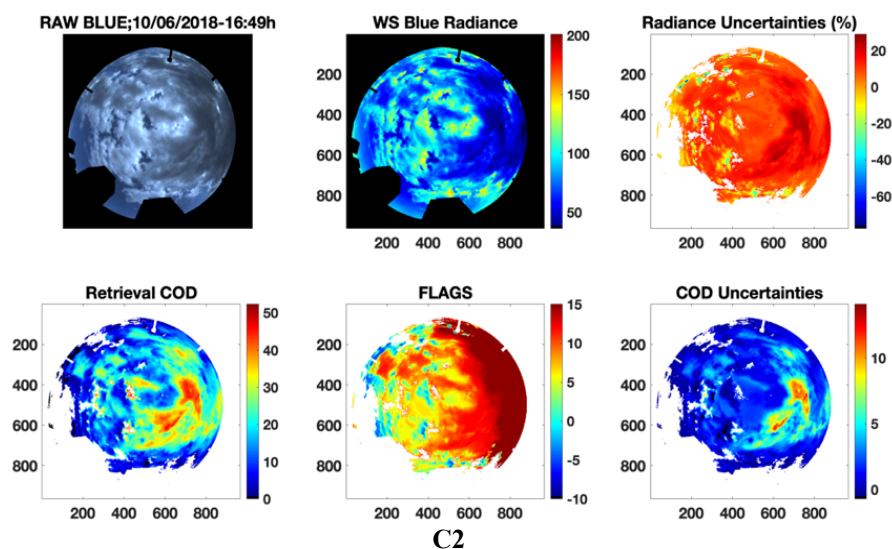
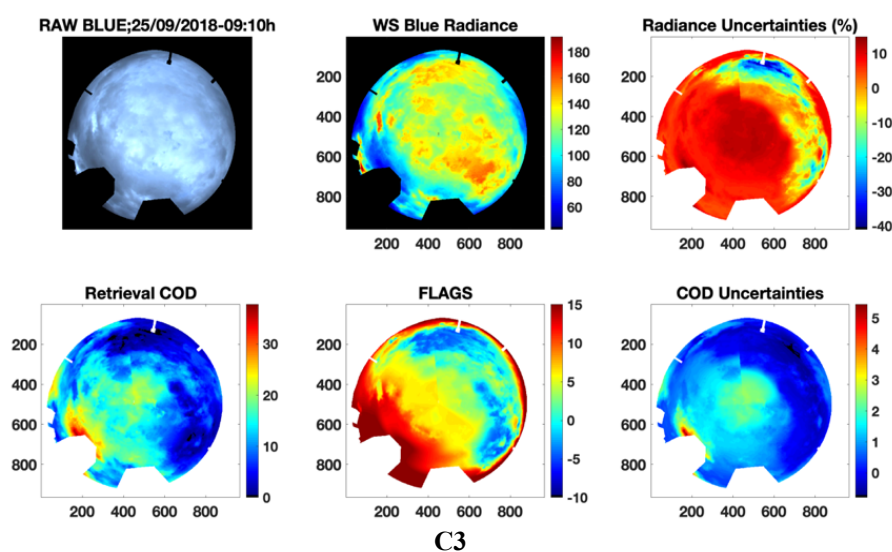


Figure 4.14 : Retrieval Results ($sza=62.2^\circ$). Zenith COD: 21 ± 2 ; AERONET COD: 17 ± 3

To end the examples of the Category 2 we introduce Figure 4.14. It is an example of a broken cloud, with very visible gaps of clear sky, most of them identified by the CS mask configuration. In the vicinity of these gaps the radiance reaches its highest values, from 100 to 150 mW/m^2sr , with some points up to 200 mW/m^2sr . This exemplifies the radiance enhancement due to the multiple reflections of radiation in cloud edges. Alternating with lighted cloud patches with COD ranging from 5 to 10, there are darker clouds with values around 20, including the sample where the AERONET's measurement takes place. To end, the thickest areas of the clouds reach COD values up to 40 and 50, making this a cloud field with high variability. The flag1 pixels are located in the areas illuminated by the multiple scattering, but they really suppose a 5% of the domain, whereas flag2 and flag3 complete the rest of lighter clouds, with a 21% and a 28% respectively. Flag4 is a majority, representing the thickest cloud pixels and occupying 46% of the domain.

To sum up, in Category 2 the positive radiance uncertainties are up to 54%. The highest radiance uncertainties appear in Figure 4.12, a case from December and solar zenith angle of 58° . On the other hand, in Category 2 the highest negative values of radiance uncertainties are much higher in absolute value than in Category 1, ranging from -105% (Figure 4.12) to -17% (Figure 4.11). As said previously, these areas present out of range values of radiances in which the COD calculation is settled to 0 since it cannot be calculated in a satisfactory way with the 1D approach. The uncertainties values correspond to the relative difference between the radiance from the sky camera and the maximum radiance possible in the 1D approximation, for the solar and sky position. Therefore, these negative values express how out of range the corresponding Radiance values are over the simulated radiances. With all that, the uncertainties associated to radiance enhancement range from -27% to -5% in average. On the other hand, the positive radiance uncertainties, due to mainly the camera calibration range from 7% to 13%.

On the other hand, the positive uncertainties in the Cloud Optical Depth retrieval range in average value from 0.5 to 6, while the negative uncertainties remain low in absolute value, ranging between -0.2 to -0.1 in average. The highest positive values of COD uncertainties reach 49, found in Figure 4.12.



**Figure 4.15 : Retrieval Results ($sza=54.9^\circ$). Zenith COD: 20 ± 2 ;
AERONET COD: 12 ± 2**

4. Results

The COD retrieved values of the case studies in Category 2 range from 11.1 (Figure 4.13) to 21 (Figure 4.14) in Zenith. In the whole domain the τ maximum values reached do not overpass 50 in most of case studies, and the minimum values are equal or close to 0. Pixels with flag1 include pure out of range cases, that is, the absolute value of flag is around -5, and the τ value is settled to 0 as it is impossible to calculate in the 1D approach. In Category 2, we have found more cloud fields with partial coverage, as Figure 4.10 and Figure 4.14 illustrate. In Figure 4.13 we find another example of overestimation of τ in the cloud edges.

As we indicated previously, some results of the retrieval are found incorrect, due to, in some cases, the limitations of the followed methodology. These results are classified in Category 3, and we recognize them mainly by the comparison with AERONET through zenith COD values under 20.

Figure 4.15 is the first example of the Category 3 classification. It belongs to a full coverage camera image taken on the 25th September at 9:10h. It has no openings and the COD is uniform over the domain, except in the vicinity of the sun, where the clouds seem to be thicker. Nevertheless, the zenith COD retrieval is 8 units higher than the AERONET estimate and is outside the error bars intervals, that is, a 67% of overestimation. We think that it is due to that the real COD (around 10) is located at the maximum of the Radiance = $f(\tau)$, where ambivalence has its greatest importance (see Section 3.1.2). Therefore, the central part of the domain and surroundings are labeled as flag3, which cover 21% of the domain. However, the FLAGS matrix has two sections with flag1 which are not distinguishable in the original image. Such pixels might indicate horizontal transport that increases the radiance up to a 40% over the simulated maximum radiance in the 1D approach, for the given solar and viewing geometry (see Radiance Uncertainties matrix). Flag1 pixels cover 17% of the domain, and flag2 pixels, distributed surrounding flag1 ones, reach up to 36%. Flag4 pixels (25% coverage) are gathered in the south east, where the sun is located and the clouds are thicker.

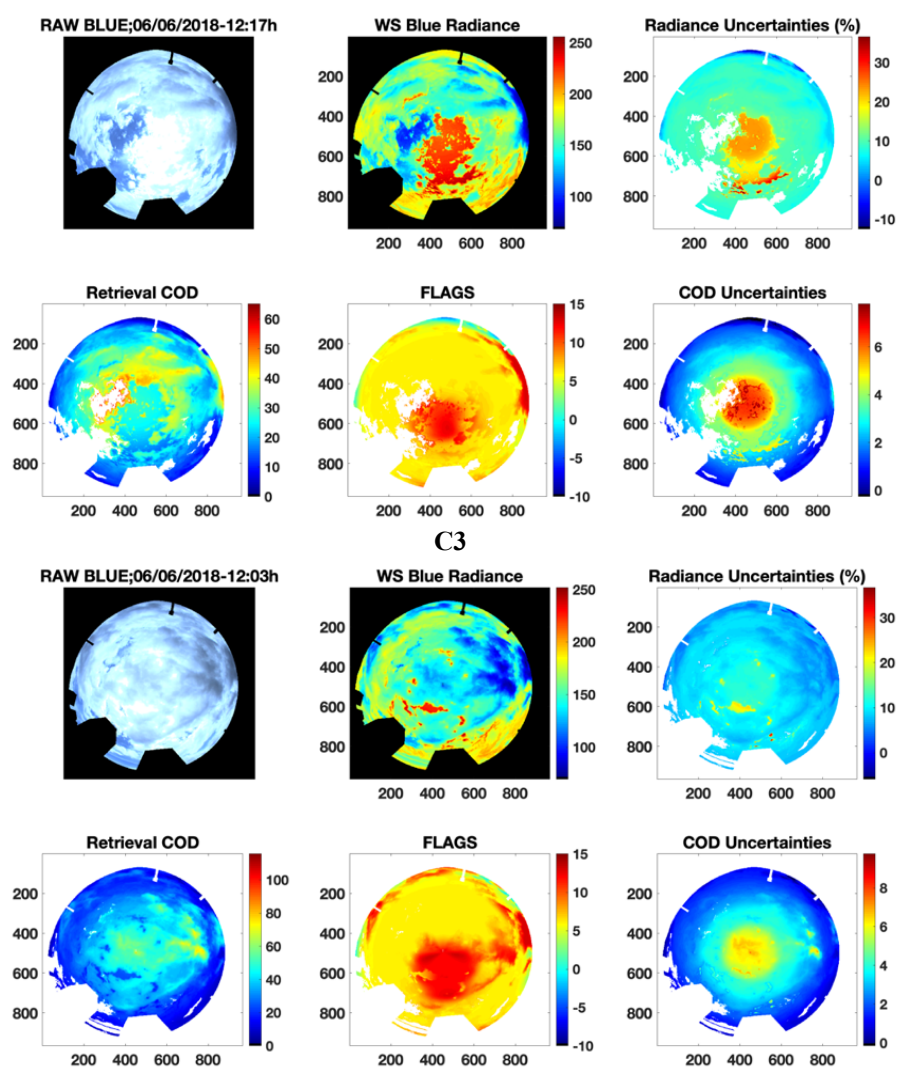


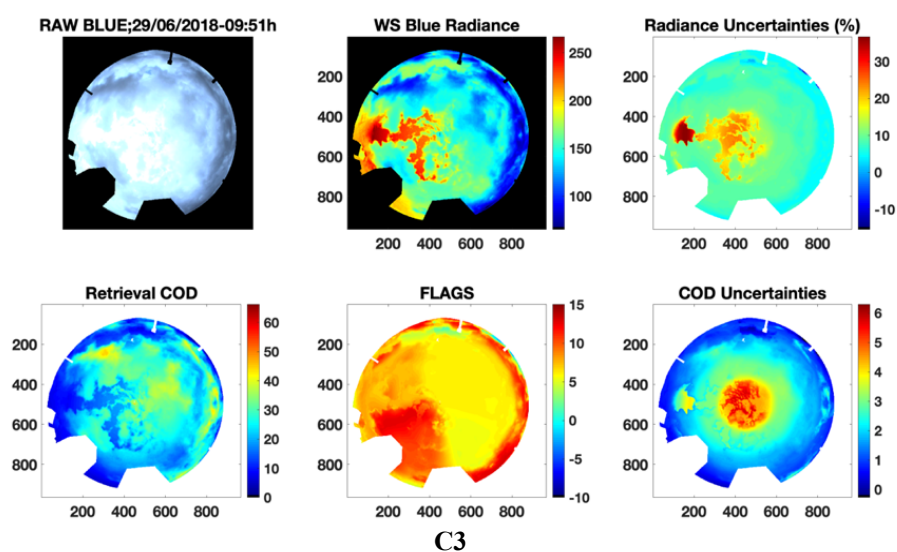
*Figure 4.16 : (a) Retrieval Results ($sza=17.2^\circ$). Zenith COD: 32 ± 7
AERONET COD: 9 ± 2
(b) Former Figure 4.3, taken 14 minutes before.*

To continue, Figure 4.16a is an example of the situation most seen in Category 3. It shows a more or less large area of clouds with the sun behind illuminating it, with radiance values up to $250 \text{ mW/m}^2 \cdot \text{sr}$ in the Figure 4.16a case. The ambivalence of COD for a given value of radiance, and the Retrieval Algorithm configuration, makes

4. Results

that these pixels get as much higher τ than it really is, as shows the comparison with AERONET (32 ± 7 and 9 ± 2), with a retrieved COD 23 units higher than the real one, meaning an overestimation of 355%. Most of the domain is labeled by flag3 (61%), as the real COD is of around 10, except in the sector where the sun lays, and in some pixels close to the horizon. Also, Figure 4.16a is a particular case in this work because in Category 1 we have found an example from an image taken only just few minutes before, that is Figure 4.3. We show it again in Figure 4.16b. In the Figure 4.3, now Figure 4.16b, the Cloud Optical Depth is comparatively high and the flags in zenith are around 12, so the algorithm performs well enough. Conversely, in Figure 4.16a there is an opening in the clouds and the COD decreases dramatically. The radiance in zenith in the Figure 4.16a image is very close to the maximum in the function $Radiance = f(\tau)$ (see Figure 3.23 in Chapter 3). Therefore, the flags in that zone are smaller and there is no way to unequivocally obtain the COD with certainty using the proposed methodology.

Figure 4.17 is a similar example to Figure 4.16a, taken at the 29th June at 9:51h. Maximum radiance values also reach $250 \text{ mW/m}^2 \cdot \text{sr}$ in the brightest pixels. The radiance uncertainties are maximum in that position, with values up to $\sim 35\%$, and 15% to 25% in the rest of the most illuminated clouds. Flag1 pixels are found in a negligible number, a 0.1%, while flag2 and flag3 occupy most of the domain, with a 26% and a 56% of the pixels, respectively. Flag4 pixels are also located around the sun position and close to the horizon. The COD also gets overall overestimated in 20 units over the AERONET's given value, except in part of the highly illuminated cloud opening and in some of the darkest cloud patches in the north and east, as well as in the pixels close to the horizon.



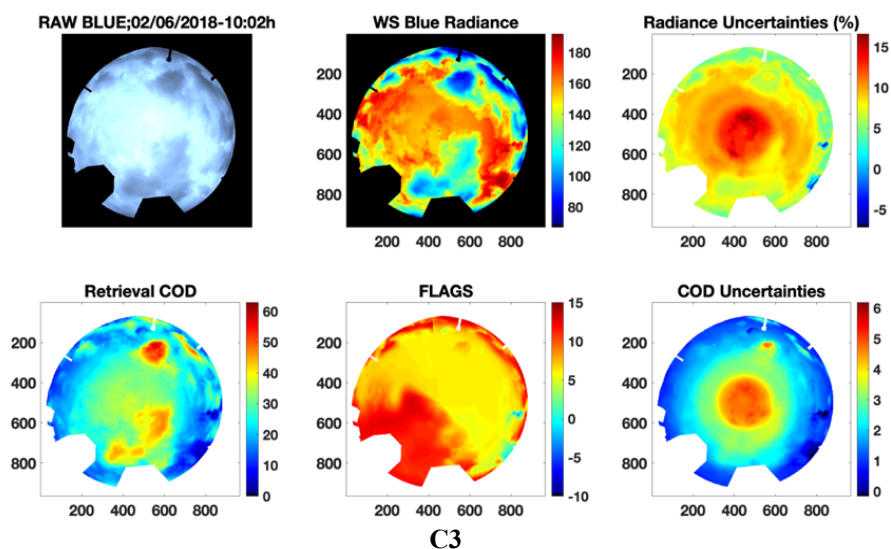
**Figure 4.17 : Retrieval Results ($sza=32.5^\circ$). Zenith COD: 32 ± 5 ;
AERONET COD: 12 ± 2**

Figure 4.18 is an example of June, taken on the 2nd June at 10:02h. The cloud field is composed mostly of thin clouds quite bright, with values from 140 to $185 \text{ mW/m}^2 \cdot \text{sr}$. These thin clouds are also in the center of the domain, where the AERONET's measurement takes place, and where COD is also overestimated by 20 units. There are also some patches of darker clouds in the south and in the north whose COD is estimated by the retrieval of 40 to 50 and up to 60 in the north. The percentages of flags are similar to Figure 4.17, but with more flag4 pixels in the vicinity of the sun.

We follow with Figure 4.19, a cloud field with more variability than the two previous examples. There are clear sky gaps, thin clouds, bright cloud openings close to the sun and thick, darker clouds. The overestimation of the thin clouds in the center of the domain in this case is of 16 units, twice the value provided by AERONET. The COD is probably better obtained in the bright opening of clouds (of around 5) and in the thicker clouds, with values from 30 to 40 and with maximum values of 50-60 in the north west. Flag3 pixels are a majority, reaching 43% of the image, whereas flag2 and flag4 have similar percentages of 22% and 26% respectively. Flag2 and flag1 pixels are located nearby in the north of the image. Flag1 pixels are more significant in Figure 4.19 than in the previous examples of Category 3, occupying a 10% in the

4. Results

higher scattering angles. The measured radiance in that area is up to 66% above the simulated radiance.



*Figure 4.18 : Retrieval Results ($sza = 30.3^\circ$). Zenith COD: 36 ± 5
AERONET COD: 16 ± 3*

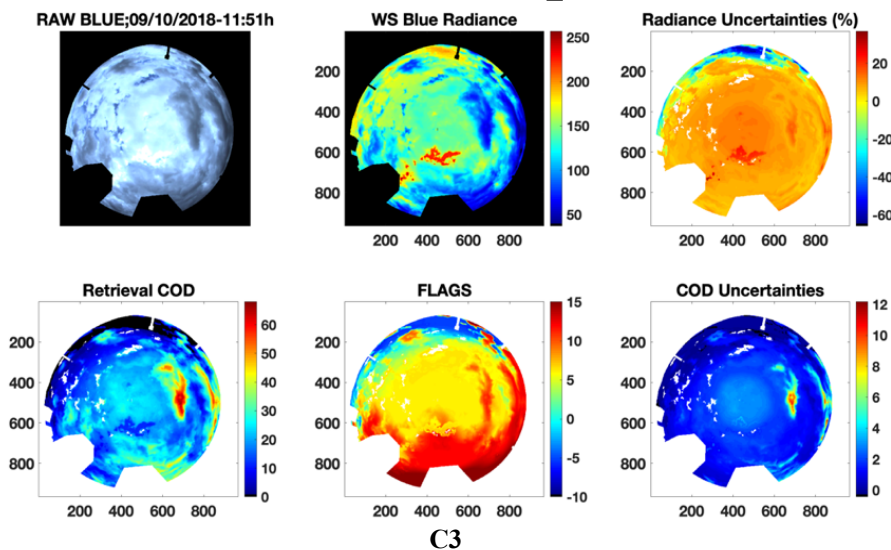


*Figure 4.19 : Retrieval Results ($sza=45.8^\circ$). Zenith COD: 24 ± 3 ;
AERONET COD: 8 ± 1*

The overestimation of the thin clouds in the center of the domain in this case is of 16 units, twice the value provided by AERONET. The COD is probably better obtained in the bright opening of clouds (of around 5) and in the thicker clouds, with values from 30 to 40 and with maximum values of 50-60 in the north west. Flag3 pixels are a majority, labeling a 43% of the image, whereas flag2 and flag4 have similar percentages of 22% and 26% respectively. Flag2 and flag1 pixels are located nearby in the north of the image. Flag1 pixels are more significant in Figure 4.19 than in the previous examples of Category 3, occupying a 10% in the higher scattering angles. The measured radiance in that area is up to 66% above the maximum simulated radiance.

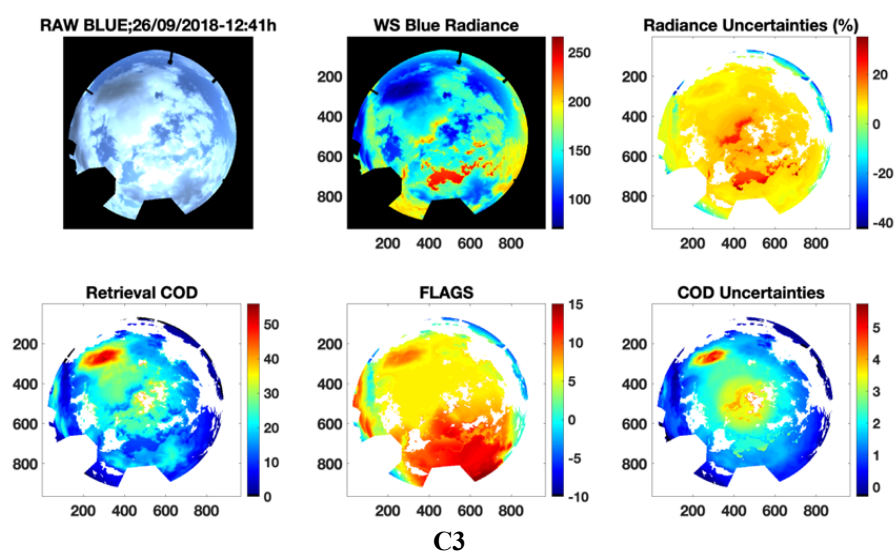


**Figure 4.20 : Retrieval Results ($sza=42.3^\circ$). Zenith COD: 28 ± 4 ;
AERONET COD: 16 ± 3**

On the other hand, Figure 4.20 is an example from the 26th September at 12:41h. It is an image of broken clouds, with a significant clear sky mask, as well as bright clouds and some darker areas. Zones of multiple reflections are easily identifiable in the original image and in the radiance image, with values reaching 200 to 250 $mW/m^2 \cdot sr$. As in the previous cases, it is not in the brightest pixels where the COD is overestimated, but in those whose radiance values range from 150 to 200 $mW/m^2 \cdot sr$, labeled with flag3. They occupy in total a 49% of the domain. The comparison with AERONET is affected by relatively thin clouds ($\tau \sim 16$) labeled by flag3, so the

4. Results

retrieval overestimates COD by 75% (28 ± 4 and 16 ± 3). Flag1 pixels are located next to the biggest clear sky gap occupying only a 4%, where the radiance is up to 40% above the simulated radiance for the given solar and viewing geometry.

To end Category 3, we introduce Figure 4.21, quite different from the examples above. It is a covered example with relatively bright and dark clouds, in a very variable domain. According to AERONET the sample in the zenith where the measurement is taken has an overall value of 6 ± 1 , while the retrieval obtains a value of 22 ± 2 . Nevertheless, in much of the rest of the domain the COD field is estimated with values similar to the provided by AERONET. With it, we cannot determine if the overestimation is due to the high variability in space and time of the cloud field or due to the ambivalence. It could be due to the latter, since the flags of the central zone are of type flag3, as in the previous cases. Flag1 related to the higher scattering angles and occupy 16% of the domain. In these areas the radiance is 40% to 96% higher than the simulated radiance in the 1D approach. Flag 2 pixels are distributed surrounding flag1 and comprise 23% of the domain, whereas flag3 occupy less, 19%. Flag4 pixels are those with the thicker clouds, with COD values up to 40-50, representing a 42%.

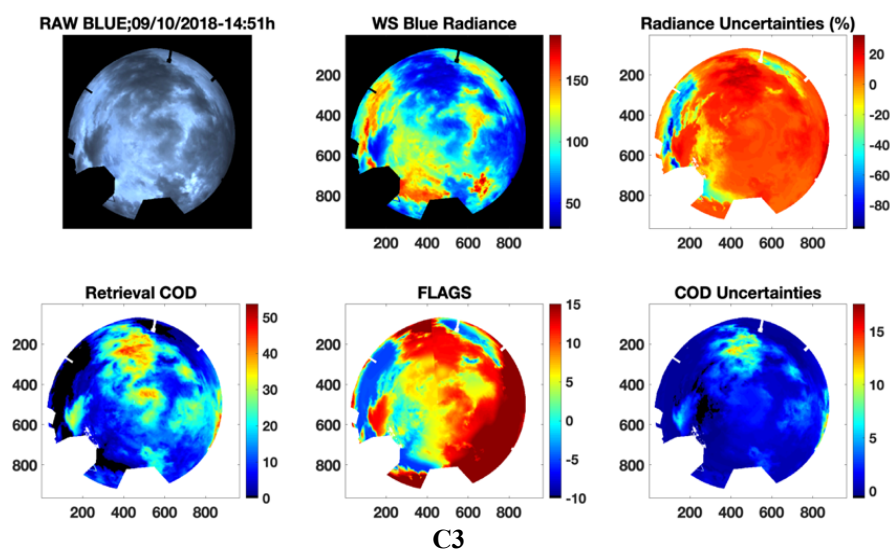


**Figure 4.21 : Retrieval Results ($sza=42.3^\circ$). Zenith COD: 22 ± 2 ;
AERONET COD: 6 ± 1**

To sum up, Category 3 shows a heterogeneous distribution of flags as in Category 2. The flag1 represents up to 17% (Figure 4.15). Flag3 ranges from 19% to 61% and

Flag 4 ranges from 9% to 42%. Flag2 has also a significant influence, ranging from 21% to 36%. From all this we infer that in the cases within Category 3, ambivalence predominates. In fact, in this Category the values of the flags in zenith are around 6-7 in average, except one of the case studies, whose flags values in zenith are ~ 10 (Figure 4.16a). Therefore, the reason for the miscalculations is the employment in the LUT of higher Cloud Optical Depths that produce the same Radiance as the lower values (Figure 3.23 in Chapter 3). This causes that in the same day with just few minutes apart we obtain two types of results (Figure 4.3 and Figure 4.16).

In general, the uncertainties in radiance in this Category are similar to those in Category 2, being the average range from 8% to 11% for the positive uncertainties, and -20% to -2%. The positive uncertainties are majority in percentage over to the negative ones due to the lower presence of out of range cases, or flag1 pixels. In the case studies with cloud openings, the radiance uncertainties reach their maximum in the radiation enhancement areas, as can be seen in Figure 4.16 and Figure 4.17, with the (positive) errors in radiance overpassing 30%. On the other hand, we still find in Category 3 huge errors due to out of range values of radiance, with values as -96% (Figure 4.21), -66% (Figure 4.19) and -43% (Figure 4.20). These uncertainties in Radiance translate in average values of positive COD uncertainties ranging from 1 to 3, and negative COD uncertainties ranging from -0.2 to -0.1. The maximum uncertainty of COD associated to these case studies is 12.2 in Figure 4.19 and 17.6 in Figure 4.21.

The AERONET zenith values are lower than 20, while the obtained values by the retrieval are 7 to 23 units higher. This makes that in Category 3 our retrieval overestimates the Cloud Optical Depth by 16.3 units on average.

Finally, in Category 4, we classify the unsatisfactory cases by a systematic underestimation of the COD. These cases are characterized by high solar zenith angles (over 58°) and a significant presence of flag1 pixels.

The first example introduced is Figure 4.22, that belongs to an overcast image taken on the 25th September at 8:09h, when the solar zenith angle was very high (65°). The clouds are generally dark except for some lighter spots with radiance over $100 \text{ mW/m}^2 \cdot \text{sr}$, which are labeled with the lower flags (flag1 and flag2, a 3% and a 17% of the domain, respectively). These pixels have according to the retrieval very small COD, including the sample measured by AERONET. With it, the comparison with AERONET is 7.6 ± 0.5 (retrieval) vs 23 ± 4 (AERONET), that is, ~ 15 units lower. Anyhow, in neighboring pixels the retrieval provides similar values to the one

4. Results

provided by AERONET. Given the very high solar zenith angle the sides of clouds with multiple reflections get radiances which fall out of range by up to 40%.

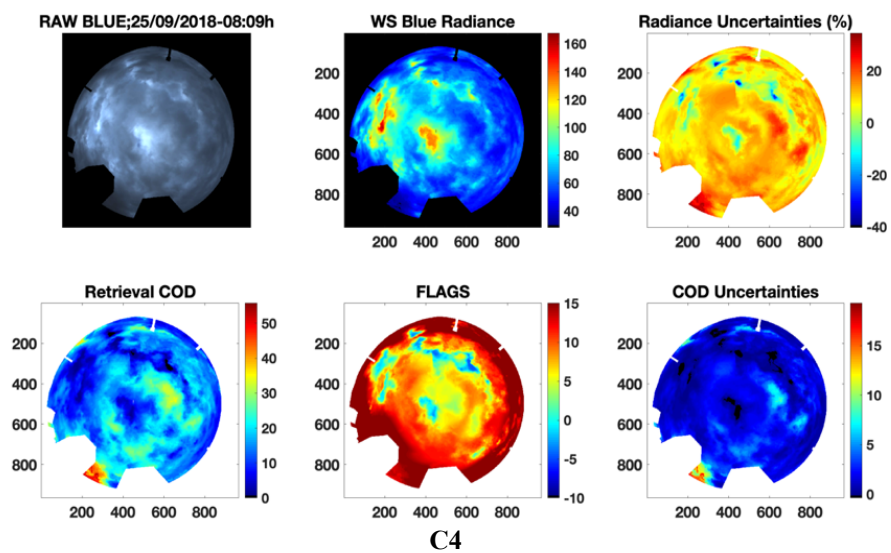


**Figure 4.22 : Retrieval Results ($sza=65^\circ$). Zenith COD: 7.6 ± 0.5
AERONET COD: 23 ± 4**

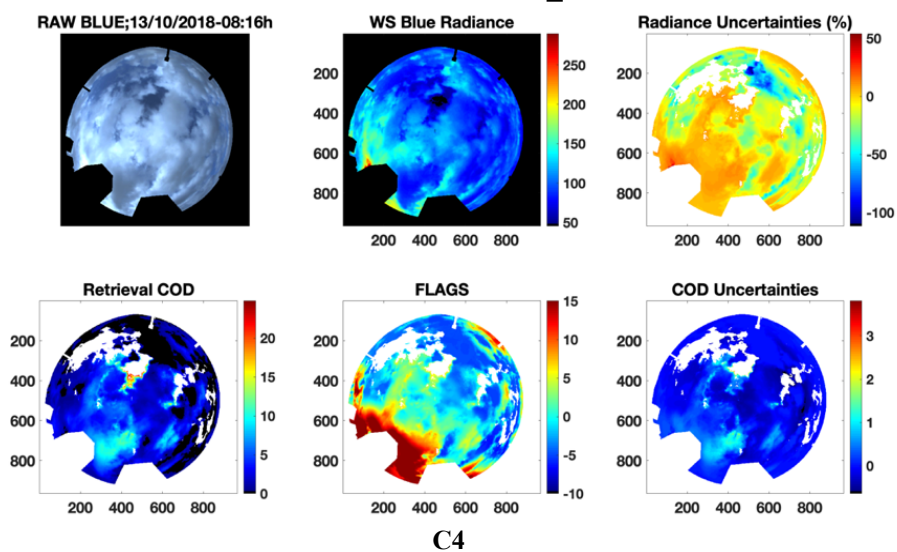


**Figure 4.23 : Retrieval Results ($sza=67.9^\circ$). Zenith COD: 3.1 ± 0.4
AERONET COD: 11 ± 2**

On the other hand, Figure 4.23 is a clearer example of the COD underestimation by the retrieval. It belongs to an image taken on the 13th October at 8:16h, with a solar zenith angle even higher than in the example of Figure 4.23. It is clearly a broken clouds field, with a cloud coverage of 89% of the domain. As seen in previous examples, the broken clouds are often scenarios of multiple scattering and reflections in the cloud sides, making a significant number of pixels to reach values out of the radiance scale. Specifically, 51% of the pixels are labeled as flag1, and a 30% as flag2. Consequently, an important part of the image, the labeled with flag1 have radiances from 30 to 60% out of range, with only few points reaching 100% and more, and the COD is set to 0 by the retrieval. On the other hand, the pixels labeled with flag2 get values from 0 to 5 in most of the image. These flag2 pixels have in reality values very close to 0, which indicate an important contribution of negative flags and therefore out of range radiances (see FLAGS matrix and Section 3.1.2). To end, we remark the small section of overestimated COD in cloud edges, with values up to 20, that can also occur in Category 4 with very high solar zenith angles.

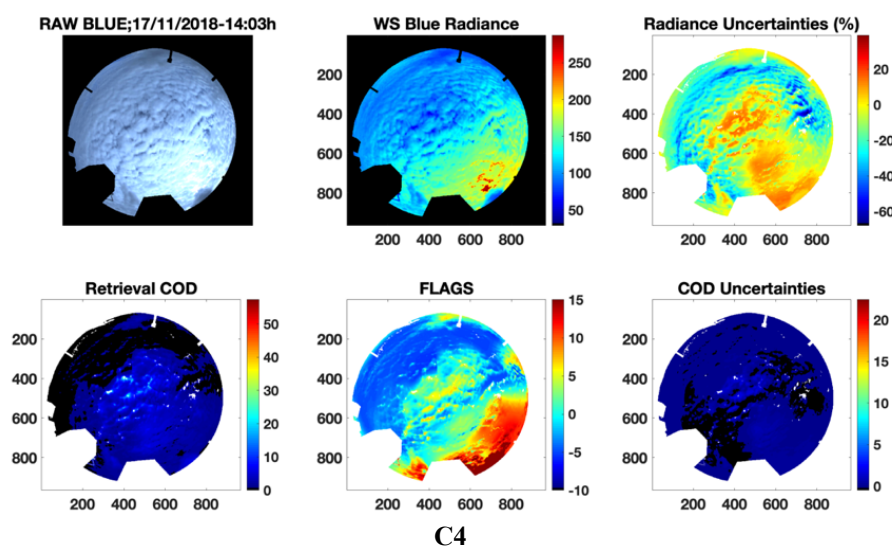
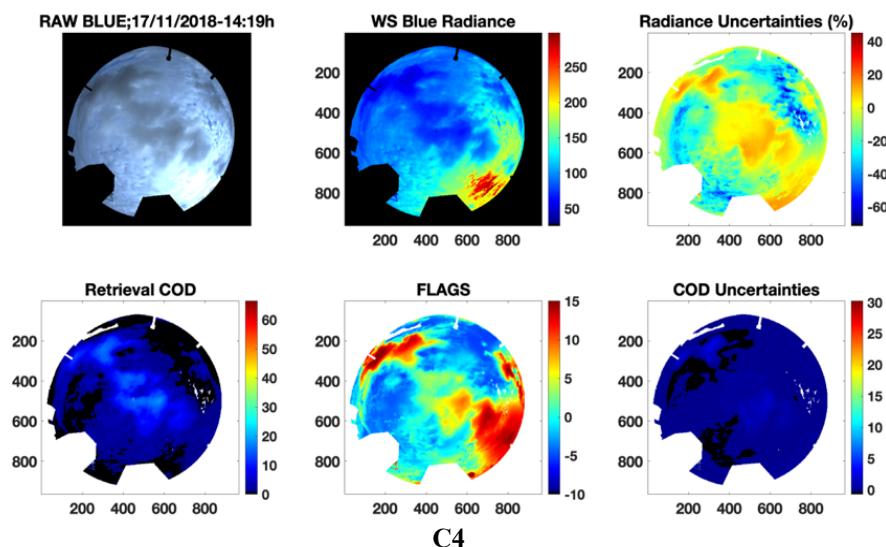


**Figure 4.24 : Retrieval Results ($sza=66.7^\circ$). Zenith COD: 7 ± 1
AERONET COD: 21 ± 4**

Figure 4.24 shows an example with similar flags occurrences to the example of Figure 4.23, with a 55% of the domain labeled as flag1 and a 29% labeled as flag2. The cloud field looks like cirrocumulus, with a more uniform structure than the

4. Results

broken cloud field from the Figure 4.23. Nevertheless, the flags distribution is somewhat similar, with flag4 (9%) pixels gathering around the sun position, followed by flag3 (8%) which also have some patches in the small clear sky gaps characteristic of this type of clouds. Flag1 pixels in Figure 4.24 are located in the higher scattering angles as in Figure 4.23, and flag2 pixels are located below, affecting to the central area of the figure, where the AERONET measurement is done. Thus, the comparison with AERONET's Cloud Mode value gives a value nearly three times the COD obtained with the Sky Camera (37 vs 13.3). We find again the highest uncertainties in absolute value associated with flag1 pixels, with radiances more than 60% over the simulated values.



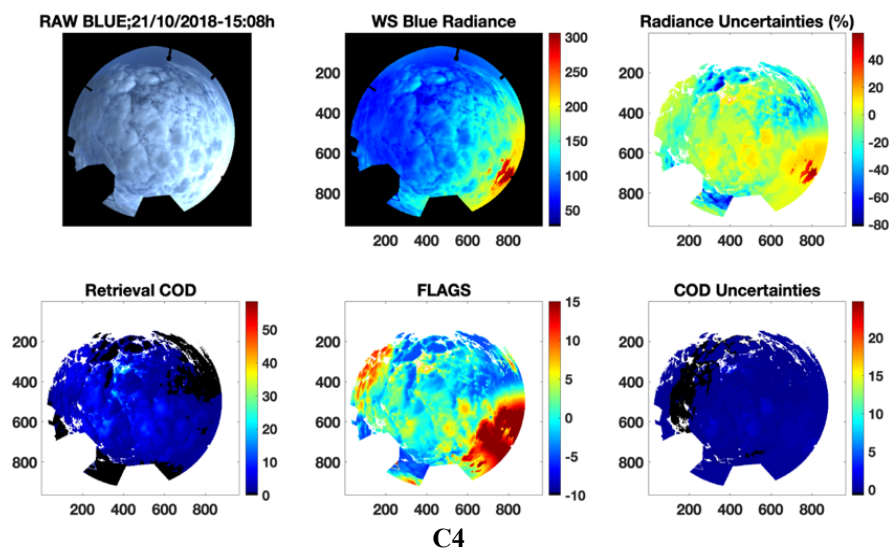
**Figure 4.25 : Retrieval Results ($sza=68.5^\circ$). Zenith COD: 13.3 ± 0.4
AERONET COD: 37 ± 7**

Figure 4.25 belongs to an image taken by the sky camera on the 17th November at 14:19h, only 16 minutes after the image of Figure 4.24, and with very similar solar zenith angle, close to 70° . Therefore, the cloud field is very similar, with the exception of the appearance of thicker clouds in the center of the image. According to AERONET these thicker clouds have a COD of around 37 (± 7) in the sample measured in the center of the domain, whereas the retrieval has obtained a value of 13.3, around 24 units lower. This indicates that the retrieval trends to underestimate COD when the solar zenith angle is high, regardless more or less of cloud type and

thickness. The distribution of flags would be the same as in Figure 4.24, except for the new thicker area along the diameter of the camera. These darker pixels are labeled as flag4 (13% in total) in the north east where the clouds are the darkest (radiance until below $50 \text{ mW/m}^2 \cdot \text{sr}$ and retrieved COD of around 10 to 15) and with flag2 occupying most of the thick clouds' extension, including the center of the domain. Flag3 pixels are mostly accumulated close to the center of the image and over one of the thickest clouds.

Next, we introduce in Figure 4.26 an image taken on the 21st October at 15:08h. It seems to be a field of altocumulus, which makes this example a little less uniform than the cases of Figure 4.24 and Figure 4.25. The original image presents a gap of clear sky on the northern part of the domain, making the cloud cover an 88%. The nature of the cloud field also adds some cloudless sky patches inside the cloudiness, the most important of them being well defined by the CS mask configuration but some others not. Most of the FLAGS matrix is occupied by flag1 and flag2, with a percentage of 42% and 39% respectively, due to the high solar zenith angle (68.7°) and the geometry of the cloud. Consequently, the cloud optical depth gets underestimated in 6 units with respect to the value provided by AERONET (6.0 ± 0.1 vs 12 ± 2). The cloudless sky reflectance reach values of radiance of 125-135 $\text{mW/m}^2 \cdot \text{sr}$, which supposes out of range radiance values up to 70-80% over the simulated radiances with the 1D approach. With these out of range radiances that are due to reflections from cloud sides and horizontal transport, the same percentage of flag1 is retrieved as 0 or close to 0 Cloud Optical Depth, whereas in other sides of clouds the retrieved COD barely reaches a value of 10.

4. Results



**Figure 4.26 : Retrieval Results ($sza=68.7^\circ$). Zenith COD: 6.00 ± 0.15 ;
AERONET COD: 12 ± 2**

And to end we introduce the cases of Figure 4.27 and Figure 4.28. They belong to two images taken on the 27th December with a time lapse of 26 minutes, at 9:50h and at 10:16h, respectively. Thus, the cloud fields are very similar among them, of altocumulus type. The field of Figure 4.28 seems to be more uniform than the one of Figure 4.27, but in neither of the two a clear sky mask has been obtained. This necessarily leads to an overestimation of optical thickness in the small patches of clear sky and in cloud borders (with values over 20), as can be seen more clearly in the COD retrieval of Figure 4.27 and to a lesser extent in Figure 4.28.

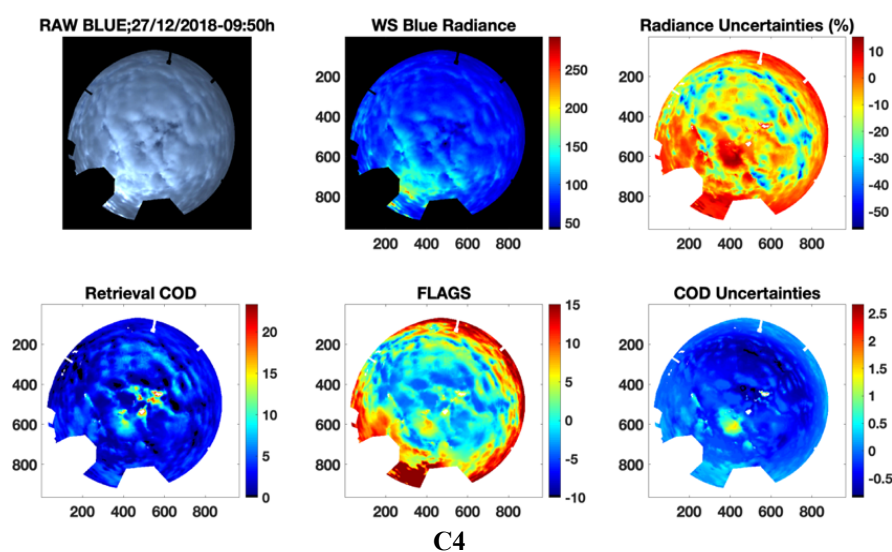


**Figure 4.27 : Retrieval Results ($sza=69.9^\circ$). Zenith COD: 2.5 ± 0.2 ;
AERONET COD: 7 ± 1**

The most representative in both Figure 4.27 and Figure 4.28 is the multiple reflections on the cloud sides facing the sun, which leads again to out of range radiance values in the pixels labeled with flag 1, with measured radiances overpassing the simulated radiances up to $\sim 50\%$. In the case of Figure 4.27, given the geometry of the field and the solar zenith angle of $\sim 70^\circ$ the flag1 pixels relate to the most illuminated cloud sides, where the retrieved COD is 0 or close to 0. This leads to the underestimation with respect to AERONET although not as dramatically as in the previous cases (2.5 ± 0.2 and 7 ± 1). In Figure 4.28 the underestimation is also of 4.5 units of COD, being the two values obtained with the camera and AERONET slightly higher than in Figure 4.27 (3.2 ± 0.4 and 8 ± 1). The distribution of flags in Figure 4.28 is more similar to Figure 4.23 and Figure 4.24, and positive radiance uncertainties are more predominant due to the camera calibration (as a function of digital counts) than the negative uncertainties due to out of range pixels.

4. Results

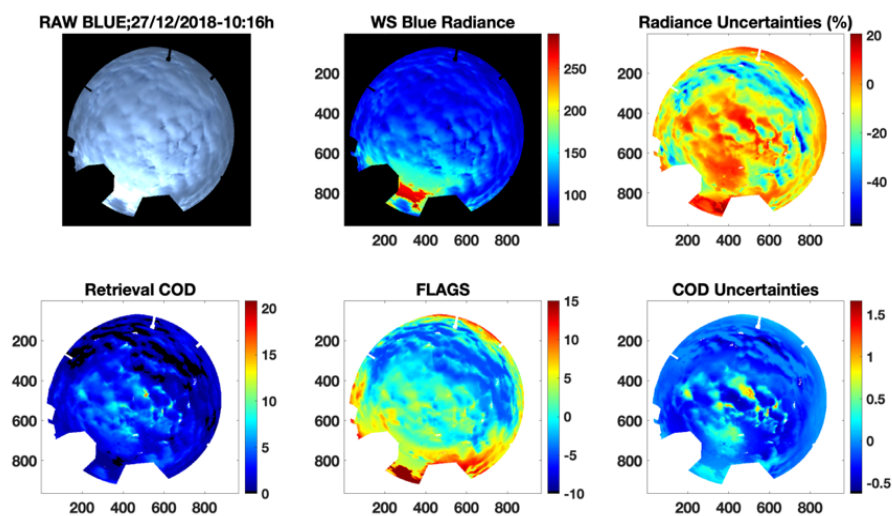


**Figure 4.28 : Retrieval Results ($sza=67.5^\circ$). Zenith COD: 3.2 ± 0.4
AERONET COD: 8 ± 1**

To sum up and finish this analysis of the results obtained with the camera, we first summarise the observed values and percentages of the flags. In Category 4 lower flags have predominance over the others, as shown in Figure 4.23, with flag1 presence over 50%. Anyhow, the presence of the other flag types is also important, with flag2 up to 48%, flag 3 up to 29% and flag 4 up to 52%, as we can see in Figure 4.22.

With these flags' percentages the areas with wide uncertainties increase, especially those affected by flag1. Therefore, in Category 4 the uncertainties are mostly negative with values reaching up to -112% in the case of Figure 4.23. This one, along with Figure 4.24 and Figure 4.25 show the largest areas with negative radiance uncertainties. In Figure 4.24 and Figure 4.25, cases 16 minutes apart, over 70% of the sky dome has negative uncertainties, and the areas corresponding to flag1 have an average of radiance uncertainty of $\sim -20\%$. Regarding the COD uncertainties, the average positive values range from 0.2 to 2, and the average negative values range from -0.3 to -0.1.

The correct COD values in zenith according to the AERONET database range from 7 to 37, whereas the obtained values by the retrieval are 4 to 24 units lower, with an average underestimation of 10.3 units. In the Category 4 can be found cases with

partial cloud coverage, like Figure 4.23 and Figure 4.26. There are also cases with small clear sky gaps that the algorithm erroneously considers cloudy, and therefore the Cloud Optical Depth gets dramatically overestimated, as can be seen in Figure 4.27 and Figure 4.28, and Figure 4.13 from Category 2.

From everything seen in this section, we can draw a series of conclusions and questions to answer throughout this dissertation.

The very good comparison with AERONET presented in Chapter 3 does not occur in each case of the analyzed database. This indicated us that the algorithm has some deficiencies both in zenith and in other viewing geometries where the 1D approximation is incomplete, or perhaps due to flaws in the methodology itself.

After the classification of results in categories and the pertinent analysis, first of all, we can state, as seen in Category 1 and Category 2, that the algorithm can work reasonably well under certain conditions, namely thick clouds and full coverage in the entire range of solar zenith angle. The COD in Category 1 has been obtained mostly with an ordinary inversion procedure. We have uncertainties of around 15% almost entirely due to the sky camera calibration, but also because of some too low radiances for the τ range considered. On the other hand, the average uncertainties due to radiance enhancement are a -3%, but in a negligible number of pixels (less than 0.1%).

The algorithm also works fine with more modest COD values and coverages, but only at some *sza* values. In those cases, we find, on a one hand, an average uncertainty of 9% due to the camera calibration and on the other hand, -13% due to radiation enhancement, for a range of solar zenith angles of 50.6° to 70°.

However, we have seen that the algorithm is not reliable or insufficient mainly due to two problems: ambivalence and the 1D approximation. Category 3 is due to ambivalence of COD for a given value of radiance, which cannot be unequivocally solved. The cases in Category 3 feature mostly thin clouds ($\tau = 0 - 20$). As we discussed in Section 3.1.2. the methodology takes the higher value of COD of the two possibilities in order to overcome the ambivalence. This implies that lower optical thicknesses are usually overestimated. The flags identify these situations in Category 3 with flag values found in zenith up to 6-8. On the other hand, the uncertainties found on average are of 9% due to the camera calibration and of -10% due to out of range values of radiance that we also find in Category 3. Unfortunately, we find cases belonging to Category 3 in the whole range of solar zenith angle. Little

4. Results

can be done with the current approximation, except quantifying the error. We leave the resolution of ambivalence to future work with more advanced instruments, that allow us to generate a dual channel ratio or index of radiances whose dependence on τ is one-to-one, as it is usually done in the bibliography. For instance, Marshak (2004) obtained COD from transmitted radiance at 673nm and 870nm, while Chiu et al., 2010 did the same but with the AERONET wavelengths of 440nm and 870nm, and Mejia et al., 2016 developed the Radiance Red-Blue Ratio. With an index similar to those applied to our methodology it is hoped that the Category 3 of results can be incorporated into the reliable ones.

Because of 1D approximation we have the pixels with lower flag values, that is, flag1 and flag2 with little influence of ambivalence. Category 4 possesses majority of these flag values occurrences, and is characterized by very high solar zenith angle values (over 65°) and underestimation of a considerably range of COD values (up to ~40 in zenith according to AERONET products). The reasons are mainly due to the 3D radiative effects non-contemplated in the Independent Pixel Approximation. Category 4 is composed mostly by measurements of broken cloud fields at high solar zenith angles, situations that are especially sensitive to 3D radiative effects (Benner and Evans, 2001). High solar zenith angles favor the side illumination, increasing the number of situations with radiance enhancement in the cloud borders that appear more illuminated from the ground (Hogan and Shonk, 2013; Nuñez et al., 2016). The multiple reflections in cloud edges is only possible with horizontal transport, that is not contemplated by the 1D approach. Therefore, the algorithm interprets the extra brightness by smaller COD than it should be. The uncertainties of the retrieval in Category 4 are on average of 6% due to the camera calibration, and of -15% due to out of range values of radiance, as expected given the high percentages of flag1 and flag2 in Category 4. We believe that those pixels with flag1 and flag2 up to certain point can be improved once we take a step beyond the 1D approach. That can be done by integrating the differences between the plane-parallel model and the 3D model in our results using parameterizations.

Therefore, we propose the Synthetic Study specified in Section 3.2, that uses 3D RT simulations to extract patterns or trends in the differences with the 1D approach that could be profitable to improve the present troublesome results.

4.2. Synthetic 3D Evaluation of Methodology and Results

To overcome the issues detected in the COD retrieval (Section 4.1), 3D radiative transfer simulations are carried out with several types of cloud fields, varying the COD, cloud cover and solar zenith angles. Chapter 3 exposes the cloud fields employed, named CF7 to CF10, and each of them constitute a case study. A Rad_sX is obtained being X the solar zenith angle of the simulation. Next the 5 sets of COD_sX and F_sX are obtained with the retrieval algorithm for each solar zenith angle and for each CFN case study. The objective of this entire Section 4.2 is to compare the COD_sX matrices with the real COD matrices of the LES fields (Figure 3.34) that were employed in the simulations. With this, we intend to quantify the error made regarding to the cloud cover and solar zenith angle. As far as possible we will also calculate the underestimation committed by the 1D approximation.

In the Annex the matrices of Rad_sX , COD_sX and F_sX can be found, for each CFN case study (CF7 to CF10). The clear sky mask is painted in white color to distinguish from the true retrieval results. The graphics and Tables that we present below are derived from the treatment and analysis applied over the COD_sX matrices in the Figure A 2, Figure A 5, Figure A 8 and Figure A 11, as explained in the methodology in Sections 3.2.3 and 3.2.4 respectively.

4.2.1. Comparison with LES fields

First, we present the comparison of our COD retrieval using the 1D approach (as in Section 4.1) results with the real optical thickness of the LES fields, that is constant for every solar zenith angle (see the description of the Figure 3.34 obtention in Chapter 3). We make the comparison for each CFN, in order to analyze the differences mainly induced by cloud cover.

Therefore, Figures such as Figure 4.29 and Figure 4.30 illustrate this comparison, made at each case study of the LES COD versus our retrieved COD, at a certain solar zenith angle. As it is explained in Section 3.2.3, the values in the graph correspond to average τ at a given distance to clear sky (Δ) (see Figure 3.38, Figure 3.39 and the example in Figure 3.40 in Section 3.2.3). In order to perform better the comparison and infer easier the quality of the results, the line 1:1 is represented as well.

4. Results

In the case of Figure 4.29 and Figure 4.30 we show the best and the worst result of the comparison regarding to the CF7. Table 4.2 shows the parameters of all the fit lines of the results matrices (COD_sX) corresponding to the CF7, also displayed in the Figure 4.29 and Figure 4.30, as well as the r^2 factors, that range from 0.61 to 0.71. In Figure 4.29 and Figure 4.30 we can also find the corresponding r^2 factors, of 0.67 and 0.61 respectively. The fit lines have been obtained in a weighted fit by number of points. In Table 4.2 we can see that at all COD_sX we have underestimation of COD, and that the slope of the graph of the case at 17° is the smallest of them all. Nevertheless, such slope of 2.4 supposes a general underestimation of the COD_s17 (Figure A 2) with respect to the ‘real COD’ (Figure 3.34a) of 260%. On the other hand, the underestimation observed at the COD_s57 matrix (Figure A 2) is extremely large, up to 400%.

We attribute this behavior to the 3D radiative effects given the partial cloud coverage. CF7 is a cluster of shallow cumulus clouds with a cloud cover of 0.69, full of vertical and horizontal inhomogeneities. A cloud field of these characteristics is the most sensitive to the 3D radiative effects (Stocker et al., 2013, Hogan and Shonk, 2013, Barker et al., 1996). The 3D radiative effects influence the albedo of the cloud field, producing enhanced transmittance to the ground in all the solar zenith angles considered. In high solar zenith angles side leakage predominates, as photons strike the cloud borders and hit the grounds in the surroundings (see Figure 1.11b). For mid solar zenith angles the side leakage increases, as the geometry of the broken clouds favors the multiple reflections in the cloud sides and an intense forward scattering is produced towards the ground. This results in radiances reaching higher values than in the simulations, and therefore the retrieved COD is obtained lower than it should be. The radiative smoothing (Marshak et al., 1995) might also influence, as photons are allowed to diffuse from optically thick regions to optically thin regions.

This might cause radiance transportation to side columns and pixels and increasing their illumination. Finally, at high solar zenith angles there is found the highest COD underestimation, which might be caused by reflected light from the cloud underside (Mejia et al., 2016), increasing one already high brightness.

On the other hand, when we look at the Figure 4.29 and Figure 4.30 the first thing that catches the eye is the ‘tail’ formed by the points corresponding to the smaller distances to clear sky, approximately until 0.2km (Figure 4.29). This tail is systematic in all the COD_sX, matrices except those corresponding to the CF10.

This ‘tail’ is due to the COD overestimation at cloud edges. In Figure A 2 and in the example in Figure 4.31 of the COD_s17 can be seen that the edges of the clouds and the nearby pixels present anomalous values of up to $\tau \sim 20$. We find that the overestimation is more evident and important the larger the cloud edge area is, or, equivalently, the smaller is the cloud cover of the LES field. The furthest are the pixels from the limit between cloud and clear sky, the τ adapt more to the general trend of the fit line, as we can see in Figure 4.29, Figure 4.30 and the foregoing Figures of COD comparisons.

The last points in the graphs in Figure 4.29 and Figure 4.30 correspond to a $\Delta = 0.6 - 0.7$ km, at the end of the domain. The τ values at those distances reach a limit value of 23-24 approximately. Such value differs of the equivalent ones in the LES field, which vary with Δ . Nevertheless, the points on average follow the same of the fit line.

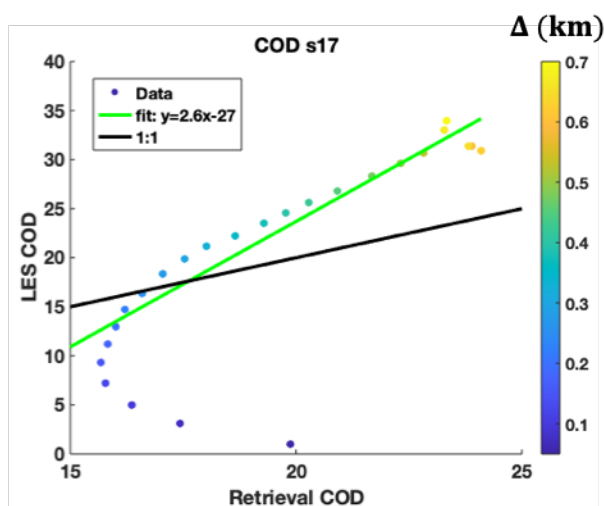


Figure 4.29 : LES COD vs retrieval COD for CF7 case study at $sza = 17^\circ$; $r^2 = 0.67$

4. Results

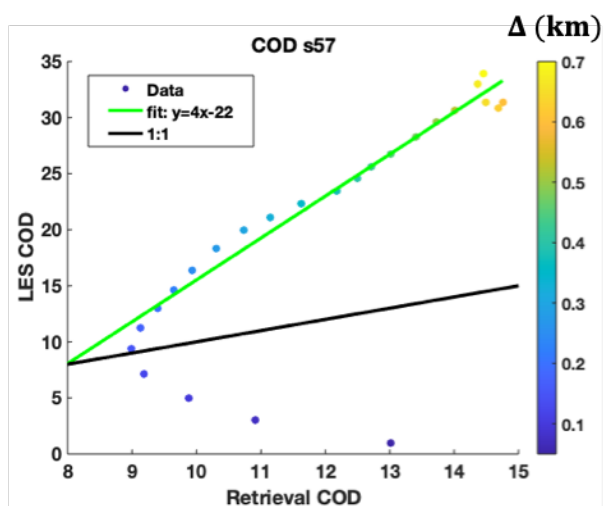


Figure 4.30 : LES COD vs retrieval COD for CF7 case study at $sza = 57^\circ$; $r^2=0.61$

Table 4.2 : Fit lines parameters of the case studies sX for CF7

Case	slope	error	v. intercept	error	r^2 factor
S17	2.6	0.5	-27	9	0.67
S30	2.8	0.4	-26	7	0.71
S42	3.7	0.5	-34	7	0.71
S53	3.3	0.5	-21	6	0.64
S57	4	1	-22	7	0.61

On the other hand, the Figure 4.32(up) illustrates all the average values of COD versus Δ , for each COD $_sX$ of the CF7, and the corresponding values of the LES field. We see in this graph first of all that all the COD $_sX$ follow the same trend of COD overestimation in the pixels at the cloud edges, and COD underestimation once $\Delta = 0.125\text{km} - 0.225\text{km}$ is exceeded.

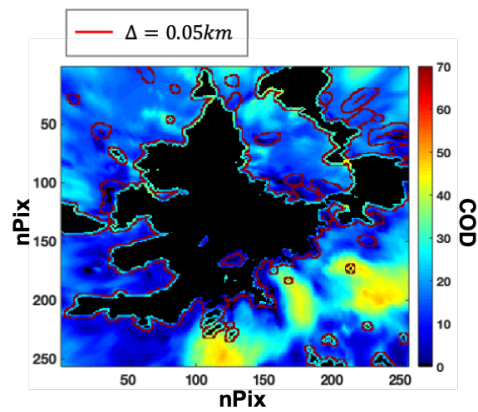


Figure 4.31 : COD_s17 for CF7. Pixels at distance to clear sky (Δ) of 0.05km in red

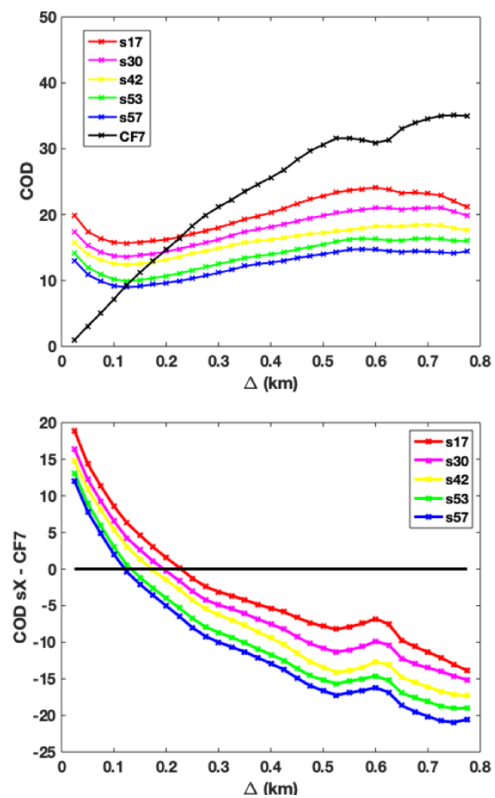


Figure 4.32 : (up) LES COD of CF7 and retrieval COD vs Δ , (down) difference between retrieval COD and LES COD vs Δ .

4. Results

Figure 4.32 (down) shows in turn the differences (σ) between the COD_sX values and the CF7 COD values. Also, Table 4.4 presents a summary of extreme values (maximum, minimum) and average of σ , to an overall description of Figure 4.32(down). As it was already stated in Figure 4.29 and Figure 4.30, as well as the Table 4.2, that the less deviated graph to the CF7 one is the corresponding COD_s17, whereas the most deviated one is the COD_s57 one, regarding to the points of the domain furthest from the clear sky. That makes that the retrieval works worst for this particular cloud field with increasing solar zenith angle. We can see in Table 4.4 that the maximum deviation in absolute value is of 19 for the COD_s17 and 20.6 for the COD_s57, being the former due to overestimation and the latter due to underestimation. The column in Table 4.4 of the average and median σ indicates that underestimation is the most important effect in the domain, for all CFN, being of -3 for COD_s17 and of -11 for COD_s57, with intermediate values for the rest of sX cases. On the other hand, Table 4.3 shows the RMSE (eq. (3.20) Section 3.1.1) derived from the differences in Figure 4.32(down). The magnitude that represents this RMSE is COD, with its units. As Table 4.3 and Figure 4.29 and Figure 4.30 show, the biggest error is committed in the COD_s57 case, of 12.3 units of COD, while the smallest is of 7.9 in the COD_s17 case, with intermediate values for the other sX cases.

Table 4.3 : Root Mean Square Error of CF7 vs COD_sX comparison. COD units

Case	RMSE (COD)
S17	7.90
S30	8.67
S42	9.91
S53	11.22
S57	12.27

Table 4.4 : Extreme and average σ between CF7 LES and retrieval COD

Case	σ MAX	σ MIN	$max \sigma $	$min \sigma $	$\bar{\sigma}$ mean	$\bar{\sigma}$ median
S17	18.89	-13.88	18.89	0.19	-2.97	-5.35
S30	16.37	-15.16	16.37	0.28	-5.21	-7.52
S42	14.73	-17.34	17.34	0.16	-7.16	-9.41
S53	13.12	-18.99	18.99	0.56	-9.28	-11.68
S57	12.02	-20.57	20.57	0.38	-10.66	-12.92

The values of RMSE in Table 4.3 can be interpreted as the average retrieval error at each solar zenith angle considered, due to the non-contemplated 3D radiative effects but also by the flaws in the methodology. As we can figure out from Table 4.3 values of errors of 8 to 12 over the smallest COD (which are the most affected) imply the largest errors of the domain.

Once we move to analyze the results of CF8, we can see in Figure 4.33 and Figure 4.34 and Table 4.5 that the comparison improves with respect to the cases of CF7, with the r^2 factors ranging from 0.79 (COD_s57) to 0.82 (COD_s17, COD_s30) for the scatters, respectively. Nevertheless, the results are also underestimated with respect to the truth at large distances from the sky gaps. We believe that the reasons are mostly similar to those given in the CF7, as the CF8 has also partial cloud coverage. The results might be better because of the less extent of cloud sides than in CF7, making the 3D effects less effective, and also because the effective cloud fraction might change with the solar zenith angle, offering a wider cloud area than it truly is, with a higher albedo (see Figure 1.11a).

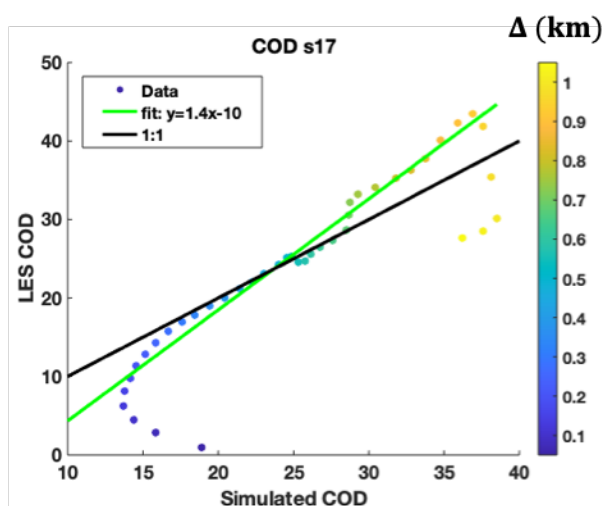


Figure 4.33 : LES COD vs retrieval COD for CF8 case study at $sza = 17^\circ$; $r^2=0.82$

4. Results

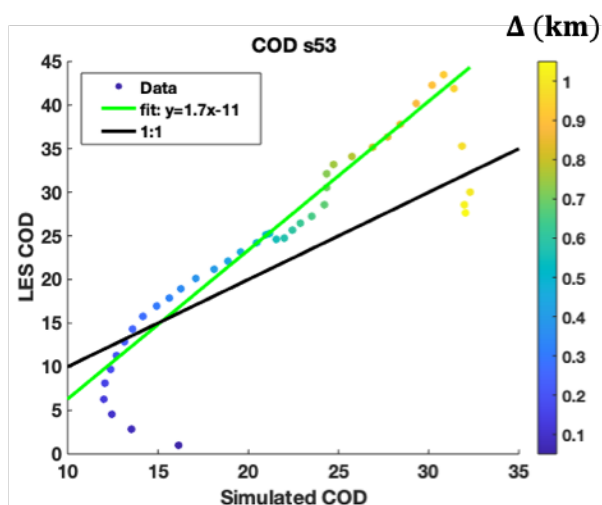


Figure 4.34 : LES COD vs retrieval COD for CF8 case study at $sza = 53^\circ$; $r^2=0.79$

Table 4.5 : Fit lines parameters of the case studies sX for CF8

Case	slope	error	v. intercept	error	r^2 factor
S17	1.4	0.1	-10	2	0.82
S30	1.4	0.1	-11	3	0.82
S42	1.6	0.1	-13	2	0.80
S53	1.7	0.1	-11	3	0.80
S57	1.6	0.1	-7	3	0.79

In Figure 4.33 and Figure 4.34 we also observe anomalous points that deviate from the general trend. As we formerly said, the overestimation of the COD at the cloud edges is systematic and is also present in CF8 results (see Figure A 5). Figure 4.35 shows again the COD comparisons and differences (σ) vs Δ . Figure 4.35 (down) illustrates that the difference between COD_sX and LES COD due to overestimation is around 18 for COD_s17 to COD_s42, but in the COD_sX matrices of higher sza (53° and 57°) is ~ 15 or less (Table 4.6). On the other hand, the underestimation is up to -6.2 for COD_s30 and -13.5 for the COD_s57, with intermediate values in between as in CF7 case (Table 4.6). The slight reduction of the overestimation, and the better fit lines with the LES COD, are reflected in Table 4.7 of the RMSE, with a maximum value of 6.94 corresponding to COD_s57. The better values of RMSE compared to CF7 might be because of the less extent of cloud sides. This might cause that the

effective cloud area gets wider by overlapping of cloud layers at mid solar zenith angles such as 30° and 42° causing a higher albedo and decreasing the transmittance, as absorption in the visible is small (Kokhanovsky, 2004). In 30° and 42°, is where the algorithm has been observed to work better for CF8 (Table 4.6)

Table 4.6 : Extreme and average σ between CF8 LES and retrieval COD

Case	σ MAX	σ MIN	$max \sigma $	$min \sigma $	$\bar{\sigma}$ mean	$\bar{\sigma}$ median
S17	17.95	-6.58	17.95	0.12	1.28	0.36
S30	18.24	-6.18	18.24	0.22	1.74	1.10
S42	17.75	-8.33	17.75	0.04	0.63	-0.08
S53	15.21	-12.63	15.21	0.29	-2.53	-3.21
S57	13.94	-13.49	13.94	0.10	-3.52	-4.28

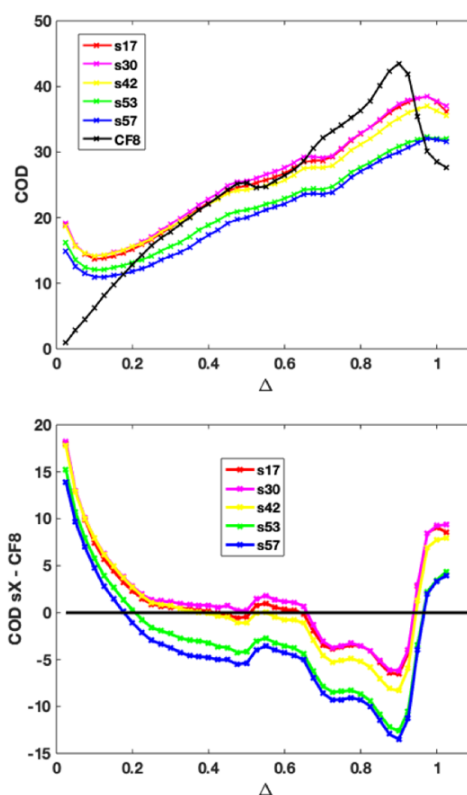


Figure 4.35 : (up) LES COD of CF8 and retrieval COD vs Δ , (down) difference between retrieval COD and LES COD vs Δ .

4. Results

On the other hand, the points that appear at a Δ beyond 0.85km descend in the graph until they reach the line 1:1 in Figure 4.33 and Figure 4.34. This is because a difference between Figure 3.38 and Figure 3.39, illustrated in Figure 4.36. The distances and the areas in the domain correspond quite well between Figure 3.38, corresponding to the LES CF8 and Figure 3.39 corresponding to the retrievals (COD_sX) of CF8, except in the area marked in red in Figure 4.36. That area at distances less than 0.85km is underestimated by all the COD_sX matrices, as shows the comparison of COD values versus Δ in Figure 4.35 (up). Nevertheless, as we can see in the squared area in red, due to the same miscalculations of the small COD's in our retrievals, the Δ of the marked area is bigger at the COD_sX matrices, rather than in the truth. As for the corresponding points, at distances beyond 0.85 km we are averaging the COD values at the squared area and in the upper right area in the retrievals, whereas the averaging in the CF8 field is done only in the upper right area.

Curiously, due to the limited good results of the algorithm in the CF8 sX cases, if the area in the red square is ignored, the retrieval rate will be closer to the regression line, when according to the general trend they should continue to be as disparate as the points at Δ less than 0.85km.

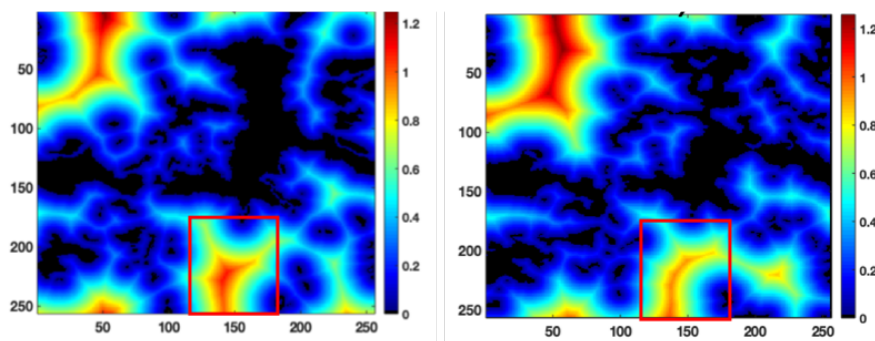


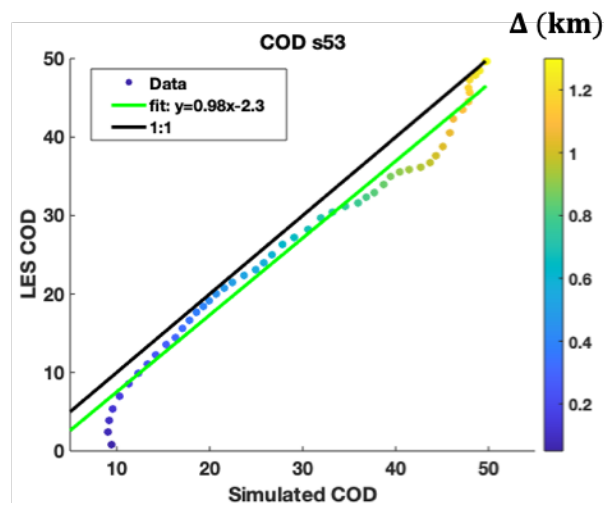
Figure 4.36 : Problem area (red square) in Δ matrix for the sX retrievals (left) and CF8 field (right)

In any case, we can see observing the Table 4.7 of RMSE and Table 4.6 that on average the highest difference between retrieval and the truth is of around -4, and that, while overestimation predominates at lower zenith angles (until $\text{sza} = 42^\circ$), underestimation influences more at higher angles (Figure 4.35 down).

Table 4.7 : Root Mean Square Error of CF8 vs COD_sX comparison. COD units

Case	RMSE (COD)
S17	5.41
S30	5.53
S42	5.70
S53	6.53
S57	6.94

Regarding to the results obtained for the CF9 case study, we can see in Table 4.8 that the variation of the solar zenith angle doesn't change the results much, and all the slopes are between 0.91 and 1, while the r^2 factors are 0.97 and 0.98. We can consider COD_s30, COD_s42 and COD_s53 as the best results. The comparison with COD_s53 is depicted in Figure 4.37, and the one with COD_s17 in Figure 4.38, with r^2 factor of 0.98 and 0.97, respectively.

**Figure 4.37 : LES COD vs retrieval COD for CF9 case study at $sza = 53^\circ$; $r^2=0.98$**

4. Results

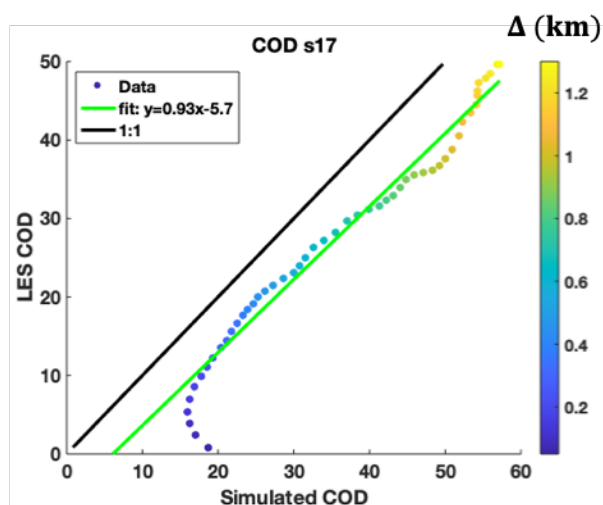


Figure 4.38 : LES COD vs retrieval COD for CF9 case study at $sza = 17^\circ$; $r^2=0.97$

From Figure 4.37, Figure 4.38 and Table 4.8 we can deduce that the COD_sX of CF9 are closer to the truth in comparison to the CF7 and CF8 cases. This seems logical as CF9 as well as CF10 offer less opportunities for horizontal transport than CF7 and CF8. The trend is very good for much of the DCS section, except for the cloud edges, as demonstrated by the square correlation coefficient of 0.97-0.98. Works by Chambers et al., 1997 and Zuidema and Evans, 1998 found the IPA accurate enough for stratocumulus clouds because the IPA albedo was close enough to the simulated one with Monte-Carlo and Landsat-derived models. The fit lines are closer to the 1:1 relationship, which vary between 0.91 to 1. Nevertheless, we observe a general overestimation in all the COD_sX, being more evident in s17, s30 and s42, as show the RMSE in Table 4.9 and the column of σ MAX in Table 4.10. The value of RMSE of 9.1 associated to s17 is due to what we can see in Figure 4.38 and Figure 4.39, that the τ values obtained in the COD_s17 are the highest of all the retrievals and greater than the τ values of CF9, producing the overestimation of 7% that appears in the S17 slope in Table 4.8. Such overestimation is attributed mostly to an enhanced albedo at low solar zenith angles, given that the cloud field is thick enough to reflect much radiation backwards and diminishing the transmittance to lower layers of the atmosphere and eventually to the ground. With it the behavior of the RMSE reduces from 9 to 4 as solar zenith angle increases. The radiative smoothing might also be preventing radiance to reach the ground by diffusing photons from the thicker to the thinner regions of the field. Given this behavior of τ in all the domain of COD_sX,

the overestimation produced at the pixels of the cloud edges (with maximum values of 18 in COD_s17 to 11 in COD_s42) does not deviate much from the general trend, as we can see in Table 4.10 and Figure 4.39 (up), also because of the high cloud cover. All this behavior translates in positive average differences of 8.6 in COD_s17 and 3 in COD_s53.

Table 4.8 : Fit parameters of the case studies sX for CF9

Case	slope	error	v. intercept	error	r ² factor
S17	0.93	0.04	-6	2	0.97
S30	0.98	0.04	-5	2	0.97
S42	0.997	0.047	-5	2	0.98
S53	0.98	0.04	-2	1	0.98
S57	0.91	0.04	-0.2	1.4	0.98

Table 4.9 : Root Mean Square Error of CF9 vs COD_sX comparison

Case	RMSE (COD)
S17	9.08
S30	6.21
S42	5.39
S53	3.66
S57	4.10

Table 4.10 : Extreme and average values of the differences between CF9 LES and retrieval COD

Case	σ MAX	σ MIN	$max \sigma $	$min \sigma $	$\bar{\sigma}$ mean	$\bar{\sigma}$ median
S17	17.80	5.31	17.80	5.31	8.61	7.88
S30	13.63	2.75	13.63	2.75	5.69	4.88
S42	11.41	1.90	11.41	1.90	4.88	4.34
S53	8.59	0.08	8.59	0.08	2.98	2.31
S57	8.01	0.05	8.01	0.05	3.29	2.88

4. Results

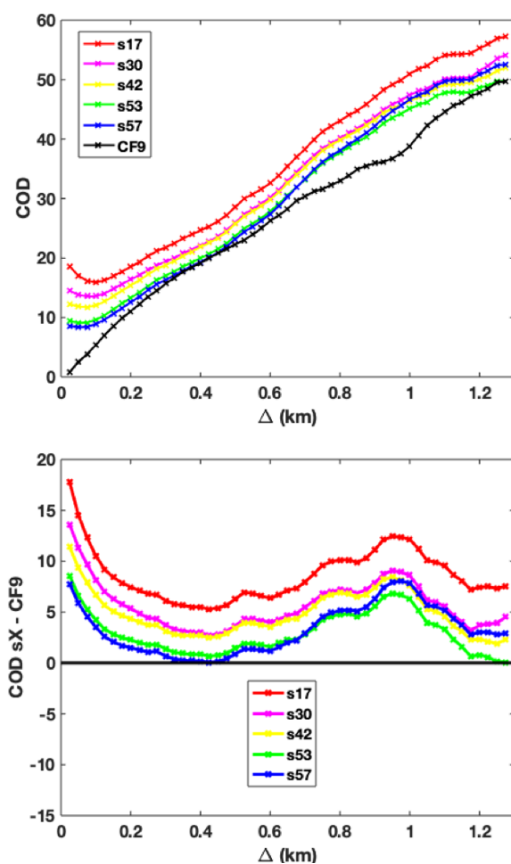


Figure 4.39 : (up) *LES COD of CF9 and retrieval COD vs Δ , (down) difference between retrieval COD and LES COD vs Δ .*

Finally, we show the results of the CF10 case study. In the same way as in CF9 matrices, we can see in Table 4.11 that the fitting lines do not vary much among them. This means that changing the sza does not produce significant differences in the cloud fields such as CF10, with a cloud cover of 99% and an average optical thickness of 42 (Table 3.14).

Anyhow, Figure 4.40 and Figure 4.41 show the best results, given that, matrix COD_{s53} comparison has a vertical intercept of $0.3(\pm 4.2)$, and matrix COD_{s57} has the slope closer to 1, even though the vertical intercept is $3(\pm 4)$. On the other hand, Figure 4.42 shows the case of matrix COD_{s30} which, in the same way as COD_{s17}

has the higher slope of all the case studies (1.2 ± 0.1) and also the highest vertical intercept in absolute value (-4 ± 4).

Table 4.11 : Fit lines parameters of the case studies sX for CF10

Case	slope	error	v. intercept	error	r ² factor
S17	1.2	0.1	-3	4	0.81
S30	1.2	0.1	-4	4	0.81
S42	1.2	0.1	-4	5	0.80
S53	1.1	0.1	0.3	4.2	0.82
S57	0.99	0.08	3	4	0.83

However, the shape of the graphs in Figure 4.40, Figure 4.41 and Figure 4.42 differ from those of the previous case studies. The reasons are mainly two. First of all, we point out that, since the cloud coverage is practically 1, the maximum value of distance to clear sky (or to the smallest optical thicknesses in CF10), increases in CF9, with distances up to 1.3km and in CF10 the maximum value of Δ is 3.55km (see Figure 3.38 and Figure 3.39).

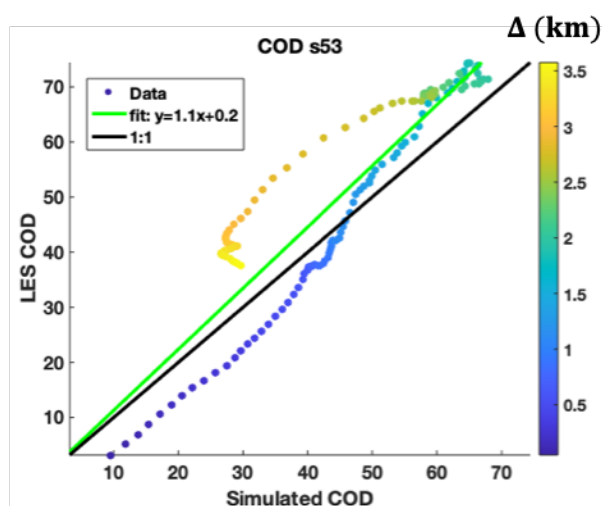


Figure 4.40: LES COD vs retrieval COD for CF10 case study at $sza = 53^\circ$; $r^2=0.82$

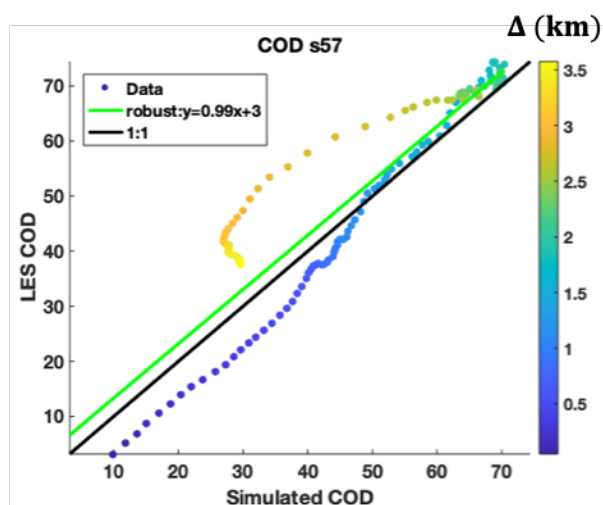


Figure 4.41: LES COD vs retrieval COD for CF10 case study at $sza = 57^\circ$; $r^2=0.83$

In addition, the ‘tail’ that we observed at CF7, CF8 and CF9 cases no longer exists because we do not have cloud edges as such, but a few pixels with low COD values (see Figure 3.38, Figure 3.39 at Chapter 3 and A11 at Annex).

Second, we can distinguish two differentiated branches with different trends in Figure 4.40 to Figure 4.43, and that is the main reason why the r^2 factors are 0.80-0.83 (Table 4.11). Generally, a slight overestimation is produced in the COD_sX results in a similar way that was seen at CF9 case study, maybe because of an enhanced albedo as the CF10 is optically and geometrically way bigger than the CF7-CF9. This overestimation reduces as Δ increases until a value of around 1.2km. Then, the τ of the retrieval and the CF10 get as similar as possible for some Δ positions, especially in the COD_s57 matrix (Figure 4.41). Next, the τ of CF10 begins to increase with respect to the equivalent values in the COD_sX matrices, forming the ‘knot’ of points at the top of the graphs, at $\Delta = 1.6\text{km}$ to 2.3km . From this point on, this difference between the retrievals’ COD and the CF10 COD remains more or less constant, although both values decrease in the areas corresponding to $\Delta \sim 2.3\text{km}$ to $\sim 3.55\text{km}$.

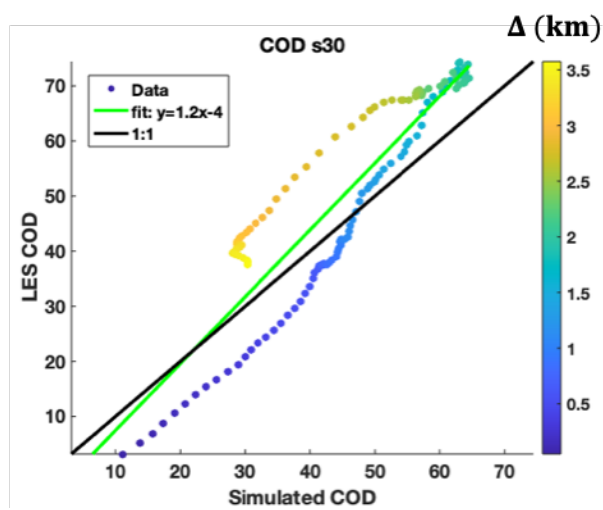


Figure 4.42 :LES COD vs retrieval COD for CF10 case study at $sza = 30^\circ; r^2 = 0.81$

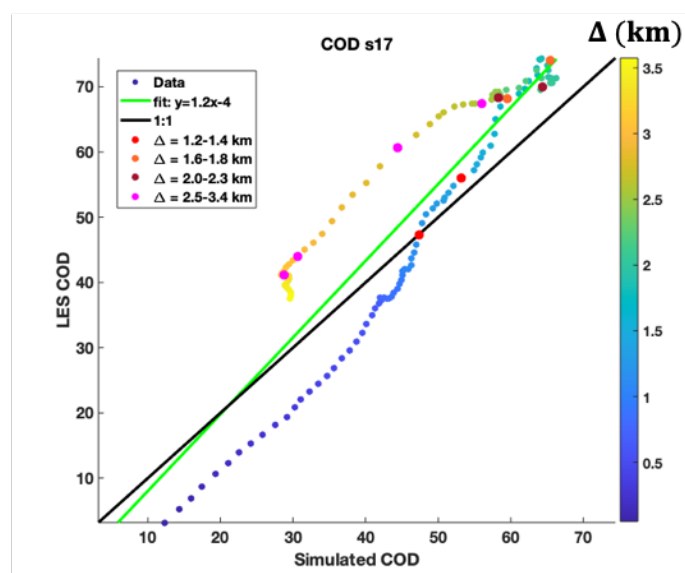


Figure 4.43 : COD comparison for case study s17, and illustrative marked points $r^2 = 0.81$

4. Results

The reason for this behavior is that the retrieval overestimates τ at CF10 case studies in the same way as CF9 ones, but there is a significant number of points that get underestimated, because the simulations of radiance to build the LUT did not exceed $\tau = 150$. This means that for values greater than $\tau = 150$ the algorithm has to extrapolate, and there are errors in estimating the maximum of $\tau = 230$ in CF10 (Figure 3.34 and Figure 4.44 to Figure 4.46). Overall the fit lines get a little worse than in CF9, as well as the RMSE (8 to 11° (42°)), as the underestimated area of the image ($\tau \sim 230$) is considerable.

We analyze now more carefully the COD_sX and the evolution of the τ with Δ . The dots marked in red color in Figure 4.43, are the average of the pixels shown in Figure 4.44, at distance $\Delta = 1.2$ km (up) and $\Delta = 1.4$ km, in the COD_sX matrices (left) and CF10 matrix (right).

The points in red in Figure 4.43 are not so far from the 1:1 line because the average in CF10 matrix do not pass over the maximum of COD, making the difference not so drastic.

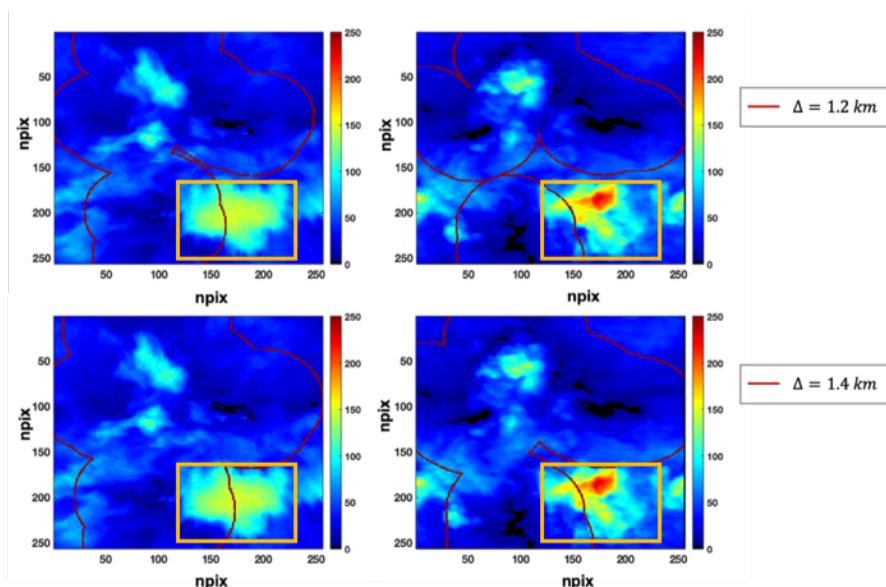


Figure 4.44 : COD_s17 matrices (left column) and CF10 matrix (right column), pixels at a distance to clear sky of 1.2km (up) and 1.4km (down), and squared troublesome area

Such difference between retrieval and the truth increases as the averaged pixels include CODs that should overpass 200 in the COD_sX matrices but they do not, as Figure 4.45 illustrates. All the points in the 'knot' in the superior part of the graphs in Figure 4.40 to Figure 4.43 have a situation alike the Figure 4.45. They are represented in Figure 4.43 with the orange and brown points, belonging to a Δ range of 1.6-1.8 km and 2.0-2.3 km, respectively.

Table 4.12 : Extreme and average values of the differences between CF10 LES and retrieval COD

Case	σ MAX	σ MIN	$max \sigma $	$min \sigma $	$\bar{\sigma}$ mean	$\bar{\sigma}$ median
S17	9.80	-16.21	16.21	0.19	-4.22	-7.17
S30	9.49	-16.79	16.79	0.13	-4.81	-7.55
S42	9.01	-18.51	18.51	0.31	-6.15	-9.16
S53	8.03	-18.92	18.92	0.08	-5.08	-6.64
S57	7.97	-19.42	19.42	0.26	-3.01	-1.83

Pixels at $\Delta \sim 2.3$ km to 2.5 km get progressively away from the area of higher COD in CF10. The averaged pixels gather around the lower right corner. In that area the difference between the COD_sX values and the CF10 values remains constant, probably due to the relatively few pixels that contribute to the average, and both averaged COD decrease as Δ increases.

Table 4.13 : Root Mean Square Error of CF10 vs COD_sX comparison

Case	RMSE (COD)
S17	9.26
S30	9.63
S42	10.68
S53	9.39
S57	8.16

4. Results

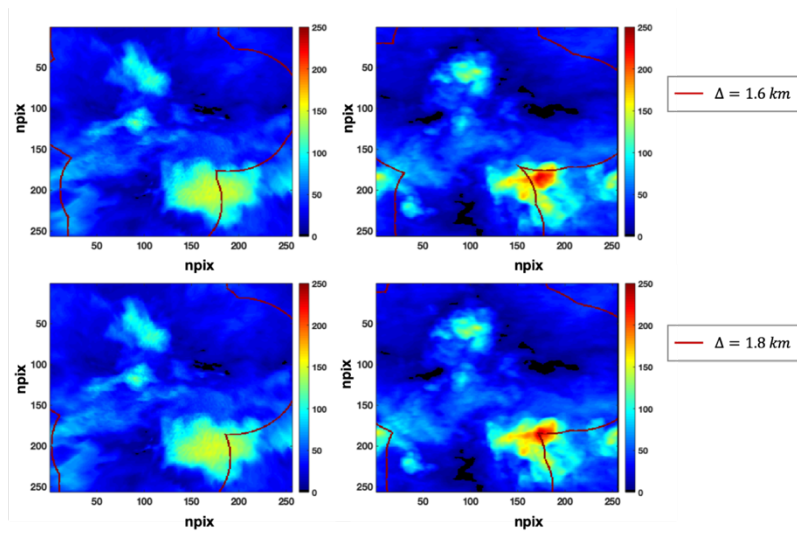


Figure 4.45 : COD_s17 matrices (left column) and CF10 matrix (right column), pixels at a distance to clear sky of 1.6km (up) and 1.8km (down)

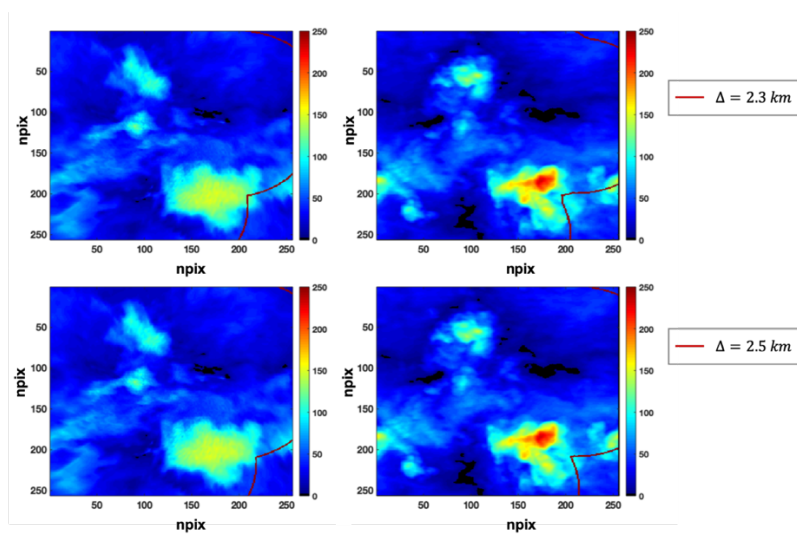


Figure 4.46 : COD_s17 matrices (left column) and CF10 matrix (right column), pixels at a distance to clear sky of 2.3km (up) and 2.5km (down)

With it, we can see in Figure 4.47 all the COD_sX values and the CF10 (up) ones, and the differences between retrieval and the truth (down), versus Δ . As it was previously stated, the change in sza is not significant, as all the graphs behave in a similar way until a value of Δ of $\sim 1.2\text{km}$ is reached. These graphs are all over the corresponding values of CF10, with a maximum difference of 9.8 for the COD_s17 matrix and 8 for the COD_s57 matrix (Figure 4.47 down and Table 4.12). The overestimation is minor with higher solar zenith angles, and decreases until a difference of ~ 0 (Table 4.12, $\min|\sigma|$ column) as overestimation becomes underestimation of higher τ values. We can see that the latter behavior affects to most of the pixels in these case studies, which is reflected in the fit lines and the RMSE values in Table 4.13, up to 10.7 in the COD_s42 case. Generally, the matrix COD_s57 is the most accurate with respect to CF10 (Figure 4.47 and Table 4.13), until $\Delta = 2.5\text{ km}$ is overpassed. Then, the underestimation at COD_s57 is the maximum of all the results, reaching a value of -19.4 (Table 4.12).

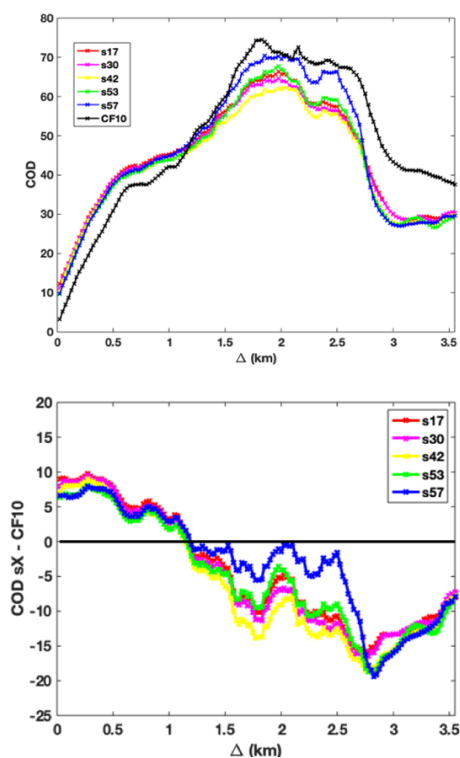


Figure 4.47 : (up) LES COD of CF10 and retrieval COD vs Δ , (down) difference between retrieval COD and LES COD vs Δ .

4. Results

To sum up, we show in Figure 4.48 all the comparisons between the COD_sX and the CFN, separated by angles. Given the results provided, we can draw some conclusions about how the algorithm and the methodology work. It can be derived from Figure 4.48 that the algorithm works well for cloud fields similar to CF8 and CF9, depending on certain conditions. On the other hand, the algorithm fails to obtain the COD of cloud fields with partial cloud coverage, such as CF7, underestimating it at all solar zenith angles. With very thick cloud fields as CF10 our algorithm generally overestimates all ranges of COD except those values higher than $\tau = 150$, as seen in the corresponding analysis.

Also, ambivalence influences highly the results obtained close to cloud edges with low values of COD, being all them systematically overestimated, the higher the overestimation the lower is the cloud coverage. CF8 and CF9 are ‘intermediate’ types of cloud fields, nor full broken clouds nor thick stratocumulus, and the error of underestimation in CF8 diminishes at angles of 17° to 42°. The results obtained at CF9 are the best of all the intercomparison study, in matter of fit lines and correlation coefficient, though certain overestimation of up to 9% is evident.

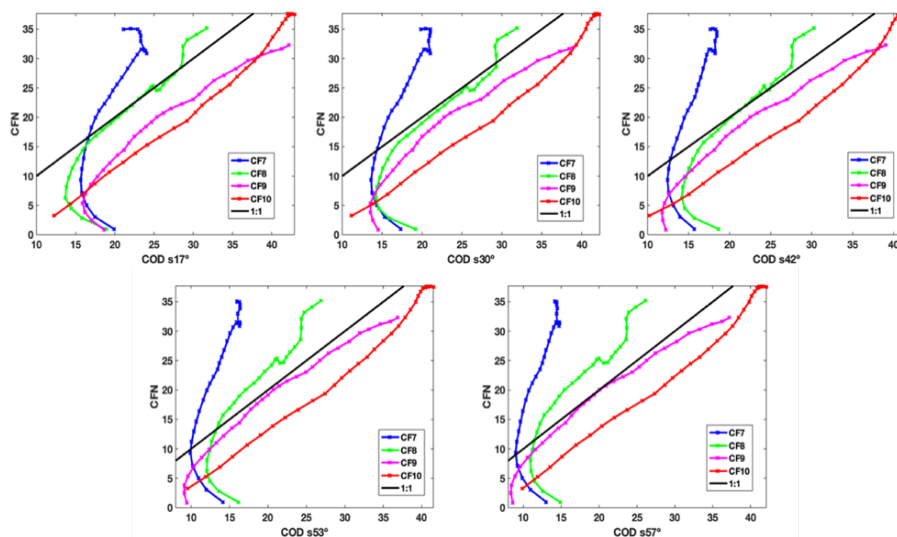


Figure 4.48 : Full comparison of all the retrieval COD with the corresponding CFN COD

4.2.2. Intercomparison of results

Considering the results obtained in the previous section 4.1, and the circumstances seen in which the algorithm works successfully or not, we wonder if it is possible to extract any parameterization of the errors that have occurred. Since we have seen in Section 4.1. a systematic underestimation of the COD at high solar zenith angles, we are inclined to believe that apart from the algorithm's own limitations of ambivalence, we might also be encountering errors derived from 3D effects, to which certain cloud fields are more sensitive than others.

Therefore, in the Section 4.2.2. we want to analyze the results from the perspective of the flags considering the solar zenith angle, by means of the COD_sX matrices intercomparison. The reason for this approach is the high presence of flag1 and flag2 in the Category 4 of results in Section 4.1. In the present Section we analyze more in deep which pixels of the results matrices are under certain Flags and why, since unlike Section 4.2.1 we do not take averages so as not to lose valuable information.

With the incoming analysis we also study more closely the overestimation of optical thickness at the cloud edges, and we try to come up with a more adjusted value of the error derived from ambivalence.

First, we must decide among all the possible combinations which ones we take and for what purpose. We decide to make the intercomparisons with the COD_s17 matrices as a reference for all the CFN. On a one hand, for CF7 and CF8, we saw in Table 4.2 and Table 4.5 respectively, that the COD matrices that are closer to the LES COD are obtained with the solar zenith angle 17° . On the other hand, regarding to the more uniform cloud fields (CF9 and CF10), although the COD_sX matrices do not differ so much from each other with the change in *sza* (Table 4.8, Table 4.11), we do observe that the best results are obtained for intermediate and high zenith angles, especially in the cases of CF10. Even so, given that the main objective of this Section is to parameterize the effect associated to the lowest flags, we choose as reference for CF9 and CF10 the result matrices with the lowest percentage of flag1 and flag2, compared to the other COD_sX matrices. We show this information in Table 4.14 to Table 4.17, with the percentages of the four flags types in all the COD_sX matrices for each CFN. These tables are in turn obtained from Figure A 3, Figure A 6, Figure A 9 and Figure A 12 in the Annex. With it, Table 4.14 to Table

4. Results

4.17 and Figure A 9 and Figure A 12 themselves, show that the COD_s17 matrices have a minimum percentage of flag1 and flag2 in total.

Table 4.14 : Flags percentages at each COD_sX of CF7

Flags type	Flags percentage (%)				
	COD_s17	COD_s30	COD_s42	COD_s53	COD_s57
flag 1	0.8	2.3	8.6	20.7	20.7
flag 2	18.4	21.2	22.6	27.3	26.1
flag 3	77.1	63.4	49.3	27.2	27.5
flag 4	3.7	13.1	19.4	24.8	25.7

Table 4.15 : Flags percentages at each COD_sX of CF8

Flags type	Flags percentage (%)				
	COD_s17	COD_s30	COD_s42	COD_s53	COD_s57
flag 1	1.5	1.6	5.0	12.5	13.2
flag 2	15.3	18.2	17.3	20.5	19.0
flag 3	76.3	66.4	58.0	37.3	33.7
flag 4	6.9	13.8	19.6	29.7	34.0

Table 4.16 : Flags percentages at each COD_sX of CF9

Flags type	Flags percentage (%)				
	COD_s17	COD_s30	COD_s42	COD_s53	COD_s57
flag 1	0.7	1.1	2.6	6.1	6.8
flag 2	7.8	9.8	10.5	12.0	10.6
flag 3	85.8	74.3	58.9	40.3	38.5
flag 4	5.6	14.7	28.0	41.6	44.1

Table 4.17 : Flags percentages at each COD_sX of CF10

Flags type	Flags percentage (%)				
	COD_s17	COD_s30	COD_s42	COD_s53	COD_s57
flag 1	0.1	0.02	0.3	0.7	1.1
flag 2	2.8	4.6	3.2	6.2	4.3
flag 3	65.1	52.7	54.2	32.9	28.4
flag 4	32.0	42.6	42.3	60.2	66.3

Thus, for a categorization of the COD results in addition to the results showed in Table 4.2, Table 4.5, Table 4.8 and Table 4.11, we represent the COD_{sX} against the reference (COD_{s17}) to observe how different the results of the same variable are, with respect to the reference. At a first glance at Figure 4.49 to Figure 4.52 it is clear that the retrieval for broken clouds is much more sensitive to the change in solar position than in the more uniform fields. We can also see that the spread of points of the intercomparison of COD_{s57} vs COD_{s17} is logically greater than in the COD_{s30} vs COD_{s17} intercomparison, given the solar zenith angles discrepancy (57° vs 17° and 30° vs 17°). Such spread is maximum in the CF7 case study (Figure 4.49), and reduces with the increase in cloud cover, that is, in the CF8-CF10 case studies, as we can also see in Table 4.18 of the scatters' RMSE.

On the other hand, Figure 4.49 to Figure 4.52 verify what we could already observe in Section 3.2.1: the COD values tend to decrease with increasing zenith angle, and this happens at CF7, CF8 and CF9 cases study. However, this behavior is not observed in the CF10 case study, where the influence of *sza* is minimal and the average of τ values in the COD matrices remains stable (Table 4.19). The CF10 scatter plots fit very well to a slope close to 1 and are practically invariable as the solar zenith angle changes.

In Figure 4.49 to Figure 4.51 the graphs of COD_{s57} vs COD_{s17} show the loss of linearity with the increase of *sza*, especially at lower cloud fractions. Such loss of linearity is derived from the errors of the algorithm associated to ambivalence, but also from 3D effects not contemplated in the plane-parallel approach. Figure 4.49 (right) especially shows, on a one hand, a range of $\tau = 0 - \sim 35$ of COD_{s57} versus a range of $\tau = 0 - 5$ in COD_{s17}. That is because of the ambivalence effects seen in Category 3 in Section 4.1, that caused overestimation of τ to a maximum of 23 units higher, and 16.3 on average. Also Figure 4.49 (right) shows a similar range of $\tau = 0 - \sim 35$ but in COD_{s17} for the smallest COD_{s57} values. This effect is directly caused by the underestimation of τ when out of range radiances occur. Figure 4.49 is an intercomparison of results at 17° and 57° belonging to CF7, a broken cloud field. On it the retrieval behaves very different for larger solar zenith angles than for the smaller ones. When the *sza* increases, also increase radiance enhancement by the intense forward scattering, which implies an underestimation of COD by the plane-parallel approximation. When the sun is high the effect is of overestimation. This is because out of range radiances are not achieved, and we are in the range most affected by ambivalence, which means overestimation of small COD values.

4. Results

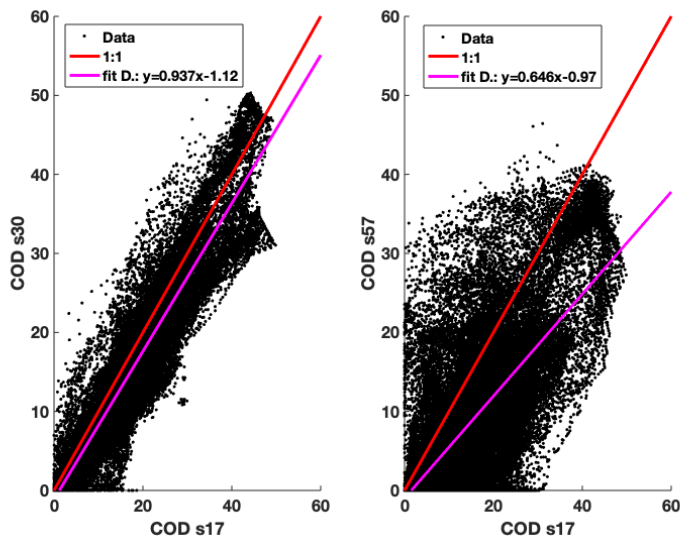


Figure 4.49 : COD_sX vs COD_s17 intercomparisons, of COD_s30 (left, $r^2=0.84$) and COD_s57 (right, $r^2=0.40$) from CF7 case study.

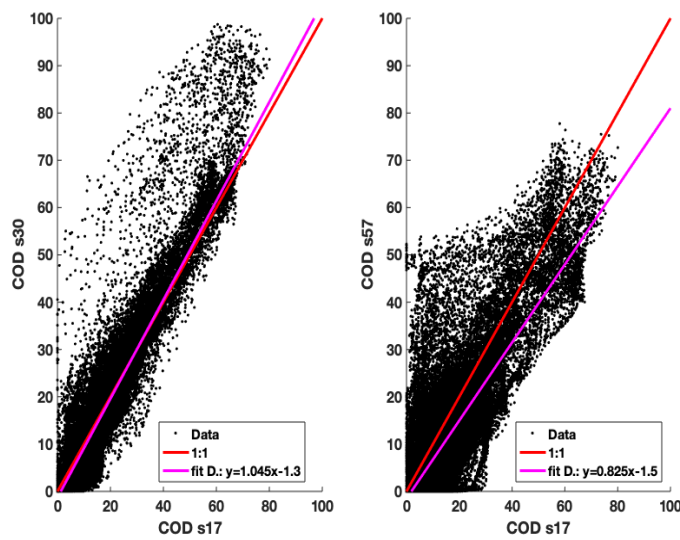


Figure 4.50 : COD_sX vs COD_s17 intercomparisons, of COD_s30 (left, $r^2=0.86$) and COD_s57 (right, $r^2=0.61$) from CF8 case study.

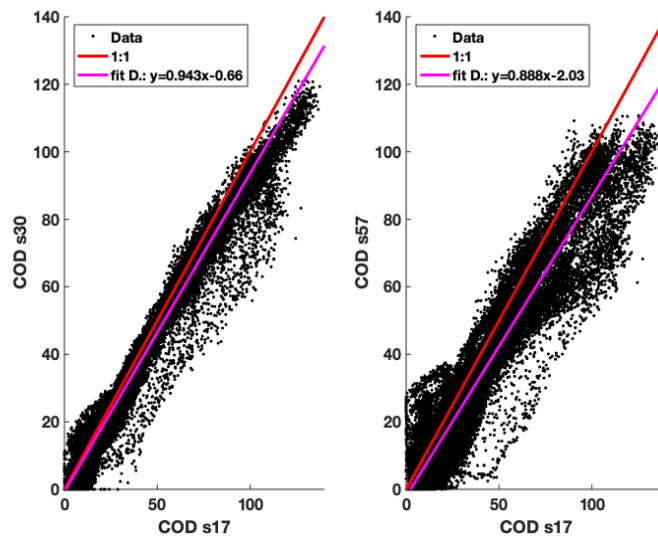


Figure 4.51 : COD_{sX} vs COD_{s17} intercomparisons, of COD_{s30} (left, $r^2=0.97$) and COD_{s57} (right, $r^2=0.89$) from CF9 case study

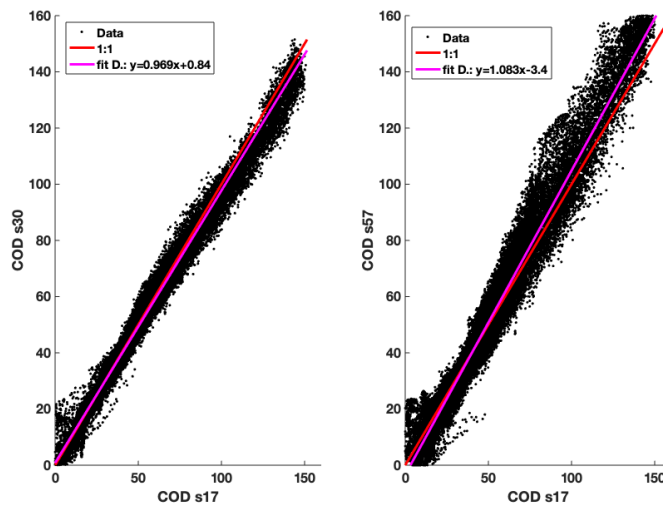


Figure 4.52 : COD_{sX} vs COD_{s17} intercomparisons, of COD_{s30} (left, $r^2=0.99$) and COD_{s57} (right, $r^2=0.97$) from CF10 case study

4. Results

Table 4.18 : RMSE values of the intercomparisons in Figure 4.49 to Figure 4.52

CFN	Intercomparison RMSE (COD)	
	s30 vs s17	s57 vs s17
CF7	4.5	10.7
CF8	5.8	9.4
CF9	5.3	9.7
CF10	3.3	6.1

Next, we represent superimposed to the scatter plots the pixels belonging to flag1 and flag2 in different color, in search of a particular trend associated to the solar zenith angle. We do this in sight of the next behaviors with the increment of SZA:

- Increasing deformation of the scatter plots,
- Decreasing value of $\bar{\tau}$,
- Increasing percentage of flag1 and flag2.

In the same graph we represent the fit line of the pixels affected by certain flag, the fit line of the whole domain and the line 1:1, for a qualitative and a quantitative analysis.

Table 4.19 : Average τ of each COD_sX and CFN (with the standard deviation)

Cloud Field	$\bar{\tau}$ (std)			
	CF7	CF8	CF9	CF10
CFN (LES)	16 (17)	16 (18)	24 (26)	42 (33)
COD_s17	19 (10)	20 (13)	30 (24)	43 (28)
COD_s30	16 (10)	20 (15)	27 (22)	43 (27)
COD_s42	15 (10)	19 (15)	26 (21)	42 (27)
COD_s53	13 (10)	17 (14)	25 (21)	42 (29)
COD_s57	12 (9)	16 (13)	24 (24)	44 (32)

Indeed, we observe in the next images, from Figure 4.53 to Figure 4.70 a constant trend of τ underestimation in the pixels labeled with flag1 and flag2. If we recall the

definitions of the categories of flags in Chapter 3, the named ‘flag1’ and ‘flag2’ include pixels whose corresponding radiance is out of range, as well as pixels affected by ambivalence. Flag1 pixels are predominantly out of range cases, and flag2 contains predominantly mixed cases, that is, pixels affected both by out of range and ambivalence. The underestimation of COD with respect to the truth COD mainly lies on the management of the out of range radiances. As we indicate in Chapter 3, we have out of range radiances when they are too high for the solar and viewing geometry considered, and there is no COD value that corresponds to such radiance value, and in the $T_{i,j,k,l,m}$ is settled to 0 (see Figure 3.28 description). Mixed cases give a little more margin, since the radiance is indeed out of range, but close enough to the $Radiance = f(\tau)$ function to possibly correspond to small COD values. All this means that the pixels labeled with flag1 and flag2 have very small τ values.

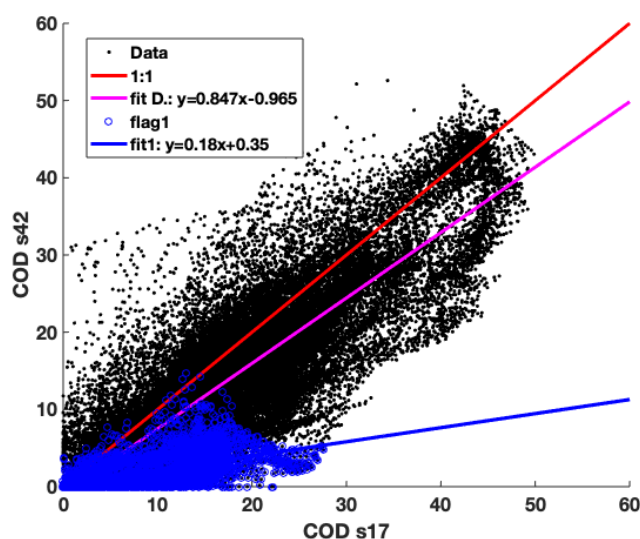


Figure 4.53 : *COD_s42-COD_s17 intercomparison in CF7 case study. Fit line (fit1) of pixels affected by flag1 vs fit line (fit) of the whole domain, and line 1:1.*

For instance, Figure 4.53 shows one of the scatter plots of the CF7 case study. The scatter shows several spreads apart from the general trend, which is $y = 0.847(\pm 0.005)x - 0.96(\pm 0.11)$. Therefore, the r^2 factor is 0.68. The fit line indicates that the τ values in the COD_s42 are $\sim 15\%$ lower than the τ values in the COD_s17 matrix. This underestimation, related to a scatter of points that we will

4. Results

discuss later, cause an overall RMSE ((3.20) in Chapter 3) between the COD_s42 and the COD_s17 of 6.8.

On the other hand, as Figure 4.53 shows, the pixels labeled with flag1 follow a different trend, with a much higher underestimation of τ . The fit line of $y = 0.18(\pm 0.01)x + 0.35(\pm 0.12)$ denotes an underestimation of τ of around 79%. The blue pixels have a higher RMSE, with a value of 10, which implies that the small COD (that is, $\tau = 0 - 15$) cannot be unequivocally obtained in these cloudy conditions with the methodology that we are following.

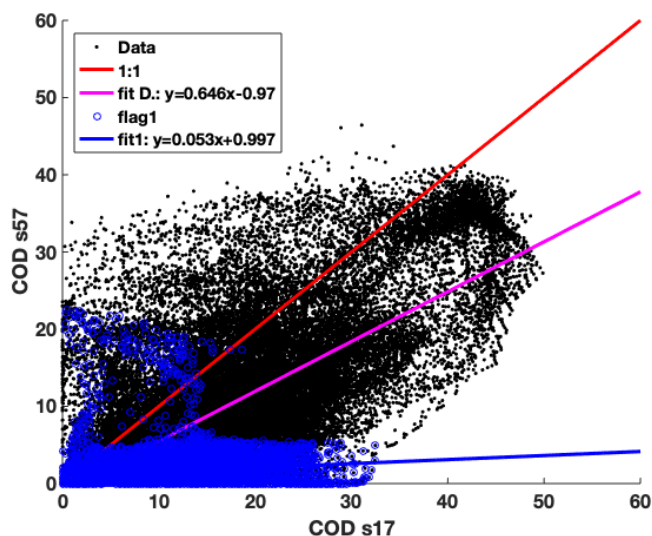


Figure 4.54 : COD_s57-COD_s17 intercomparison in CF7 case study. Fit line (fit1) of pixels affected by flag1 vs fit line (fit) of the whole domain, and line 1:1.

The scatter plot seen in Figure 4.49 (right, $r^2=0.40$), exhibits the highest RMSE of the COD intercomparison, of 10.7 (Table 4.18). From the fit line of $y = 0.65(\pm 0.01)x - 0.97(\pm 0.14)$ (Figure 4.54) we extract that the τ values in the COD_s57 matrix are underestimated approximately by 35%. That is the highest underestimation from the retrieval for a domain. The pixels labeled in flag1 have a RMSE of 12.8 and a fit line of $y = 0.053(\pm 0.006)x + 0.99(\pm 0.09)$. Therefore, the τ in the COD_s57 labeled with flag1 are underestimated on average by 92%.

This value of RMSE of 13 implies that small values of COD up to at least 13 cannot be unequivocally obtained with the methodology followed. On the other hand, the spread of points separated from the bulk of the blue scatter are few compared to the whole and are caused by the way that the algorithm treats the ambivalence.

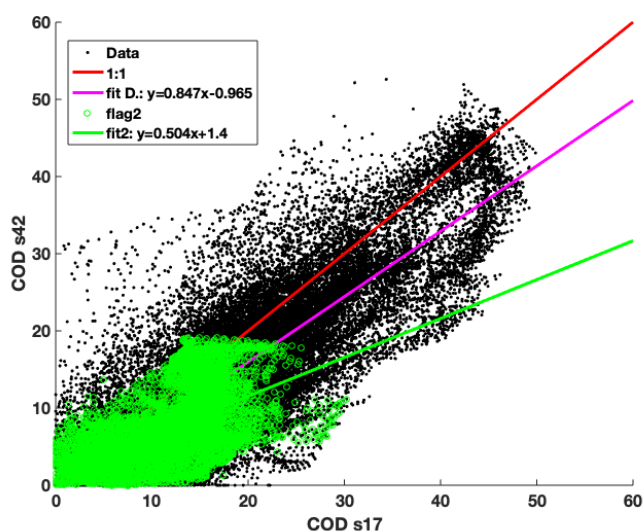


Figure 4.55 : COD_s42-COD_s17 intercomparison in CF7 case study. Fit line (fit2) of pixels affected by flag2 vs fit line (fit) of the whole domain, and line 1:1.

Ambivalence is more present in the pixels labeled with flag2, as can be seen in Figure 4.55 and Figure 4.56, in the higher spread of points and in the vertical intercept of the fit2 lines (1.4 and 3.6, respectively). This comes associated with an RMSE of 6.1 and 10.1, being the latter very similar to the total RMSE of the COD_s57 vs COD_s17 intercomparison. Since pixels labeled with flag2 can also come from out of range cases, we find an underestimation of τ of 41% in Figure 4.55 and 65% in Figure 4.56, derived from both fit2 lines. Of these two values, the most reliable is the one obtained from Figure 4.55, since the fit2 line in Figure 4.56 is too influenced by ambivalence, as shown in the vertical intercept of 3.6 ± 0.2 . The lower underestimation found in flag2 pixels with respect to flag1 might be due to the fact that out of range radiances and ambivalence compensate to some extent with each other.

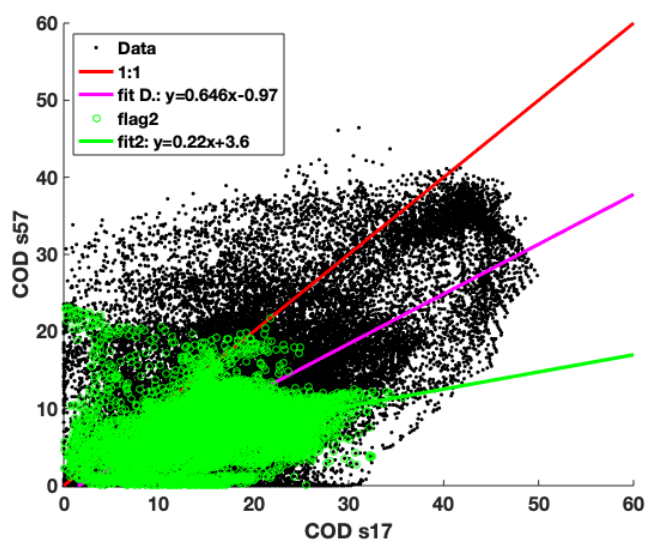


Figure 4.56 : COD_s57-COD_s17 intercomparison in CF7 case study. Fit line (fit2) of pixels affected by flag2 vs fit line (fit) of the whole domain, and line 1:1.

Finally, we see that the pixels with flag3 are difficult to characterize in the CF7 case study, since they only present linear behavior in the comparison of COD_s30 vs COD_s17 (Figure 4.57), where the solar zenith angles are similar enough. In Figure 4.57 we can see that the pixels with flag3 follow the same trend for the whole domain, partly because they represent a high percentage of the domain (~63%, Table 4.14). The opposite behavior happens in other intercomparisons such as Figure 4.58. Flag 3 pixels represent pure ambivalence and also ordinary cases. This means that the range of τ encompasses all the possibilities and is very difficult in some case studies, like the one we are dealing with, to unequivocally obtain the COD. Besides, the CF7 is mostly formed by intermediate values of τ , which are usually affected by the ambivalence of COD (see Figure 3.23 and Figure 3.24 of Chapter 3). For solar zenith angles higher than 30° , the pixels labeled with flag3 do not show a clear linear trend, as in Figure 4.58. A fit line has been obtained, ($y = 0.44(\pm 0.01)x + 6.6(\pm 0.3)$) but with a low correlation coefficient of 0.46. This underestimation as denoted by the slope in the fit3 of Figure 4.58 is 40%, but it's not well determined due to the ambivalence, which is the main cause of the vertical intercept of 6.6 ± 0.3 .

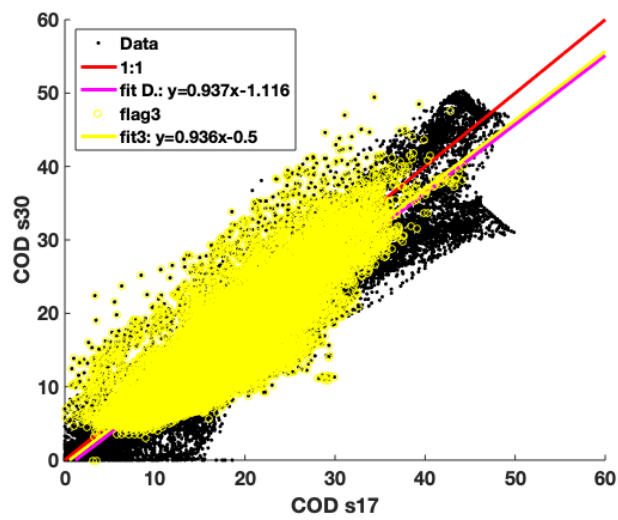


Figure 4.57 : COD_s30-COD_s17 intercomparison in CF7 case study. Fit line (fit3) of pixels affected by flag3 vs fit line (fit) of the whole domain, and line 1:1.

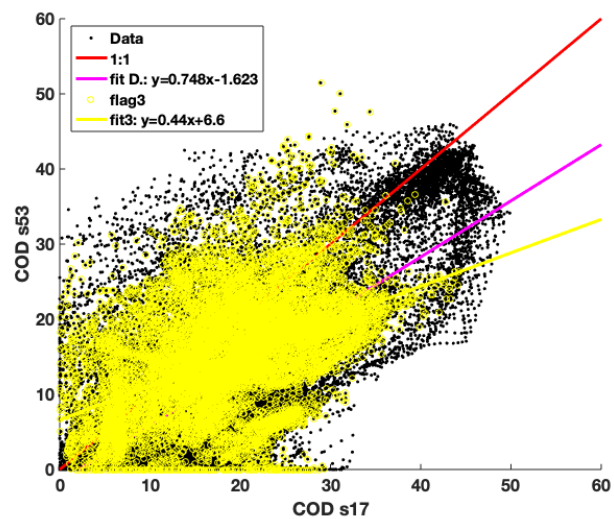


Figure 4.58 : COD_s53-COD_s17 intercomparison in CF7 case study. Fit line (fit3) of pixels affected by flag3 vs fit line (fit) of the whole domain, and line 1:1.

4. Results

Figure 4.59 to Figure 4.62 show the scatter plots of the CF8 case study. We can see that the slope of the fit line between COD_s42 and COD_s17 is close to 1 and the intercept is small, denoting a better fit than the comparison in CF7. The scatter plot of the COD_s42 vs COD_s17 (Figure 4.59, Figure 4.61) intercomparison has an r^2 factor of 0.75, whereas the one of the scatter in Figure 4.60 is 0.60, and the one of Figure 4.62 is 0.62. The fit line in Figure 4.59 of $y = 0.977(\pm 0.003)x - 1.0(\pm 0.1)$ shows that the average τ in the COD_s42 matrix is a 98% of the τ in COD_s17. The spread of points over the scatter is due to miscalculations on the cloud edges, as it will be discussed later, and the whole intercomparison has an associated RMSE of 7.5. As to the Figure 4.60, it shows the intercomparison of the results obtained at 57° vs the reference. The fit line of $y = 0.825(\pm 0.004)x - 1.5(\pm 0.1)$ indicates that the average τ in the COD_s57 is an 83% of the reference, and therefore the COD is underestimated up to 18%. As can be deduced from the higher spread of points in Figure 4.60 and Figure 4.62, the intercomparison of COD_s53 and COD_s57 matrices with the reference has a total RMSE of 9.1 and 9.8, respectively.

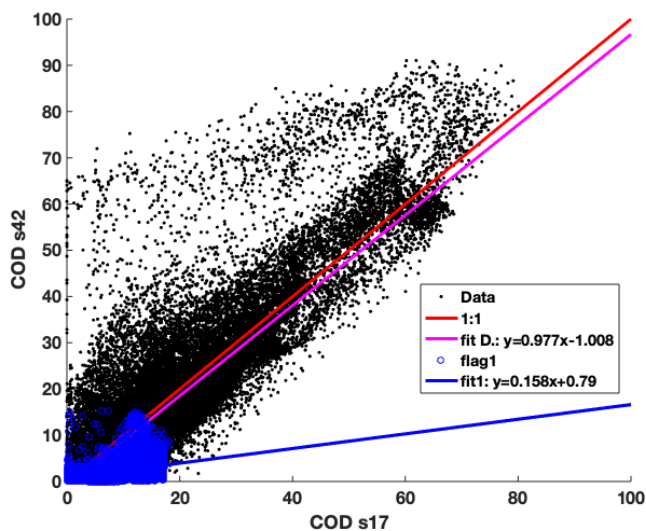


Figure 4.59 : COD_s42-COD_s17 intercomparison in CF8 case study. Fit line (fit1) of pixels affected by flag1 vs fit line (fit) of the whole domain, and line 1:1.

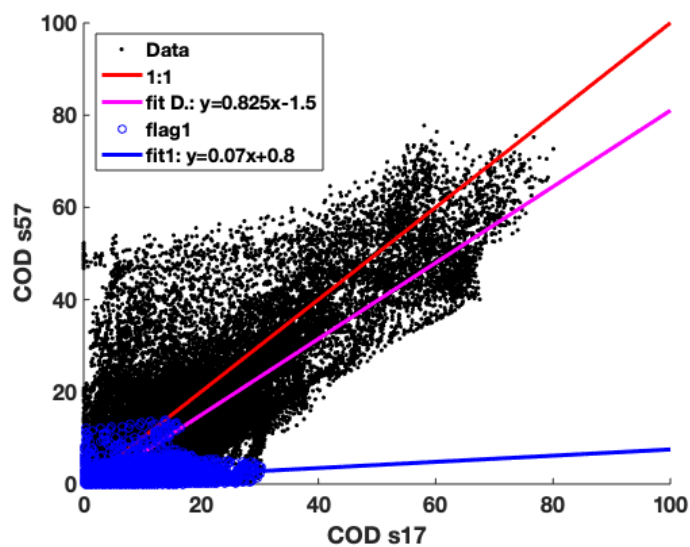


Figure 4.60 : COD_s57-COD_s17 intercomparison in CF8 case study. Fit line (fit1) of pixels affected by flag1 vs fit line (fit) of the whole domain, and line 1:1.

Regarding to the pixels labeled with flag2 in the CF8, the underestimations range from 40% to 48%, in Figure 4.61 and Figure 4.62, respectively. These values are also affected by ambivalence as in CF7, as can be seen in the vertical intercepts of 2.2 ± 0.2 and 1.9 ± 0.2 , and the spread of points. This influences the RMSE associated to flag2, with a value of 5.4 and 7.5, respectively for Figure 4.61 and Figure 4.62, a little less than their counterparts in CF7. The fit2 line at the COD_s57 vs COD_s17 intercomparison (not represented) is $y = 0.17(\pm 0.01)x + 5.4(\pm 0.2)$. The vertical intercept is caused by ambivalence and is too high to obtain a reliable underestimation factor associated to flag2.

4. Results

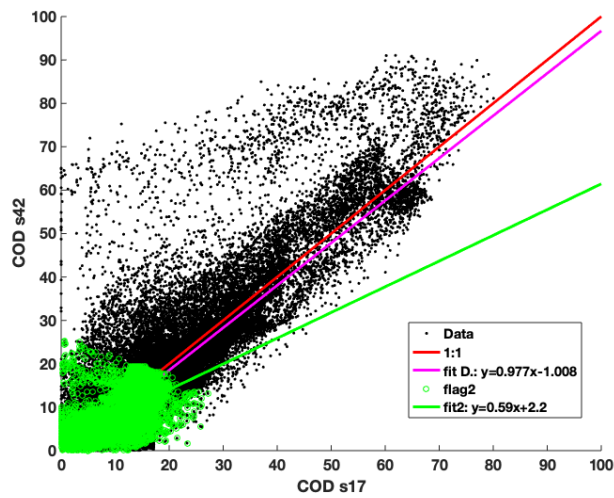


Figure 4.61 : COD_s42-COD_s17 intercomparison in CF8 case study. Fit line (fit2) of pixels affected by flag2 vs fit line (fit) of the whole domain, and line 1:1.

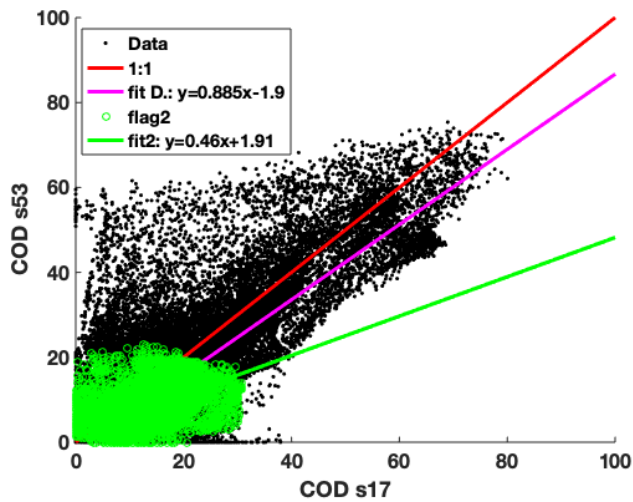


Figure 4.62 : COD_s53-COD_s17 intercomparison in CF8 case study. Fit line (fit2) of pixels affected by flag2 vs fit line (fit) of the whole domain, and line 1:1.

In case study CF9 (Figure 4.65 to Figure 4.67), the intercomparison with reference (COD_s17) varies visibly with solar zenith angle. The r^2 factor on the other hand is 0.97, 0.95 and 0.88 in three scatter plots from Figure 4.65 to Figure 4.67, respectively. The RMSE associated to these intercomparisons vary from 5.3 to 9.9 with increasing sza (Table 4.18). The fit lines again indicate a COD underestimation with respect to the reference, ranging from 11% (COD_s42) to 16% (COD_s53). These results are similar to the CF8 and much less than in the CF7.

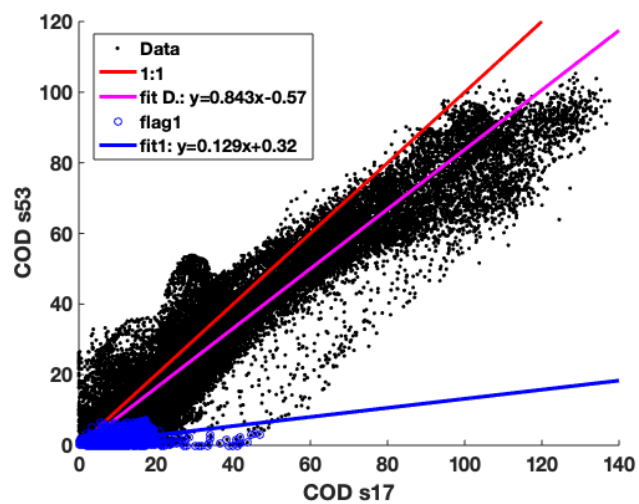


Figure 4.63 : COD_s53-COD_s17 intercomparison in CF9 case study. Fit line (fit1) of pixels affected by flag1 vs fit line (fit) of the whole domain, and line 1:1.

4. Results

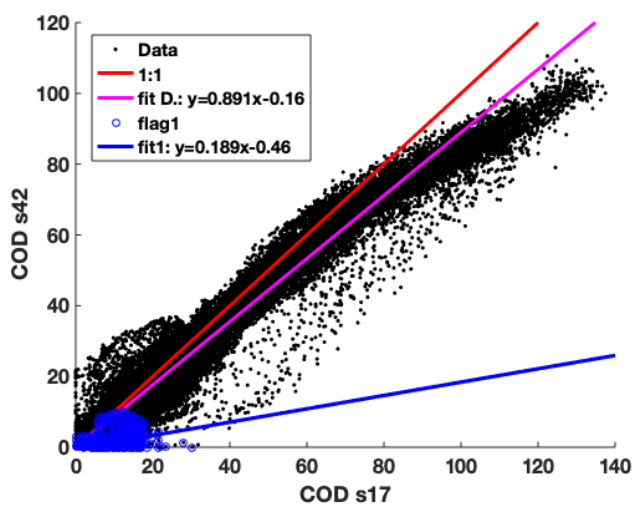


Figure 4.64 : COD_s42-COD_s17 intercomparison in CF9 case study. Fit line (fit1) of pixels affected by flag1 vs fit line (fit) of the whole domain, and line 1:1.

On the other hand, the underestimations related to the retrieval at the pixels labeled as Flag1 remain high as in the previous case studies (CF7 and CF8), ranging from 79% to 85%, as the fit1 lines in Figure 4.63 and Figure 4.64 show.

Thus, we can see in Figure 4.65 and Figure 4.67 that the underestimation associated to flag2 pixels ranges from 21% (COD_s30) to 50% (COD_s42 and COD_s53). The vertical intercept of the fit2 line at the COD_s57 vs COD_s17 intercomparison is too high (3.9 ± 0.2) for a reliable underestimation.

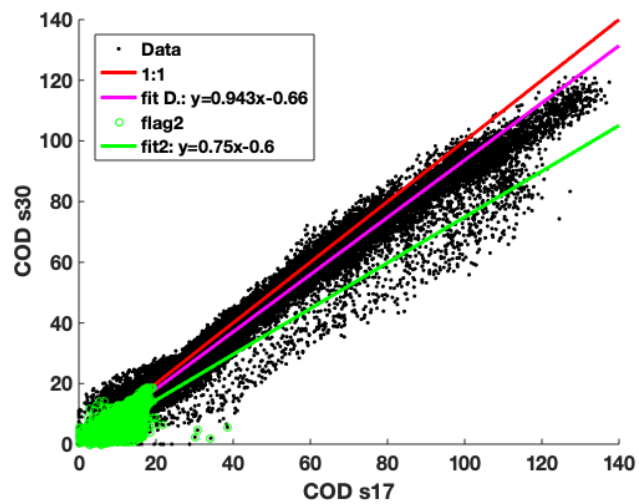


Figure 4.65 : COD_s30-COD_s17 intercomparison in CF9 case study. Fit line (fit2) of pixels affected by flag2 vs fit line (fit) of the whole domain, and line 1:1.

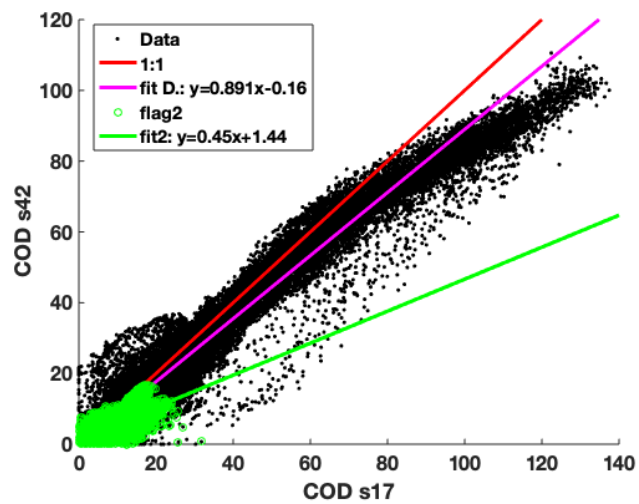


Figure 4.66 : COD_s42-COD_s17 intercomparison in CF9 case study. Fit line (fit2) of pixels affected by flag2 vs fit line (fit) of the whole domain, and line 1:1.

4. Results

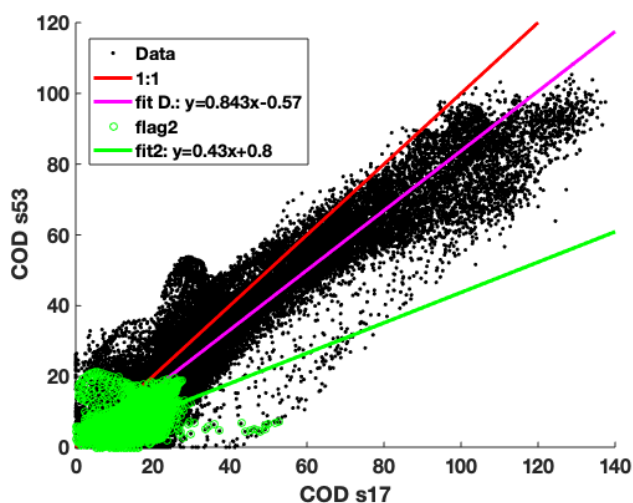


Figure 4.67 : *COD_s53-COD_s17 intercomparison in CF9 case study. Fit line (fit2) of pixels affected by flag2 vs fit line (fit) of the whole domain, and line 1:1.*

We show in Figure 4.68 to Figure 4.70 the intercomparisons with CF10. First of all, we can observe a low spread of points in comparison to the previous scatters, which makes the RMSE the smallest of this whole synthetic study. In addition, the r^2 factors are logically the highest in this study and have the values of 0.99, 0.98 and 0.97 respectively in the three scatter plots from Figure 4.68 to Figure 4.70. The number of points labeled with Flag1 are insufficient to obtain a trend, but there are enough flag2 points to do so.

The fit2 lines in Figure 4.68 and Figure 4.69 denote an underestimation of τ with respect to the reference ranging from 12% (Figure 4.68 of COD_s30 intercomparison, slope 0.85 ± 0.02) to 37% (Figure 4.69, COD_s42 and COD_s53 intercomparison, slope 0.59 ± 0.04). Ambivalence is not so important in the CF10 case study, as can be seen in the spreads of green points, the vertical intercepts in Figure 4.68 to Figure 4.70, and the RMSE associated to flag2, under 5 for solar zenith angles up to 53° . Nevertheless, there is still ambivalence influence in the COD_s57 matrix, as shows the vertical intercept in the fit2 line: $y = 0.37(\pm 0.03)x + 5.7(\pm 0.4)$.

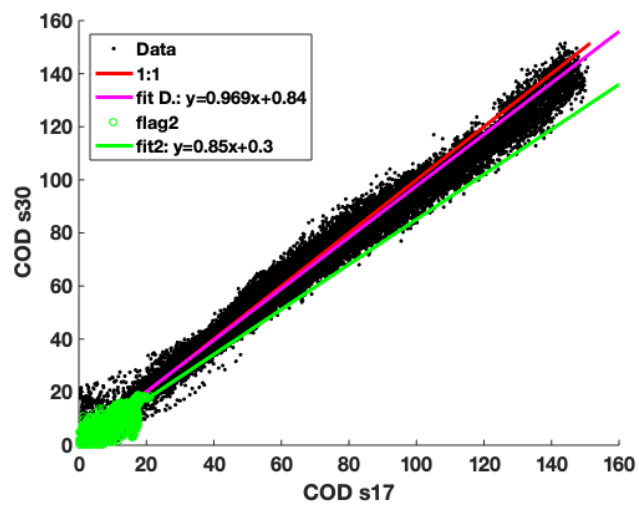


Figure 4.68 : COD_s30-COD_s17 intercomparison in CF10 case study. Fit line (fit2) of pixels affected by flag2 vs fit line (fit) of the whole domain, and line 1:1.

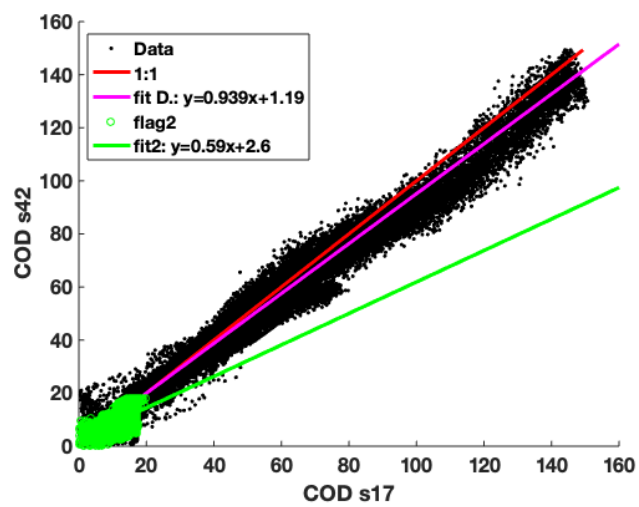


Figure 4.69 : COD_s42-COD_s17 intercomparison in CF10 case study. Fit line (fit2) of pixels affected by flag2 vs fit line (fit) of the whole domain, and line 1:1.

4. Results

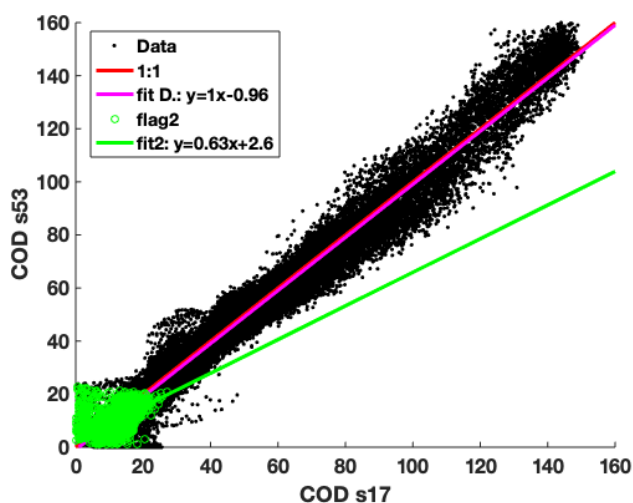


Figure 4.70: COD_s53-COD_s17 intercomparison in CF10 case study. Fit line (fit2) of pixels affected by flag2 vs fit line (fit) of the whole domain, and line 1:1.

To end, we analyze the artifacts that appear in the previous scatters, their position in the matrices and their contribution to the error of the intercomparisons. We consider outliers those points beyond 2σ away from the fit line of the whole scatter plot (see Chapter 3). Figure 4.71 shows the points that fulfill that condition in the considered scatter plots. The so-called positive outliers are those whose COD_sX value is higher than the corresponding fit line value, and the negative outliers have a value lower than the fit line value.

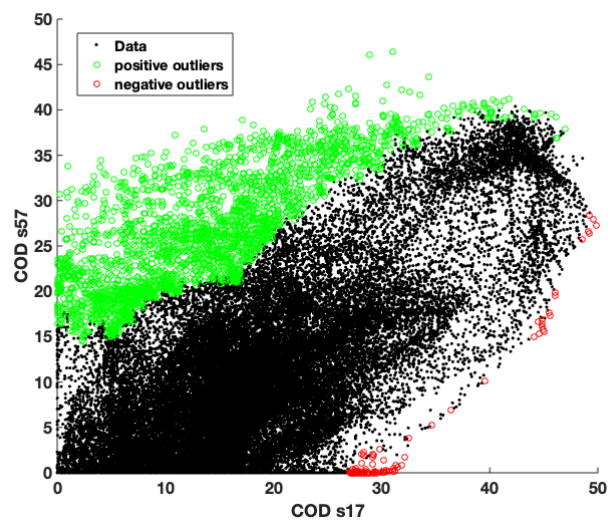


Figure 4.71 : Outliers in COD_s57 vs COD_s17 intercomparison for CF7 case study

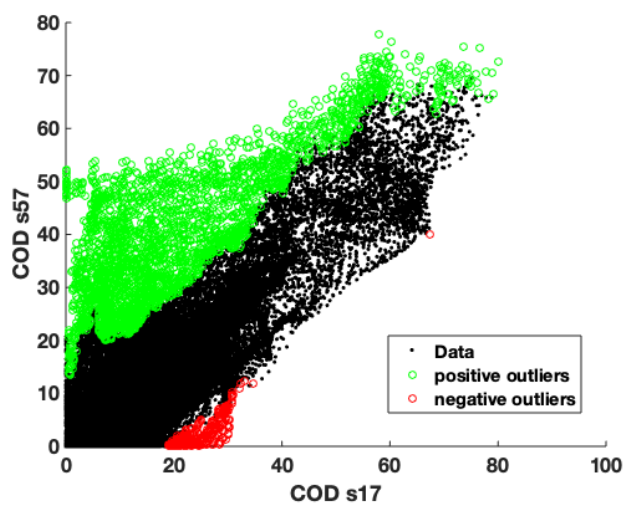


Figure 4.72 : Outliers in COD_s57 vs COD_s17 intercomparison for CF8 case study

4. Results

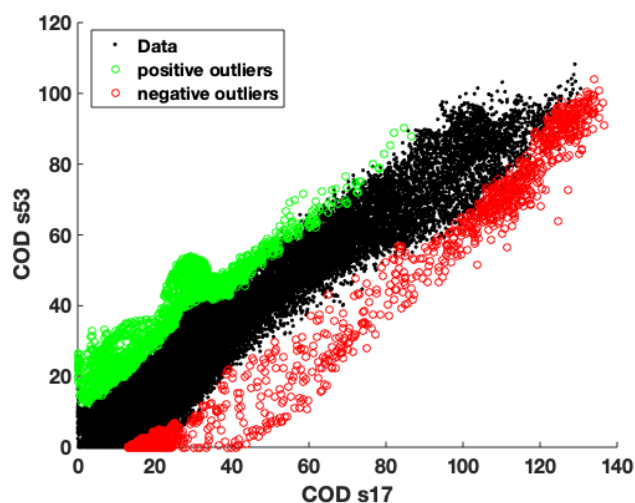


Figure 4.73 : Outliers in COD_s53 vs COD_s17 intercomparison for CF9 case study

In the CF7 and CF8 (Figure 4.71 and Figure 4.72) we can see that the positive outliers far outnumber the negative outliers. These points correspond mostly to the cloud edges, as we can see in Figure 4.74.

In the cloud edges usually, our algorithm produces an overestimation of τ due to the ambivalence. This is an effect already seen in Section 4.2.1 with the ‘tails’ in the graphs of the COD LES vs COD_sX intercomparisons. These tails encompass pixels that are always at a distance to clear sky under 0.3km. But also, we have seen already that at higher solar zenith angles we have usually radiances out of range by reflections in cloud sides that the algorithm interprets as smaller COD that it should be. This is the reason why Figure 4.71 and Figure 4.72 have undefined shape, covering both anomalous high and anomalous low COD’s.

Unfortunately, due to the algorithm limitations it is impossible this flaw in broken clouds. What we can do in this work is to quantify the error at the cloud edges through the RMSE obtained from these specific points. The RMSE is up to 14.7 in CF7 (Figure 4.71) and up to 26.2 in CF8 (Figure 4.72).

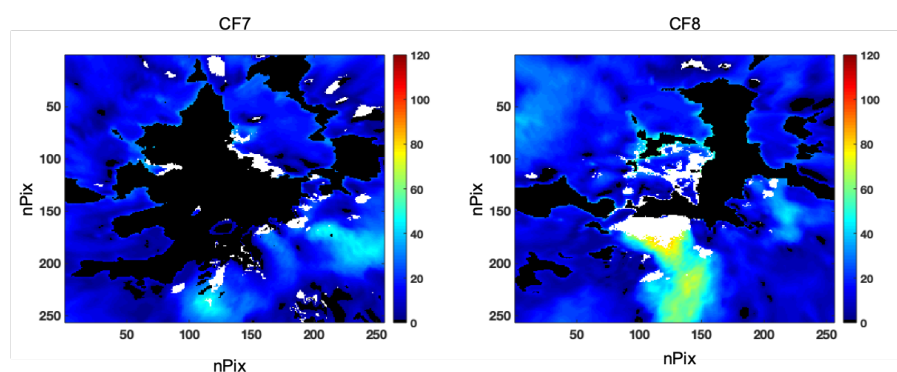


Figure 4.74 : Troublesome areas (in white) for the retrieval in CF7 and CF8 cases study

Regarding to CF9 (Figure 4.73), there are not many cloud edges as in the CF7 and CF8, but they also contribute to the τ overestimation. An additional effect has been observed in the CF9, and it is related to the albedo change with the sun position.

It has been observed in CF9 a general overestimation of τ where the sun is located in the simulation. It might be due to a higher extinction that the plane-parallel approximation does not takes in account. So, the COD_s17 the central area of the domain (squared area in Figure 4.75) gets higher values of τ than the LES field and the rest of the COD_sX matrices. That area corresponds to a zenith angle around 17° and it is where the sun is located in the Rad_s17 simulation. In Figure 4.75 can also be observed the small areas of cloud edges that get overestimated in COD_s17 with respect the other COD_sX matrices.

On the other hand, in the COD_s53 the optical thickness is greater than in the COD_s17 matrix in the squared area in Figure 4.76. That same area is located around the 53° of zenith angle. These pixels are the painted in green in Figure 4.73 due to the higher values of τ in COD_s53 than COD_s17.

4. Results

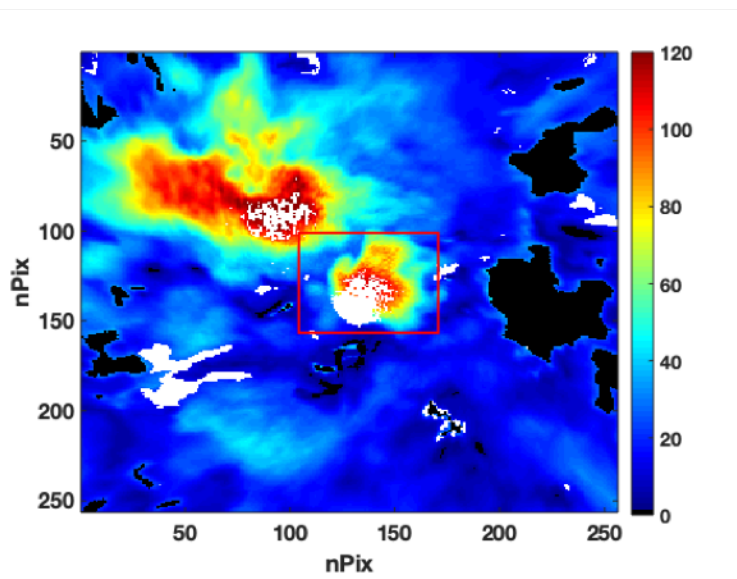


Figure 4.75 : (White) Area of overestimation of τ in COD_s17 due to sun position

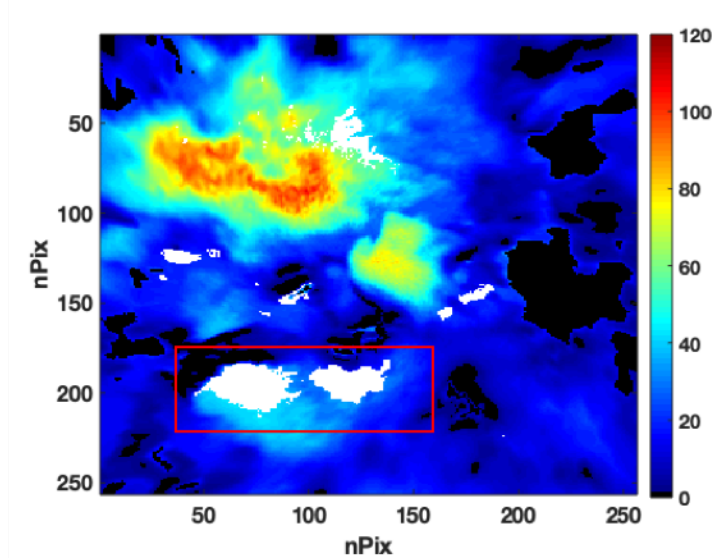


Figure 4.76 : (White) Area of overestimation of τ in COD_s53 due to sun position

4.3. Synthetic study application over Sky Camera results

To end this chapter and to recap, we propose to obtain some correction factors for the retrieval applied over the sky camera images, by the use of the results obtained in the synthetic study. The variables employed have been mainly the cloud fraction and the solar zenith angle. Based on these two parameters, the fitting lines in Table 4.20 are obtained in Section 4.2.1 as the relationship between the LES COD fields, taken as ‘the truth’, and the retrieval results, with its limitations and the one-dimensional plane-parallel approximation. In Section 4.2.1, the x variable is the retrieved COD, and the y variable is the LES COD.

Table 4.20 : Fit lines as a function of the cloud cover and the solar zenith angle from the Results in Section 4.2.1

SZA	CFN(CC)			
	CF7 (0.695)	CF8 (0.824)	CF9 (0.906)	CF10 (0.990)
17°	$y = 2.6x - 27$	$y = 1.4x - 10$	$y = 0.93x - 6$	$y = 1.2x - 3$
30°	$y = 2.8x - 26$	$y = 1.4x - 11$	$y = 0.98x - 5$	$y = 1.2x - 4$
42°	$y = 3.7x - 34$	$y = 1.6x - 13$	$y = 0.997x - 5$	$y = 1.2x - 4$
53°	$y = 3.3x - 21$	$y = 1.7x - 11$	$y = 0.98x - 2$	$y = 1.1x + 0.3$
57°	$y = 4x - 22$	$y = 1.6x - 7$	$y = 0.91x - 0.2$	$y = 0.99x + 3$

A way to correct the COD obtained with the sky camera is to apply the fit lines in Table 4.20 to the array, as in (4.1).

$$COD'_{i,j} = M \cdot COD_{i,j} + B \quad (4.1)$$

Being M and B the slope and vertical intercept parameters derived from those from Table 4.20. They would be obtained by interpolating to the solar zenith angle and the cloud cover in the sky camera image.

We have inferred from the fit lines in Table 4.20 and the overall synthetic study in Section 4.2, that the retrieval systematically underestimates τ in broken clouds. The COD average values decreases with the increasing of solar zenith angle. This might be caused by the 3D effects that are not taken in account in the plane-parallel

4. Results

approach. According to the bibliography, the cumulus clouds are especially sensitive to the 3D effects of side leakage and side illumination (Benner and Evans, 2001; Hogan and Shonk, 2013). These effects influence the albedo of the cloud field, being the IPA albedo too low for solar zenith angles (see Chapter 1, Section 1.3.2). This results in a greater amount of radiation reaching the ground in our calculations, and therefore the retrieved COD is obtained lower than in reality. The side leakage and side illumination, as well as all the other 3D effects that influence the cloud field albedo are stronger the smaller is the cloud fraction, and therefore the error or underestimation of COD is higher at the CF7. Another important 3D-effect in our results might be that the heterogeneous clouds are brighter than homogeneous clouds with the same COD (Mejia et al., 2016). This is caused by the reflected light from the cloud underside, that increases brightness. As the 1D approach does not consider the radiative smoothing, or in short, photon transport between pixels, the enhanced brightness is considered as smaller COD than in reality.

An opposite behavior has been observed at the more homogeneous case studies (CF9 and CF10). Generally, the results are closer to reality, since side leakage and side illumination is reduced or inexistent. The slight overestimation of τ with respect to the LES fields (see Figure 4.39 and Figure 4.40 until distance to clear sky of around 1.3km) might be caused by a strong reflection of radiation and radiative smoothing that prevents radiation reaching the ground. In the plane-parallel approach this results in an enhanced COD with respect to the reality.

On the other hand, a correction based on the flags' categories can be obtained from the intercomparisons in Section 4.2.2. As we have seen in Figure A 3, Figure A 6, Figure A 9 and Figure A 12 in Annex pixels located around the cloud edges are labeled with flag1 and flag2, and there the COD gets underestimated up to a 92% and up to 65%, respectively. Aside ambivalence, the underestimation is produced due to an enhanced radiation caused by side escape. Photons strike the cloud edges and are strongly forward scattered towards the ground (Hogan and Shonk, 2013).

The correction factors could be obtained from the fit1 and fit2 lines in Section 4.2.2, conveniently interpolated to the solar zenith angle and cloud fraction of the image. The further correction only can be done as long as the vertical intercept in the resulting fit lines divided by the average τ of the fit line is comprised within the calibration error, which is difficult in most cases since pixels labeled with Flag1 affect to very small COD.

If it were the case, the vertical intercept is not considered in the correction, and the pixels labeled by flag1 and flag2, respectively, is corrected by multiplying the τ value by the inverse of slope of the fit1 and fit2 lines. In that way the COD gets modified according to the reference, that is the COD_s17 matrix. Next, the pixels with these flags must be corrected with the row of 17° in Table 4.20.

To conclude, it must be mentioned that the retrieval of Cloud Optical Depth at cloud edges is complicated by ambivalence. These pixels are usually not affected by radiation enhancement but yes by ambivalence. They can be pixels labeled with flag2 and flag3 with high vertical intercept and therefore cannot be corrected in the approach described here. However, the errors have been quantified and it is a matter of a future work to derive a closure methodology that removes ambivalence from the retrieval, and so only concentrates on 3D effects with improved parameterizations.

Conclusions and Future Work

In this work we have obtained the Cloud Optical Depth with the blue channel of a Sky Camera, by means of a radiative closure between measurements and radiative transfer modeling using libRadtran. This has been achieved through a previous characterization of the camera, following the methodology proposed by Roman et al., (2012 and 2017). The characterization consists in, on one hand, obtaining the effective wavelengths of the camera, and on the other hand, calibrating the instrument geometrically and radiometrically. Through the geometric calibration we obtain the maps of viewing coordinates of the camera associated with each pixel, while with the radiometric calibration we obtain the radiometric constant that converts the digital counts of each pixel to radiance.

The methodology of COD acquisition is based in the works of Mejia et al., (2016) and Schwartz et al., (2017), with the application of the Independent Pixel Approximation to each pixel of the camera grid. In addition to the cloud optical thickness of the whole sky-camera images, ancillary products have been obtained for a better understanding and the subsequent analysis of the results. One of them consists in the data quality flags matrices, that indicate the reliability of results and the procedure of inversion for COD acquisition. The other product consists in the uncertainties' matrices of radiance measurements and COD retrieval. Our results are in agreement with the observed COD in zenith by the AERONET's Cloud Mode, with a validation's slope close to one (0.996 ± 0.045) and a correlation coefficient of 0.96. Nevertheless, such good concordance does not happen in each and every case of the analyzed database, which means that the algorithm has certain deficiencies both in the zenith and in other viewing geometries where the 1D approach is incomplete.

Therefore, through the comparison with AERONET and other criteria, four categories of results based on their quality have been defined, in order to classify them and analyze the common characteristics. In Category 1 and Category 2 the best results have been found, with a very good correspondence with AERONET. In Category 1 most of results are obtained by means of an ordinary inversion procedure and all radiances are found within the simulated radiances. The retrieved COD ranged from 0 to 120 in the cases found within the Category 1, while the average uncertainty is of 15% due to the camera calibration. On the other hand, in Category 2, besides the satisfactory correspondence with the CIMEL CE-318, there are significant zones

Conclusions

of the image with out of range radiances, and also zones affected by the ambivalence of COD for a given radiance value. The acquired COD ranged from 0 to 50, with a 9% of uncertainties due to the calibration and a 13% of uncertainties due to radiance enhancement. Must be pointed out that some systematic overestimation has been found in cloud edges due to the way in which the methodology solves the ambivalence of COD.

The two remaining categories deal with the unsatisfactory results, being the Category 3 due to COD overestimation and Category 4 for COD underestimation. The causes found for the overestimation are mainly because of the ambivalence of COD for a given value of radiance, which cannot be unequivocally solved. The cases within Category 3 are most affected by it, since the cloud fields analyzed are mainly composed by thin clouds ($\tau = 0 - 20$). The methodology followed in order to overcome the ambivalence takes the higher value possible of COD when ambivalence is found, so lower cloud optical thicknesses are usually overestimated. The data quality flags identify these situations in order to quantify the errors, and because of the possibility of parameterize them.

Within Category 4 the results systematically underestimate the Cloud Optical Depth, with uncertainties in average of -15%. The reasons are mainly the 3D radiative effects non-contemplated in the plane-parallel model of the Independent Pixel Approximation. The cases within this category happen always under very high solar zenith angles and in broken cloud fields most of the times, which are especially sensitive to 3D radiative effects. On the other hand, high solar zenith angles favor the side illumination, producing many situations of radiation enhancement in the cloud borders and seen from the ground the clouds appear more illuminated. Since the 1D plane-parallel approach does not contemplate the extra income of radiance from side cloud pixels the algorithm interprets the increment of transmittance as lower COD than it should be.

The results found with the sky camera lead to the second part of the present work, in which we carry out a synthetic study employing the strengths of full 3D Monte Carlo Radiative Transfer.

The second part of the work is about analyzing the errors made in the COD acquisition. This is done through a synthetic study that relates the flags meanings to the miscalculations. With the synthetic study we evaluate the methodology followed and determine the origin of the flaws perceived in Section 4.1 and we extract some valuable deductions with which to improve the results obtained with the 1D

approach. We employ the 3D Radiative Transfer model MYSTIC integrated in a non-free libRadtran package to simulate ground radiances in a mode that imitates a sky camera view, under conditions of 3D cloud fields with high spatial resolution and different geometry and cloud cover. These cloud fields (CFN) are obtained with the UCLA-LES model, and are named CF7, CF8, CF9 and CF10 for the respective cloud coverages of 0.7, 0.8, 0.9 and 1. The simulations are performed with different solar zenith angles ($17^\circ, 30^\circ, 42^\circ, 53^\circ$ and 57°) in order to study and quantify the influence of solar geometry as well the cloud structures and properties in the retrieval.

The radiance matrices are analyzed with the retrieval of the Section 4.1 in order to obtain the same products of COD and flags. The retrieved COD is compared with the truth COD from the LES fields (obtained by column integration at each $[x,y]$ position), once the results matrices in spherical coordinates are converted to the LES COD coordinates (cartesian).

The comparison is carried out by means of an ancillary parameter named ‘Distance to Clear Sky’ (DCS), or distance of each pixel to the edge of clouds, in cartesian coordinates. We do that because the conversion between spherical and cartesian coordinates is not perfect and some discrepancies in the cartesian position of the elements of the cloud fields have been observed. The DCS determines which pixels of the COD_sX image and the CFN image correspond to the same spatial position in the sky, even with the deformation that occurs in the change of coordinates. For each of the DCS values (0 to 3.55 km in the case of CF10) all the τ pixels located at such distance are averaged, in the retrieved COD and in the LES COD. In that way we obtain a series of points that can be represented in a scatter plot for each CFN case study and each considered solar zenith angle.

In the comparison of the CF7 results with the LES COD we observe a general underestimation of the optical thickness in all the solar zenith angles considered by means of the scatters’ fit lines. Such underestimation is of 260% in the case at 17° (COD_s17) and up to 400% in the case at 57° (COD_s57). That is, the results get worse with the increasing solar zenith angle, as also shows the Root Mean Square Error, that changes from 8 to 12 as sza increases. The values of RMSE can be interpreted as the retrieval error at each sza considered, due to the non-contemplated 3D radiative effects but also by the flaws in the methodology. Logically values as 8 to 12 over the smallest COD imply the largest errors of the domain.

The CF7 cloud field is a cluster of shallow cumulus clouds with partial cloud coverage (0.69), with an important clear sky gap in the central part of the domain.

Conclusions

Most of the field is composed by an optical thickness of 0 to 20, with some isolated patches with COD up to 60 and only one small extension with COD over 100. A cloud field of these characteristics is the most sensitive to the 3D radiative effects, as it is full of vertical and horizontal inhomogeneities (Stocker et al., 2013, Barker et al., 1996). Thus, the underestimation might be general for all the considered illumination conditions because of side leakage under high sun and side illumination under mid and low sun. The high number of cloud edges favors multiple scatterings and reflections that imply radiation enhancement and an intense forward scattering to the ground, that in turn increases with solar zenith angle. Since the 1D does not consider the horizontal transport that suppose the reflections in cloud edges, such extra illumination is interpreted as a thinner COD than it actually is.

On the other hand, in the CF7, as in all results that involve cloud edges, a systematic overestimation of COD in such cloud borders has been observed. This error is more dramatic as the cloud cover decreases, precisely because the number of pixels in the boundaries increases. This is due to the way in which the algorithm deals with ambivalence. For a given solar and viewing geometry, there is a range of τ in which a given value of radiance corresponds to two values of COD. The algorithm in such conditions cannot unequivocally decide which one of the two τ is most suitable and chooses the highest one. This implies that small τ as in the cloud edges gets overestimated. The CF8 on the other hand is also a field of shallow cumulus with a cloud coverage of 0.82. It is actually the CF7 cloud as it has grown thicker and higher. With the CF8 the COD is also underestimated in the same way as in CF7 but to a lesser extent, as the underestimation observed in the COD_s17 is of 140% and in higher solar zenith angles is 160-170%. The Root Mean Square Error also shows improvement with respect to the CF7, with values from 5 to 7 as solar zenith angle increases. We believe that the results improve because the less extent of cloud sides than in CF7. This might cause that the effective cloud area gets wider by overlapping of cloud layers at mid solar zenith angles such as 30° and 42°, causing a higher albedo and in turn decreasing the transmittance, as absorption in the visible is small (Kokhanovsky, 2004). In such angles, 30° and 42°, is where the algorithm has been observed to work better for CF8.

To end the comparison with the LES fields, the influence of 3D radiative effects and solar zenith angle occurs to a much lesser extent in the CF9 and CF10. They are overcast stratocumulus clouds much more uniform and thicker than the CF7 and CF8. Therefore, CF9 and CF10 are the less sensitive to the problems observed in the previous case studies, as they offer less opportunities for horizontal radiative

transport. In CF9 we find the best results of the comparison. In CF9 all the trends for the considered solar zenith angles are very good for much of the DCS section, as show the coefficient of variance of 0.97-0.98. This agrees with previous studies, given that Chambers et al., 1997 and Zuidema and Evans, 1998 found the IPA accurate enough for stratocumulus clouds as it was proven that the IPA albedo was close enough to the simulated one with Monte-Carlo and Lansat-derived models.

The fit lines obtained are closer to the 1:1 relationship. The slopes vary between 0.91 and 1, and the vertical intercepts between -0.2 and -6. The slopes imply a light overestimation of COD of 7%-9% that we attribute to an enhanced albedo when the sun is behind the cloud field, especially in low solar zenith angles such as 17°. When the albedo is higher there is less transmitted radiance to the ground, which is interpreted with a higher COD than it should be. With it the behavior of the RMSE reduces from 9 to 4 as solar zenith angle increases. In CF9 the overestimation of cloud sides is minimal given the high cloud coverage. This higher albedo seems to increase in the CF10 case, which is logical given that it is optically and geometrically way bigger than the CF7-CF9. In the comparison two different trends are found as a function of the DCS: one of them is the one attributable to the enhanced albedo as it shows an overestimated COD. Then, for a section of DCS the comparison has a trend close to the 1:1, until a series of values of distance to clear sky are reached that are all on the thickest area of the CF10. Here all the results underestimate the COD given that is way higher (~230) than the considered τ range in the LUT, and the algorithm extrapolated τ for the retrieval in these pixels. With this we find that the fitting lines are a little worse than those in the CF9, as well as the RMSE (8 to 11 (42°)), because the area of greatest optical thickness (~230) of CF10 is quite extensive.

Another analysis of the results in the Annex has been done, as the intercomparison between the matrices of results at different solar zenith angles. This is done in order to quantize the influence of solar zenith angle change, as well as to parameterize the influence of flags in the results, given the high presence of flag1 and flag2 in the Category 4 of results in Section 4.1. The COD matrices obtained at 17° (COD_s17) are those employed as reference, since they have less flag1 and flag2 presence in CF9 and CF10, and they show the best results in the LES comparison in CF7 and CF8. The intercomparison results show more graphically the influence of the solar zenith angle change in the broken cloud fields. The CF10 scatter plots fit very well to a slope close to 1 and remain practically invariable as the comparison with COD_s17 changes from COD_s30 to COD_s57. In the case of CF9, the change of SZA is more influential, with the spread of points increasing in the COD_s57 vs COD_s17 scatter

Conclusions

with respect to the COD_{s30}/COD_{s17} one. In the CF9 scatters it is very visible a certain group of isolated points that denote overestimation of COD in the COD_{s17} matrix with respect to the results at other solar zenith angles, that might be caused by a too high albedo in that point because the sun is located directly behind at 17°.

In the case of the broken cloud fields, CF7 and CF8, the change of solar zenith angle implies a dramatic change of linearity in the scatter plots, denoting that the retrieval is very different for the smaller solar zenith angles than for the larger ones. As the angle increases the illumination in the cloud edges also increases, causing radiances up to out of range by intense forward scattering, and the retrieval tends to underestimate the optical thickness in these areas as there is no COD in the plane-parallel approximation that matches these radiance values. For low zenith angles the effect at the cloud edges is the opposite, overestimation. When the pixels in cloud edges don't reach out of range radiance values, the algorithm overestimates the COD because of the way of solving ambivalence. This overall is the reason why in the CF7 COD_{s57}/COD_{s17} intercomparison such an undefined shape, as in the place of small CODs the other retrieval provides values of $\tau = 0 - \sim 35$. These edge effects represent an RMSE of up to 14.7 in CF7 and up to 26.2 in CF8.

Regarding to the flags influence, some fit lines have been obtained as well as the associated RMSE to flag1 and flag2 pixels. As already seen and mentioned above, the pixels marked with these flags underestimate the COD with respect to reality, mainly due to out of range values. The highest underestimation has been found in the COD_{s57}/COD_{s17} intercomparison of CF7 of a 92% in the points labelled as flag1. The associated RMSE in these points is of 13, and denotes that effectively the small COD up to at least a value of 13 cannot be unequivocally obtained with the methodology followed. More values of underestimations of COD have been found associated to the points labelled with flag2 up to 65%, therefore with less importance than those of flag1, partly due to the fact that out of range radiances and ambivalence compensate to some extent to each other. But precisely due to the predominant effect of ambivalence we cannot really quantify such underestimations of COD.

With all this, we propose parameterizations extracted from the synthetic study in order to improve the results obtained with the sky camera. These parameterizations depend on the studied variables, that is, the solar zenith angle and the cloud cover and are the relationships between the COD of the LES fields and the corresponding retrieved COD. The proposal is to apply the fit line that corresponds to the cloud cover and solar zenith angle in question to the results of the sky camera. When the

cloud cover, SZA are not found the fit lines should be interpolated to the desired values. The parameterizations obtained based on the flags could also be applied as long as they are not too influenced by ambivalence and previous correction.

In conclusion, the methodology designed for the acquisition of COD with the sky camera is useful and accurate for certain types of uniform, overcast clouds fields such as stratocumulus, as shown in the Category 1 of results in Section 4.1, the comparison of CF9 retrievals with the LES COD and the CF10 intercomparisons. However, the methodology requires improvements that concern overcoming first of all the ambivalence. The ambivalence has been solved in several ways in the bibliography, for example with the RED vs NIR index from Marshak (2004) or the Radiance Red-Blue Ratio (RRBR) Algorithm from Mejia et al., 2016. Once ambivalence has been resolved, a more thorough study of what has begun to be glimpsed in this work regarding to 3D radiative effects.

For future work it is proposed the use of a sky camera with a sensor characterized by a more differentiated channel responses than in the SONA 201-D. In that way it could be possible to define two channels index free of ambivalence. We intend to rely on the so-called bi-spectral method or dual-wavelength technique, given the different interaction of clouds with light frequency. We can also apply the deductions made by the systematic overestimation of COD in cloud edges, by identifying them in the first place and choosing the smaller possible optical thickness. It is also proposed to apply the advances made by the GRSV in the matter of obtaining HDR images from the original blue, green and red matrices of the sky camera. With it, the dynamic range of the images would be much more extended and the radiometric calibration improved, with its corresponding uncertainties. With these new improvements a new LUT would be defined, probably as a function of the scattering angle or of the same viewing zenith and azimuth angles, and with a wider range of cloud optical thickness. Due to the absence of ambivalence, the retrieval results would be much more accurate and the problems would only be a matter of the non-considered 3D radiative effects. In order to study more deeply such 3D radiative effects and obtain improved parameterizations with which apply the strengths of 3D radiative transfer to the 1D approach, improved synthetic studies should be realized, expanding to investigate the albedo of cloud fields and estimating the real horizontal transport at different horizontal scales. With all of this, it might be possible to greatly improve the retrieval at the edges of clouds that in the present work were unfortunately miscalculated, and extend and thus expand the study of interactions between aerosols and clouds, that precisely takes place in the cloud borders.

Annex

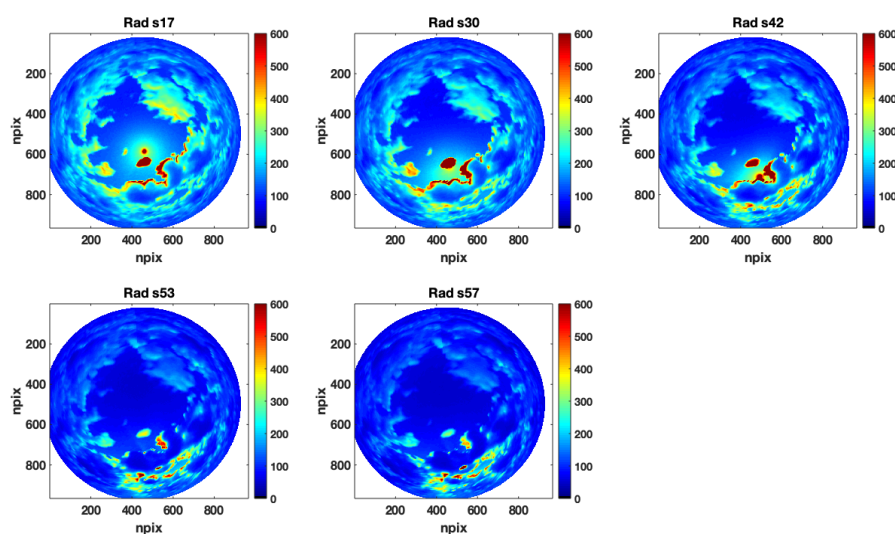


Figure A 1: Radiance matrices evolution with solar zenith angle (sX) under CF7 LES field

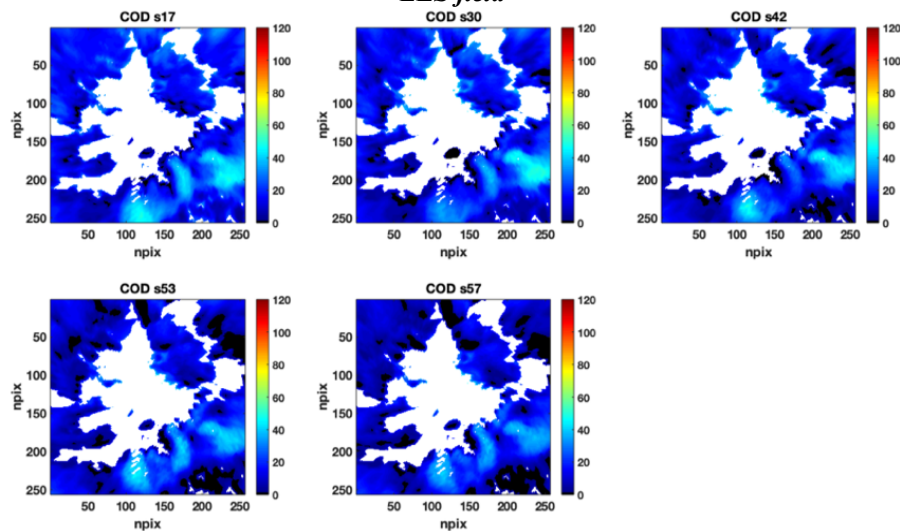


Figure A 2: COD matrices evolution with solar zenith angle (sX) under CF7 LES field

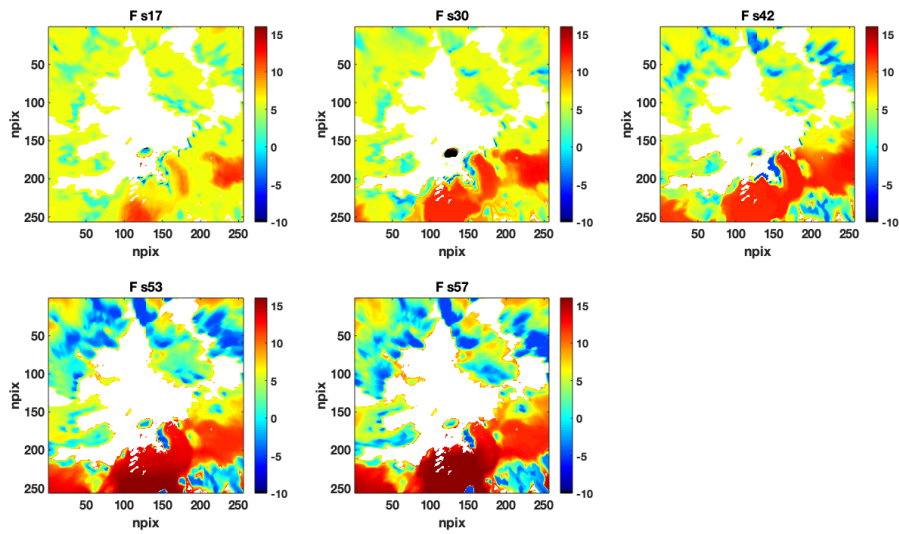


Figure A 3 : Flags matrices evolution with solar zenith angle (sX) under CF7 LES field

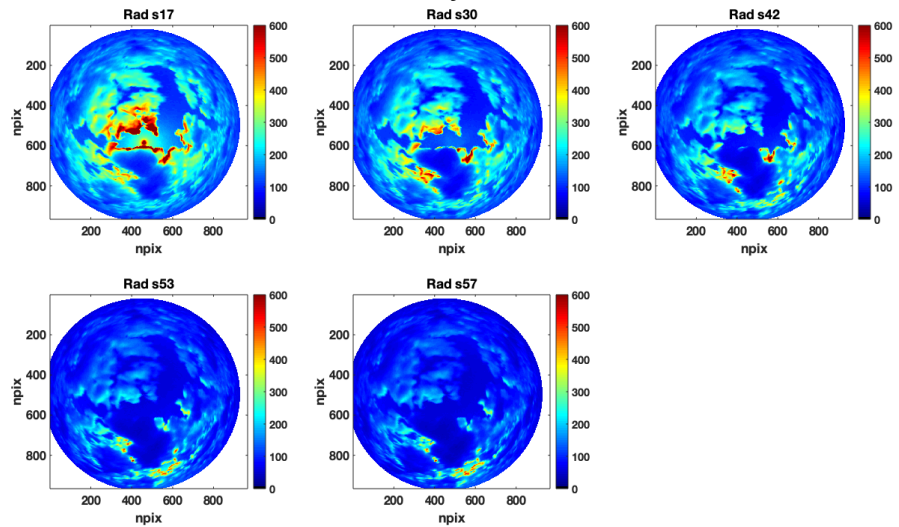
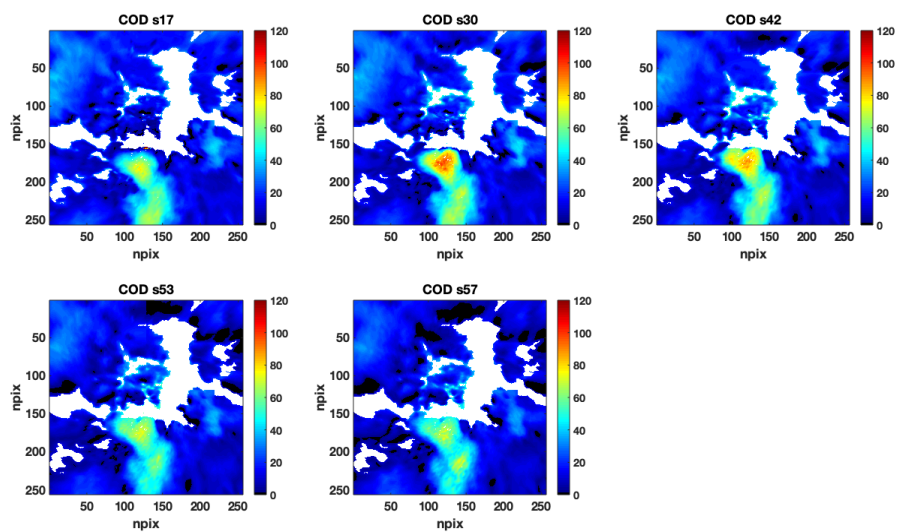
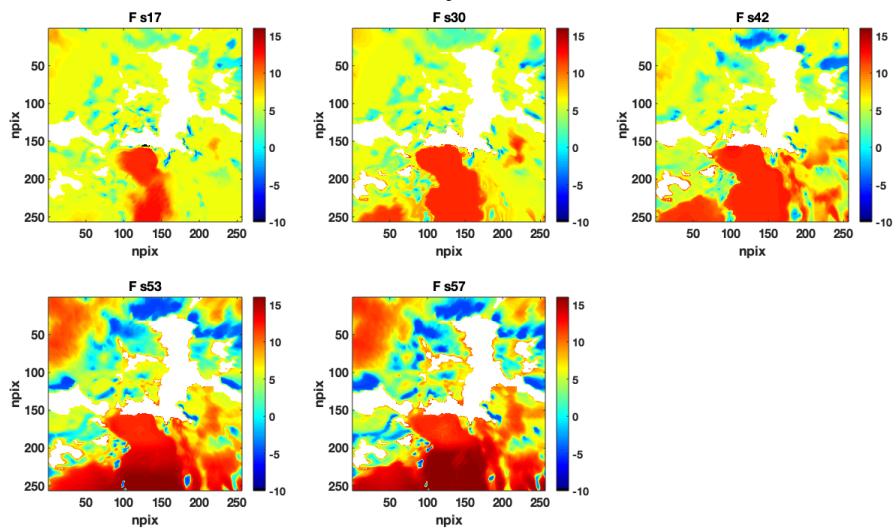


Figure A 4 : Radiance matrices evolution with solar zenith angle (sX) under CF8 LES field



*Figure A 5 : COD matrices evolution with solar zenith angle (sX) under CF8
LES field*



*Figure A 6 : Flags matrices evolution with solar zenith angle (sX) under CF8
LES field*

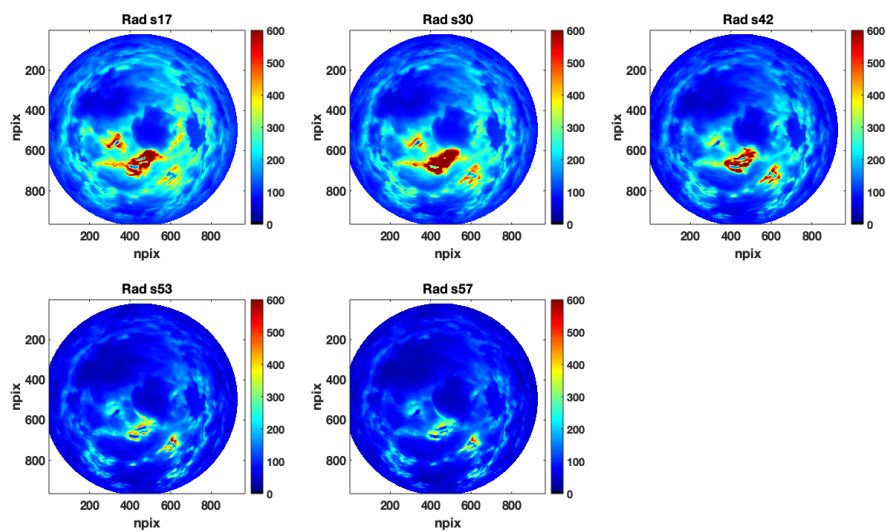


**Figure A 7 : Radiance matrices evolution with solar zenith angle (sX) under CF9
LES field**

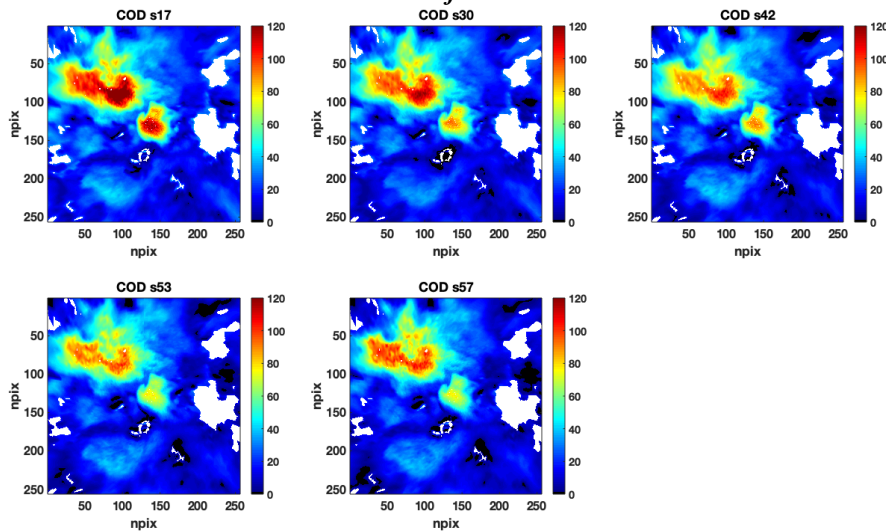


**Figure A 8 : COD matrices evolution with solar zenith angle (sX) under CF9
LES field**

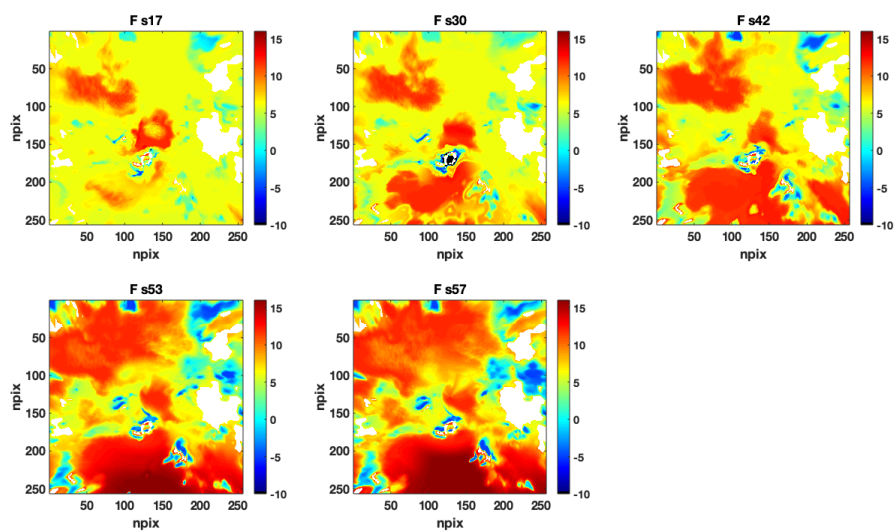


Figure A 9 : Flags matrices evolution with solar zenith angle (sX) under CF9 LES field

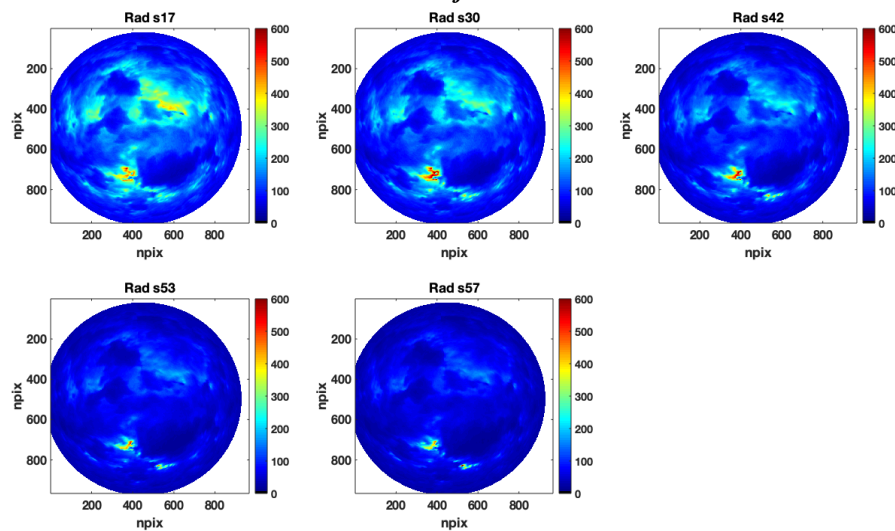


Figure A 10: Radiance matrices evolution with solar zenith angle (sX) under CF10 LES field

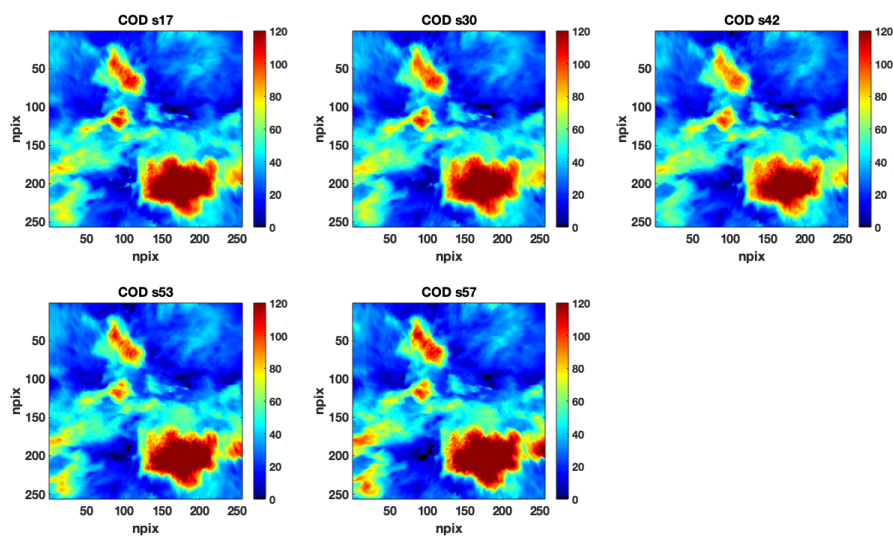


Figure A 11: COD matrices evolution with solar zenith angle (sX) under CF10 LES field

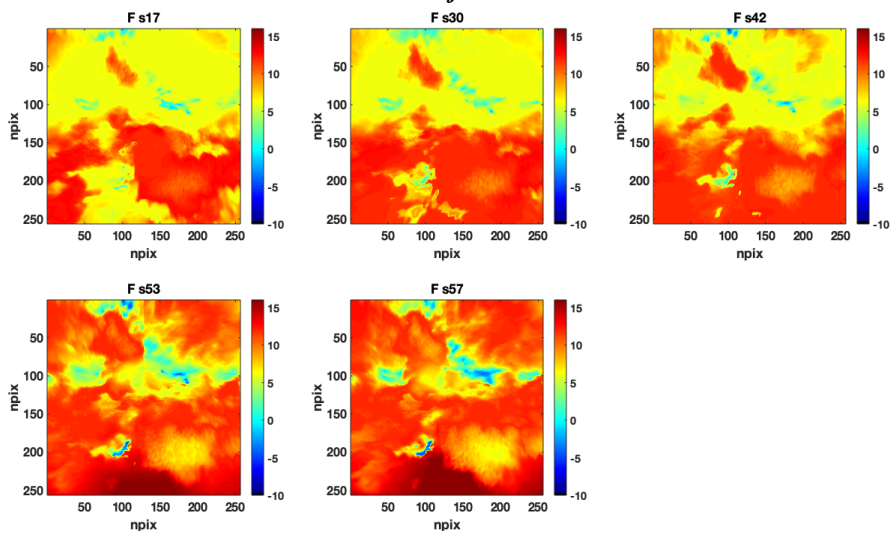


Figure A 12: Flags matrices evolution with solar zenith angle (sX) under CF10 LES field

Bibliography

- Administration, National Oceanic and Atmospheric. n.d. *National Weather Service*. Accessed 2020. <https://www.weather.gov/jetstream/energy>.
- Aebi, C., J. Gröbner, N. Kämpfer, and L. Vuilleumier. 2017. "Cloud radiative effect, cloud fraction and cloud type at two stations in Switzerland using hemispherical sky cameras." *Atmospheric Measurement Techniques* (10): 4587-4600.
- Aebi, C., J. Gröbner, S. Kazadzis, L. Vuilleumier, A. Gkikas, and N. Kämpfer. 2020. "Estimation of cloud optical thickness, single scattering albedo and effective droplet radius using a shortwave radiative closure study in Payerne." *Atmospheric Measurement Techniques* 13 907-923.
- Aelsnet. 2013. Accessed 2020. www.aelsnet.net/eportal/pluginfile.php/413/mod_imsdp/content/1/weather_station_model_continue.html.
- Alados-Arboledas, L., I. Alados, I. Foyo-Moreno, F.J. Olmo, and A. Alcántara. 2003. "The influence of clouds on surface UV erythemal irradiance." *Atmospheric Research* 66 (4) 273-290.
- Alonso, J., F.J. Batlles, G. López, and A. Ternero. 2014. "Sky camera imagery processing based on a sky classification using radiometric data." *Energy* 68 599-608.
- Antón, M., J. E. Gil, A. Cazorla, J. Fernández-Gálvez, I. Foyo-Moreno, F. J. Olmo, and L. Alados-Arboledas. 2011. "Short-term variability of experimental ultraviolet and total solar irradiance in Southeastern Spain." *Atmospheric Environment* 45 (28) 4815-4821.
- Barker, H.W., B.A. Wiellicki, and L. Parker. 1996. "A Parameterization for Computing Grid-Averaged Solar Fluxes for Inhomogeneous Marine Boundary Layer Clouds. Part II: Validation Using Satellite Data." *Journal of the Atmospheric Sciences* 53 (16).
- Benner, T.C., and F. Evans. 2001. "Three-dimensional solar radiative transfer in small tropical cumulus fields derived from high-resolution imagery." *Journal of Geophysical Research: Atmospheres* 106 (D14).

Bibliography

- Berg, L.K., E.I. Kassianov, C.N. Long, and D.L. Mills. 2011. "Surface summertime radiative forcing by shallow cumuli at the Atmospheric Radiation Measurement Southern Great Plains site." *Journal of Geophysical Research: Atmospheres* 116 (D01202) 1-13.
- Bilbao, J., R. Román, A. de Miguel, and D. Mateos. 2011. "Long-term solar erythemal UV irradiance data reconstruction in Spain using a semiempirical method." *Journal of Geophysical Research: Atmospheres* 116 (D22211).
- Bohren, C.F., and E.E. Clothiaux. 2006. *Fundamentals of Atmospheric Radiation. An Introduction with 400 Problems*. Weinheim: Wiley-VCH.
- Bony, S., R. Colman, V.M. Kattsov, R.P. Allan, C.S. Bretherton, J.-L. Dufresne, A. Hall, and et al. 2006. "How well do we understand and evaluate climate change feedback processes?" *J. Climate* 19 3445-3482.
- Boucher, O., Randall, D., P. Artaxo, C. Bretherton, G. Feingold, P. Forster, V.-M. Kerminen, Y. Kondo, H. Liao, U. Lohmann, and et al. 2013. *Climate Change 2013: The Physical Science Basis. Contribution of Working Group I to the Fifth Assessment Report of the Intergovernmental Panel on Climate Change*. Environmental, Cambridge: Cambridge University Press.
- Brenguier, J. L., H. Pawlowska, L. Schüller, R. Preusker, J. Fischer, and Y. Fouquart. 2000. "Radiative properties of boundary layer clouds: Droplet effective radius versus number concentration." *Journal of Atmospheric Sciences* 57 803-821.
- Brion, J., A. Chakir, J. Charbonnier, D. Daumont, C. Parisse, and J. Malicet. 1998. "Absorption Spectra Measurements for the Ozone Molecule in the 350-830nm Region." *Journal of Atmospheric Chemistry* 30 291-299.
- Buglia, J.J. 1986. *Introductio to the theory of atmospheric radiative transfer*. Washington DC: NASA, Scientific and Technical Information Branch.
- Bugliaro, L., T. Zinner, C. Keil, B. Mayer, R. Hollmann, M. Reuter, and W. Thomas. 2011. "Validation of cloud property retrievals with simulated satellite radiances: a case study for SEVIRI." *Atmospheric Chemistry and Physics* 11 (12) 5603-5624.
- Buras, R., and B. Mayer. 2011. "Efficient unbiased variance reduction techniques for Monte Carlo simulations of radiative transfer in cloudy atmospheres: The

- solution." *Journal of Quantitative Spectroscopy and Radiative Transfer* 112 (3) 434-447.
- Cahalan, R., W. Ridgway, W. Wiscombe, T.L. Bell, and J.B. Snider. 1994. "The Albedo of Fractal Stratocumulus Clouds." *Journal of Atmospheric Sciences* 51 (16) 2434-2455.
- Cahalan, R.F., W. Ridgway, W.J. Wiscombe, S. Gollmer, and Harshvardhan. 1994. "Independent pixel and Monte Carlo estimates of stratocumulus albedo." *Journal of the Atmospheric Sciences* 51 (24) 3776-3790.
- Calbó, J., D. Pagès, and J.A. González. 2005. "Empirical studies of cloud effects on UV radiation: A review." *Reviews of Geophysics* 43 1-28.
- Chambers, L.H., B.A. Wielicki, and K.F. Evans. 1997. "Accuracy of the independent pixel approximation for satellite estimates of oceanic boundary layer cloud optical depth." *Journal of Geophysical Research* 102 (D2) 1779-1794.
- Chandrasekhar, S. 1960. *Radiative Heat Transfer, vol 11*. New York: Dover Publications.
- Chiron de la Casinière, A. 2003. *Le Rayonnement solaire dans l'environnement terrestre*. Paris: Editions Publibook.
- Chiron de la Casinière, A., and Victoria E. Cachorro Revilla. 2008. *La Radiación Solar en el sistema Tierra-Atmósfera*. . Valladolid: Secretariado de Publicaciones e intercambio editorial, Universidad de Valladolid.
- Chiu, J.C., A. Marshak, C.-H. Huang, T. Várnai, R.J. Hogan, D.M. Giles, Giles, B.N. Holben, and et al. 2012. "Cloud droplet size and liquid water path retrievals from zenith radiance measurements: examples from the Atmospheric Radiation Measurement Program and the Aerosol Robotic Network." *Atmospheric Chemistry and Physics* 12 10313-10329.
- Chiu, J.C., C.-H. Huang, A. Marshak, I. Slutsker, D.M. Giles, B.N. Holben, Y. Knyazikhin, and W.J. Wiscombe. 2010. "Cloud optical depth retrievals from the Aerosol Robotic Network (AERONET) cloud mode observations." *Journal of Geophysical Research: Atmospheres* 10 11295-11303.

Bibliography

- Chow, C.W., B. Urquhart, M. Lave, A. Dominguez, J. Kleissl, J. Shields, and B. Washom. 2011. "Intra-hour forecasting with a total sky imager at the UC San Diego solar energy testbed." *Solar Energy* 85 (11) 2881-2893.
- Coakley, J.A., and P. Yang. 2014. *Atmospheric Radiation: A Primer with Illustrative Solutions*. Wiley VCH.
- Crnivec, N., and B. Mayer. 2019. "Quantifying the bias of radiative heating rates in numerical weather prediction models for shallow cumulus clouds." *Atmospheric Chemistry and Physics* 19 8083-8100.
- de Bruyn, V. 2014. Accessed 2018. <https://www.sciencelearn.org.nz/images/691-cloud-types>.
- de Miguel, A., D. Mateos, J. Bilbao, and R. Román. 2011. "Sensitivity analysis of ratio between ultraviolet and total shortwave solar radiation to cloudiness, ozone, aerosols and precipitable water." *Atmospheric Research* 102 (1) 136-144.
- de Miguel, A., R. Román, J. Bilbao, and D. Mateos. 2011. "Evolution of erythemal and total shortwave solar radiation in Valladolid, Spain: Effects of atmospheric factors." *Journal of Atmospheric and Solar-Terrestrial Physics* 73 (5-6) 578-586.
- Di Lauro, C. 2013. *Rotational Structure in Molecular Infrared Spectra*. Elsevier.
- Dubovik, O., and M.D. King. 2000. "A flexible inversion algorithm for retrieval of aerosol optical properties from Sun and sky radiance measurements." *Journal of Geophysical Research: Atmospheres* 105 (D16).
- Dupont, J.-C., M. Haefelin, E. Waersted, J. Delanoe, J.-B. Renard, J. Preissler, and C. O-Dowd. 2018. "Evaluation of Fog and Low Stratus Cloud Microphysical Properties Derived from In Situ Sensor, Cloud Radar and SYRSOC Algorithm." *Atmosphere* 9 (5) 1-19.
- Eckhardt, R. 1987. "Stan Ulam, John von Neumann, and the Monte Carlo method." *Los Alamos Science* 131-137.
- Elachi, C., and J. van Zyl. 2006. *Introduction to the Physics and Techniques of Remote Sensing, Second Edition*. John Wiley & Sons, Inc.

- Emde, C., R. Buras-Schnell, A. Kylling, B. Mayer, J. Gasteiger, U. Hamann, J. Kylling, et al. 2016. "The libRadtran software package for radiative transfer calculations (version 2.0.1)." *Geoscientific Model Development* 9 (5) 1647–1672.
- Estellés, V., J.A. Utrillas, M.P. Martínez-Lozano, and M. Campanelli. 2007. "Columnar aerosol properties in Valencia (Spain) by ground-based Sun photometry." *Journal of Geophysical Research Atmospheres* 112 (D11) 1–9.
- Estellés, V., M.P. Utrillas, J.A. Martínez-Lozano, A. Alcántara, F.J. Olmo, L. Alados-Arboledas, J. Lorente, et al. 2004a. "Aerosol related parameters intercomparison of Cimel sunphotometers in the frame of the VELETA 2002 field campaign." *Óptica pura y aplicada* 37 (3) 3289–3297.
- Estellés, V., M.P. Utrillas, J.L. Gómez-Amo, R. Pedrós, and J.A. Martínez-Lozano. 2004b. "Aerosol size distributions and air mass back trajectories over a Mediterranean coastal site." *International Journal of Remote Sensing* 25 39–50.
- Esteve, A., M.J. Marin, F. Tena, M. Utrillas, and J. Martínez-Lozano. 2010. "Influence of cloudiness over the values of erythemal radiation in Valencia, Spain." *International Journal of Climatology* 30 (1) 127–136.
- Esteve, A.R., V. Estellés, M.P. Utrillas, and J.A. Martínez-Lozano. 2014. "Analysis of the aerosol radiative forcing over a Mediterranean urban coastal site." *Atmospheric Research* 137 195–204.
- Fielding, M.D., J.C. Chiu, R.J. Hogan, G. Feingold, E. Eloranta, E.J. O'Connor, and M.P. Cadetdu. 2015. "Joint retrievals of cloud and drizzle in marine boundary layer clouds using ground-based radar, lidar and zenith radiances." *Atmospheric Measurement Techniques* 8 (7) 2663–2683.
- Finger, F., F. Werner, M. Klingebiel, A. Ehrlich, E. Jäkel, M. Voigt, S. Borrmann, P. Spichtinger, and M. Wendisch. 2016. "Spectral optical layer properties of cirrus from collocated airborne measurements and simulations." *Atmospheric Chemistry and Physics* 16 (12) 7681–7693.
- Ghonima, M. S., Urquhart, B., Chow, C. W., Shields, J. E., A. Cazorla, and J. Kleissl. 2012. "A method for cloud detection and opacity classification based on

Bibliography

- ground based sky imagery." *Atmospheric Measurement Techniques* 5 (11) 2881-2012.
- Gordy, W., and R.L. Cook. 1970. *Microwave Molecular Spectra (Techniques of Organic Chemistry S.)*. John Wiley & Sons Inc.
- Gouveia, D.A., B. Barja, H.M.J. Barbosa, P. Seifert, H. Baars, T. Pauliquevis, and P. Artaxo. 2017. "Optical and geometrical properties of cirrus clouds in Amazonia derived from 1 year of ground-based lidar measurements." *Atmospheric Chemistry and Physics* 17 (5) 3619–3636.
- Graham, S. 1999. *Earth Observatory*. March 1. Accessed 2020. <https://earthobservatory.nasa.gov/features/Clouds>.
- Grandy, W.T. 2000. *Scattering of light from large spheres*. Cambridge: Cambridge University Press.
- Gómez-Amo, J.L., V. Estellés, C.R. Marcos-Segovia, S. Segura, A.R. Esteve, R. Pedrós, M.P. Utrillas, and J.A. Martínez-Lozano. 2017. "Impact of dust and smoke mixing on column-integrated aerosol properties from observations during a severe wildfire episode over Valencia (Spain)." *Science of The Total Environment* 599-600 2121–2134.
- Höppler, L., F. Gödde, M. Gutleben, T. Kölling, B. Mayer, and T. Zinner. 2020. "Synergy of Active- and Passive Remote Sensing: An Approach to Reconstruct Three-Dimensional Cloud Macro- and Microphysics." *Atmospheric Measurement Techniques* Preprint.
- Ham, S., S. Kato, H.W. Barker, F.G. Rose, and Sun-Mack S. 2014. "Effects of 3-D clouds on atmospheric transmission of solar radiation: Cloud type dependencies inferred from A-train satellite data." *Journal of Geophysical Research: Atmospheres* 119 (2) 943-963.
- Han, Q., W.B. Rossow, and A.A. Lacis. 1994. "Near-global survey of effective droplet radii in liquid water clouds using ISCCP data." *Journal of Climate* 7 465-497.
- Hansen, J.E., and L.D. Travis. 1974. "Light scattering in planetary atmospheres." *Space Science Reviews* 16 527-610.

-
- Henderson, G. 1979. "How a Photon is Created or Absorbed." *Journal of Chemical Education* 56 (10) 631-635.
- Heney, L.G., and J.L. Greenstein. 1941. "Diffuse radiation in the Galaxy." *Astrophysical Journal* 93 70-83.
- Hogan, R.J., and J.K. Shonk. 2013. "Incorporating the Effects of 3D Radiative Transfer in the Presence of Clouds into Two-Stream Multilayer Radiation Schemes." *Journal of Atmospheric Sciences* 70 (2) 708-724.
- Holben, B.N., T.F. Eck, I. Slutsker, D. Tanré, J.P. Buis, A. Setzer, E. Vermote, et al. 1998. "AERONET - A federated instrument network and data archive for aerosol characterization." *Electrical and Computer Engineering* 66 (1) 1-16.
- Hollas, M.J. 2002. *Basic Atomic and Molecular Spectroscopy*. Cambridge: Royal Society of Chemistry.
- Holton, J.R., J.A. Curry, and J.A. Pyle. 2003. *Encyclopedia of Atmospheric Sciences*. Elsevier.
- Horvath, H. 2014. "Basic optics, aerosol optics, and the role of scattering for sky radiance." *Journal of Quantitative Spectroscopy & Radiative Transfer* 139 3-12.
- Inman, R., Y. Chu, and C.F.M. Coimbra. 2016. "Cloud enhancement of global horizontal irradiance in California and Hawaii." *Solar Energy* 130 128-138.
- IPCC. 2007. *Climate Change 2007: Synthesis Report. Contribution of Working Groups I, II and III to the Fourth Assessment Report of the Intergovernmental Panel on Climate Change [Core Writing Team, Pachauri, R.K. and Reisinger, A. (eds)]*. Environmental, Geneva, Switzerland: IPCC.
- IPCC. 2014. "Climate Change 2014: Synthesis Report. Contribution of Working Groups I, II and III to the Fifth Assessment Report of the Intergovernmental Panel on Climate Change. Pachauri, R.K.; Meyer, L.A. (eds)." Environmental, Geneva.
- IPCC. 2018. *Global Warming of 1.5°C. An IPCC Special Report on the impacts of global warming of 1.5°C above pre-industrial levels and related global*

Bibliography

- greenhouse gas emission pathways, in the context of strengthening the global response to the threat of climate change.*, Environmental, Geneva: IPCC.
- ISCCP. 2014. Accessed 2018. <https://isccp.giss.nasa.gov/cloudtypes.html>.
- Kholopov, G.K. 1975. "Calculation of the effective wavelength of a measuring system." *Journal of Applied Spectroscopy* 23 1146–1147.
- Kim, D., and V. Ramanathan. 2008. "Solar radiation budget and radiative forcing due to aerosols and clouds." *Journal of Geophysical Research Atmospheres* 113 (D02203) 1-34.
- Kniffka, A., M. Stengel, M. Lockhoff, R. Bennartz, and R. Hollman. 2014. "Characteristics of cloud liquid water path from SEVIRI onboard the Meteosat Second Generation 2 satellite for several cloud types." *Atmospheric Measurement Techniques* 7 (4) 887-905.
- Koehler, T.L., R.W. Johnson, and J.E. Shields. 1991. "Status of the whole sky imager database." *Proc. Cloud Impacts on DOD Operations and Systems—1991 Conference*. El Segundo, CA. 77-80.
- Kokhanovsky, A. 2004. "Optical properties of terrestrial clouds." *Earth-Science Reviews* 64 189-241.
- Kokhanovsky, A.A. 2001. *Light Scattering Media Optics: Problems and Solutions*. Chichester: Praxis-Springer.
- Kokhanovsky, A.A., and E.P. Zege. 1997. "Physical parameterization of local optic characteristics of cloudy media." *Izvestiya RAN, Fizika Atmosfer i Okeana* 33 209-218.
- Kreyszig, E. 2005. *Advanced Engineering Mathematics (9 ed.)*. Wiley.
- Lenoble, J. 1993. *Atmospheric Radiative Transfer*. Hampton, Va.: A. Deepak Publishing.
- . 1985. *Radiative Transfer in Scattering and Absorbing Atmospheres: Standard Computational Procedures*. Hampton, VA: A. Deepak.

-
- Leontyeva, E., and K. Stamnes. 1994. "Estimations of Cloud Optical Thickness from Ground-Based Measurements of Incoming Solar Radiation in the Arctic." *The Journal of Climate* 7 (4) 566-578.
- Lin, X., D.A. Randall, and L.D. Fowler. 2000. "Diurnal variability of the hydrologic cycle and radiative fluxes." *Journal of Climate* 13 (23) 4159-4170.
- Liou, K.N. 1992. *Radiation and Cloud Processes in the Atmosphere*. Oxford: Oxford University Press.
- Long, C.N, J.M. Samburg, J. Calbo, and D. Pages. 2006. "Retrieving cloud characteristics from ground-based daytime colour all-sky images." *Journal of Atmospheric and Oceanic Technology* 23 (5) 633-652.
- Lynch, D.K. 1996. "Cirrus clouds: Their role in climate and global change." *Acta Astronautica* 38 (11): 859-863.
- Marcos, C.R. 2017. *Determination of the vertical distribution of aerosols in Valencia, Spain, by means of lidar measurements*. Valencia: Universitat de València.
- Marcos, C.R., J.L. Gómez-Amo, C. Peris, R. Pedrós, and M.P. y Martínez Lozano, J.A. Utrillas. 2018. "Analysis of four years of ceilometer-derived aerosol backscatter profiles in a coastal site of the western Mediterranean." *Atmospheric Research* 213 (D16) 331-345.
- Marshak, A., A. Davis, W. Wiscombe, and R. Cahalan. 1995. "Radiative smoothing in fractal clouds." *Journal of Geophysical Research: Atmospheres* 100 (D12) 26247-26261.
- Marshak, A., and A. Davis. 2005. *3D Radiative Transfer in Cloudy Atmospheres*. Springer.
- Marshak, A., Y. Knyazikhin, K. D. Evans, and W. J. Wiscombe. 2004. "The RED versus NIR plane to retrieve broken-cloud optical depth from ground-based measurements." *Journal of Atmospheric Sciences* 61 (15) 1911-1925.
- Marskak, A., Y. Knyazikhin, A. Davis, W. Wiscombe, and P. Pilewskie. 2000. "Cloud-vegetation interaction: Use of normalized difference cloud index for estimation of cloud optical thickness." *Geophysical Research Letters* 27 1695-1698.

Bibliography

- Masunaga, H., T.Y. Nakajima, T. Nakajima, T. Kachi, and K. Suzuki. 2002. "Physical properties of maritime low clouds as retrieved by combined use of Tropical Rainfall Measuring Mission (TRMM) Microwave Imager and Visible/Infrared Scanner: 2. Climatology of warm clouds and rain." *Journal of Geophysical Research: Atmospheres* 107 (D10) 1-11.
- Mayer, B. 2009. "Radiative transfer in the cloudy atmosphere." *EPJ conferences* 1 75-99.
- Mayer, B., and A. Kylling. 2005. "Technical note: The libRadtran software package for radiative transfer calculations - description and examples of use." *Atmospheric Chemistry and Physics* 5 (7) 1855-1877.
- McBride, P. J., Schmidt, K. S., P. Pilewskie, A. S. Kittelman, and D. E Wolfe. 2011. "A spectral method for retrieving cloud optical thickness and effective radius from surface-based transmittance measurements." *Atmospheric Chemistry and Physics* 11 (14) 7235-7252.
- Mejia, F.A., B. Kurtz, K. Murray, L.M. Hinkelman, M. Sengupta, Y. Xie, and J. Kleissl. 2016. "Coupling sky images with radiative transfer models: a new method to estimate cloud optical depth." *Atmospheric Measurement Techniques* 9 (8) 4151-4165.
- Mejia, F.A., B. Kurtz, K. Murray, L.M. Hinkelman, M. Sengupta, Y. Xie, and J. Kleissl. 2016. "Coupling sky images with radiative transfer models: A new method to estimate cloud optical depth." *Atmospheric Measurement Techniques* 9 (8) 4151-4165.
- Mie, G. 1908. "Beiträge zur Optik trüber Medien, speziell kolloidaler Metallösungen." *Annalen der Physik* 330 (3) 377-445.
- Minnis, P. 1989. "Viewing zenith angle dependence of cloudiness determined from coincident GOES East and GOES West data." *Journal of Geophysical Research* 94 (D2) 2303-2320.
- Moosmüller, H., and C.M. Sorensen. 2018. "Small and large particle limits of single scattering albedo for homogeneous, spherical particles." *Journal of Quantitative Spectroscopy & Radiative Transfer* 204 250-255.
- Morrill, T.C., R.M. Silverstein, and G.C. Bassler. 1981. *Spectrometric Identification of organic compounds*. New York: Wiley.

- Núñez, M., M. Marín, D. Serrano, M. Utrillas, K. Fienberg, and J. Martínez-Lozano. 2016. "Sensitivity of UVER enhancement to broken liquid water clouds: A Monte Carlo approach." *Journal of Geophysical Research: Atmospheres* 121 (2) 949-964.
- NASA. 2019. *EARTHDATA LAADS DAAC*. November 2. Accessed 2020. <https://ladsweb.modaps.eosdis.nasa.gov/missions-and-measurements/modis/https://ladsweb.modaps.eosdis.nasa.gov/missions-and-measurements/modis/>.
- . 2002. *NASA Earth Science Mission*. Accessed 2020. <https://cloud1.arc.nasa.gov/solveII/implement.html>.
- Niple, E.R., H.E. Scott, J.A. Conant, S.H. Jones, F.J. Iannarilli, and W.E. Pereira. 2016. "Application of oxygen A-band equivalent width to dis-ambiguate downwelling radiances for cloud optical depth measurement." *Atmospheric Measurement Techniques* 9 (9) 4167-4179.
- Ohring, G., B. Wielicki, R. Spencer, B. Emery, and R. Datla. 2005. "Satellite Instrument Calibration for Measuring Global Climate Change: Report of a Workshop." *Bulletin of the American Meteorological Society* 86 (9) 1303-1313.
- Peach, G. 1981. "Theory of the pressure broadening and shift of spectral lines." *Advances in Physics* 30 (3) 367-474.
- Pérez-Juste, I., and O. Nieto-Faza. 2015. "Chapter 1: Interaction of Radiation with Matter." In *Structure Elucidation in Organic Chemistry: The Search for the Right Tools*, by M.M. Cid and J. Bravo. Wiley-VCH.
- Pidwirny, M. 2006. "Atmospheric Effects on Incoming Solar Radiation." *Physical Geography*. Accessed 2020. <http://www.physicalgeography.net/fundamentals/7f.html>.
- Pinsky, M.B., and A.P. Khain. 2002. "Effects of in-cloud nucleation and turbulence on droplet spectrum formation in cumulus clouds." *Quarterly Journal of the Royal Meteorological Society* 128 (580) 501-534.
- Platnick, S. 2000. "Vertical photon transport in cloud remote sensing problems." *Journal of Geophysical Research* 105 (D18) 22919-22935.

Bibliography

- Platnick, S., K.G. Meyer, M.D. King, G. Wind, N. Amarasinghe, B. Marchant, and et al. 2017. "The MODIS cloud optical and microphysical products: Collection 6 updates and examples from Terra and Aqua." *IEEE Transactions on Geoscience and Remote Sensing* 55 (1) 502-525.
- Randall, D., S. Krueger, C. Bretherton, J. Curry, M Duynkerke, M. Moncireff, B. Ryan, and et al. 2003. "Confronting models with data." *Bulletin of the American Meteorological Society* 84 455-469.
- Rauber, R.M., B. Stevens, H.T. III Ochs, C. Knight, B.A. Albrecht, A.M. Blyth, C.W. Fairall, J.B. Jensen, and et al. 2007. "Rain in Shallow Cumulus Over the Ocean: The RICO Campaign." *Bulletin of the American Meteorological Society* 88 (12) 1912–1928.
- Rawlins, F., and J.S. Foot. 1990. "Remotely Sensed Measurements of Stratocumulus Properties during FIRE Using the C130 Aircraft Multi-channel Radiometer." *Journal of Atmospheric Sciences* 47 (21) 2488-2504.
- Rayleigh, Lord. 1899. "XXXIV. On the transmission of light through an atmosphere containing small particles in suspension, and on the origin of the blue of the sky." *The London, Edinburgh, and Dublin Philosophical Magazine and Journal of Science* 47 (5) 375-384.
- Reid, J.S., P.V. Hobbs, A.L. Rango, and D.A. Hegg. 1999. "Relationship between cloud droplet effective radius, liquid water content, and droplet concentration for warm clouds in Brazil embedded in biomass smoke." *Journal of Geophysical Research* 104 (D6) 6145-6153.
- Richardson, M., and G.L. Stephens. 2018. "Information content of OCO-2 oxygen A-band channels for retrieving marine liquid cloud properties." *Atmospheric Measurement Techniques* 11 (3) 1515-1528.
- Rohde, R.A. 2016. *Global Warming Art*. Accessed 2020. https://web.archive.org/web/20160325031536/http://www.globalwarmingart.com/wiki/Global_Warming_Art>About.
- Román, R., A. Cazorla, C. Toledano, F.J. Olmo, V.E. Cachorro, A. de Frutos, and L. Alados-Arboledas. 2017. "Cloud cover detection combining high dynamic range sky images and ceilometer measurements." *Atmospheric Research* 196 238-252.

-
- Román, R., M. Antón, A. Cazorla, A. de Miguel, F.J. Olmo, J. Bilbao, and L. Alados-Arboledas. 2012. "Calibration of an all-sky camera for obtaining sky radiance at three wavelengths." *Atmospheric Measurement Techniques* 5 (8) 2013-2024.
- Rothman, L.S., I.E. Gordon, Y. Babikov, A. Barbe, D. Benner, P.F. Bernath, M. Birk, L. Bizzocchi, and et al. 2013. "The HITRAN2012 molecular spectroscopic database." *Journal of Quantitative Spectroscopy and Radiative Transfer* 130 4-50.
- Ryder, C.L. 2011. *Summary of Phase Function from scatter90 and for RFM-DISORT*. Reading, March 18.
- Schwartz, S.E., D. Huang, and D.V. Vladutescu. 2017. "High-resolution photography of clouds from the surface: Retrieval of optical depth of thin clouds down to centimeter scales." *Journal of Geophysical Research: Atmospheres* 122 (5) 2898-2928.
- Segura, S., V. Estellés, A.R. Esteve, C.R. Marcos-Segovia, M.P. Utrillas, and J.A. Martínez-Lozano. 2016. "Multiyear In-Situ Measurements Of Atmospheric Aerosol Absorption Properties At An Urban Coastal Site In Western Mediterranean." *Atmospheric Environment* 129 18-26.
- Serrano, D., M. Núñez, M.P. Utrillas, M.J. Marín, C.R. Marcos-Segovia, and Martínez-Lozano J.A. 2014. "Effective cloud optical depth for overcast conditions determined with a UV radiometers." *International Journal of Climatology* 34 3939–3952.
- Shaw, G.E. 1979. "Atmospheric Ozone: Determination by Chappuis-Band Absorption." *Journal of Applied Meteorology* 18 (10) 1335-1339.
- Shettle, E. 1989. "Models of Aerosols, Clouds and Precipitation for Atmospheric Propagation Studies." *Atmospheric propagation in the UV, Visible, IR and MM-Wave region and related systems aspects*. Copenhagen, Denmark: AGARD Conference Proceedings No.454.
- Shifrin, K.S. 1951. *Scattering of Light in a Turbid Media*. Washington DC: NASA.
- Shifrin, K.S., and G. Tonna. 1993. "Inverse problems related to light scattering in the atmosphere and ocean." *Advances in Geophysics* 175-252.

Bibliography

- Siegman, A.E. 1986. *Lasers*. University Science Books.
- Sobrino, J.A., N. Raissouni, Y. Kerr, A. Oliosio, M.J. López-Gardía, A. Belaid, M.H. El Kharraz, J. Cuenca, and L. Dempere. 2001. *Teledetección*. Valencia: Servicio de Publicaciones, Universidad de Valencia.
- Song, S., K.S. Schmidt, P. Pilewskie, M.D. King, A.K. Heidinger, A. Walther, H. Iwabuchi, G. Wind, and et al. 2016. "The spectral signature of cloud spatial structure in shortwave irradiance." *Atmospheric Chemistry and Physics* 16 (21) 13791–13806.
- Stamnes, K. 1986. "The theory of multiple scattering of radiation in plane parallel atmospheres." *Reviews of Geophysics* 24 299.
- Stamnes, K., S.C. Tsay, W. Wiscombe, and K. Jayaweera. 1988. "Numerically stable algorithm for discrete-ordinate-method radiative transfer in multiple scattering and emitting layered media." *Applied Optics* 27 (12) 2502-2509.
- Stocker, T.F., Qin, D., G.-K. Plattner, M. Tignor, S.K. Allen, J. Boschung, A. Nauels, Y. Xia, V. Bex, and P.M. (eds.) Midgley. 2013. *IPCC, 2013: Climate Change 2013: The Physical Science Basis. Contribution of Working Group I to the Fifth Assessment Report of the Intergovernmental Panel on Climate Change*. Environmental, Cambridge and New York: Cambridge University Press.
- Twomey, S. 1977. "The influence of pollution on the shortwave albedo of clouds." *Journal of the Atmospheric Sciences* 34 (7) 1149-1152.
- Utrillas, M.P. 1995. *Estudio de los aerosoles a partir de las medidas de irradiancia solar espectral. Tesis Doctoral, Departament de Termodinàmica*. Valencia: Universitat de València.
- Vaisala, O. 2010a. *Sky Condition Algorithm for Vaisala Ceilometer's*. Helsinki.
- . 2010b. *Vaisala Ceilometer CL51 User's Guide*. Helsinki.
- Van de Hulst, H.C. 1957. *Light scattering by small particles*. New York: John Wiley & Sons.
- . 1980. *Multiple Light Scattering: Tables, Formulas and Applications*. New York: Academic Press.

-
- Wacker, S., J. Gröbner, C. Zysset, L. Diener, P. Tzoumanikas, A. Kazantzidis, L. Vuilleumier, R. Stoeckli, S. Nyeki, and N. Kämpfer. 2015. "Cloud observations in Switzerland using hemispherical sky cameras." *Journal of Geophysical Research* 120 695-707.
- Wallace, J.M., and P.V. Hobbs. 2006. *Atmospheric Science: An Introductory Survey*. Academic Press.
- Wapler, K., and B. Mayer. 2008. "A Fast Three-Dimensional Approximation for the Calculation of Surface Irradiance in Large-Eddy Simulation Models." *Journal of Applied Meteorology and Climatology* 47 (12) 3061-3071.
- Werkmeister, A., M. Lockhoff, M. Schrempf, K. Tohsing, B. Liley, and G. Seckmeyer. 2015. "Comparing satellite- to ground-based automated and manual cloud coverage observations – a case study." *Atmospheric Measurement Techniques* 8 (5) 2001-2015.
- Whitman, W. 2011. *National Science Foundation*. May 11. Accessed January 2018. https://www.nsf.gov/news/news_summ.jsp?cntn_id=119462.
- Wielicki, B.A., and L. Parker. 1992. "On the determination of cloud cover from satellite sensors: The effect of sensor spatial resolution." *Journal of Geophysical Research: Atmospheres* 97 (D12) 12799-12823.
- Wild, M., D. Folini, C. Schär, N. Loeb, E.G. Dutton, and G. König-Langlo. 2012. "The global energy balance from a surface perspective." *Climate Dynamics* 40 3107-3134.
- Wild, M., D. Folini, M.Z. Hakuba, and et al. 2015. "The energy balance over land and oceans: an assessment based on direct observations and CMIP5 climate models." *Climate Dynamics* 44 3393-3429.
- Winker, D.M., M.A. Vaughan, A. Omar, Y. Hu, K.A. Powell, Z. Liu, W.H. Hunt, and S.A. Young. 2009. "Overview of the CALIPSO Mission and CALIOP Data Processing Algorithms." *Journal of Atmospheric and Oceanic Technology* 26 (11) 2310–2323.
- WMO. 2008. *Guide to meteorological instruments and methods of observation (WMO-No.8)*. World Meteorological Organization.

Bibliography

- . 2017. *International Cloud Atlas*. Accessed 2018. <https://cloudatlas.wmo.int/home.html>.
- Wood, R., and D.L. Hartmann. 2006. "Spatial variability of liquid water path in marine low cloud: The importance of mesoscale cellular convection." *The Journal of Climate* 19 (9) 1748-1764.
- Woodhouse, I.H. 2006 . *Introduction to Microwave Remote Sensing*. CRC Press.
- Zeng, S., C. Cornet, F. Parol, J. Riedi, and F. Thieuleux. 2012. "A better understanding of cloud optical thickness derived from the passive sensors MODIS/AQUA and POLDER/PARASOL in the A-Train constellation." *Atmospheric Chemistry and Physics* 12 (23) 11245-11259.
- Zuidema, P., and K.F. Evans. 1998. "On the validity of the independent pixel approximation for boundary layer clouds observed during ASTEX." *Journal of Geophysical Research* 103 (D6) 6059-6074.

Clouds affect significantly the Earth's radiative budget and its influence on incoming climate change remains unknown. Its systematic, widespread study using ground-based instruments is vital to overcome the uncertainties associated to the cloud's radiative properties.

These advances in clouds' research go through taking a step beyond the 1D, plane-parallel approaches, towards the studies of more realistic atmospheres with the help of 3D Radiative Transfer Models.